

**EUV and X-ray Observations
of Late-Type Stars**

Thesis submitted for the degree of
Doctor of Philosophy
at the University of Leicester.

by

Simon T. Hodgkin
X-ray Astronomy Group
Department of Physics and Astronomy
University of Leicester

June 1995

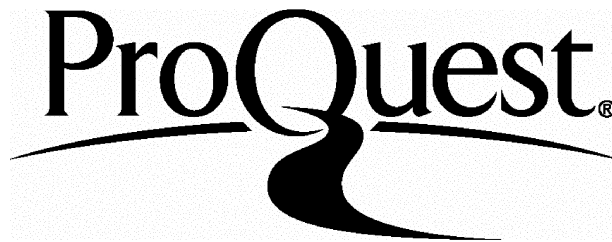
ProQuest Number: U072553

All rights reserved

INFORMATION TO ALL USERS

The quality of this reproduction is dependent upon the quality of the copy submitted.

In the unlikely event that the author did not send a complete manuscript and there are missing pages, these will be noted. Also, if material had to be removed, a note will indicate the deletion.



ProQuest U072553

Published by ProQuest LLC(2015). Copyright of the Dissertation is held by the Author.

All rights reserved.

This work is protected against unauthorized copying under Title 17, United States Code.
Microform Edition © ProQuest LLC.

ProQuest LLC
789 East Eisenhower Parkway
P.O. Box 1346
Ann Arbor, MI 48106-1346



EUV and X-ray Observations of Late-Type Stars

Simon T. Hodgkin

ABSTRACT

In this thesis I describe a number of projects arising from the ROSAT mission, inspired by a desire to understand better the activity of late-type stars from studies of their coronal EUV and X-ray emission.

A brief introduction summarises some of the most important work on cool star coronae. The second chapter describes the mechanisms by which X-rays are produced in coronal plasmas. I also discuss the ROSAT mission, its instrumentation and applicability for observing cool stars.

In Chapter 3 I describe the discovery of one of the brightest sources in the EUV sky, the hot white dwarf companion to HD 33959C. I discuss the importance of such binaries for the determination of more accurate measurements of mass, radius and distance than is possible for isolated white dwarfs. Chapter 4 is a WFC survey of all known late-type stars within 25 parsecs of the Sun. I construct and discuss the first ever EUV luminosity functions for such a sample and show that stars in interacting binaries are more active than single stars. In Chapters 5 and 6 I present a deep PSPC survey of the Hyades, comprising 11 overlapping pointings. In Chapter 5 I derive the Hyades dK and dM X-ray luminosity functions down to $L_X \sim 5 \times 10^{27}$ erg s⁻¹. In Chapter 6 I investigate the X-ray spectra of the more luminous Hyads, both non-parametrically using hardness ratios, and parametrically using simple one-temperature and two-temperature fits to the data. Flares were observed in VB 50 and VA 334; both stars show increases in temperature and emission measure during the flaring episodes.

In Chapter 7 I summarise my conclusions and discuss projects which arise from the work presented in this thesis. Finally I describe some of the impacts that we may expect to see from three future missions, *JET-X*, *AXAF* and *XMM*.

Declaration

I hereby declare that no part of this thesis has been previously submitted to this or any other university as part of the requirement for a higher degree. The work described herein was conducted by the undersigned except for contributions from colleagues and other workers who are acknowledged in the text.

Simon T. Hodgkin
June 1995

To Jenny, Judy, Jessie, Dossie, Matty

Contents

1 Introduction	1
1.1 Stellar X-ray astronomy pre-ROSAT	1
1.2 The Sun as a star	3
1.3 X-ray emission across the HR diagram	6
1.4 Characteristics of cool-star coronae	9
1.4.1 Coronal temperatures	9
1.4.2 Spatial structures	10
1.4.3 X-ray variability	11
1.5 The activity-rotation-age paradigm	13
1.6 EUV astronomy	14
1.7 Outline of the thesis	15
2 Observing cool stars with ROSAT	17
2.1 X-ray/EUV emission from an optically thin thermal plasma	17
2.2 The local interstellar medium	18
2.3 The ROSAT mission	20
2.4 The WFC	22
2.4.1 Filters	22

2.4.2	Background	25
2.4.3	The all-sky survey	25
2.4.4	The efficiency history of the WFC	28
2.5	The PSPC	29
2.5.1	The Point Spread Function	31
2.5.2	Background	31
2.5.3	Spectral capabilities	32
2.5.4	The all-sky survey	33
2.6	Summary	34
3	ROSAT/IUE discovery of a white dwarf companion to HD 33959C	36
3.1	Introduction	36
3.2	Observations and data analysis	37
3.2.1	ROSAT EUV and X-ray sky survey	37
3.2.2	Optical CCD images	38
3.2.3	Optical high resolution spectra	40
3.2.4	IUE spectra	40
3.2.5	ROSAT pointed observations	42
3.3	Parameters of the white dwarf	42
3.4	Discussion	46
4	An EUV survey of nearby late-type stars	48
4.1	Introduction	48
4.2	Constructing a sample	49
4.2.1	Completeness	50

4.2.2	Multiplicity: spectroscopic binaries	52
4.3	Measurement of counts	55
4.3.1	The problem	55
4.3.2	Description of technique	55
4.3.3	Source recognition and upper limits	58
4.3.4	Multiplicity: visual binaries	62
4.4	Flux conversion	63
4.5	Results	65
4.5.1	The complete sample	65
4.5.2	Comparison with the WFC-BSC	65
4.5.3	L_{EUV} dependance on colour	68
4.5.4	Correlation of L_{EUV} with absolute magitude and bolometric luminosity.	68
4.5.5	Kinematics of the EUV sources	72
4.6	Survival analysis	73
4.7	The EUV luminosity functions	75
4.7.1	Summary of simulations	79
4.7.2	Effects of multiplicity	80
4.7.3	Comparison with <i>Einstein</i> X-ray luminosity functions	80
4.7.4	logN-logS distribution	88
4.7.5	K-Star discrepancy	91
4.7.6	dM stars	94
4.7.7	Relative contributions	95
4.8	Summary	95
5	ROSAT observations of the Hyades: 1. A statistical study	100

5.1	Introduction	100
5.2	Previous X-ray observations	101
5.3	The optical catalogue	104
5.4	ROSAT pointed observations and source identifications	105
5.4.1	Source detection and identification	107
5.5	XLFs of the dK & dM stars	109
5.5.1	Definition of the sample	111
5.5.2	The XLFs	111
5.5.3	Test of results	114
5.5.4	The XLFs in summary	117
5.5.5	Coronal activity in the coolest stars	118
6	ROSAT observations of the Hyades: 2. Spectra	121
6.1	Introduction	121
6.2	Procedure	123
6.3	Results	125
6.3.1	Hardness ratios	125
6.3.2	One-temperature fits	127
6.3.3	Two-temperature fits	132
6.3.4	Spectral variability	140
6.4	Discussion	143
6.4.1	Cluster membership	145
6.4.2	The giants	145
6.4.3	Effect of a multi-temperature model on the derived X-ray luminosity . . .	146

7	Concluding remarks and future prospects	148
A	<i>ROSAT</i> EUV-detected nearby stars	153
B	Simulations	162
B.1	Aims	162
B.2	Procedure	163
B.3	Results	164
B.4	Discussion	166

Chapter 1

Introduction

1.1 Stellar X-ray astronomy pre-ROSAT

The temperature of the Solar corona was first determined – not by X-ray observations – but through the identification of “coronium” lines seen in the visible solar spectrum during eclipses. Grotrian & Edlén identified these lines as atomic transitions in highly ionized iron and calcium at million degree temperatures (e.g. Grotrian 1939, Edlén 1942). The average density of the corona falls from about $1.7 \times 10^{-16} \text{ g cm}^{-3}$ (electron/proton density $\sim 10^8 \text{ cm}^{-3}$) at $1.1 R_{\odot}$ to $5 \times 10^{-19} \text{ g cm}^{-3}$ (electron/proton density $\sim 3 \times 10^5 \text{ cm}^{-3}$) at $3 R_{\odot}$. The high temperature of the corona compared with the relatively cool (5800 K) photosphere requires a non-thermal energy input.

The first detections of the Sun in X-rays were obtained from sounding rocket flights made by a number of groups in the 1960's. Rocket-based X-ray observations of the Sun (e.g. Vaiana et al. 1968, Van Speybroeck, Krieger & Vaiana 1970) as well as high resolution data obtained by the EUV and X-ray instruments on board *Skylab* (Reeves 1976, Vaiana et al. 1973) first showed the corona to be composed of a variety of complex looplike structures generally associated with the underlying chromospheric and photospheric features, in particular, magnetic field structures. The intensity of the X-ray emission seemed to be directly related to the magnetic field configuration; strong X-ray emission was found in the neighbourhood of large field complexity, while the regions of weakest coronal X-ray emission corresponded to photospheric regions devoid of magnetic activity. Thus a solar coronal model was suggested to comprise of magnetically confined

small-scale "coronae" of differing temperature and pressure by, among others, Rosner, Tucker & Vaiana (1978). Taking loops as the basic coronal building block, Rosner, Tucker & Vaiana argued that magnetic field related heating theories *alone* were consistent with the observations and that models based on coronal heating via the dissipation of acoustic modes were inconsistent.

Before 1979 only a few stellar coronal X-ray sources were known. The coronae of Capella (Catura, Acton & Johnson 1975) and α Cen (Nugent & Garmire 1978) could still be explained by an acoustic heating mechanism. The detection by HEAO-1 of high temperature components in the coronae of RS CVn systems (Walter et al. 1980) indicated the need for a non-gravitational confinement.

In 1978 the *Einstein* Observatory was launched carrying an imaging proportional counter (IPC: Gorenstein, Harnden & Fabricant 1981), a high resolution imager (HRI) and two spectrometers – a solid state spectrometer (SSS) and an objective grating spectrometer (OGS). The IPC demonstrated the pervasiveness of X-ray emission throughout the HR diagram. The results of an X-ray survey of 150 stars were reported by Vaiana et al. (1981). They concluded that, with the exception of late-B/early-A main sequence stars and late giants and supergiants, all stars are X-ray emitters. Further, they showed that the high levels of X-ray emission could not be explained in terms of acoustic heating. Additionally, at a given spectral type, X-ray luminosity (0.3–3.5 keV) was observed to vary by orders of magnitude, whereas acoustic heating should be a unique function of spectral type. An alternate mechanism, probably magnetic (in line with thinking in the Solar case), was required. The Solid State Spectrometer (SSS) on *Einstein* confirmed thermal line emission from Capella with the identification of Mg, Si, S, and Fe features (Holt et al. 1979). It also showed that the gas was not isothermal. Most of the emission was consistent with $\sim 5 \times 10^6$ K, but about a tenth of the luminosity was at a higher energy and could be explained by a 5×10^7 K gas.

EXOSAT flew between 1983 and 1986 providing long (several day) uninterrupted observations made possible by its highly eccentric orbit. *EXOSAT* carried a low energy experiment (LE), a medium energy array (ME) and a transmission grating spectrometer (TGS). The LE had imaging capabilities, but no intrinsic spectral resolution, although a number of filters allowed broad band photometry in the range $\sim 0.04 - 2$ keV. The ME was an array of eight proportional counters with a total collecting area of 1600 cm^2 and a spectral resolution of $\Delta E/E = 0.25$ at 3

keV, providing coverage from 1 to 20 keV. The TGS permitted the study of line complexes over a wide wavelength range from 10 to 300 Å (0.04–1.2 keV) with approximately 3 Å resolution ($\Delta E/E = 0.01$ at 300 Å and 0.5 at 10 Å). The TGS obtained spectra for two RS CVn systems (Capella and σ CrB) and for Procyon (e.g. Schrijver, Lemen & Mewe 1989, Lemen et al. 1989) confirming the multi-temperature nature of these coronae.

The Japanese satellite *Ginga*, operating between 1987 and 1991, has detected relatively few coronal sources with the LAC (large area counter) due to the low count-rates obtained from relatively soft and low-luminosity sources. The LAC consisted of eight sealed Be-window collimated proportional counters, having a total peak effective area of ~ 4000 cm² and a $1.08^\circ \times 2.0^\circ$ FWHM field of view. The LAC is sensitive to X-rays in the range 1.2–37 keV with an energy resolution of 18% at 5.9 keV (see Turner et al. 1989). Tsuru et al. (1989) provided the first evidence of a lower than expected and variable high-temperature Fe XXV–XXVI equivalent width during two flares on UX Ari. A similar effect is found for Algol by Stern et al. (1992b), the observed equivalent width is lower than predicted using solar abundances. *Ginga* has shown that there is a significant amount of material in the coronae of active stars with temperatures around 3×10^7 K. During flares, temperatures reach as high as 8×10^8 K.

The observational database provided by HEAO-1, *Einstein*, *EXOSAT* and *Ginga* has provided astronomers with an invaluable resource from which a coherent description of stellar coronal physics has now begun to emerge. In Table 1.1 I summarise the instruments flown in the pre-ROSAT era.

1.2 The Sun as a star

The Sun was the first star to be observed at X-ray wavelengths. Fig. 1.1 shows a soft X-ray image of the solar corona obtained with the Japanese Yohkoh satellite. Some of the structures visible in this image include active regions, coronal loops and arcades. The darkest region extending from the south pole to north of the solar equator is a large coronal hole. Coronal holes have lower densities (by a factor 3 or more) and lower temperatures (about 10^6 K as compared to 1.5 to 3×10^6 K) than the surrounding regions.

The solar corona is a useful starting point in understanding the structure of stellar coronae.

Table 1.1: X-ray orbiting detectors flown pre-ROSAT (adapted from Bradt, Ohashi & Pounds, 1992).

Mission	Dates	X-ray Instruments
OSO-3	1967–1968	H
OSO-5	1969–1972	H
Vela Series	1969–1979	M
Uhuru	1970–1973	M
OSO-7	1971–1973	M, H
Copernicus	1972–1981	M, C
ANS	1974–1976	L, M, C, B
Ariel V	1974–1980	M, B, Pol, SM, MC
SAS-3	1975–1979	L, M, MC, C
OSO-8	1975–1978	L, M, H, B, Pol
HEAO-1	1977–1979	L, M, H, MC
Einstein (HEAO-2)	1978–1981	F, IPC, HRI, B, SSS, M, TG
Ariel VI	1979–1981	L, M, C
Hakucho	1979–1984	M, MC, SM
Tenma	1983–1984	L, M, G, C, SM, MC
EXOSAT	1983–1986	L, M, G, F, TG
Ginga (ASTRO-C)	1987–1991	M, SM
Röntgen/Kvant	1987–	M, H, CM, G
Granat	1989–	M, H, CM
ROSAT	1990–	F, HRI, IPC, WFC
ASTRO-1	1990	F, SSD

Key B - Bragg crystal spectroscopy; C - collector (reflecting); CM - coded-mask imaging; F - focusing optics; G - gas scintillation proportional counter; H - high-energy (10-200 keV) crystal scintillator; HRI - high resolution imager; IPC - imaging proportional counter; L - low-energy (0.1-1 keV) proportional counter; M - medium energy (1-20 keV) proportional counter; MC modulation collimator; Pol - polarimetry; SM - sky monitor; SSD - solid-state detector; SSS - solid-state spectrometer; TG - transmission gratings; WFC - EUV wide-field camera.

Withbroe & Noyes (1977) showed that the relationship between the topology of the solar magnetic field and the physical parameters of the corona (size, temperature, density) is a very strict one. Virtually all of the solar coronal X-ray emission comes from topologically closed magnetic structures (loops), with regions of open field lines characterised by substantially lower X-ray fluxes (Maxson & Vaiana 1977). Thus, the solar corona is an ensemble of these loops whose physical parameters (length, field strength, plasma temperature and density) are determined by the behaviour of the magnetic field, not only in terms of topology, but very likely the major energy input to the corona is also magnetic in origin.

Even on the Sun we do not fully understand the mechanism(s) which heat the corona. Where field lines are closed and twisted, energy may be released by the dissipation of electric currents



Figure 1.1: Yohkoh soft X-ray image of Sun

or by annihilation and recombination of magnetic fields. In magnetically open regions, such as coronal holes, some form of wave heating may be responsible – magnetohydrodynamic (MHD) waves could both heat the plasma and accelerate the solar wind. The temperature distribution within a coronal loop is then determined by the energy balance between the heat input and the cooling mechanisms of electromagnetic radiation (seen as X-rays) and heat conduction to the lower stellar atmosphere. However, as summarised by Ulmschneider (1991), atmospheric heating by acoustic shock waves is viable in many types of stars. On the Sun and in other stars there is likely to be a basal level of acoustic heating (Schrijver 1987) and may actually dominate in certain types of star and in certain regions of the Sun (Schrijver 1992). For example Mathioudakis et al. (1994) are examining the possibility that the M dwarf HD 4628 may be acoustically heated

since it was detected by EUVE but is not an X-ray source.

Applications of the solar analogy to other stars requires, as a minimum, the existence of a similar internal structure, i.e. the presence of an outer convective zone. Coupling of (differential) rotation and convection with existing ambient magnetic fields leads to a regenerative magnetic dynamo. These fields rise to the surface by magnetic buoyancy, as magnetic flux tubes, which rise above the photosphere forming loops.

If the Sun is a typical late-type dwarf, what would observers have expected to see in the first ever X-ray survey of cool stars? The Sun's mean soft X-ray luminosity (integrated over the whole disk) is $\sim 2 \times 10^{27} \text{ ergs s}^{-1}$ and is observed to vary by approximately one order of magnitude over a complete activity cycle. The flux limit of a typical *Einstein* pointing (or the ROSAT all-sky survey) would place the detection limit of the Sun at a distance of about 9 parsecs. Surprisingly, the *Einstein* stellar surveys found that the Sun lies near the bottom end of the observed range of X-ray luminosities for late-type stars (the luminosity functions span over three orders of magnitude) and most detected stars are beyond 9 parsecs.

1.3 X-ray emission across the HR diagram

X-ray emission is prevalent amongst most types of stars, and can be summarised in the points below. Fig. 1.2 is reproduced from Linsky (1990) and shows X-ray emission throughout the HR diagram.

Main Sequence

- **O–B:** All stars earlier than roughly B5 are found to be X-ray emitters with luminosities in the range 10^{26} to $10^{34} \text{ ergs s}^{-1}$. Harnden et al. (1979) showed that the ratio of L_X (X-ray luminosity) to L_{bol} is $\sim 10^{-7}$, independent of luminosity class. O–B stars should not undergo the dynamo action seen in later-type (F and cooler) stars with outer convective zones. Though they may possess a corona at the base of their outer atmosphere, their X-ray emission is more likely to come from the shock-heated material in a strong stellar wind.

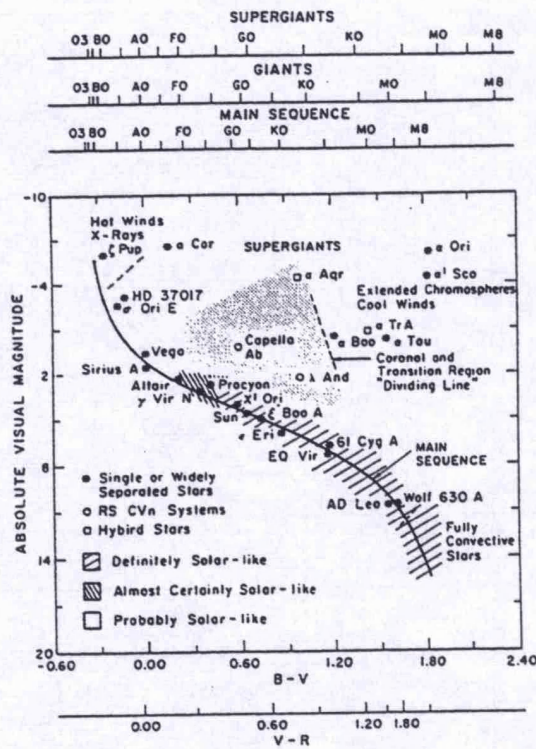


Figure 1.2: An H-R diagram showing the location of different types of stars. Regions of the diagram where magnetic fields have definitely been measured are labelled “definitely solar-like.” Also two of the Bp stars with both measured fields and non-thermal radio emission are HD 37017 and σ Ori E. Stars for which magnetic fields are probably present but not yet measured are labeled “almost certainly solar-like” or “probably solar-like.” **Diagram and Caption taken from Linsky (1990).**

- **B7–A5:** Appear not to be X-ray emitters at a detectable level. Almost all apparent exceptions have been shown to be binary systems with faint cooler companions as the likely X-ray emitters. The general lack of X-ray emission is in accord with expectations of no dynamo action in stars lacking convection zones.
- **Late-A/Early-F:** Schmitt et al. (1985) report the results of a survey of stars with shallow convection zones. They concluded that the onset of detectable stellar coronae begins at around spectral type F0V. Only weak evidence for a correlation of L_X with rotation was found. Walter & Shrijver (1987) argue that a non-magnetic heating process, perhaps simple acoustic waves, is increasingly more important in the hotter F stars until it disappears rapidly for stars just hotter than $B-V=0.30$.

- **dF–dM:** The X-ray luminosity functions (see e.g. Rosner, Golub & Vaiana 1985) are consistent with all stars being X-ray emitters with L_X between roughly 10^{26} and 10^{31} ergs s^{-1} .
- **dM4 and Beyond:** Stars with spectral types later than this are fully convective (see e.g. Liebert & Probst 1987) and hence the mechanism for magnetic flux generation is expected to change from a shell dynamo (Parker 1975; Golub et al. 1981) to a distributive dynamo (Rosner 1980) or a fibril dynamo (Weiss 1993). Various authors have looked for a signature of this change using X-rays as a proxy for magnetic activity (e.g. Barbera et al. 1993; Hodgkin, Jameson & Steele 1995; Fleming 1993). All have found that at least some very low mass stars can support coronae that are as active as those found in stars with radiative cores.

Giants

A ‘coronal dividing line’ was discovered by Ayres et al. (1981) and Haisch & Simon (1982) as a line separating X-ray emitting yellow giants and supergiants from non X-ray emitting red giants and supergiants. This discovery was preceded by the discovery of a ‘wind dividing line’ with the IUE satellite (Linsky & Haisch 1979), i.e. a line separating giants with evidence for transition region temperature material in their ultraviolet spectra from giants showing evidence of massive cool winds (but no warm or hot material). Both dividing lines lie at the same position in the H–R diagram, passing through spectral type K2 III.

Close binaries:

- **Detached – RS CVn’s:** These are the most X-ray luminous non-degenerate stars, with L_X in the range 10^{30} to a few 10^{31} ergs s^{-1} . Most are synchronous rotators with periods of less than a day up to weeks. The class was defined by Hall (1976, 1981) to contain an evolved G/K IV star with an F/G IV/V companion. See Majer et al. (1986), Dempsey et al. (1993a, 1993b) for discussions of their X-ray properties.
- **Semi-Detached – Algols:** Algol itself has a period of 2.87 days and consists of a B8 V primary and a K2 IV secondary which fills its Roche lobe. *EXOSAT* observations of Algol covering the secondary optical eclipse showed evidence for a very shallow X-ray eclipse,

suggesting a large scale for the X-ray emitting region (White et al. 1986). Large X-ray flares have been observed with *EXOSAT* and *Ginga* (Stern et al. 1992b).

- **Late-type contact – W UMa’s:** These systems are not as bright in X-rays as RS CVn’s despite faster rotation (periods are typically 6–8 hours) and greater chromospheric flux. The stars share a common outer envelope which gives both components similar effective temperature (and therefore spectral type) despite mass-ratios which are nearly always less than unity. The most complete X-ray survey of W UMa systems published to date is the *Einstein* survey, Cruddace & Dupree (1984). A recent review is given by Rucinski (1993).
- **BY Dra, UV Cet type systems:** These systems are generally active (i.e. flaring, spotted) single or binary dK/dM stars. They show X-ray luminosities comparable with those measured for young rapidly rotating dK/dM stars in the Hyades and Pleiades, and are themselves characterised by rapid rotation – either arising from their youth or from tidal interactions in close binaries, see e.g. Jeffries & Bromage (1993), Bromage et al. (1992).

Pre-main sequence stars

Montmerle et al. (1983) showed the extreme variability of pre-main sequence (PMS) stars on timescales as short as one day. Their high luminosities ($L_X \sim 10^{29}$ to 10^{31} ergs s⁻¹) can be ascribed to the large surface areas of these still contracting stars. Their X-ray properties have been recently reviewed by Walter (1993).

1.4 Characteristics of cool-star coronae

1.4.1 Coronal temperatures

The combination of limited spectral resolution and no spatial resolution severely inhibits the extent to which the physical attributes of stellar (and non-stellar) coronal plasmas can be deduced. However, even the very modest energy resolution of the *Einstein* IPC showed that single-component temperature models for stellar X-ray spectra are generally inadequate provided one has sufficient signal-to-noise (see e.g. Schmitt et al. 1990a), and often a bimodal temperature distribution is required. Schmitt et al. (1990a) and Majer et al. (1986) have argued that this bimodality is in fact instrumental in origin. Majer et al. (1986) reason that any

given coronal loop structure must be characterised by an internal temperature distribution, and hence by a fractional distribution of matter (the differential emission measure or DEM; Jordan 1976, Withbroe 1975) as a function of temperature. Furthermore, taking our Solar analogy, we have a superposition of loops with different mean properties (i.e. length, mean temperature, mean gas pressure). The result is a convolved DEM distribution, which for a spatially unresolved steady source cannot be deconvolved into its component constituents. Thus for a moderate energy resolution instrument, we detect a multicomponent temperature distribution; the best fit temperature components found are strongly dependent on the number and energy of well-distinguished spectral windows in the detector (the IPC had two, centred at roughly 0.2 and 1.5 keV). The data obtained with the pre-ROSAT detectors indicate that the coronae of late-type stars are characterised by a broad range of plasma temperatures, from $T \sim 10^6$ K to $T > 3 \times 10^7$ K. Swank et al. (1981) were able to obtain *Einstein* SSS spectra of seven RS CVn systems and Algol. The spectra cannot be fit well by an isothermal plasma, but each can be fit by a two-temperature plasma with $\log T_{\text{cool}} = 6.6 - 6.9$ and $\log T_{\text{hot}} = 7.3 - 8.0$ (T_{hot} is poorly constrained). Swank (1985) has argued that the bimodality is not an artifact of the limited spectral resolution of the SSS, because fits to the spectra with emission measure distributions including appreciable plasma at intermediate temperatures are poorer than the fits with bimodal distributions. This view is supported by Lemen et al. (1989) in their analysis of *EXOSAT* TGS spectra of Capella, σ CrB and Procyon. It is perhaps significant that the strongest evidence for truly bimodal temperature distributions comes from the spectra of RS CVn systems. Additionally, White et al. (1990) have argued that the observations of eclipsing binary systems with *EXOSAT* provide direct evidence that the two-temperature solutions found from spectral fits refer to spatially separated structures in the coronae of such systems.

1.4.2 Spatial structures

Except for the Sun, we have very limited knowledge of coronal spatial structures. Eclipsing binary systems, however, lend themselves to mapping techniques where we may attempt to determine X-ray emitting spatial structures. An example of this is the *EXOSAT* study of AR Lac discussed by White et al. (1990). They report observing a definite X-ray eclipse at low energies (< 1 keV) during primary minimum and a smaller decrease preceding the secondary minimum. At higher energies (> 1 keV) no significant orbital modulation of X-ray eclipses are

evident in the data, indicating that the high temperature plasma envelopes the whole binary. Modelling of the low energy X-ray modulation suggests multiple solutions for the distribution of the cooler plasma which must be constrained much closer to the stellar surfaces. The same technique has been applied to AR Lac with ROSAT (Ottmann, Schmitt & Kuerster 1993). They find that the phase-resolved spectra are well described by two-temperature models, with mean temperatures at 3×10^6 K and 1.4×10^7 K; both temperatures appear to be phase-invariant. Modelling of the eclipses leads to the conclusion that the spatial extent of both temperature components can be inferred to lie well below the dimension of the binary system. The best fit model suggests one prominent emitting feature on each star with scale heights of $0.03 R_{\odot}$ and $1.9 R_{\odot}$ on the G and K stars respectively. Both stars are found to contribute approximately equally to the system's total intensity. Studies like this prove very valuable, but need to be coordinated with optical and UV measurements to fully map stellar atmospheres from chromosphere through transition region to corona.

1.4.3 X-ray variability

Rotational Modulation

Taking the Sun as a prototype we would expect to see large variations in quiescent stellar X-ray emission due to rotational modulation (factors of 10) and stellar cycles (factors of 10) in addition to short term dramatic flaring events. But the X-ray observations obtained so far do not support the existence of such large variations in the quiescent emission of most stars. Before ROSAT, nearly all X-ray detected coronal sources were found to be very active stars ($\sim 1\%$ of the stars detected by *Einstein* emit at levels as low as the Sun). The amplitude of the variations that can be detected in the quiescent emission of stars depends on the fraction of the surface covered by active regions. A few observations of rotational modulation stand out. Barstow et al. (1992) report the results of ROSAT WFC all-sky survey observations of the active binaries BY Dra and HR1099. Both observations show periodic variability from rotational modulation of active regions and non-periodic activity in the form of large flares. Variability in EUV emission due to rotational modulation has been detected by EUVE in the RS CVn system HR 1099 (V711 Tau). Drake et al. (1994) find evidence for $\sim 40\%$ modulation in the 100\AA flux, with minimum flux occurring near phase $\phi = 0.5$ and maximum flux at $\phi \sim 0.0$. Their interpretation is that the

EUV modulation arises from a long-lived, compact, and bright coronal structure on the more active component in the system.

Flares

Extensive analysis of *Einstein* and *EXOSAT* data (Haisch 1983, Pallavicini, Tagliaferri & Stella 1990) has shown that the light curves, time scales and flare temperatures are all similar to those typically observed in solar flares, but the released energies are often orders of magnitude greater. The peak temperatures are usually in the range $2-4 \times 10^7$ K, although higher temperatures have occasionally been reported for some flares on RS CVn and Algol-type systems (e.g. Stern 1992). Typical time scales range from several minutes to a few hours and there is some indication of the existence of different classes of stellar X-ray flares, similar to the Solar compact and 2-ribbon events (Pallavicini et al. 1990). The total energies released in the X-ray passband range from 10^{30} to 10^{34} ergs for flares on dMe stars and from 10^{35} to 10^{36} ergs for flares on RS CVn binaries and PMS objects. For comparison the typical energies of Solar X-ray flares are 10^{28} to 10^{31} ergs. The events observed on RS CVn binaries and PMS objects are usually more energetic and longer-lived than those observed on dMe stars; smaller shorter-lived events cannot be observed on these systems due to the high levels of quiescent emission.

Stellar cycles

The HK Project (begun by O. C. Wilson in 1966) has been investigating variations in the Ca II H and K chromospheric levels in cool dwarfs. The results (see e.g. Baliunas & Jastrow 1990) show that the majority of dwarf stars undergo fluctuations that are apparently or possibly cyclic, with periods that range from 2.5 years to as long as 20 years. Only stars more massive than the Sun are found to exhibit cyclic periods shorter than five years. About one-third of the stars at solar age are essentially constant, in agreement with tree-ring measurements which indicate that the Sun spends about one-third of its life in a state of little or no cycle variability, exemplified by the Maunder Minimum. The relative youth of X-ray astronomy combined with competition for observing time has all but ruled out similar monitoring projects at X-ray wavelengths. Gagné, Caillault & Stauffer (1995) compare all X-ray observations of the Pleiades giving sampling timescales of ~ 16 days, ~ 12 months and ~ 10 years. They find evidence for both short-term variability (hours to days) probably arising from flaring, and long-term variability (months to

years) which could tentatively be ascribed to solar-like coronal activity cycles.

1.5 The activity-rotation-age paradigm

Since the beginning of the 1980's, astronomers have attempted to explain the dependence of X-ray emission on fundamental stellar parameters. This has been a difficult and confusing task, and is by no means fully resolved. However in recent years a more coherent and satisfactory picture has begun to emerge. An important review article by Simon (1992) summarises those results which combine to define our current understanding. In 1972 Skumanich published his paper on the 'square root relations' for the time decay of stellar rotation and chromospheric activity. These empirical relations suggested that the rotational velocity and strength of the chromospheric Ca II H & K emission of a late-type star decay with the square root of the star's age. This has now been shown to be inconsistent with detailed measurements of rotation velocities of stars in open clusters. Observations of the rotation velocities of pre-main sequence stars and low mass stars in young clusters have shown that stars arrive on the ZAMS with a wide range in their intrinsic rotation rates. It seems likely that those stars with the fastest rotation suffer the strongest braking, while the slower rotators suffer the least. This is seen clearly in the Pleiades (age 70 Myr) and the Hyades (age 800 Myr). Stauffer & Hartmann (1987) have shown that the $1M_{\odot}$ Pleiads exhibit a broad distribution of rotational velocities, while the $1M_{\odot}$ Hyads tend towards a narrow range of nearly uniform rotation. Stauffer (1994) summarises the results of observations in three open clusters as follows:

(a) very rapid rotators ($v \sin i > 100 \text{ km s}^{-1}$) exist at all spectral types in the youngest of the three clusters, α Persei (age ~ 50 Myr); (b) relatively rapid rotators ($v \sin i > 50 \text{ km s}^{-1}$) are still present in the next oldest cluster – the Pleiades – among the K and M dwarfs but are nearly absent among the G dwarfs; (c) in the oldest cluster – the Hyades – all of the G and K dwarfs are slow rotators ($v \sin i < 10 \text{ km s}^{-1}$), and only among the M dwarfs does one find a significant population of relatively rapid ($v \sin i \sim 15 - 20 \text{ km s}^{-1}$) rotators; (d) in all three clusters, and for all spectral types later than G0, despite the presence of the rapid rotators it is still true that more than half of the stars are slow rotators (with $v \sin i \leq 10 \text{ km s}^{-1}$).

Stauffer discusses models (new and old) which attempt to explain these observations, i.e. the simultaneous presence of the rapid rotators and the slow rotators and the apparent longer spindown timescales for lower mass stars. Additionally he discusses a 'saturated' wind model in which the angular momentum loss rate is constant above 10 km s^{-1} , and proportional to rotation rate to some power for rotational velocities below that. Simon (1992) concludes that the relation between rotation and age and between activity and age must be implicit, not explicit as the scaling formulae assume.

Noyes et al. (1984) demonstrated that the brightness of the H-K emission of a star located on the lower half of the main sequence can be related to the Rossby number, N_R , defined to be the ratio of the equatorial stellar rotation period to a convective turnover time (which is derivable from models of the stellar interior). Jordan & Montesinos (1991) showed that coronal parameters such as the temperature, T_C , the emission measure, $EM(T_C)$, and the implied magnetic field, B_C , required to produce the heating, can all be expressed simply in terms of N_R , with a small gravity dependence. An important feature of the dependence of activity on rotation based parameters is saturation, first discussed by Vilhu (1984) and more recently by Stauffer et al. (1994: X-rays) and Soderblom et al. (1993: $H\alpha$). Vilhu showed that at $N_R < 0.3$ the strong dependence of strong transition line fluxes on N_R flattens. He interpreted this 'saturation' to be caused by the total filling of the stellar surface by active regions. Simon (1992) discusses a similar effect observed in chromospheric lines and argues that the cause is unknown; it could be a cutoff in the amount of magnetic flux created by the dynamo, or it could be a limit on area filling factors (in line with Vilhu), or possibly a radiative transfer effect. L_X / L_{bol} increases with decreasing mass and peaks at around 10^{-3} to 10^{-2} for the lowest mass stars, see e.g. Wood et al. (1994), Fleming, Schmitt & Giampapa (1995).

1.6 EUV astronomy

In this introduction I have concentrated almost exclusively on results obtained from observations in the X-ray passband. Much of the work in this thesis discusses data obtained in the passband 60–200 eV, i.e. at EUV and very soft X-ray wavelengths. Before the launch of ROSAT (Trümper et al. 1991), and specifically the Wide Field Camera (WFC: Sims et al. 1990), there were only a handful of EUV sources known (apart from the Sun); the Apollo-Soyuz EUV telescope (Lampton

et al. 1976) observed some 30 targets in about 20 hours detecting one coronal source – Proxima Centauri, together with the white dwarf systems HZ 43, Feige 24 and the cataclysmic variable SS Cyg. *EXOSAT* TGS observations, reaching to wavelengths as long as 300 Å, have shown EUV emission from Capella, σ CrB and Procyon.

But why is the energy range important for stellar coronal physics? The EUV region is a key portion of the electromagnetic spectrum for studying the outer atmospheres of cool stars. X-ray observations have shown that almost all late-type stars are soft X-ray sources, with emission arising from coronal material with temperatures $> 3 \times 10^6$ K. Ultraviolet observations with the International Ultraviolet Explorer (IUE) and the Hubble Space Telescope (HST) have been used to study the chromospheres and transition regions of many late-type stars, where the temperatures are $\leq 3 \times 10^5$ K. But the material in stellar outer atmospheres with temperatures between 10^5 K and $\sim 3 \times 10^6$ K has not been well studied. As shown by synthetic spectral models (e.g. Raymond & Smith 1977; Landini & Monsignori-Fossi 1985, 1990), the emission at these temperatures is principally (line emission) in the EUV. The EUV, therefore, represents a gap in our understanding of the overall temperature structure and energy balance within coronae.

On the Sun, it is known that the DEM has a rather similar shape, as a function of temperature, for a wide range of solar features (see Bruner & McWhirter 1988). Is there, then, a universal shape for the DEM? The real key for a detailed investigation of DEM functions is spectroscopy. Analysis of the EUVE spectrum of Capella indicates a DEM which is very different from the solar case (Dupree et al. 1993).

1.7 Outline of the thesis

The rest of this thesis is set out as follows. In Chapter 2 I introduce the mechanisms by which a hot optically thin plasma emits at X-ray and EUV wavelengths and describe how this emission is absorbed by the interstellar medium. I also discuss the instruments on board ROSAT and their effectiveness for observing this emission. In Chapter 3, I describe the discovery of a hot white dwarf – one of the brightest sources in the EUV sky, hidden in the optical by the light of its main-sequence companion. Chapter 4 is a WFC survey of all known late-type stars that lie within 25 parsecs of the Sun. In Chapter 5, I present the ROSAT deep survey of the Hyades

centre. Approximately 75 per cent of the Hyads within the 11 PSPC fields are detected in X-rays, including 13 out of 17 dK stars and 23 out of 32 dM stars. I construct the dK and dM luminosity functions and discuss their significance. In Chapter 6, I discuss the X-ray spectra of Hyades stars and attempt to describe their coronae in terms of simple models. I close with Chapter 7, my concluding remarks and a discussion of some of the possible contributions from future missions.

Chapter 2

Observing cool stars with ROSAT

2.1 X-ray/EUV emission from an optically thin thermal plasma

The X-ray emission from a stellar corona is typically from a very hot, tenuous and highly ionized gas in which the atoms have all, or almost all, of their electrons stripped due to collisions with energetic electrons. Temperatures are typically above one million degrees Kelvin. Radiative power loss is compensated by heating so that the gas is in a steady state of statistical equilibrium both for the bound atomic states and for the ionization balance. Electron collisions control the ionization state and emissivity of the gas and the plasma electrons (and ions) are relaxed to Maxwellian energy distributions with a local common temperature T (e.g. Mewe 1991). Deviations from this model due to photo-ionization, optical depth, high density, non-Maxwellian electron densities, and transient ionization are discussed by e.g. Raymond (1988).

Radiation results mainly from various collisional interactions between electrons and ions, the ionization balance of the plasma being determined from the ionization and recombination rates of the elements present. A plasma of cosmic abundance is made up by number of $\sim 90\%$ H, $\sim 10\%$ He, and only $\sim 0.1\%$ heavy ($Z \geq 6$) elements ($n_e \simeq 1.2n_H$, because H and He are almost fully ionized). At very high temperatures ($T \gtrsim 10^8$ K) the heavy elements are almost fully ionized, and the X-ray emission is dominated by a featureless bremsstrahlung continuum mainly from H^+ and He^{++} with a spectral emissivity proportional to n_e^2 . Below these temperatures the line emission from heavy elements becomes significant, making the emissivity dependent on the ionization state and the atomic abundances. Spectral lines therefore are indicative of the

thermal nature of the source.

Spectral models have been calculated by Raymond & Smith (1977), Mewe, Gronenschild & van den Oord (1985), Landini & Monsignori-Fossi (1970, 1985, 1990) among others. Fig. 2.1 shows X-ray spectra calculated for a range of temperatures (using code supplied to the X-ray astronomy group at Leicester by John Raymond, based on an update to the model of Raymond & Smith 1977). The spectral shape clearly varies strongly with temperature, an indicator that we may use the overall shape of the spectrum to estimate the temperature of a plasma when energy resolution is low. In the simplified case of an isothermal plasma of temperature T and volume V the X-ray luminosity L_X in an energy band $E \pm \Delta E/2$ can be written as

$$L_X(T, \Delta E) = F(T, \Delta E)\epsilon \quad (2.1)$$

where $F(T, \Delta E)$ ($= F_C(T, \Delta E) + \Sigma_{\Delta E} F(T, E)$) is the total line plus continuum emissivity (radiated power per unit electron density), and $\epsilon = \int n_e^2 dV \simeq n_e^2 V$ is the volume emission measure. In the general case of a plasma with a temperature distribution we can compute the emission from different parts of the plasma using the concept of a differential emission measure (see e.g. Pan & Jordan 1995 and references therein, although there are other definitions) $\phi(T) = d(\int n_e^2 dV)/dT$, thus

$$L_X = \int F(T, \Delta E)\phi(T)dT. \quad (2.2)$$

2.2 The local interstellar medium

If the local interstellar medium (ISM) were uniformly cold and dense there would have been little point in building the WFC. During the 1970's, the rich potential of EUV astronomy first became clear with ultraviolet and optical spectroscopy of bright stars showing that the opacity of the local ISM is surprisingly low (e.g. Cruddace et al. 1974, Paresce 1984). Models were developed which depicted the ISM as a network of hot and cold components (e.g. McKee & Ostriker 1977). It was suggested (Innes & Hartquist 1984) that the solar system sits in an extended,

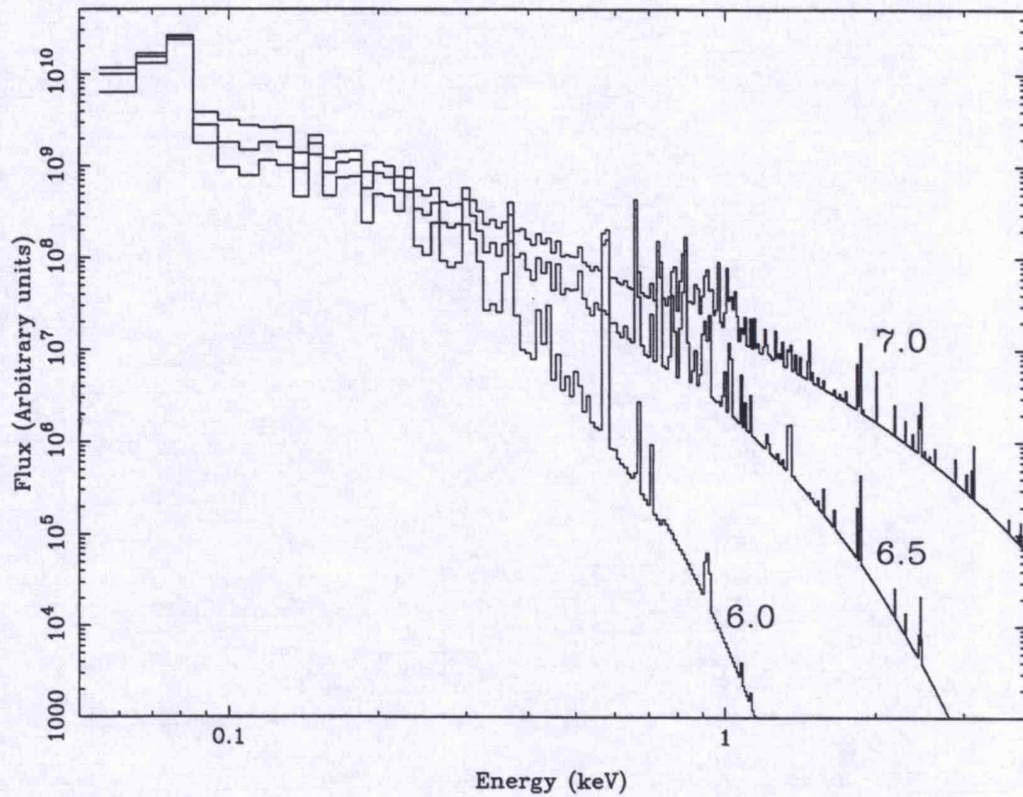


Figure 2.1: Spectral models generated from Raymond & Smith (1977) for temperatures of $T = 10^{6.0}$ K, $10^{6.5}$ K, $10^{7.0}$ K.

warm, tenuous region, or 'local bubble'. The walls of this bubble appear to be as close as 10 parsecs in directions towards the galactic centre and as far as 100 parsecs or more towards e.g. β CMa. This model is not only consistent with the low opacity measurements, but also with the diffuse EUV background emission observed during the Apollo-Soyuz mission (Stern & Bowyer 1979). Observations of the X-ray background at energies $E \leq 1$ keV (e.g. McCammon et al. 1983) have shown strong evidence that the local cavity is (at least partially) filled with a hot ($T \sim 10^6$ K), tenuous ($n_e \sim 0.01 \text{ cm}^{-3}$) gas surrounding the solar system. Snowden et al. (1990) have formulated a model in which the hot gas is distributed at uniform density throughout some fraction of the cavity and the variations in intensity of the diffuse background across the sky are due to the geometry of the emission volume, i.e. high background corresponds to an increased path length through the hot gas to the boundary of the emitting gas. Possible explanations for the formation of the cavity include a supernova event around 10^5 years ago, or a series of events

over the last 10^7 years which have successively reheated the gas within the void and kept it at X-ray emitting temperatures. The recent identification of the Geminga γ -ray pulsar (Halpern & Holt 1992; Bertsch et al. 1992; Bignami, Caraveo & Mereghetti 1993) within the local bubble of approximately the correct age ($\sim 3 \times 10^5$ yr) has further added to the attractiveness of the model (Gehrels & Chen 1993). The column density map, in galactic coordinates, as determined by Paresce (1984) is presented in Fig. 2.2 (but see also Frisch & York 1983). This figure clearly shows the local cavity.

2.3 The ROSAT mission

ROSAT was launched on June 1st 1990 into a circular orbit at an altitude of 575 km, giving an orbital period of almost 95 minutes. The orbital inclination of 53° provides 5-6 spacecraft contacts (each of about 10 minutes) per day with the ground station at Weilheim. ROSAT started its planned 6 month all-sky survey on July 30th, and completed it ~ 2 weeks early after the spacecraft attitude control was lost for a time on January 25th 1991. The gap was filled in (at reduced sensitivity) during August 1991. The sky was scanned by rotating the ROSAT spacecraft on an axis, once per orbit, such that its two coaligned telescopes always looked away from the earth. The resulting scan path was a series of great circles, passing over both ecliptic poles, and crossing the ecliptic plane at a fixed angle to the Sun (nominally $90 \pm 12^\circ$). The scan path precessed at about 1° per day, giving complete sky coverage within 6 months.

ROSAT carries both a German X-ray telescope (XRT: Trümper et al. 1991) and the British EUV telescope – the Wide Field Camera (WFC: Sims et al. 1990). The XRT has two types of detector which can be interchanged at the focus. These are the Position Sensitive Proportional Counter (PSPC: built at the Max-Planck-Institut für Extraterrestrische Physik [MPE]) and the High Resolution Imager (HRI: built by the Smithsonian Astrophysical Observatory [SAO] for NASA). These instruments are described below. The survey was followed by a series of pointed phases for detailed observations, with observing time available to the German, American, British and world-wide astronomical communities.

The satellite is three-axis stabilised using gyroscopes and high torque momentum wheels (which allow slew speeds of up to 180° in ~ 15 minutes). The Attitude Measurement and Control

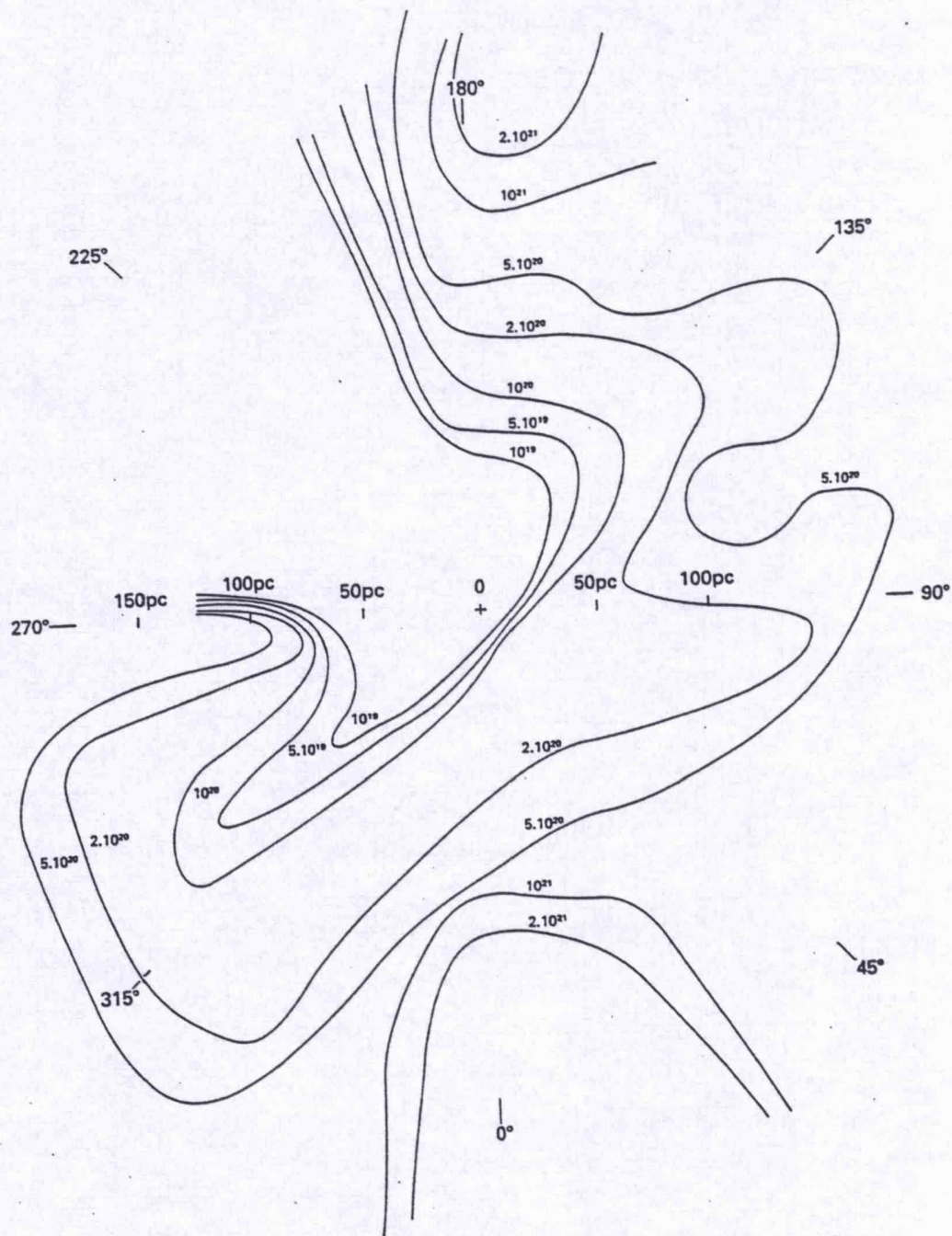


Figure 2.2: Map of the local ISM in the galactic plane ($b < 30^\circ$) represented as contours of constant N_H . The position of the Sun is at the origin of the coordinate system. Reproduced from Paresce (1984).

System (AMCS) achieves a pointing control accuracy of better than 1 arcmin. Using CCD star sensors the satellite pointing direction is reconstructed post facto at the German Space Operations Center (GSOC) to 6 arcsec accuracy. During observations with the PSPC, the satellite's pointing direction was wobbled over ± 3 arcmins (with period 400 seconds) in order to prevent unwanted shadowing of X-ray sources behind opaque structures in front of the PSPC. A similar, but lower amplitude, wobble is performed for the HRI (± 1.5 arcminutes in 400 seconds of time). The WFC carries its own star sensor for independent attitude determination; however this sensor is not used for attitude control.

The PSPC is fully described by Pfeffermann et al. (1986), while the WFC is covered in detail by Sims et al. (1990). Below I give a brief summary of both these instruments.

2.4 The WFC

The WFC optics consist of a nested set of 3 Wolter-Schwarzschild Type I mirrors, fabricated from aluminium and covered with gold for maximum reflectance. The mirrors provide a geometrical collecting area of 456 cm^2 with a common focal length of 525 mm. The grazing incidence angles (typically 7.6°) have been chosen to allow optimization of the collecting area whilst retaining a wide (2.5° radius) circular field of view. The high energy cut off is at 210 eV.

The detector at focus is a microchannel plate (MCP) curved to match the optimum focal surface. It consists of an array of $\sim 10^7$ closely packed channels, drawn and etched from a lead glass matrix. A CsI photocathode is deposited directly onto the front face of the front MCP to enhance the EUV quantum efficiency. Thus each channel of the MCP behaves in much the same way as a photomultiplier tube. The detector has a 4.5 cm diameter sensitive area, giving a 5° diameter field of view (FOV). On axis the spatial resolution is 1 arcminute (FWHM), degrading to 3 arcminutes at the edge.

2.4.1 Filters

Since microchannel plates have little intrinsic energy resolution, the WFC makes use of 8 filters to define the observing wavebands. These are mounted on a filter wheel in front of the detector.

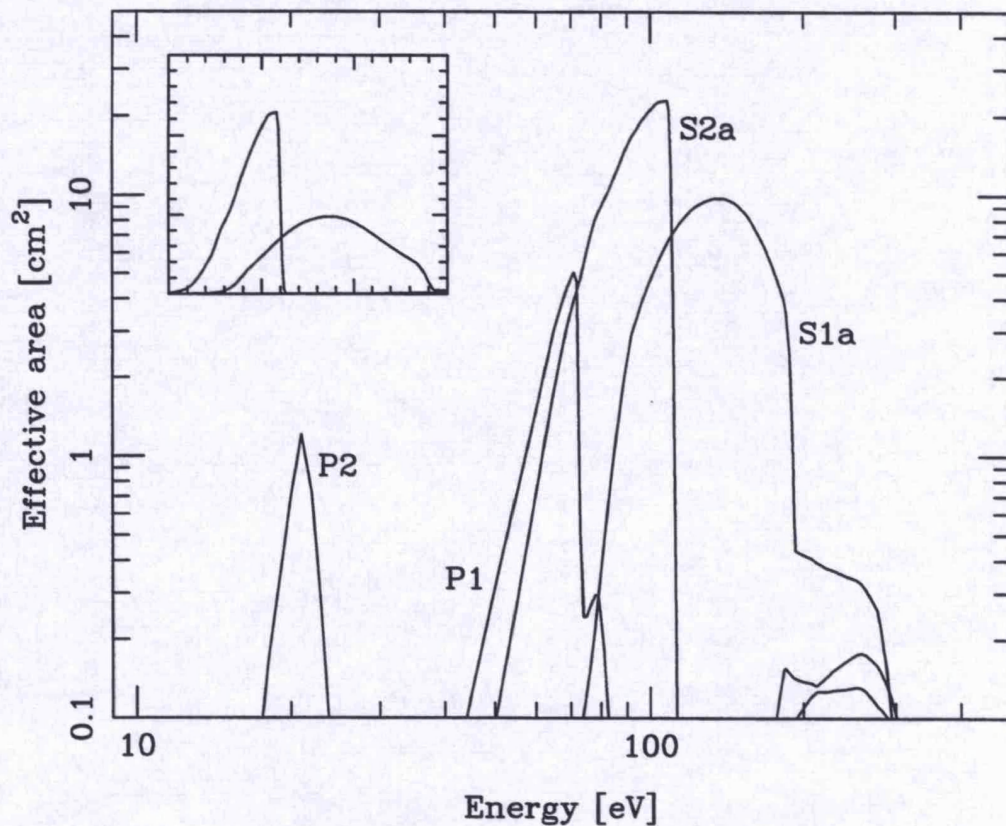


Figure 2.3: Effective areas of the WFC S1, S2, P1 and P2 filters. The insert shows the S1 and S2 filters on a linear scale.

There are two survey filters (plus duplicates to provide redundancy) referred to as S1 and S2. Strictly these are S1a/S1b and S2a/S2b, the duplicate filters are not identical having different coatings. Filters S1a and S2a were used in the survey, but are referred to as S1 and S2 from hereon. The remaining filters are for pointed observations (P1 and P2) and calibration. The WFC science filters are listed, with their band passes, in Table 2.1. The effective areas of the WFC filters are shown in Fig. 2.3, and for comparison purposes, together with that of the PSPC in Fig. 2.9. The filters consist of thin ($< 5\mu\text{m}$) foils of metalized plastic based on a substrate of Lexan which is UV cured to a high transmission stainless steel mesh. The low energy limit to the filter passbands is defined by the absorption cross-sections of the filter constituents, and the high energy limit by absorption edges. The S1 filter is composed of Carbon, Lexan and Boron and has a 10% peak efficiency range of 90–210 eV. The S2 filter is considerably softer at 60–110 eV due to its composition of Beryllium and Lexan. The pointed and survey-averaged point spread functions are described by Pye et al. (1995b) and are reproduced below in Fig. 2.4.

Table 2.1: ROSAT WFC filters and wavebands

Filter Name	Filter Type	Survey (S) / Pointed (P)	FOV Diam. (degree)	Mean λ (\AA)	Bandpass at 10% peak efficiency (\AA)
S1	C/Lexan/B ($\times 2$)	S + P	5.0	100 (120) ¹	60-140 (210-90)
S2	Be/Lexan ($\times 2$)	S + P	5.0	140 (90)	112-200 (110-60)
P1	Al/Lexan	P	2.5	180 (70)	150-220 (80-60)
P2	Sn/Al	P	2.5	600 (20)	530-720 (25-15)

¹ numbers in brackets give the approximate energies in eV.

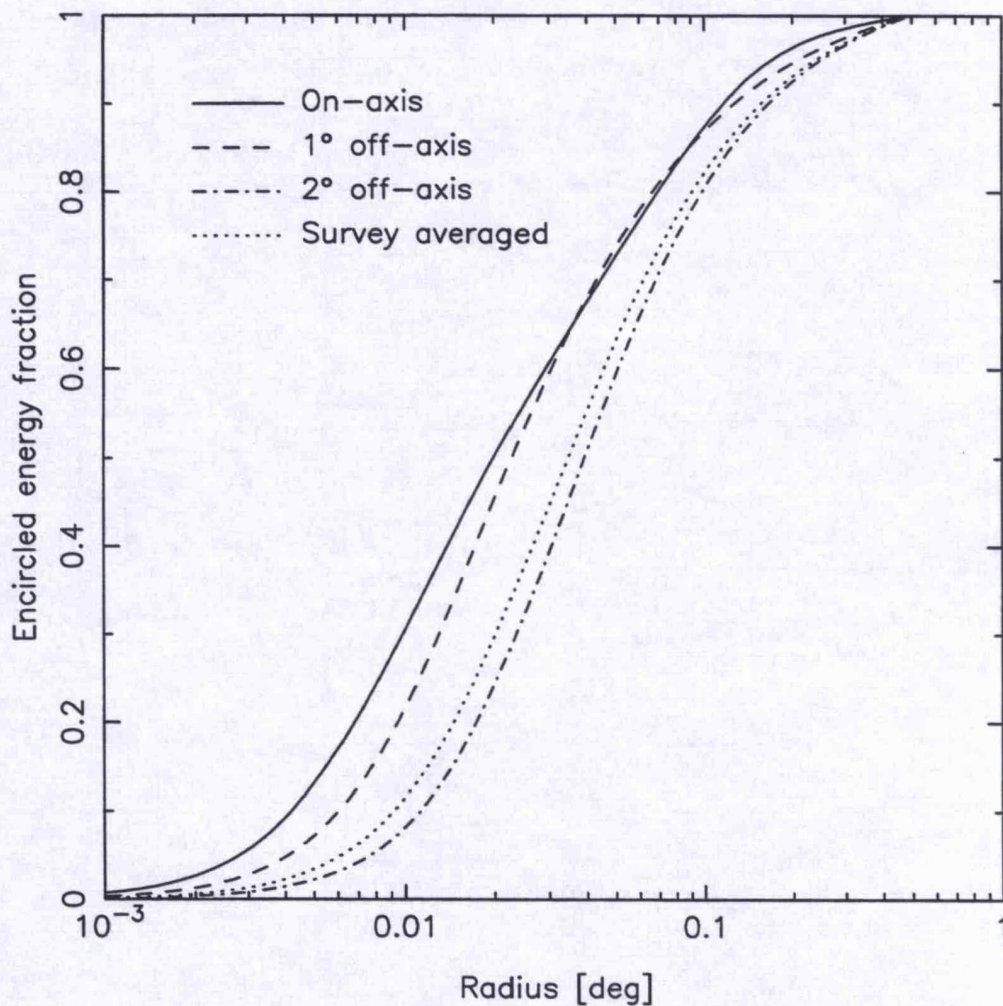


Figure 2.4: Integral point spread function (PSF) on-axis, at off-axis angles of 1.0° and 2.0° , and survey-scan-averaged over the full field of view.

2.4.2 Background

The background during the survey was highly variable, but for much of the ROSAT orbit was of order 20 count s^{-1} across the full FOV, well below the telemetry saturation limit of 200 count s^{-1} . In the S1 filter, the background consists largely of charged particles. Extra background from scattered solar photons (geo-coronal background) is visible in the S2 filter. A third and unexpected background component has also been identified, strongly correlated with the velocity-view angle of the satellite. This has been attributed to a spacecraft glow effect, similar to that observed on the Space Shuttle (West et al. 1994).

2.4.3 The all-sky survey

During the survey, the S1 and S2 filters were used on alternate days, providing a map of the sky in two EUV bandpasses, between 60 \AA (200 eV) and 200 \AA (60 eV). A source would take up to one minute to cross the detector every orbit (96 minutes), over an interval of $\sim 5/\cos \lambda$ days, where λ is the ecliptic latitude of the source. Fig. 2.5 shows the final total exposure on the sky in both filters.

In Fig. 2.6 I show the anticipated count rate for a given incident flux from a grid of Raymond & Smith model spectra observed with both the S1 and S2 filters. The curves have been calculated for a range of intervening hydrogen column densities (N_{H}). These curves are necessary if we wish to calculate the intrinsic luminosity of a given star in the WFC passband. By combining the results from both filters we may attempt to do two colour photometry. Also shown in Fig. 2.6 are the expected S1/S2 filter ratios as a function of coronal temperature and N_{H} . However, uncertainties in the spectral models and calibration of the survey filters, combined with low count rates, largely prohibit a detailed study of late-type stars using S1:S2 ratios. In spite of this they can be useful for examining the gross properties in a large sample of sources (see Fig. 2.7 below).

The results of the WFC all-sky survey are summarised in two catalogues: The Bright Source Catalogue (BSC: Pounds et al. 1993) and the 2RE Source Catalogue (Pye et al. 1995b). The BSC contained 383 sources, the results of an initial analysis. The 2RE catalogue contains 479 sources and improves on the BSC by rejecting poor aspect periods, better screening of background,

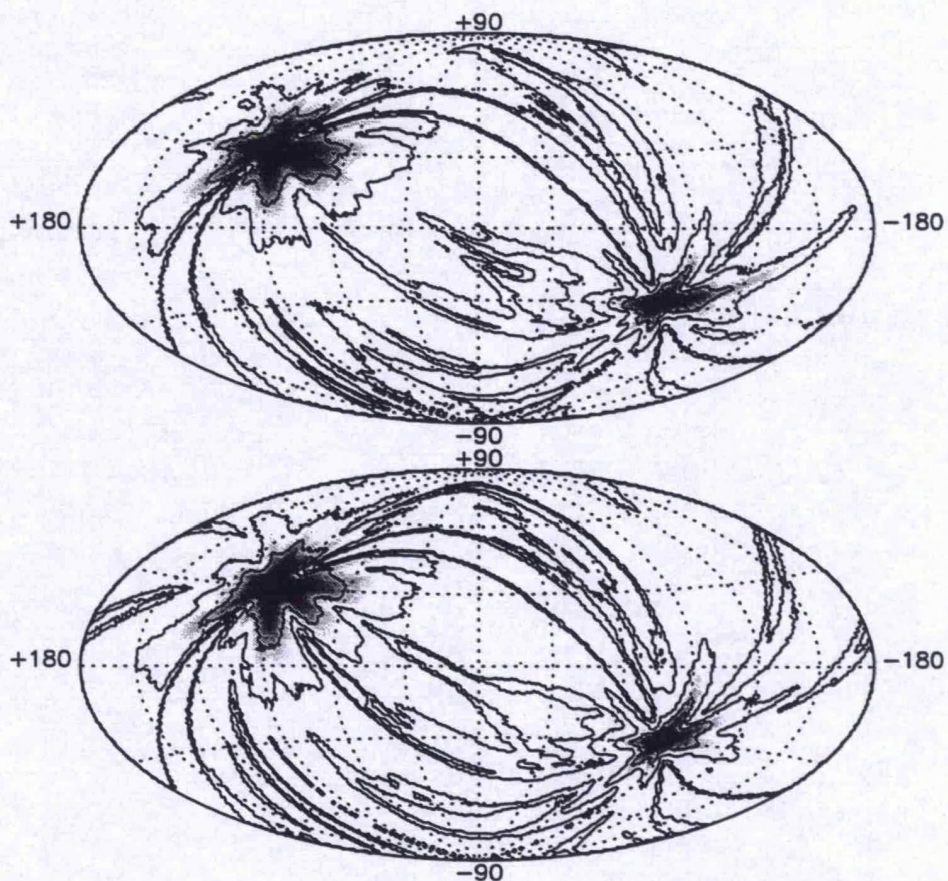


Figure 2.5: Exposure map of the sky in galactic coordinates for (top) the S1 waveband and (bottom) the S2 waveband. The projection is Hammer ('Aitoff') equal area. The contours are 1.0, 1.5, 3.0, 5.0, 10 and 20 ks exposure time. The grey shading increases with exposure time. Figure supplied by R.G. West (*priv. comm.*)

and using a more sensitive detection algorithm. In the 2RE list, active late-type stars and hot DA white dwarfs form the great majority of optical counterparts, with about 255 and 126 identifications respectively. Cataclysmic variables (CVs), active galactic nuclei (AGNs), B-type stars, X-ray binaries (XRBs) and supernova remnants (SNRs) contribute 17, 7, 8, 2 and 2 counterparts respectively. For 387 sources in the 2RE catalogue, detections are recorded in both filters, allowing the derivation of an EUV colour (S1:S2 ratio), which is plotted as a function of S1 count rate in Fig. 2.7. White-dwarfs are clearly the softest objects, while late-type stars cover a wide range of colour — more likely due to temporal variability of the sources during the survey, and differences in intervening column densities, than intrinsic spectral differences between the stars. The extra-galactic sources all have harder filter ratios, reflecting the high intervening column densities. The properties of the WFC all-sky survey sources are discussed by Pounds et

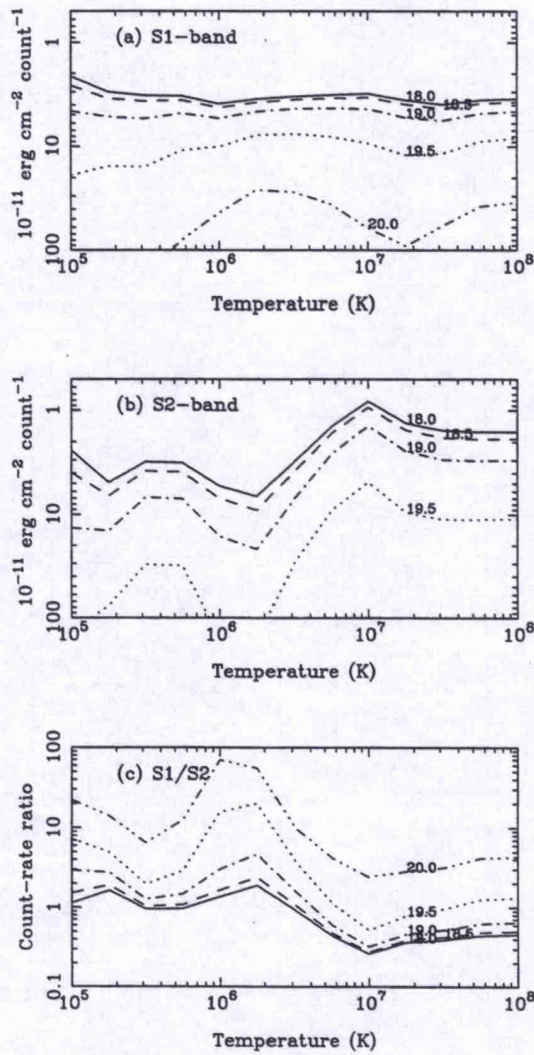


Figure 2.6: Conversion factors (units of $10^{-11} \text{ erg cm}^{-2} \text{ count}^{-1}$) for WFC count rate to unabsorbed EUV flux, as a function of source temperature T and line of sight column density N_H . Computations are for the S1 filter (a) and S2 filter (b), while (c) is the count rate ratio S1/S2. The assumed source spectrum is that due to an optically thin thermal plasma.

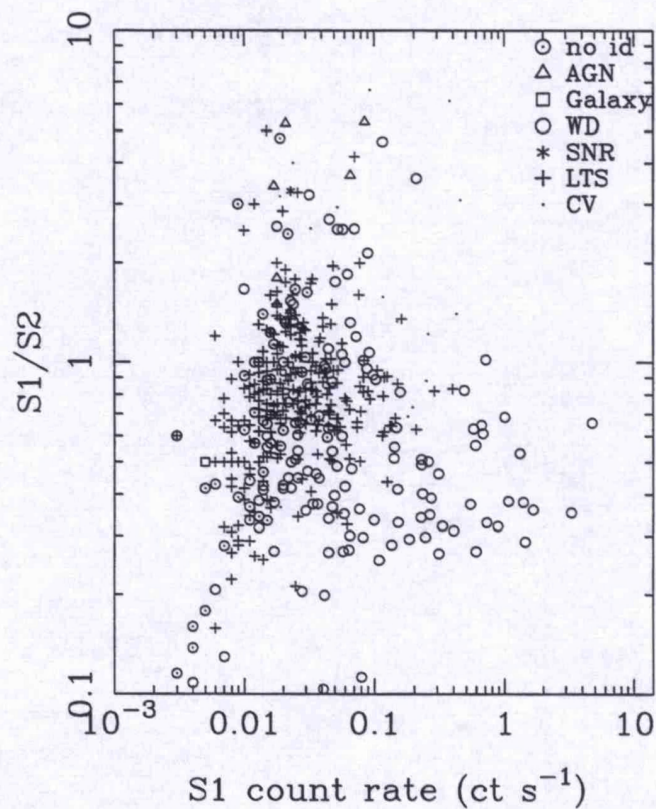


Figure 2.7: EUV colour (S1:S2 ratio) as a function of S1 count-rate for sources in the 2RE catalogue.

al. (1993) and Warwick et al. (1993). A plot of e.g. EUV luminosity against distance (see e.g. Fig. 4.7 in Chapter 4) shows that the WFC selected sample of late-type stars is almost entirely made up of stars which are much more X-ray luminous than the Sun, and is thus extremely useful as an activity selected sample.

2.4.4 The efficiency history of the WFC

In-flight measurements with the on-board UV calibration system and observations of the white dwarf HZ 43 have shown that the efficiency of the detector was falling gently throughout the calibration and survey phases. The survey was brought to a premature conclusion by the AMCS failure and subsequent Sun pointing on 25th January 1991 which resulted in a catastrophic loss in sensitivity of around a factor ten (see Fig 2.8). Since then, the UV calibration measurements have continued to show a loss in sensitivity, reaching a value around 1% of the launch value by the

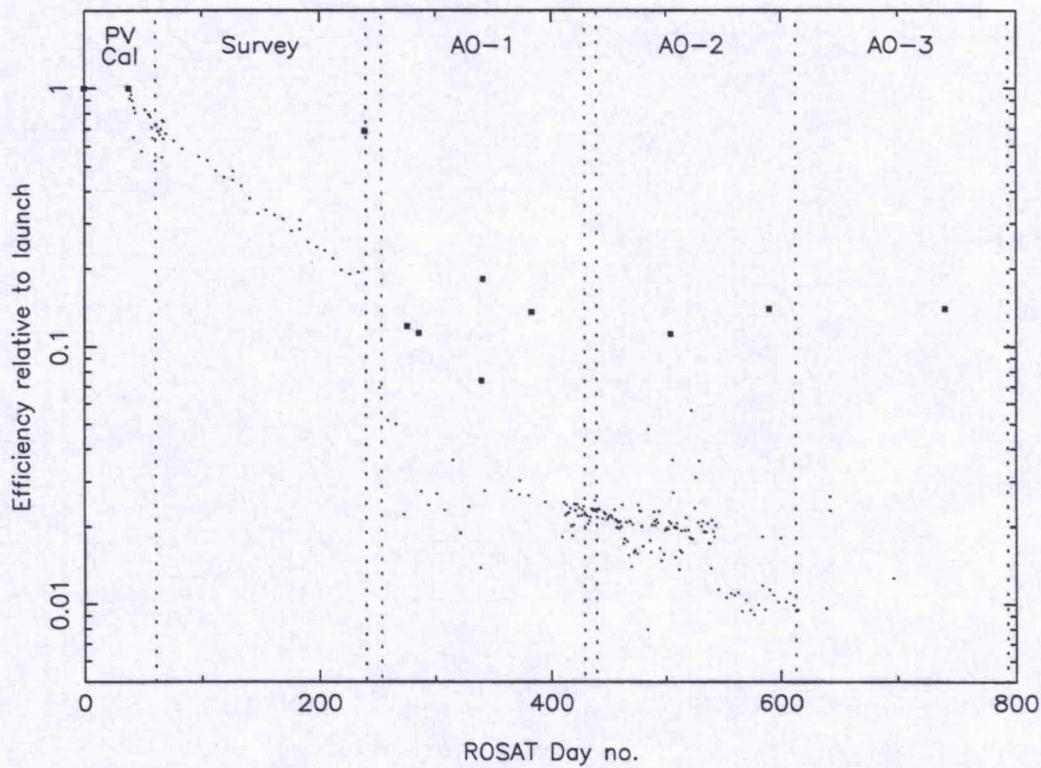


Figure 2.8: The efficiency history of the WFC detector. Data are from the on-board UV calibration system (dots) and from observations of the EUV-bright white dwarfs HZ 43 and Meaty (squares). Figure supplied by R.G. West.

beginning of 1993, while calibration observations of astrophysical sources using the science filters show a different trend; the sensitivity of the detector has been recovering gradually, reaching about 15% of the nominal launch value by early 1993. As yet no conclusive explanation for the loss in sensitivity has been arrived at.

2.5 The PSPC

The XRT on ROSAT consists of the X-ray Mirror Assembly (XMA), the PSPC and the HRI. The XMA comprises a grazing incidence four-fold nested Wolter type I configuration. All of the 8 mirror shells are made out of Zerodur, a glass ceramic with a very low thermal expansion coefficient, and are coated with a thin layer of gold to improve X-ray reflection. Typical grazing angles are between 1 and 2 degrees, depending on the mirror subshell considered. The geometrical collecting area of the mirrors is 1141 cm^2 , with a focal length of 240 cm and an aperture

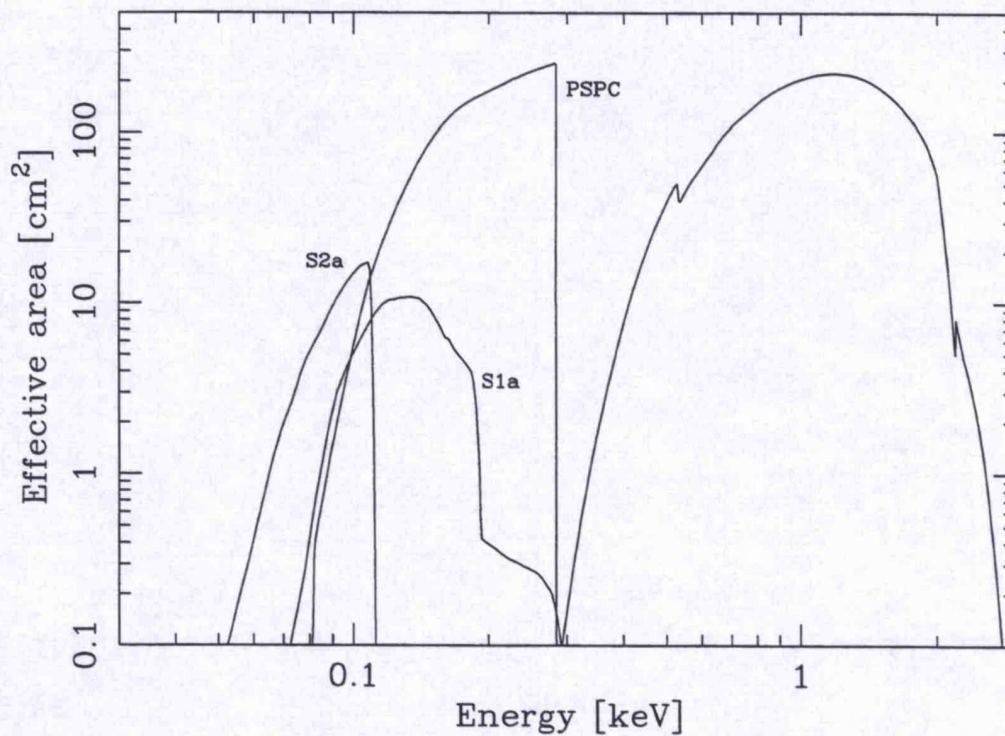


Figure 2.9: PSPC and WFC (S1 and S2) effective areas.

of 84 cm.

Two PSPCs and the HRI are mounted on a carousel in the XRT focal plane. For details on the HRI the reader is referred to David et al. (1995). The PSPC is a multiwire proportional counter with a cathode strip readout scheme for position determination. It has an 8 cm diameter sensitive area, using the full 2° FOV of the XMA. The entrance window of the detector is polypropylene coated with carbon and lexan to decrease UV transmission. A filter wheel with four positions is mounted in front of the detector: open for standard observations; closed for particle background monitoring; a boron filter allows increase in spectral resolution at lower energies; and the fourth filter is used for spectral calibrations. The X-ray absorption of the counter gas (a mixture of Argon, Xenon and Methane) is close to 100% below incident energies of 2.0 keV where the XMA cuts off. The quantum efficiency of the detector is therefore almost solely determined by the transmission of the window. The total effective area of the XMA + PSPC combination is shown in Fig. 2.9 for an on-axis observation, together with the WFC effective areas for the S1 and S2 filters. The effective area of the PSPC falls off gradually to off-axis angles of 50 arcmins or so, but then drops dramatically as can be seen in Fig. 2.10

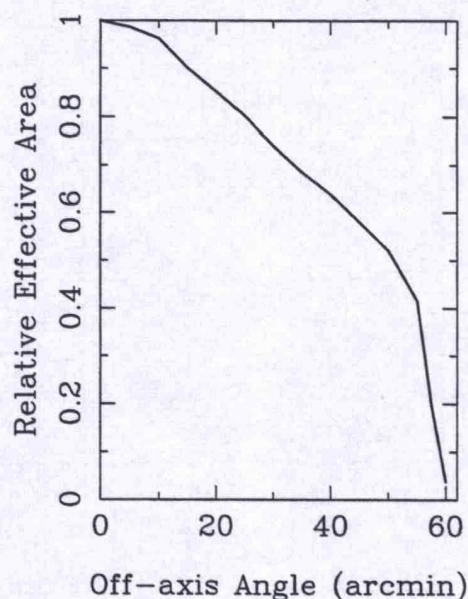


Figure 2.10: The relative PSPC effective area as a function of off-axis angle at 1.0 keV.

2.5.1 The Point Spread Function

The PSF of the PSPC is dominated by two components: (1) the detector's intrinsic response, which is a strong function of pulse height; (2) the response from the mirrors which is a complex function of energy and off-axis angle. The parameterisation derived by Georgantopoulos, Saxton & Pye (1992) is used throughout this thesis. Fig. 2.11 shows the corresponding radii for enclosing 50% and 90% of the counts from a point source as a function of off-axis angle.

2.5.2 Background

The PSPC is subject to several sources of background contamination which must be addressed when analysing pointed data. The known contaminants, as discussed by Snowden et al. (1994a), include high energy particles, solar scattered X-rays, auroral X-rays, 'afterpulses' and long term intensity enhancements of unknown origin.

The onboard rejection of particles is carried out by an event vetoing system. Anodes and cathodes which cover the sides and rear of the detector are linked together in anticoincidence with the detector anodes. Nominally, particles can be rejected with 99.8 per cent efficiency,

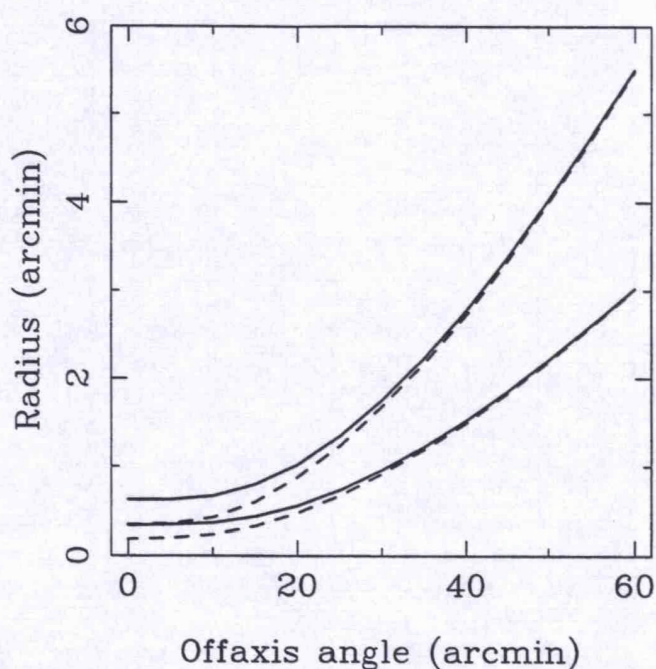


Figure 2.11: The curves show the radii for enclosing 50% and 90% of the counts from a point source as a function of off-axis angle. Energy dependence is shown by a solid line for 0.25 keV and a dashed line for 1.0 keV

however, when the particle detection rate exceeds 170 count s^{-1} , the rejection efficiency drops substantially (Plucinsky et al. 1993; Snowden et al. 1992). This threshold is therefore applied to all PSPC data analysed in this thesis.

The remaining contaminants are likely to be dominated by Solar-induced X-ray events. It is simplest to reject time-slots where these events are unusually high. This is achieved by imposing an upper limit to the detector housekeeping parameter AXE which records the total accepted X-ray events. An “optimum” upper limit of 18 count s^{-1} is set (see Barber, 1994).

2.5.3 Spectral capabilities

The PSPC offers limited spectral resolution through event pulse heights as well as through the use of the boron filter. Because of the good counter resolution, events occurring in the carbon band can be separated from those at higher energies without significant pulse height smearing. Approximately four independent ‘channels’ can be determined over the whole PSPC bandpass. Use of the boron filter allows a further subdivision of the carbon band by comparison of the

Table 2.2: ROSAT SASS bins

SASS bin	E_{low}	E_{high}	PI bins	SASS bin	E_{low}	E_{high}	PI bins
1	0.07	0.09	7–8	18	0.84	0.91	84–90
2	0.09	0.11	9–10	19	0.91	0.99	91–98
3	0.11	0.14	11–13	20	0.99	1.07	99–106
4	0.14	0.17	14–16	21	1.07	1.15	107–114
5	0.17	0.20	17–19	22	1.15	1.23	115–122
6	0.20	0.24	20–23	23	1.23	1.32	123–131
7	0.24	0.28	24–27	24	1.32	1.41	132–140
8	0.28	0.32	28–31	25	1.41	1.50	141–149
9	0.32	0.37	32–36	26	1.50	1.60	150–159
10	0.37	0.42	37–41	27	1.60	1.70	160–169
11	0.42	0.47	42–46	28	1.70	1.80	170–179
12	0.47	0.52	47–51	29	1.80	1.91	180–190
13	0.52	0.58	52–57	30	1.91	2.02	191–201
14	0.58	0.64	58–63	31	2.02	2.13	202–212
15	0.64	0.70	64–69	32	2.13	2.24	213–223
16	0.70	0.77	70–76	33	2.24	2.36	224–235
17	0.77	0.84	77–83	34	2.36	2.48	236–247

count rate with and without filter. This filter selectively absorbs most photons between 0.18 and 0.28 keV. Therefore the filter/open count rate ratio is sensitive to the spectral intensity between 0.1 and 0.18 keV.

Each event is allocated to one of 256 PHA (Pulse Height Analysis) channels, which is in turn converted to a PI (Pulse Invariant) channel – to account for variations in gain across the detector and with time. These PI channels were not originally intended for use during scientific analysis, rather it was intended that they be binned up such that each new bin contains the same oversampling of the spectral resolution. The SASS (Standard Analysis Software System) channels were selected to provide this, and are listed in Table 2.2.

2.5.4 The all-sky survey

The ROSAT all-sky survey scanned almost the whole sky down to a limiting flux of approximately 2×10^{-13} ergs cm^{-2} s^{-1} in the passband 0.1–2.0 keV; considerably fainter flux limits have been achieved near the ecliptic poles. As with the WFC, an observation of a source consisted of a sequence of individual scans, each scan lasting between 20 to 30 seconds. Initial processing

of the survey data indicates that some 60000 X-ray sources have been detected (Schmitt, 1991). The results are consistent with the results previously obtained from the *Einstein* Medium Sensitivity Survey (Stocke et al. 1991), i.e., about a quarter of the high galactic latitude sources are of coronal origin. At lower latitudes the fraction of coronal sources increases to 50 percent; it is even higher in open clusters and star forming regions. Thus around a third of the source content of the all-sky survey is expected to be of coronal origin. As with the *Einstein* stellar survey (Vaiana 1981), the majority of these sources are late-type stars, typically much more active than the Sun. The PSPC's high sensitivity ensures that the stars detected in the all-sky survey constitute the most extensive sample of active stars known — although a great deal of optical identification work is still required.

2.6 Summary

The scientific instruments on board ROSAT make it an ideal tool to study the upper transition regions and coronae of cool stars with a sensitivity and spectral coverage unprecedented by previous missions. Because the all-sky survey is essentially complete (there are a few small gaps, where exposure is very low), every star in the sky has been observed (albeit rather briefly) with both the PSPC and the WFC, creating the first all-sky X-ray and EUV surveys. With these datasets we are able to examine the global X-ray and EUV properties of an unprecedented number of late-type stars. Many of the biases inherent in previous surveys (i.e. targets were often chosen on the basis of extreme optical behaviour such as flaring, very strong chromospheric emission etc.) are not present in the ROSAT survey data. This completeness plays an important part in this thesis. In Chapter 4 I present a WFC survey of all known late-type stars within 25 parsecs of the Sun. I derive luminosity functions for both survey filters to examine the X-ray characteristics of a sample of late-type stars. In Chapters 5 and 6 I examine the X-ray properties of Hyades cluster members observed in a deep pointed PSPC survey. Briefly, galactic star clusters are a useful sample for a number of reasons. Firstly stars within one cluster are essentially all the same age. This is important when trying to decouple the effects of rotation (believed to be the predominant factor in the generation of coronal heating) from the effects of aging. The Hyades is relatively young (age $\sim 7 \times 10^8$ years) and correspondingly a large number of members are still rotating fairly rapidly and thus have high coronal luminosities. This of course makes our work easier because we have more photons to analyze than from an

older cluster. Secondly, the Hyades in particular is very close to our solar system (distance ~ 45 parsecs), but other clusters such as Praesepe, the Pleiades and α Perseus are all within reach of the PSPC's high sensitivity. Thirdly, the clusters mentioned so far cover a small area on the sky, thus observing them in pointed mode is a very efficient way of examining the properties of a large number of stars. For this thesis I have worked with a mosaic of PSPC and WFC pointings with good areal coverage of the Hyades. An additional 'feature' is that they are very well studied in the optical, thus their visual magnitudes, spectral types and hence masses are well determined.

Chapter 3

ROSAT/IUE discovery of a white dwarf companion to HD 33959C

3.1 Introduction

This chapter discusses the discovery, from the ROSAT EUV and X-ray all-sky surveys, and from IUE spectra, of a white dwarf (WD) companion to HD 33959C (= ADS 3824C, F4 V, $m_v = 7.95$). RE 0515+324 is among the ten brightest EUV sources in the sky in the 100–200 Å band. I present a summary of the efforts of J.P. Pye, M.A. Barstow (who performed all the spectral modelling), R. Monier (who carried out the IUE observations of HD 33959C) and T.A. Fleming (who supplied the PSPC survey data), as well as my own.

HD 33959C (= ADS 3824C, F4 V, $m_v = 7.95$) is a visual companion to the bright δ Scuti-type variable KW Aur (= HD 33959A = ADS 3824A, A9 V, $m_v \approx 5.0$ (Abt & Cardona 1984, Abt 1988)), their separation on the sky being about 15 arcsec. KW Aur is itself a single-lined spectroscopic binary; the secondary has roughly one solar mass, but its spectral type is not known (Fitch & Wiśniewski 1979). HD 33959 -A and -C are, on present evidence, considered not to form a physical binary system (Abt 1988), with estimated distances of ≈ 40 pc (Abt 1988) and ~ 100 pc (see Section 3.3) for HD 33959 -A and -C respectively.

During the ROSAT EUV and X-ray all-sky surveys, conducted from 1990 July to 1991 January, a bright EUV and X-ray source was detected close to the HD 33959 system. Initial interest was roused because it was one of the ten brightest EUV sources in the sky (and because of

its proximity to KW Aur, though the latter turned out not to be the optical counterpart). In order to establish which object was responsible for the EUV and X-ray emission, a programme of optical and UV spectroscopy was undertaken. In addition, further ROSAT observations were obtained, now in pointed mode, to view the source at longer EUV wavelengths than reached in the survey.

It took IUE measurements to finally show that the counterpart to the EUV/X-ray source is a (previously unknown) hot DA white dwarf (WD) companion to the eighth magnitude F4 V star HD 33959C. IUE and optical spectroscopy show no indications of either stellar chromospheric activity or WD emission from HD 33959A (KW Aur). In Section 3.2 I present the observations made in the X-ray, EUV, UV and optical wavebands, and describe the analysis of these data. The possible parameters of the white dwarf are estimated in Section 3.3. In Section 3.4 I discuss the importance of these results with reference to other similar systems discovered with ROSAT

3.2 Observations and data analysis

Details of the relevant observations are listed in Table 1. The description of the various observations follows, as far as possible, the chronological sequence of the investigation (and hence our understanding of the object).

3.2.1 ROSAT EUV and X-ray sky survey

The first all-sky catalogue of 384 relatively bright ROSAT EUV sources has been completed (Pounds et al. 1993), including the object of interest in the present study, designated RE 0515+324. It was singled out for further investigation at an early stage due to its large EUV flux in both WFC survey wavebands (S1: 60–140 Å, S2: 112–200 Å), at 1.17 ± 0.03 count s^{-1} and 2.63 ± 0.04 count s^{-1} , in S1 and S2 respectively, which ranks it as 8th and 7th in the catalogued count rates. The source was found to be bright also in the PSPC data, at 6.5 ± 0.2 count s^{-1} (5–100 Å). The source positions from the X-ray and EUV data respectively are: $\alpha = 05^h15^m23.8^s$, $\delta = +32^\circ41'10''$ and $\alpha = 05^h15^m23.7^s$, $\delta = +32^\circ40'44''$ (equinox J2000). For such a bright source, the positional uncertainties are dominated by residual systematic and attitude errors;

Table 3.1: HD 33959 observing log.

Waveband	Telescope & Instrument	Sequence id.	Passband (Å)	Observing dates	Exposure time (s)	Target ^a
X-ray	ROSAT -PSPC survey		5-100	90-Aug-31 to 90-Sep-02	404	
EUV	ROSAT -WFC survey		S1: 60-140 S2: 112-200	90-Aug-30 to 90-Sep-04	2061 2083	
UV	ROSAT -WFC pointed IUE-SWP, low disp., large aperture	200815 SWP40718 SWP42554	P1: 150-220 1150-1950 1150-1950	92-Feb-24 91-Jan-31 91-Oct-25	3293 480 720	KW Aur HD 33959C
Optical	JKT-CCD	JKTD1318 & JKTD1321	U R	91-Mar-23 91-Mar-23	4 × 512 4 × 64	
	INT-IDS		3650-4250 3650-4250 6350-6800 6350-6800	91-Jan-25 91-Jan-25 91-Jan-25 91-Jan-25	100 100 60 60	KW Aur HD 33959C KW Aur HD 33959C

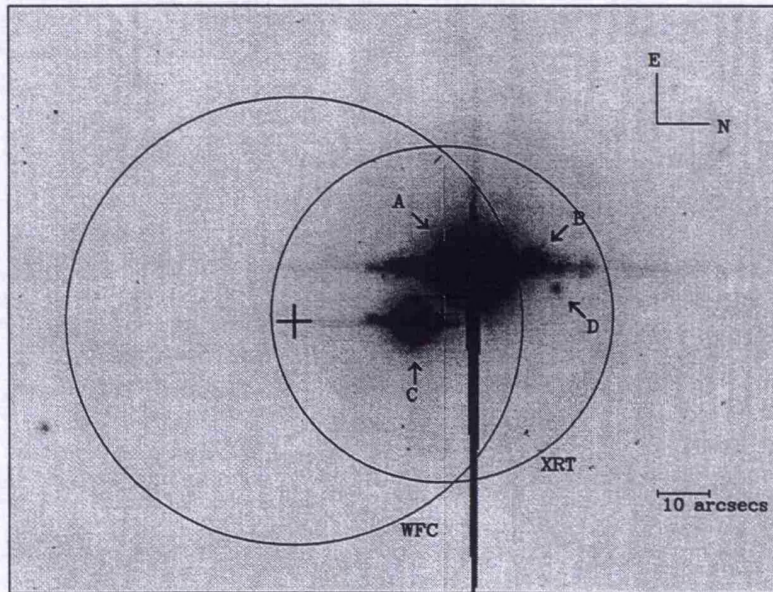
a. Where applicable.

resulting in error circles of 30 and 40 arcsec (90% confidence radius) for the PSPC (Voges 1992) and WFC (Pounds et al. 1993) respectively, as indicated in Fig.1. The spectral ‘hardness’ ratios from both X-ray and EUV data were noted as being typical of emission from a hot WD (see e.g. Fleming et al. 1991; Barstow et al. 1992, 1993a,b). On timescales ≈ 1.5 hours (the ROSAT survey sampling interval), any time variability in the source flux is $\lesssim 20\%$ of the mean.

3.2.2 Optical CCD images

An initial list of candidate objects for further investigation was drawn up from stellar catalogues (mainly via the CDS SIMBAD and Starlink STADAT databases) and visual inspection of the POSS prints. To aid the search for faint candidates, especially in view of proximity to such a bright star as KW Aur, several CCD frames were obtained through the service observing programme on the JKT at La Palma. Exposures were taken in both the R and U wavebands, with KW Aur offset towards the edge of the CCD to reduce saturation. Example images (flat-fielded, but not flux calibrated) are shown in Fig.1. The final candidate list consisted of 4 objects, lying within about 30 arcsec of KW Aur itself. These are indicated in Fig.1 and listed in Table 2. Three of the objects were previously catalogued (SIMBAD); for the other, the equatorial coordinates and (very approximate) magnitude were estimated from the CCD images.

CCD Image for RE0515+32 (U band)



CCD Image for RE0515+32 (R band)

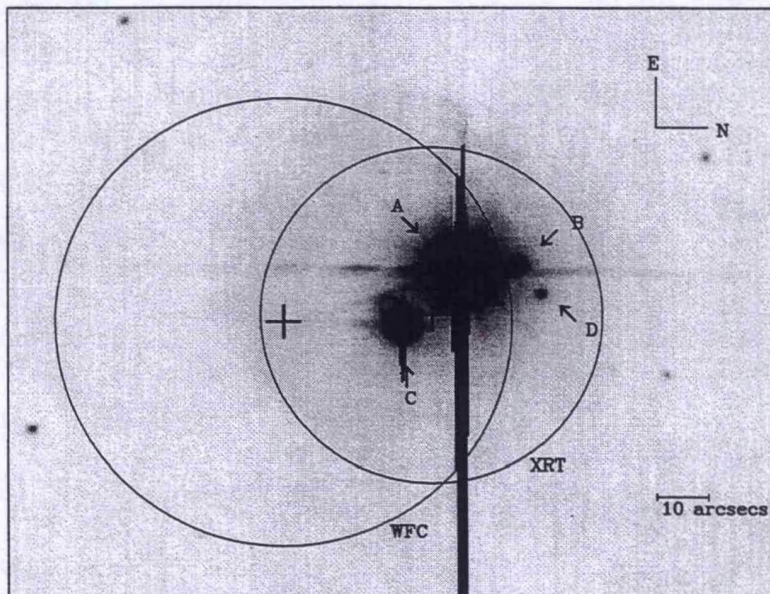


Figure 3.1: Optical, U and R band CCD images (from JKT La Palma) in the vicinity of HD 33959. The objects indicated by letters A–D are as listed in Table 2. The 90% confidence error circles for the ROSAT X-ray and EUV source locations are marked.

Table 3.2: Optical objects within the WFC and PSPC 90% error circles.

Object id.	m_v	R.A. (J2000)	Decl. (J2000)	Spectral Type
A (= ADS 3824A = HD 33959A = KW Aur)	5.05	05 15 24.43	+32 41 14.9	A9 IV
B (= ADS 3824B = BD +32 922B)	11.1	05 15 24.2	+32 41 25	
C (= ADS 3824C = HD 33959C)	7.95	05 15 23.55	+32 41 05.9	F4 V
D	~ 12	05 15 24	+32 41 30	

Coordinates for stars A,B,C from CDS Simbad database. Coordinates for D measured from CCD image, using stars A,B,C as reference positions.

3.2.3 Optical high resolution spectra

The two brightest candidate stars HD 33959 -A and -C were observed with the IDS on the INT at La Palma using the R1200B grating (1200 lines per mm). Spectra (resolution $\sim 1\text{\AA}$) were obtained around the CaII H/K and the H α lines, and are shown in Fig.2. It is apparent that the spectra are very similar for the two stars. Neither shows any emission line core to the absorption features (which would be indicative of stellar chromospheric activity).

3.2.4 IUE spectra

Low dispersion IUE SWP spectra of HD 33959 -A and -C were obtained, and are shown in Fig.3. The spectrum of HD 33959A was obtained by R.W. Tweedy at my request (only a very short exposure was required). IUE was pointed at HD 33959C via a ‘blind offset’ from HD33959A, i.e. the latter was first acquired in the SW large aperture (SWLA) and then the spacecraft was moved to bring HD33959C into the centre of the SWLA; all the other stars in Table 2 were outside the aperture during the HD33959C pointing. The spectrum of HD 33959C was obtained by R. Monier on my behalf. The spectrum of HD 33959A (KW Aur) is typical for a late A-type star. In contrast, the spectrum of HD 33959C is steeply rising towards short wavelengths, characteristic of emission from a hot white dwarf, and not at all that expected from an early to mid F-type star. The flattening of the slope longwards of 1600 \AA is due to emission from the F-star. In using the IUE spectrum to model the WD atmosphere (Section 3.3), a contribution appropriate to the F-star has been removed by subtracting off the spectrum of HD197692 (IUE SWP17033L) (normalised by m_v), an F4 V star ($m_v = 4.14$) in the IUE Uniform Low Dispersion Archive. Also the UV flux was compared to that for a range of available SWP WD spectra of

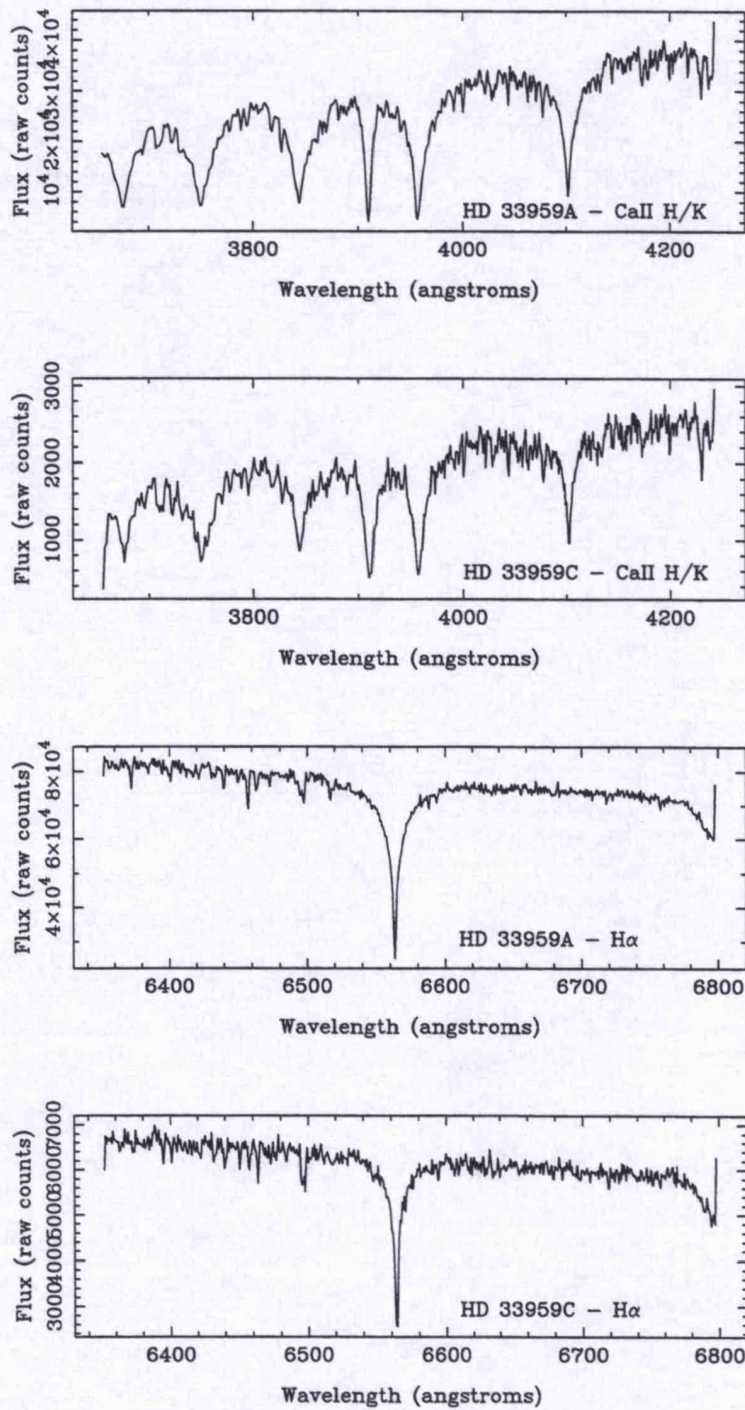


Figure 3.2: Optical high resolution spectra (from INT IDS La Palma) of HD 33959. (a) HD 33959A in the region of the CaII H/K lines; (b) as (a) for HD 33959C; (c) HD 33959A in the region of H α ; (d) as (c) for HD 33959C.

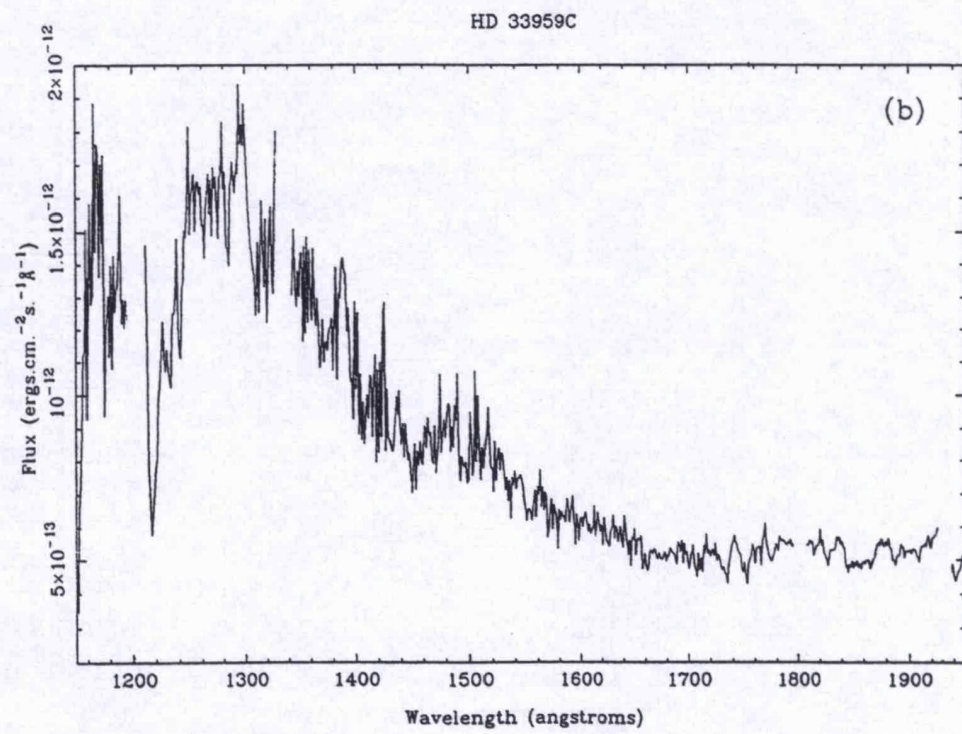
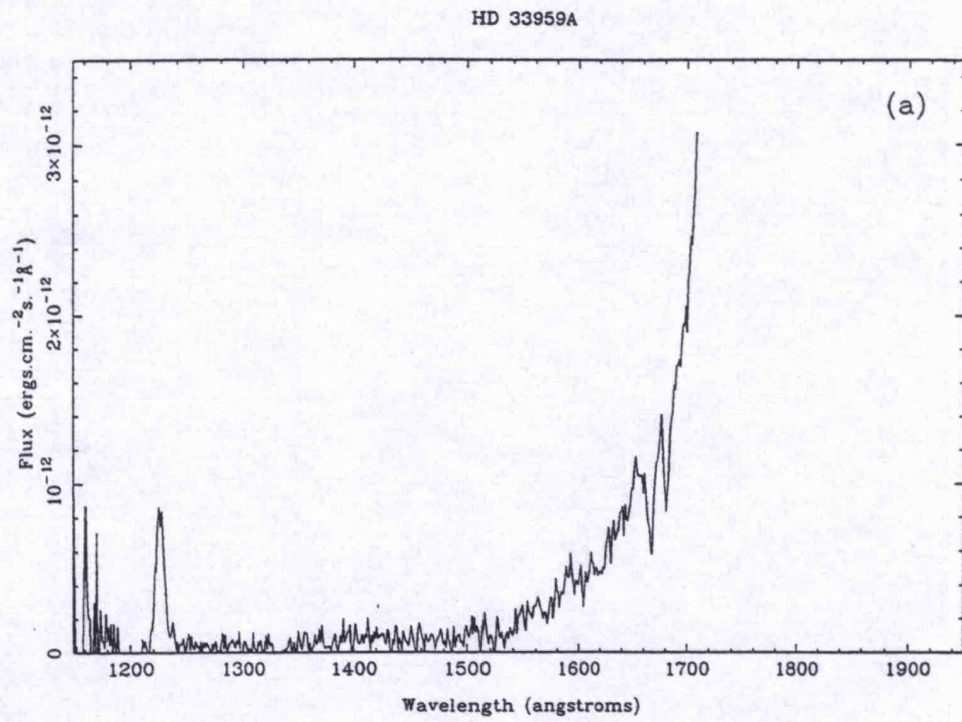


Figure 3.3: IUE SWP spectra of (a) HD 33959A; (b) HD 33959C.

similar shape in order to estimate the visual magnitude of the WD companion to HD 33959C (see Section 3.3).

3.2.5 ROSAT pointed observations

In order to provide a measurement at longer wavelengths than was available during the ROSAT survey, a pointed observation was made using the WFC P1 filter (150–220 Å). The source was detected at a count rate of 0.030 ± 0.004 count s^{-1} . Correcting for the large efficiency change in the WFC since January 1991 (R.Willingale, private communication; ROSAT AO-4 Proposer's Guide, 1992 November), this is equivalent to an 'at launch' value of 0.17 ± 0.02 count s^{-1} . This datum provides an important, additional constraint in the WD atmosphere modelling (Section 3.3).

3.3 Parameters of the white dwarf

It is reasonable to assume that the WD is physically associated with HD 33959C, and hence at the same distance. For HD 33959C, based on an apparent magnitude $m_v = 7.95$ (Abt & Cardona 1984), an absolute magnitude $M_v = 3.2$ (Allen 1973, for a spectral type F4 V, Abt & Cardona 1984), and ignoring reddening, a distance of 90 pc is estimated. As there are significant uncertainties in spectral type and luminosity class (Abt 1988), the distance has also been estimated allowing a range in those parameters. For F2 V, F6 V, F2 IV, F4 IV, F6 IV distances of 100, 80, 150, 140, 130 pc respectively are obtained.

Barstow et al. (1992, 1993ab) have carried out detailed studies of the photospheric composition and structure of a number of isolated white dwarfs detected in the ROSAT all-sky survey. In these studies they have compared the observed EUV and X-ray count rates with the predictions of model atmosphere calculations. A χ^2 statistic is calculated to determine the quality of agreement between the data and predictions, taking into account the uncertainties in the measured count rates and instrument calibrations. Two types of atmospheric model have been tested, one comprising only H+He in a homogeneous mixture and a second with H+He in stratified configuration where the H forms a thin layer lying on top of an otherwise pure He envelope. There are five variables that determine the predicted EUV and X-ray fluxes for each

model structure – the stellar effective temperature T_{eff} , interstellar HI column density (N_{H}), \log (stellar surface gravity, g), stellar helium opacity (either He:H ratio or H layer mass) and a stellar distance/radius related normalisation constant. Since there are only four independent data points from the ROSAT observations, additional information is required to specify at least one of the parameters. For an isolated white dwarf one would normally measure the V magnitude and/or determine T_{eff} and $\log g$ by fitting synthetic spectra to the observed Balmer line profiles. However, in HD33959C the optical spectrum of the white dwarf is swamped by that of its companion and so none of this information is available.

It is possible to obtain an estimate of the apparent V magnitude of the white dwarf by comparing the flux in the IUE spectrum with values for other white dwarfs, where V is well known, and then scaling appropriately. As the value of T_{eff} is not known, the extreme cases of CoD-38° 10980 one of the coolest white dwarfs detected by ROSAT (at 25,000K) and HZ43, one of the hottest (50,000K) have been considered. Since there is considerable contamination from the companion star at the longer wavelengths of the IUE spectrum we have chosen to use the 1300Å flux for the HD33959C white dwarf which is $1.4 \times 10^{-12} \text{erg cm}^{-2} \text{s}^{-1} \text{Å}^{-1}$. The low dispersion IUE SWP spectra of HZ43 and CoD-38° 10980 are available in the archive; fluxes of 4.0×10^{-12} and 1.2×10^{-11} are measured. From the published V magnitudes of HZ43 (12.99) and CoD-38° 10980 the magnitude of this new white dwarf lies in the range $V \approx 13.3 - 14.1$, depending upon the value of T_{eff} in the interval 25,000–50,000K, with the larger magnitude corresponding to the higher temperature.

An alternative approach to estimating the V magnitude is to scale a model atmosphere to the 1300Å flux and then convert the resulting 5500Å flux into a magnitude. Table 3 summarises the results of the magnitude estimates as a function of temperature. It can be seen that this technique, as expected if the models are good representations of the continuum flux, gives similar results to the scaling method discussed above. From the V magnitudes it is possible also to estimate the distance to the white dwarf by including an assumption about its radius. A typical white dwarf with $\log g = 7.5$ has a radius $\approx 0.017R_{\odot}$. However, there is no information regarding the surface gravity of this particular object. Sirius B for example, which is also in a binary system, has $\log g = 8.5$ and a radius $\approx 0.007R_{\odot}$. Distance estimates as a function of temperature are included in Table 3 for these radii and for the intermediate value corresponding to $\log g = 8.0$, $\approx 0.014R_{\odot}$.

Table 3.3: Estimated V magnitude, and distance as a function of T_{eff} and stellar radius r , for the white dwarf in HD33959C.

T_{eff} (K)	m_v	distance (pc)		
		$r=0.017R_{\odot}$	$r=0.014R_{\odot}$	$r=0.007R_{\odot}$
25,000	13.1	50	41	27
35,000	13.9	87	71	46
40,000	13.95	99	81	53
50,000	14.13	120	98	64
55,000	14.17	127	104	67
60,000	14.2	134	110	71

Table 3.4: Best fit parameters and error ranges for stratified H+He models

m_v	χ^2	T_{eff} (K)	N_{H} (10^{19} cm^{-2})	H mass ($10^{-13} M_{\odot}$)
13.3	0.26	51,700 (46,600–57,000)	3.3 (2.5–4.0)	1.1 (0.8–1.7)
14.1	0.23	56,283 (52,200–60,000)	3.0 (2.4–3.7)	1.1 (0.8–1.7)

Distance estimates for the F star range from 80 to 150 pc. Hence, it would appear that the white dwarf cannot be as massive as Sirius B but probably has $\log g$ in the range typical of most white dwarfs, between 7.5 and 8.0. In fitting the models to the data the V magnitude normalisation and surface gravity have been fixed at the extremes estimated during each run. With a homogeneous H+He model the best fit models always yield a χ^2 in excess of 8.0 (with 1 degree of freedom), excluding them with a confidence level much greater than 99%. However, the stratified models produce good fits and the results of these, with $\log g$ fixed at 7.5 are summarised in Table 4. Repeating the exercise for $\log g = 8.0$ yields negligible changes to these results. All the parameter ranges quoted are formal 1σ errors and assume that the stated model is applicable.

Within the stratified-atmosphere interpretation of the data, it is clear that the white dwarf has a temperature in excess of 46,000K, placing it in the hotter end of the range considered for the V magnitude estimates. Given a temperature this high the V magnitude of the star must then be in the range $\approx 14.1 - 14.2$ (see Table 3.3) and only the fit at $V=14.1$ need be considered. The remaining uncertainty of 0.1 in V will have a negligible effect on the value of the parameters determined. If, in fact, there are heavier elements ('metals') present, the derived temperature would be even higher.

3.4 Discussion

Accepting the stratified-atmosphere interpretation, the temperature of the white dwarf appears to be in the range 52,200–60,000K. This places the star in the very hottest group of DAs. Analysis of a sample of well-studied DA stars detected in the ROSAT survey shows that most objects in this temperature range appear to contain photospheric opacity in the form of trace metals (see, Barstow et al., 1992 and 1993b). In this example, there are insufficient data to draw the same conclusion, but note that they could be present. However, if the stratified model is the correct interpretation then the white dwarf has formed with a H layer mass at the lower end of the range observed for the general population. If the opacity source is not He then the level of absorption from trace metals is similar to that found in several DAs of the same temperature. Further EUV and far-UV observations are required to search for evidence of trace metals and determine whether any He is in fact present.

More recent work (Barstow et al. 1994 and references therein) has shown HD 33959C to be a single-lined spectroscopic binary with a period of 2.99 days. Analysis of IUE and *Voyager* data (Barstow et al.) has enabled the use of the Lyman α (1216 Å) and Lyman β (1026 Å) lines to better constrain the temperature and gravity of the white dwarf to $T=46,000$ K and $\log g=8.0$. This is in agreement with the preliminary measurements presented here. The masses of primary and white dwarf are $1.3 M_{\odot}$ and $0.55 M_{\odot}$ respectively (Barstow et al.) giving a separation of $10R_{\odot}$. It is likely that the system has undergone a period of common envelope evolution during the red giant phase of the white dwarf progenitor. Barstow et al. point out that the slow rotation velocity of HD 33959C ($v \sin i < 10 \text{ km s}^{-1}$) argues against the binary being a post-Algol system.

The majority of known white dwarfs are isolated stars. Any dK or earlier spectral type companion will dominate the visible spectrum. Nonetheless a number of binary systems containing white dwarfs (excluding cataclysmic variables) have been discovered. Sirius is easily resolved from the Earth, while V471 Tau is an eclipsing binary. Four other systems containing binaries have been discovered serendipitously in their IUE spectra: ζ Cap, 56 Peg, σ^1 Ori, HD 27483 (Barstow et al. and references therein). A further 9 hot white dwarfs with A–K companions (including HD 33959C) have been detected in the ROSAT all-sky surveys to date. These are an important group with periods ranging from a few days to several years. Barstow et al. comment that coronal activity levels are unusually high in the majority of these primaries, given that the

presence of a white dwarf places a lower limit of some 10^9 years on their ages. A mechanism to produce these activity levels could be tidally reinforced rapid rotation, which leads to speculation that these systems may be evolutionarily related to RS CVn or similar systems. The very nature of these binaries allows more accurate determination of physical stellar parameters (mass, radius, distance etc.) than is possible for isolated objects.

Chapter 4

An EUV survey of nearby late-type stars

4.1 Introduction

The completeness of the WFC EUV all-sky survey provides an excellent resource to enable the statistical study of a large number of objects in an as yet virtually unexplored part of the electromagnetic spectrum. Nearly every object in the sky has been observed, albeit somewhat fleetingly, and the detection or non-detection of specific objects can impart useful information - whether about the intrinsic properties of the source, or the nature of the intervening material.

An obvious 'target' for such a study is the local stellar population. Much time has been devoted over the years to the cataloging and investigation of the stars in the solar neighbourhood, so their optical properties are well documented. In addition the total absorbing column to these stars will be in general low. Firstly because they are so close, and secondly studies by e.g. Frisch and York (1983), Paresce (1984), Snowden et al. (1990) and Warwick et al. (1993) have shown that the Sun appears to be located in a tenuous hot local bubble in the neutral material of the disk. It is only within the Solar neighbourhood that one can perform reasonably complete studies of the lowest luminosity stars in the Galaxy.

In theory, the stellar population of the Solar neighbourhood is likely to be well mixed and homogenous. From the motions of nearby stars we see that the orbital timescale is shorter than the evolutionary timescale, and that stars oscillate over distances of up to a kiloparsec radially

and vertically. Thus a star currently in the local neighbourhood may have been half a kiloparsec closer to the galactic centre and on the opposite side of the galaxy several orbital revolutions (about 10^9 years) ago. Stars of spectral type F–M comprise ~ 90 per cent of catalogued objects within 25 parsecs of the sun. Stars with relatively low space densities ($\lesssim 10^{-3} \text{ pc}^{-3}$) such as spectral types O–B, and hot white dwarfs, will be poorly sampled in such a volume limited survey.

Measurement of stellar EUV luminosity functions (hereafter ELF's) define the coronal activity levels in specific classes of stars (e.g. Rosner, Golub & Vaiana 1985, Barbera et al. 1993), and provide data for examining the evolution of this activity (and hence the rotation/convection driven magnetic dynamo that is thought to power the coronae, e.g. Rosner, Golub & Vaiana 1985).

4.2 Constructing a sample

In order to undertake this study, a complete and well defined sample of nearby stars is required. Available catalogues are:

- The **Nearby Star Catalogue** (Gliese 1969) which includes data for 1899 stars within 22 parsecs of the Sun and its supplement (Gliese & Jahreiss 1979) listing 333 stars within 22 parsecs of the Sun.
- The **Catalogue of Stars within 25 Parsecs of the Sun** (Woolley et al. 1970) containing 2150 stars.
- The **Third Catalogue of Nearby Stars** (CNS3 – Gliese and Jahreiss 1992) is a preliminary version containing 3803 stars within 25 parsecs of the Sun.

The most complete sample to date is the CNS3. In table 4.1 I give a breakdown of the catalogue by spectral type and luminosity class. The spectral types used are as listed in the CNS3 which have been collected from a number of different sources using varying techniques. Some of the classifications are tentative (denoted by lower case letters k, m, ...). Where no luminosity class is given, the star is assumed to be main sequence. The binary status of the stars in the catalogue

Table 4.1: Contents of the CNS3.

Type	Total	III	IV	V
O	0	0	0	0
B	3	0	0	3
A	66	6	9	51
F	265	12	59	194
G	494	15	55	424
K	828	19	37	772
M	1821	2	0	1819
WD	163			
Unknown	163			
Total	3803	72	142	2263

This table shows the number of stars in the CNS3 for spectral types O–M and the White Dwarfs, for luminosity classes III (=I–III: giants and supergiants), IV (sub giants) and V (main sequence).

is unknown to a considerable degree, it is further discussed below. The distance of each star was taken as the reciprocal of the CNS3 ‘resultant parallax’. The version of the CNS3 used here was supplied by the Starlink project at Rutherford Appleton Laboratory, with the original equinox B1950, epoch 1950.0 coordinates transformed to equinox J2000, epoch 1990.0 for use with the ROSAT survey data. I have corrected an error in the original CNS3 coordinates of Gl 841A, using values from the Hipparcos Input Catalogue (Turon et al. 1992).

Kinematic information, in the form of heliocentric U (+ve to galactic centre), V (+ve in direction of galactic rotation) and W (+ve to north galactic pole) velocities, is available for a large proportion of stars in this catalogue and are shown in Fig. 4.1. The irregular polygon delimits the region of kinematically young disk stars (Eggen 1983 and references therein), and should contain stars which are younger than the Hyades ($\sim 5 \times 10^8$ years). Stars outside this region include old disk stars and, towards the extremes of the distribution, halo population stars (Eggen 1973a, 1973b, 1973c). So the Solar neighbourhood contains stars with a large spread in kinematic ages.

4.2.1 Completeness

Before proceeding, the completeness of the catalogue must be ascertained. It is likely that many fainter stars have not been observed in the surveys that have gone into the construction of the

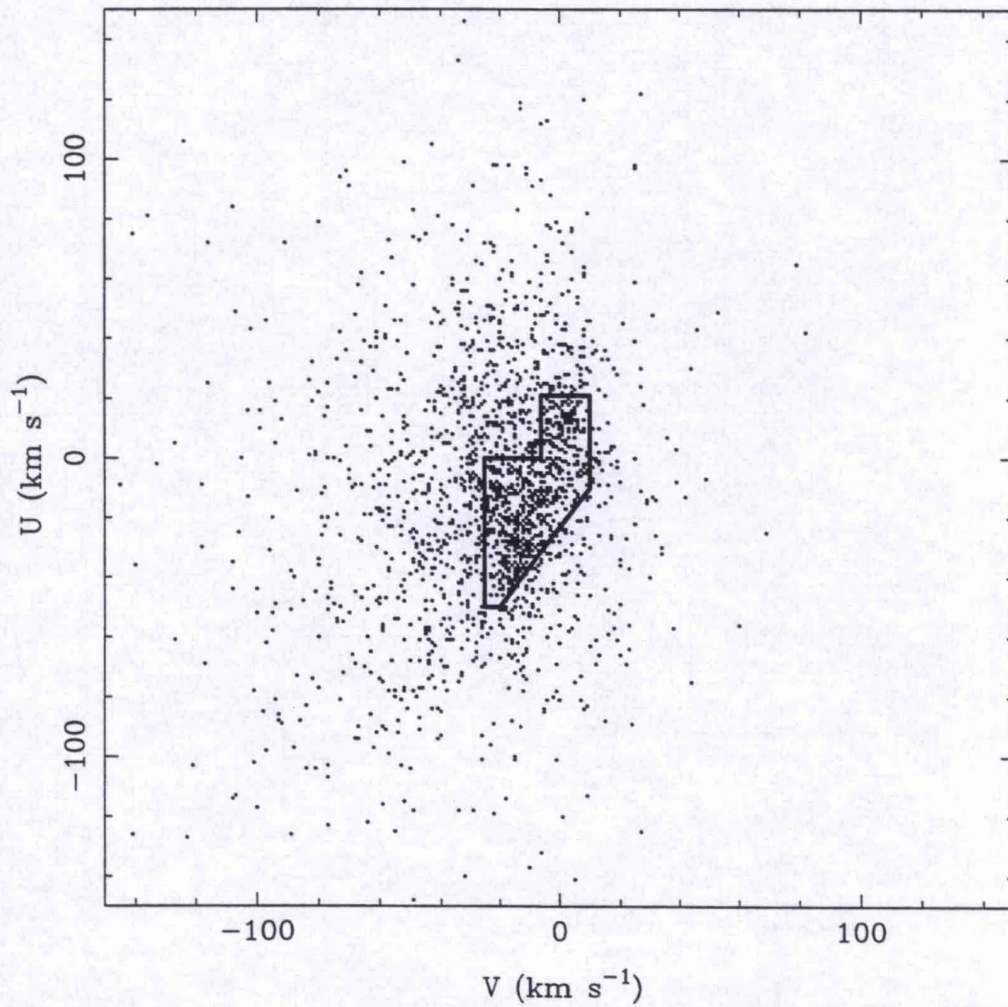


Figure 4.1: The (U, V) distribution of stars in the CNS3. The irregular polygon delimits the region populated by kinematically young disk stars. U is the space velocity component in the galactic plane and directed to the galactic centre, while V is the component in the galactic plane and in the direction of galactic rotation.

catalogues. Upgren & Armandroff (1981) have examined the degree of completeness of the then catalogued nearby stars as a function of B-V. They find that main-sequence stars bluer than $B-V = 1.40$ (equivalent to a spectral class of about M0) are uniformly distributed over the entire sky and throughout the volume within a limiting distance of 22pc. For stars of later spectral-type they confirm the well known incompleteness of M dwarfs and comment on the distance dependency.

In order to examine the completeness of the CNS3, the relationship between number density (ρ) and distance is investigated for each spectral type under study. In addition the method of V/V_{\max} (after Schmidt, 1975 and Upgren & Armandroff, 1981) is employed to test for uniformity. The ratio V/V_{\max} is formed for each object under consideration, where V is the spherical volume enclosed within the distance r to that object, and V_{\max} is the volume enclosed by r_{\max} , the maximum distance at which the object would still be included in the sample. For a uniform space distribution, the ratio V/V_{\max} for all objects in the sample would be constant between 0 and 1 and its mean would be equal to 0.5 with a standard deviation $\sigma_{V/V_{\max}} = 1/\sqrt{12n}$. Within 25pc it is reasonable to assume that the true distributions of stars of all kinds (except perhaps the brightest ones which are comparatively rare) are uniform and that interstellar absorption is negligible. The only statistically significant deviations of $\langle V/V_{\max} \rangle$ from 0.5 are then assumed to be due to incompleteness imposed by observational selection effects operating among the stars in the sample. Fig. 4.2 shows that $\rho(r)$ is constant out to 25 parsecs for all but the M stars where incompleteness appears to set in at 6 parsecs. Fig. 4.3 indicates that V/V_{\max} is constant at 0.5 for spectral types F-K as a function of distance. For M stars the ratio begins to drop steadily away beyond about 16 parsecs.

Therefore I can conclude that the CNS3 is complete for spectral types F, G, and K out to the limiting distance of 25pc, while for the M dwarfs it is necessary to impose a distance limit of 16pc where incompleteness becomes highly significant. Although incompleteness is still a factor beyond 6 parsecs, this must be offset against the disadvantages of selecting too small a sample.

4.2.2 Multiplicity: spectroscopic binaries

A binary system is defined as a pair of stars revolving in a stable orbit about their common centre of mass. This definition is extended here to include common proper motion pairs. Binaries

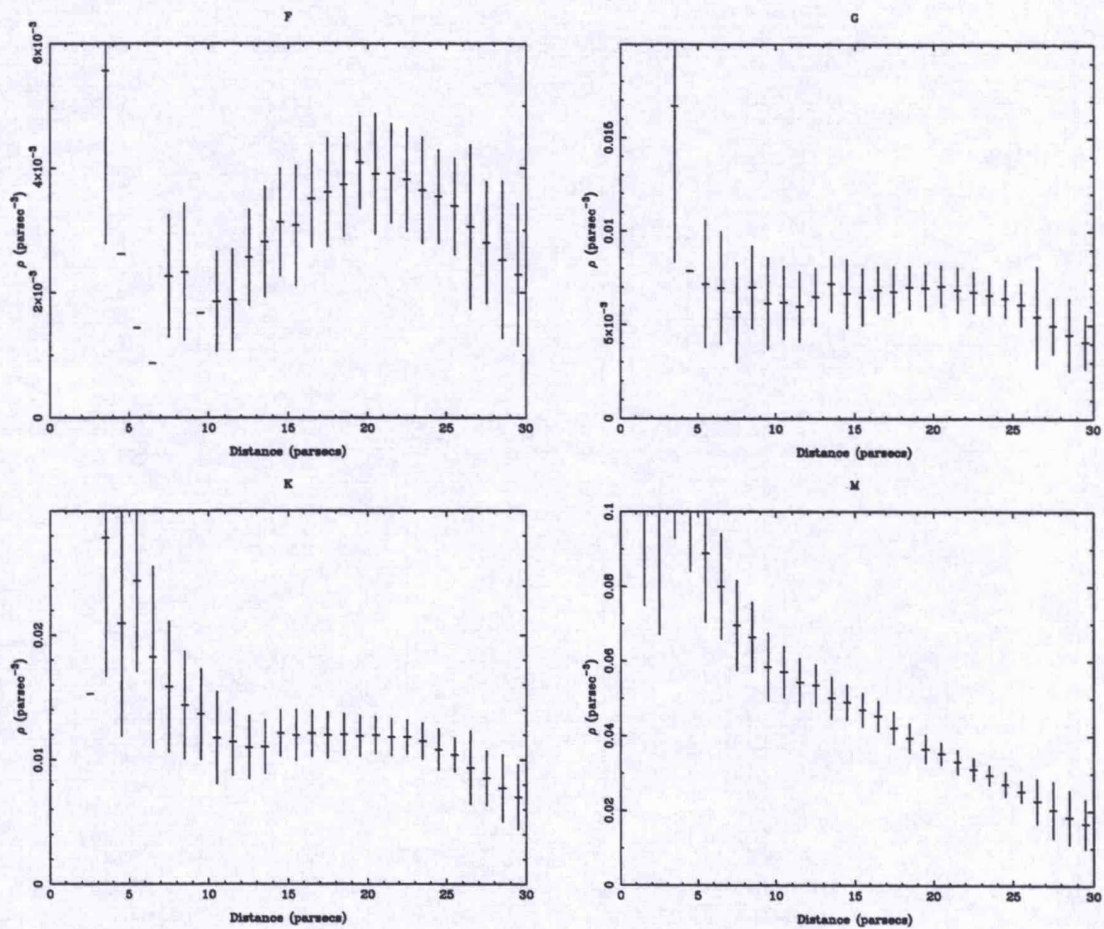


Figure 4.2: Number density (ρ) of CNS3 stars as a function of distance. Note that the points without error bars contain only one star in the bin.

are classified as *Visual*, *Spectroscopic* or *Eclipsing*. If the stars in a binary are sufficiently close (corresponding to an orbital period \lesssim a few days) tidal interactions may become important. The effect is to circularise the orbit and maintain high rotational velocities which will lead to enhanced activity. Many authors (e.g. Kroupa et al. 1993) have estimated that a half or more of all stars are in binaries, i.e. more stars are to be found in binary systems than in isolation. In addition many more complex systems exist, consisting of three or more stars.

In this chapter an attempt will be made to take account of the binary nature of the stars in the sample. To this end I will deem spectroscopic and eclipsing binaries to be interacting, while visual binaries will be deemed non-interacting. Data has been obtained from the Eighth

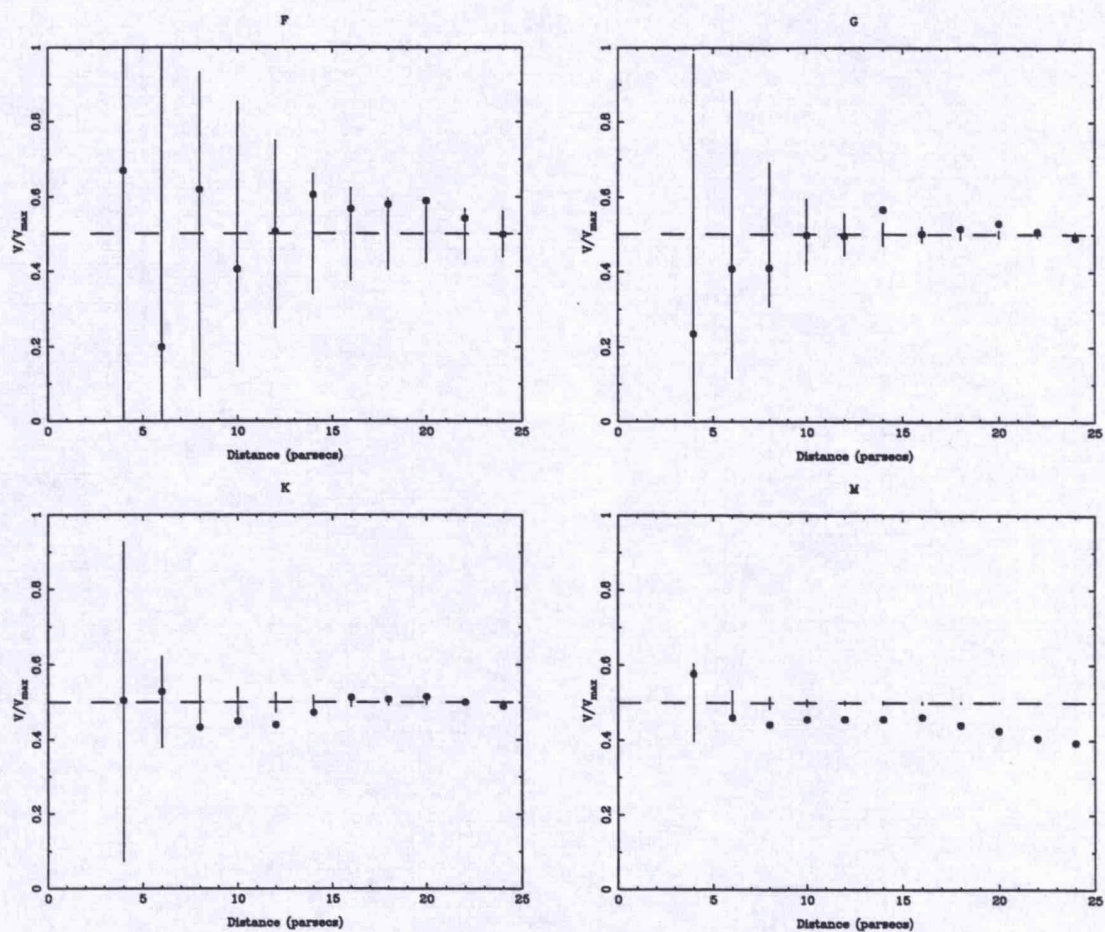


Figure 4.3: V/V_{\max} as a function of distance for CNS3 stars. The 3σ errors are shown, where $\sigma_{\langle V/V_{\max} \rangle} = 1/\sqrt{12n}$

Catalogue of the Orbital Elements of Spectroscopic Binary Systems (Batten et al. 1989), the Catalogue of Chromospherically Active Binaries (CCABS, Strassmeier et al. 1988), from the CNS3 itself, and in one case from a report in the literature (for Gl 841A, Jeffries & Bromage 1993).

A total of 195 of the stars in the CNS3 have been classified as spectroscopic binaries. A further 45 are noted in the CNS3 as suspected spectroscopic binaries, while 43 stars show a variable radial velocity. Therefore 283 stars in the CNS3 have been flagged accordingly in order to investigate the properties of single stars as distinct from those which are (or are suspected to be) spectroscopic binaries.

4.3 Measurement of counts

4.3.1 The problem

EUV images from the WFC are dominated by Poisson noise, due to the small numbers of photons detected in each pixel. The background is extremely variable on a day-night timescale and is high with respect to the EUV fluxes from the sources. I wish to determine whether a given star has been detected and, independently, I need to deduce constraints on the true flux from the star. Two approaches to measuring the counts are

- Cross-correlate the CNS3 with the standard detection algorithm results (*e.g.* NIPS or PSS) used in the pipeline processing of the WFC all-sky survey data. Upper limits can be determined from the minimum detectable count rate map as determined by Pounds et al. (1993).
- Measure source cell and background counts directly from the $2^\circ \times 2^\circ$ small map images

The former method is comparatively simple to implement. It is, however inflexible in the sense that the detection threshold cannot be varied. In addition the measurements of the upper limits will be insensitive to small scale fluctuations in the background as the minimum detectable count rate map has been constructed with a resolution of 15 arcminutes. The latter approach will allow adjustment of the threshold for detection, and can cope with local background variations such as the day-night gradients seen in many survey images. The second method is to be preferred, although a comparison will be shown with the results of cross-correlating the CNS3 with the full S2NIPS catalogue as a check for consistency.

4.3.2 Description of technique

For each star in the CNS3, the relevant $2^\circ \times 2^\circ$ small map image has been measured. The detection cell containing N counts must be optimized such that the ratio (ρ) between the source counts, S , and the uncertainty in the background counts, B , within the cell is maximized.

$$\rho = \frac{S}{\sqrt{B}} \quad (4.1)$$

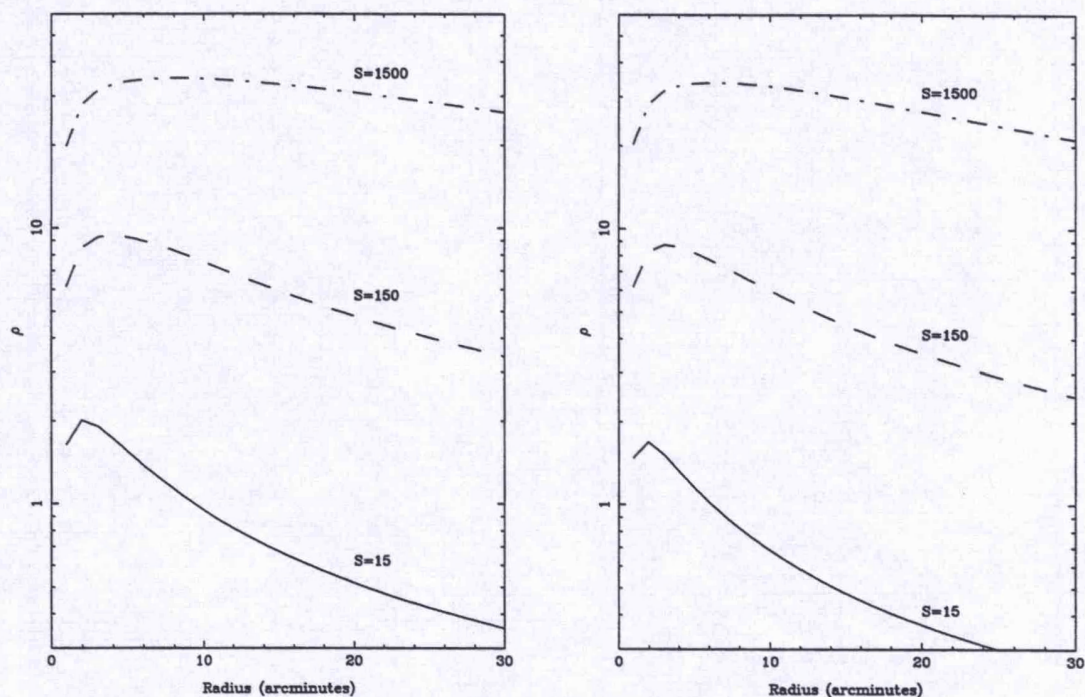


Figure 4.4: ρ as a function of detection cell radius for total source counts of 15, 150, 1500 for filters S1a (left) and S2a (right). I have assumed a 'low' background count-rate of $0.5 \text{ counts s}^{-1}$ for the S1a filter and for comparison a 'high' background count-rate of 4 counts s^{-1} for the S2a filter.

In Fig. 2.4 (Section 2.4) the WFC survey-averaged point spread function (PSF) is shown. For a variety of source strengths and background levels I have calculated the optimum radius for detection (Fig. 4.4 shows how ρ varies as a function of radius for high and low background and source count-rates). To keep the PSF correction fairly low, and to allow for inaccuracies in catalogue/WFC positions, a circular detection cell radius of 4 arcminutes was taken. For a typical weak WFC source the total error on position is ~ 1 arcminute (which is significantly less accurate than the CNS3 catalogued coordinates).

I must consider a number of factors when deciding how to measure the background. Traditionally for pointed observations an annulus is used and by increasing the area I can improve my estimate of the mean, assuming no spatial variations. For the survey data, one small map image may contain data taken from typically 5 days. This is often apparent as 'ramping' or 'rippling' in the images as the viewing conditions change, e.g. the satellite passing from day to night. If I wish

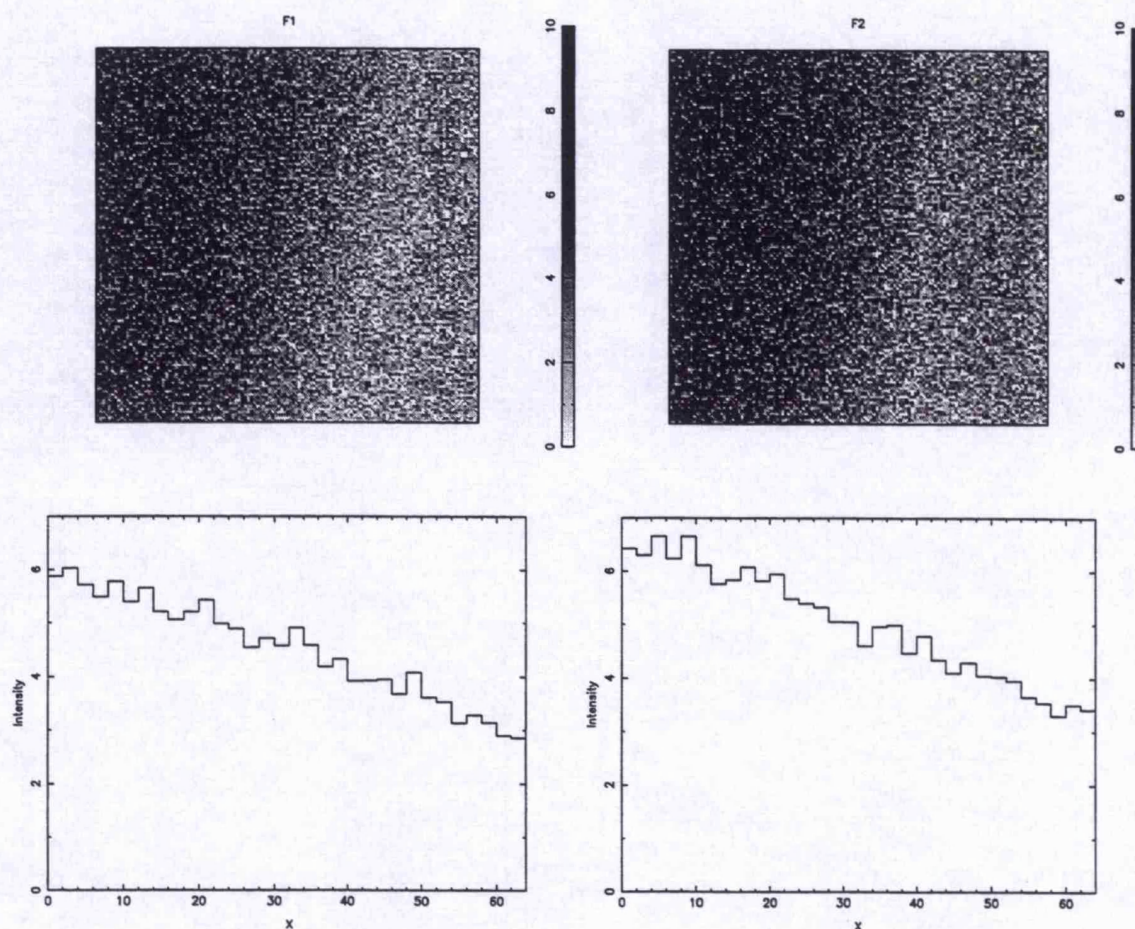


Figure 4.5: WFC small map ($2^\circ \times 2^\circ$) images showing background ramping in filters S1a and S2a. Also shown are cuts across these images.

to measure the background in the source cell I should measure my background from regions of the sky that were observed at approximately the same time as the star. There is therefore a trade-off between using a large background cell to improve the statistics on the measurement of the mean background, and the need to avoid the introduction of extra variations. Thus I chose the background region to be four source cell sized circles aligned along the scan path (i.e. ecliptic north-south in the images). Fig. 4.5 shows a typical WFC $2^\circ \times 2^\circ$ small-map image exhibiting this background ‘ramping’.

The source cell counts and background estimate were measured for each member of the CNS3 as outlined above.

4.3.3 Source recognition and upper limits

It is important to separate the question of detection from the determination of confidence levels on the 'true' number of counts from the source. Kraft et al. 1991 (hereafter KBN91) discuss this problem in some depth. They point out that a common mistake is to derive an $n\sigma$ (where σ ($\equiv \rho$) is defined in Equation 4.1) upper limit using the Poisson distribution for the mean number of background counts per detection cell. Whilst this is a correct procedure for determining the level of significance of a source detection, it does not correctly obtain upper or lower limits on the source counts. The $n\sigma$ uncertainty in the background only gives the probability that a statistical fluctuation on the background could have given the observed number of counts in the absence of a source.

Source detection

I adopt the null hypothesis that no sources are present in both the detect and background cells and that the counts in both these cells are derived from similar parent Poisson distributions whose means scale like the areas of the two cells. Let N and B be the counts in the detect and background cells respectively (the latter normalised to the area of the detect cell). Then the probability of having N counts in the detect cell, when the background in that cell is B is given by

$$P(N, B) = \frac{B^N e^{-B}}{N!} \quad (4.2)$$

I may choose the threshold for rejection of the null hypothesis, i.e. the confidence level for detection (CL), such that

$$CL = \sum_{n=0}^{n=N-1} \frac{B^n e^{-B}}{n!} \quad (4.3)$$

To investigate whether this formulation holds true, the detection procedure was performed for a random sample of coordinates (the CNS3 coordinates were all shifted by 15 arcmin). Table 4.2 shows the results for a number of runs with different confidence levels for detection.

Table 4.2: Confidence levels for source detection

Poisson Confidence	WFC Filter	Number of 'detections'		
		At CNS3 Coordinates	At Random Coordinates	Expected
(1)	(2)	(3)	(4)	(5)
0.900	S1a	443	199	380
	S2a	712	291	
0.950	S1a	395	146	190
	S2a	547	242	
0.990	S1a	283	81	38
	S2a	281	81	
0.995	S1a	251	52	19
	S2a	216	50	
0.999	S1a	198	19	4
	S2a	156	16	

Key:(1) theoretical confidence level CL for source detection, from Poisson counting statistics; (2) ROSAT WFC survey filter; (3) number of detections recorded at coordinates of 3803 CNS3 stars; (4) number of spurious detections recorded at 3803 'random' coordinates; (5) number of spurious detections [3803(1-CL)] expected from Poisson confidence level CL.

Especially for low confidence levels, the detection algorithm is giving many times more spurious detections than would be expected if the background fluctuations were purely Poissonian. The true source density at the sensitivity of the WFC is extremely low. In the S2NIPS catalogue there are 1537 sources which is equivalent to 0.037 sources per square degree. Assuming a uniform sky density I would expect only ~ 2 sources to be detected by coincidence using a 4 arcminute radius detection cell. By selecting a *theoretical* detection threshold of 0.999, I expect in *practice* approximately 10% of my sources to be spurious detections.

Constraining the 'true' source counts

The 'classical' method. Assuming the existence of a source, in the Poisson regime, the probability of detecting N photons in observation time t is

$$P(N) = \frac{(S + B)^N e^{-(S+B)}}{N!}, \quad (4.4)$$

where S is the true mean number of counts from the source and B is the true mean number of counts from the background in time t . B is assumed to be accurately determined and therefore error free. But in the detection cell, in practice, $N = N_S + N_B$, and in any particular observation N_B cannot be determined as it is subject to Poisson fluctuations. Given the observationally determined values of N and B , what can I then say about S ? One can form the confidence interval between S_{\max} and S_{\min} such that $S_{\min} \leq S \leq S_{\max}$ with confidence greater than or equal to CL ($0 \leq CL \leq 1.0$). The confidence interval is defined such that if many observations are made, then $100 \times CL\%$ of the observations would generate values of S_{\min} less than S and S_{\max} greater than S .

So one may formulate the one sided lower limit on S with the assumption $B = 0$ thus

$$\sum_{n=0}^{N-1} \frac{e^{-S_{\min}} S_{\min}^n}{n!} = CL, \quad (4.5)$$

and similarly for the upper limit,

$$\sum_{n=0}^N \frac{e^{-S_{\max}} S_{\max}^n}{n!} = 1 - CL \quad (4.6)$$

(KBN91, Gehrels 1986 and references therein). It would be incorrect to reformulate the above such that $S = N - B$ where B is the (finite) mean background, because this completely ignores the fluctuations in the background. An obvious case is that for $N < B$ which would require negative source counts. However I may subtract the mean number of background counts, B , from the calculated limits. Negative limits are then set to zero. This method will give confidence limits that satisfy the classical definition of confidence intervals, but KBN91 discuss several objections to this method. The first is that this technique does not minimize the confidence interval; the smallest interval will set the tightest constraints on the model parameters. A further criticism is that a downward fluctuation in the number of background counts detected has the effect of decreasing the apparent uncertainty with which the source counts are determined. Their last point is that if there is any uncertainty in the measurement of the background, then there is no simple way to extend the classical method.

The Bayesian method. Bayes's theorem is given by

$$f_{N,B}(S) \propto p(S)P_S(N) \quad (4.7)$$

(KBN91), where $f_{N,B}(S)$ is called the posterior probability function for the parameter S as a function of the observables, N and B . The first term on the right hand side, $p(S)$, is the 'prior'. The second term on the right hand side is (in our case) the Poisson distribution for S . KBN91 then construct the posterior probability distribution for $S + B$ thus,

$$f_{N,B}(S) = C \frac{e^{-(S+B)}(S+B)^N}{N!} \quad (4.8)$$

for $S \geq 0$. The normalization constant, C , is given by

$$C = \left[\int_0^\infty \frac{e^{-(S+B)}(S+B)^N}{N!} dS \right]^{-1} = \left(\sum_{n=0}^N \frac{e^{-B} B^n}{n!} \right)^{-1}. \quad (4.9)$$

The lower limit of the integration is zero as I wish the prior to exclude negative values of the source flux. The distinction between the classical and Bayesian functions is explained well in KBN91. To summarise, The classical function gives the absolute probabilities of obtaining different N for a given S and B . The Bayesian function reverses the roles of N and S , i.e. it is the continuous probability distribution for the source flux, S , given N and B . The interpretation in the Bayesian approach is that $f_{N,B}(S)$ gives the relative probabilities that the observed number of counts could have been produced by sources of different flux S . They show that the confidence limits for S in the Bayesian case are obtained simply by integrating the probability distribution function, $f_{N,B}$, over S and solving numerically for S_{\min} and S_{\max} such that

$$\int_{S_{\min}}^{S_{\max}} f_{N,B}(S) dS = CL, \quad (4.10)$$

where CL is the probability of the source flux lying between the limits S_{\min} and S_{\max} .

Another important aspect to the approach described in KBN91 concerns the choice of confidence

limits which satisfy equation 4.10. They define a procedure for finding the minimum confidence interval, that is the confidence region which most tightly constrains S . I have adopted this procedure.

To summarize, for all the CNS3 stars I have assigned upper and lower limits to the source flux (number of counts), S , using the Bayesian approach as described in KBN91. Detections are defined by the rejection of the null hypothesis (at a specified confidence level) that the background and detect cell counts are drawn from similar parent Poisson distributions.

4.3.4 Multiplicity: visual binaries

Many of the detected stars are members of multiple systems which cannot be resolved into their separate components by the WFC. Any two stars with a separation of ≤ 8 arcminutes (the detect cell radius is 4 arcminutes) that are both detected in the same filter are quite likely to have their detect cells overlapping the same source. The problem is to decide which star (or stars) is the true source of the EUV radiation. In Appendix A is a list of all detections with footnotes pertaining to individual objects for which decisions re: multiplicity have been made. By visual inspection of the survey images one can check whether or not there are two separate sources. Using the error circle for the source, for widely separated objects, one or more of the candidates may be ruled out. For close visual binaries (separation $\lesssim 1$ arcmin) and spectroscopic binaries it is necessary to resolve the dilemma using information from the optical identification programme (Mason et al. 1995) or from catalogues, to estimate the most likely source of the EUV emission (cf. Pounds et al. 1993). Where such information is not available or of no help, then the EUV emission must be ascribed to one, some or all of the candidates in a semi-arbitrary fashion. A particular detection may have a significant effect on later results - for example a very low luminosity detection may strongly affect the luminosity function. Where a detection is allocated to one star in a multiple system, the other members are assigned upper limits equal to the detected count-rate.

I find 61 detections coincident with multiple systems, containing a total of 130 stars. For some 47 of these systems, an extensive literature search has helped to decide the most likely source of the EUV emission, on the basis of such properties as: Calcium II H & K flux, H α flux, *Einstein* HRI observations (which may resolve the components), IUE observations of

chromospheric transitions. The remaining 14 systems are all visual binaries, 6 of which are known to have both components active; the other 8 are made up of 1 F-star, 3 G-stars, 5 K-stars and 7 M-stars. The EUV flux has been divided equally between the stars in each of these 14 systems. The footnotes to the table in Appendix A discuss in some detail the allocation of the EUV flux for each multiple system.

4.4 Flux conversion

Fig. 2.4 (Section 2.4) shows that approximately 75% of the source photons will lie within the detect cell, so I must correct for this. The counts may now be converted to count rates by extracting the exposure time for every star from a 1° resolution exposure map of the sky. In Fig. 4.6 I plot the NIPS count-rate (as derived by cross-correlating the S2NIPS catalogue with the CNS3) against the count-rates measured in this survey. There is a very strong one to one correlation between the two independently measured count-rates. The three points which lie below the correlation will not have a significant impact on later results. The reason for the discrepancy is unclear.

In order to convert the WFC count rates to apparent ‘unabsorbed’ fluxes and hence into luminosities, an incident spectrum has to be assumed. A conversion factor was chosen that is appropriate for a thermal spectrum from an optically thin plasma at a temperature of $T \sim 10^6$ K and a line of sight photoelectric absorption $N_H \leq 10^{18.5} \text{cm}^{-2}$ (Raymond & Smith, 1977). I use the same conversion factor for all the stars in the CNS3; the validity of this assumption will be investigated further under the heading ‘Simulations’ (Appendix B and Section 4.7.1). The S1a and S2a filters show greatest sensitivity to hot gas at temperatures of about 10^6 K. The count-rate to flux conversion factors are essentially independent of temperature for plasmas between 5×10^5 K and 5×10^6 K. There is however an expected $\sim 30\%$ error in these curves caused by a combination of the uncertainty in the spectra produced by hot optically thin plasmas and the uncertainties inherent in the calibration of the WFC filters. Also errors are introduced by my assumption of the same temperature for all coronae. Fig. 2.6 in Section 2.4 shows that the S2a filter is significantly more sensitive to changes in the assumed plasma temperature.

Additional inaccuracies arise from the assumption of equal and very low N_H in all directions.

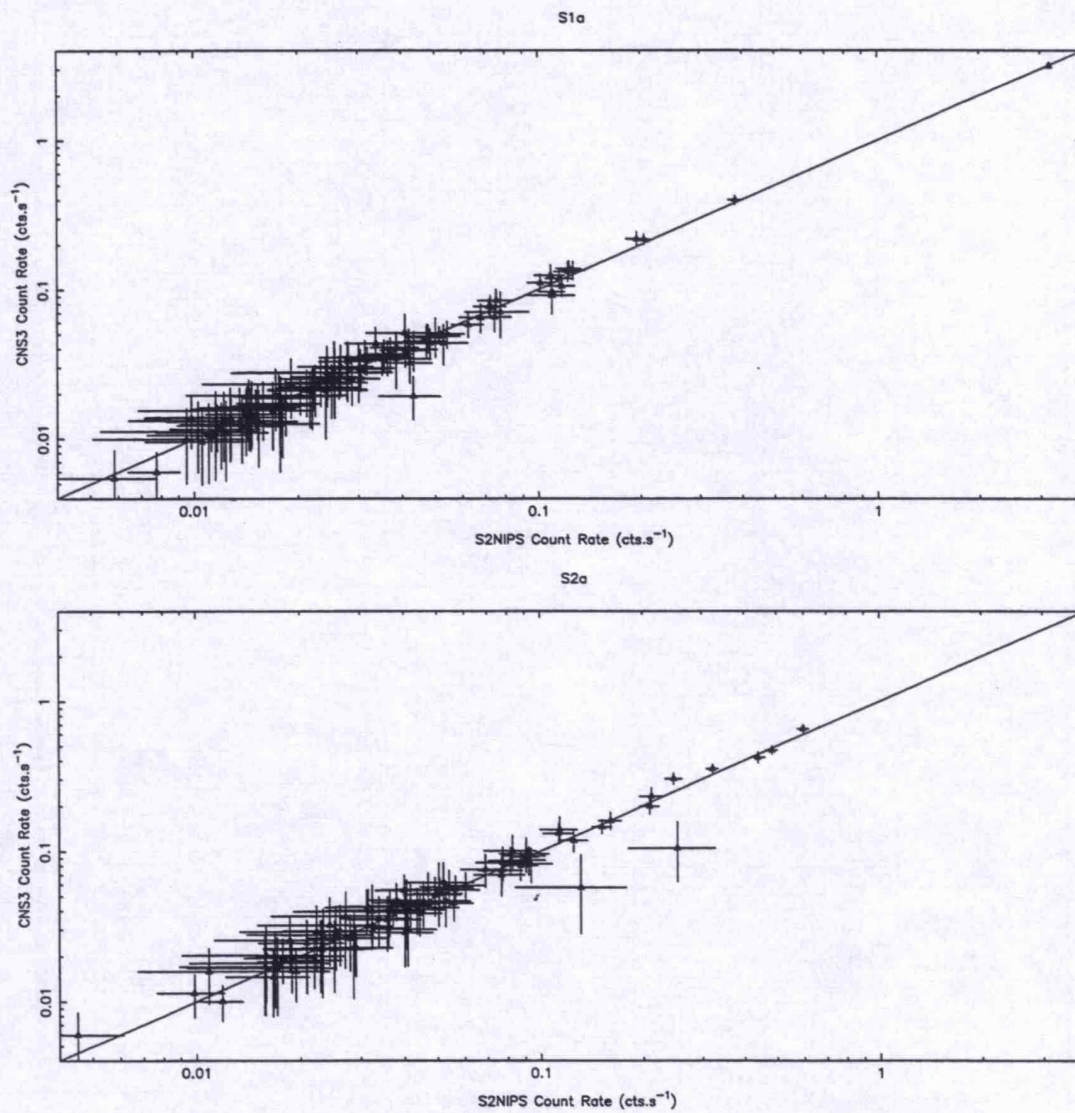


Figure 4.6: Comparison between NIPS and CNS3 survey count-rates. The solid line represents a one to one correlation.

There is strong observational evidence that the sun is located in a hot tenuous bubble, but the wall of this bubble may come as close as 10 parsecs in the general direction of the Galactic Centre (Frisch & York 1983, Paresce 1984, Snowden et al. 1990, Warwick et al. 1993). However, the effect of the ‘wall’ on the CNS3 survey results is expected to be marginal given that it occupies only $\sim 10\%$ of the sky. The distances used to convert flux to luminosity are derived from the resultant parallaxes listed in the CNS3. These are generally the trigonometric parallaxes for $\sim 70\%$ of the stars in the catalogue. (The remainder are spectroscopic or photometric parallaxes). In total, counting statistics aside, we anticipate errors (mainly arising from uncertainties in the CNS3 parallaxes and WFC flux/count-rate conversions) of the order of 50% in the EUV luminosity estimates.

4.5 Results

4.5.1 The complete sample

A list of all the detected stars and their properties are listed in Appendix A. Table 4.3 summarises the results for the detection algorithm for each of the spectral-type samples in both filters. Note that almost all the RS CVn systems are classified as spectral type G, while the BY Dra systems are exclusively K or M type stars. In addition table 4.3 lists the number of spectroscopic binaries (known and suspected) detected in each spectral-type bin.

Fig. 4.7 shows the EUV luminosity-distance distribution for the whole distance limited CNS3 sample in both filters. Many of the upper limits are significant, being ‘below’ the detections at comparable distances. The minimum detected L_{EUV} is from Gl 551 (Proxima Cen, dM5e). Fig. 4.7 implies that the nearest stars are also the (intrinsically) faintest stars. This demonstrates very clearly the inherent bias in the volume limited survey. Lower luminosity stars probably exist, but their luminosities cannot be constrained below that of the nearest stars.

4.5.2 Comparison with the WFC-BSC

In addition I have cross-correlated the CNS3 with the WFC-BSC using a maximum separation of 1 arcminute. In this case, where there are multiple stars for a single WFC detection, I have

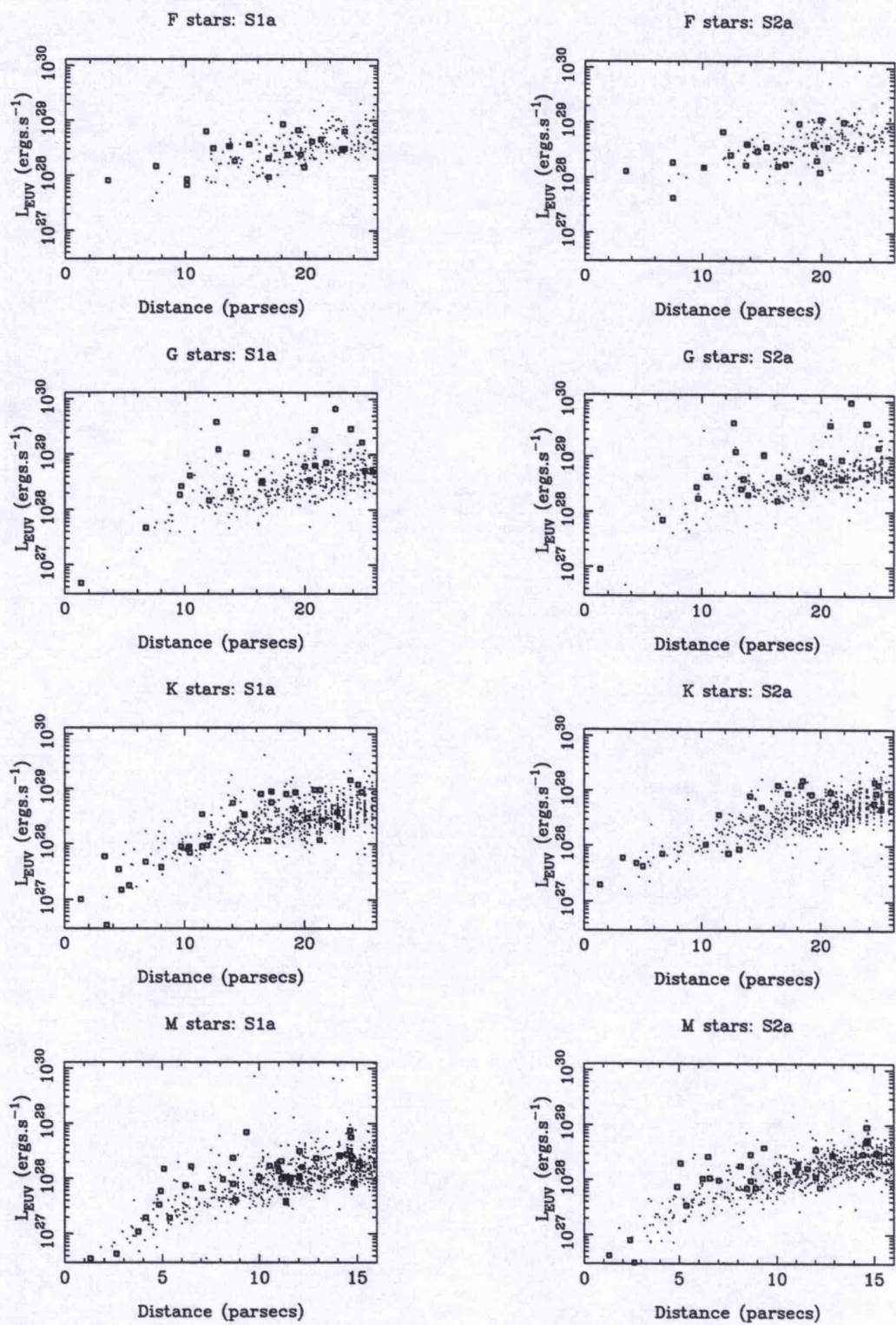


Figure 4.7: The luminosity-distance distribution for the CNS3. Squares are detections. Dots are upper limits.

Table 4.3: WFC Detections

Type	D _{LIM} (pc)	N _{CNS3}		NDET			NDET _{RS}			NDET _{BY}			NDET _{SB}		
		S1a	S2a	S1a	S2a	Total	S1a	S2a	Total	S1a	S2a	Total	S1a	S2a	Total
F	25	219	219	22	22	30	1	1	1	0	0	0	11	11	16
G	25	404	404	23	22	28	7	8	8	0	0	0	12	12	13
K	25	688	680	38	25	47	0	0	0	5	5	5	10	12	13
M	16	731	726	47	34	54	0	0	0	4	3	4	10	7	10
Total		2042	2029	130	103	159	8	9	9	9	8	9	43	42	52

D_{LIM} is the limiting distance for stars in my sample.

N_{CNS3} is the number of stars in CNS3 out to D_{LIM} observed in each filter (sky coverage slightly less than 4 π steradians).

NDET is the number of detections in each filter out to D_{LIM}.

NDET_{RS}, NDET_{BY} are the number of RS CVn and BY Dra systems (as listed in Strassmeier et al., 1988 and included in the CNS3) detected in each filter out to D_{LIM}. NDET_{SB} is the number of spectroscopic binaries (known or suspected) detected out to D_{LIM}.

Table 4.4: Bright Source Catalogue Detections

Type	NDET			NDET _{CNS3}		
	S1a	S2a	Total	S1a	S2a	Total
F	20	12	22	12	9	14
G	60	36	60	15	14	18
K	49	34	53	17	15	20
M	40	29	49	26	18	36
Total	169	111	184	70	56	88

removed the duplicate(s) using information from the WFC optical identification program, or from the literature, to estimate the most likely source of the EUV emission (cf. Pounds et al., 1993). The results of this cross-correlation are listed in table 4.4.

By comparing the last column of table 4.4 with the total number of detections for the survey method (Table 4.3, column 7), I can see that the latter technique has detected nearly twice as many stars overall. Table 4.4 also enables me to assess the degree of overlap between the WFC-BSC and the CNS3. For the F and M-stars, about 60-70 % of the WFC-BSC are made up of stars contained in this survey. For the G and K-stars this fraction is in the range 30-40 %.

4.5.3 L_{EUV} dependance on colour

The $L_{\text{EUV}} - (B - V)$ colour relation is shown in Fig. 4.8 for all CNS3 stars within 16 pc. There is no obvious correlation, but at a given $B - V$ there is a very large spread in luminosity (greater than two orders of magnitude). There are 4 white dwarf apparent detections which do not appear in Fig. 4.8. These comprise two DA stars (hot white dwarfs), one DZ7 and one DC (cool white dwarfs). The DC white dwarf is very likely too cool to be the EUV source - another field star is the more probable candidate. A number of stars have no measured value of $B - V$. This lack of correlation is not surprising. Observations of the Pleiades (Stauffer et al. 1994) show that the dominant contribution to the dispersion in L_X at a given mass comes from the dispersion in rotation among low mass stars (for stars with $(B - V) \geq 0.60$).

4.5.4 Correlation of L_{EUV} with absolute magnitude and bolometric luminosity.

In Fig. 4.9, L_{EUV} is plotted versus M_V for detections and upper limits within 16 pc. Also shown are lines of constant $L_{\text{EUV}}/L_{\text{bol}}$ which is the fraction of the total energy output emitted in the WFC passband. This ratio can be taken as an indicator of coronal heating efficiency (see e.g. Fleming et al. 1993). Interpretation of this heavily censored data set is difficult. While L_{EUV} appears to drop with decreasing mass, $L_{\text{EUV}}/L_{\text{bol}}$ does not appear to depend on M_V for low mass stars.

To test this further $L_{\text{EUV}}/L_{\text{bol}}$ is plotted against M_V in Fig. 4.10 for stars with $M_V > 8.0$ (again using a distance limit of 16 pc). The Bolometric Correction (BC_V) and hence M_{bol} is derived from the formula given by Petterson (1981).

$$BC_V = -0.397M_V + 2.386 \quad (4.11)$$

An important question concerns the behaviour of coronae as low mass stars develop very deep (or even fully) convective interiors (e.g. Liebert and Probst 1987; Cox et al. 1981; Dorman et al. 1989), i.e those stars with mass $\lesssim 0.3M_{\odot}$, roughly corresponding to spectral type $\geq \text{dM4}$, $M_V \gtrsim 13.5$. For the small number of very late M dwarfs with detections in the WFC, Fig. 4.10 suggests that $L_{\text{EUV}}/L_{\text{bol}}$ does not drop with the (expected) onset of full convection.

Fleming et al. (1993) present PSPC all-sky survey results for most known M dwarfs later than

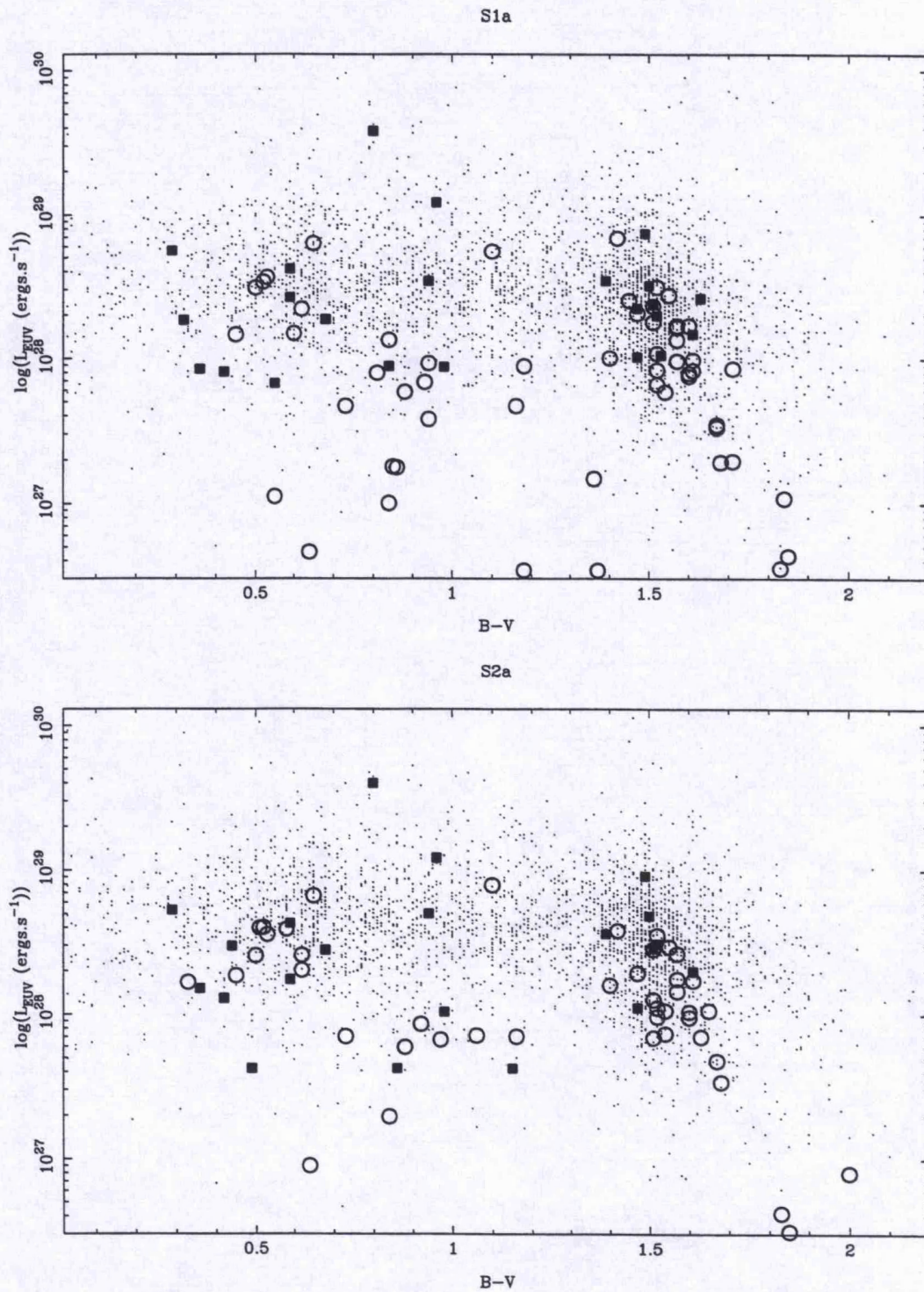


Figure 4.8: The luminosity-colour relation for the CNS3. Single stars are open circles, spectroscopic binaries (suspected and known) are solid squares. Dots are upper limits. The upper panel is for the S1a filter, the lower panel for S2a.

Table 4.5: Late M dwarf detections

Gliese Number	Name	Sp. Typ.		B-V		M_V	
		A	B	A	B	A	B
Gl 275.2	—	sdM5	DC WD ¹	1.71	—	13.25	—
Gl 54.1	LTT 670	dM5e	—	1.84	—	14.19	—
Gl 65	UV Cet	dM5.5e	dM5.5e	1.85	—	15.47	15.60
Gl 551	Proxima Cen	dM5e	—	1.83	—	15.49	—
Gl 896	EQ Peg	dM4e	dM6e	1.54	1.65	11.29	13.30

1) The DC White Dwarf has been ruled out as the EUV source on the grounds of being too cool.

type M5, as well as some selected ROSAT pointed observations. Their sample contains early M stars previously detected in the *Einstein* EMSS and optically selected very late M stars. The EMSS stars (being X-ray selected) are used to define the saturation boundary. They perform a regression analysis of L_X/L_{bol} on M_V incorporating censored data. They find a 5% probability that L_X/L_{bol} and M_V are related, and find a best fit slope of zero. They argue that these results indicate that late M dwarfs can have coronae which are just as active as those for the early M dwarfs and that coronal heating for 'saturated' stars does not drop at spectral type dM6, although they acknowledge the potential incompleteness in their sample. A similar study by Barbera et al. (1993) finds a steep drop in L_X and surface X-ray flux for stars later than $M_V \sim 13.4$. They argue that this is at odds with the results of Fleming et al., who, by searching for a linear correlation have ignored the possibilities of a rapid (i.e. non-linear) change of effectiveness of stellar dynamos.

When comparing the WFC results (which are not subject to the X-ray selection effects of the Fleming et al. study and have significantly better sky-coverage than the Barbera et al. survey) I must first note that the WFC has detected only 5 stars with $M_V > 13.5$ (see table 4.5). So, although the EUV observations appear to support the results of Fleming et al. (1993), I must be cautious not to attach too much significance to them. This question must wait until the substantial incompleteness in the CNS3 for very faint stars has been removed, before the ROSAT X-ray and EUV all-sky survey can be properly used to address it.

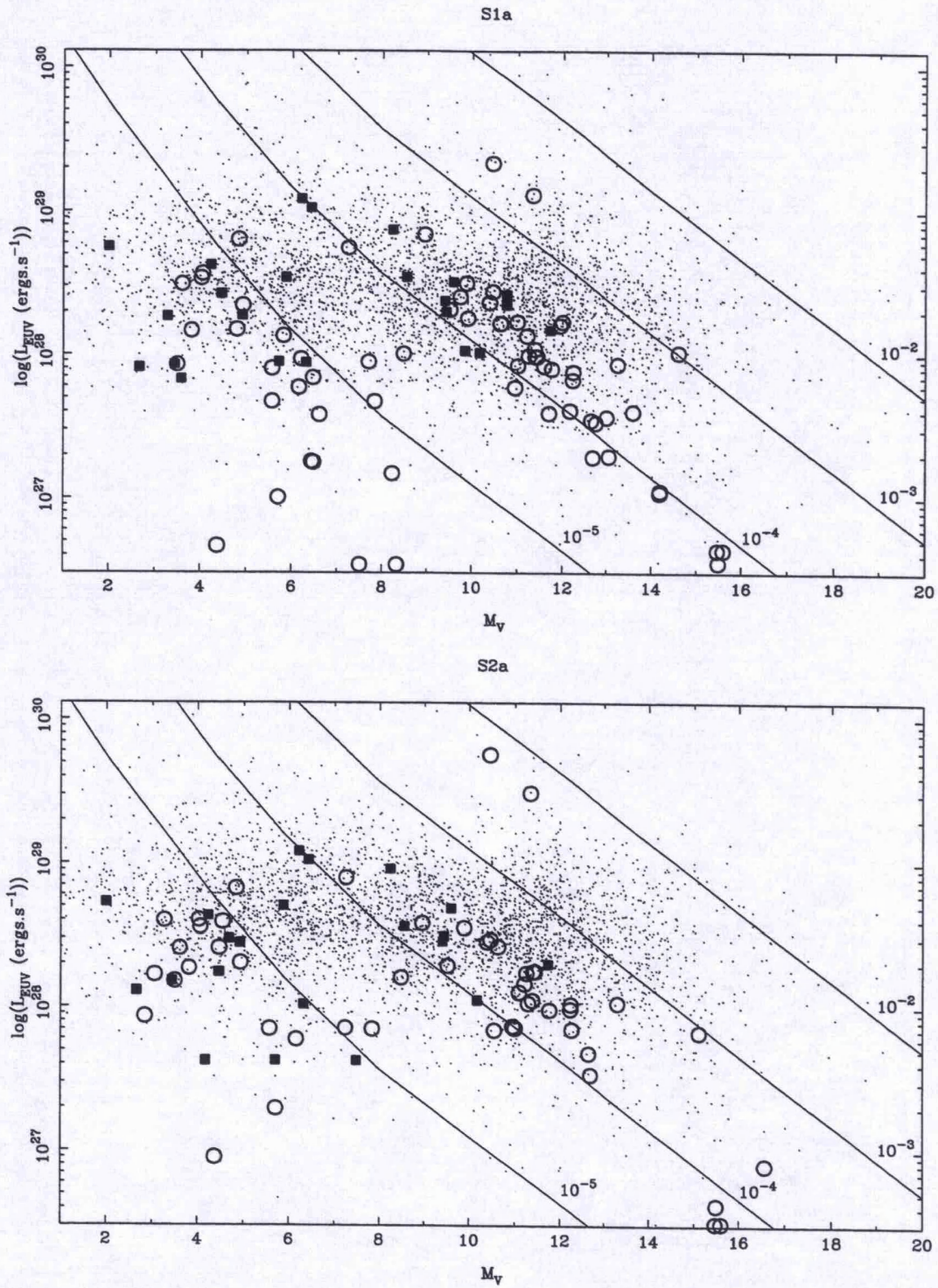


Figure 4.9: The $L_{\text{EUV}} - M_V$ distribution for the CNS3. Open symbols are single stars, solid symbols are spectroscopic binaries (suspected and known). The contours represent lines of constant $L_{\text{EUV}}/L_{\text{bol}}$.

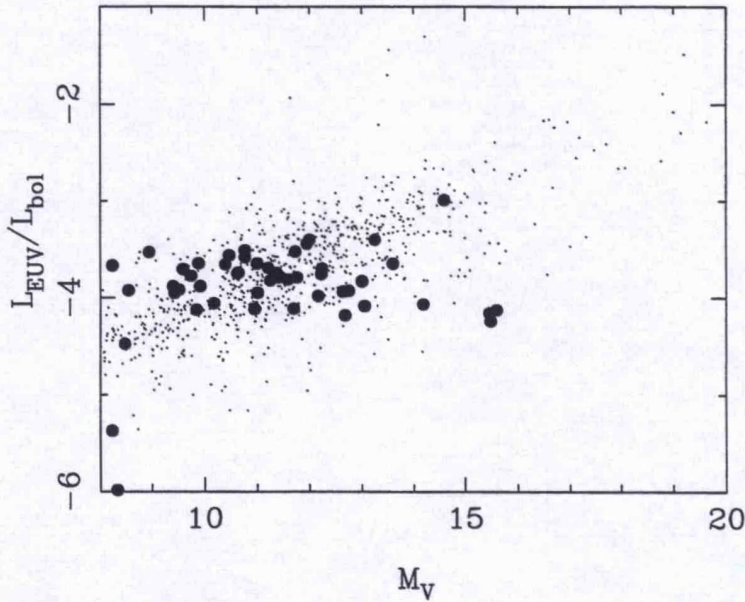


Figure 4.10: $L_{\text{EUV}}/L_{\text{bol}}$ against M_V for the S1a filter.

4.5.5 Kinematics of the EUV sources

The detections (in either S1a or S2a) are plotted in the (U , V) plane in Fig. 4.11 for both single stars and spectroscopic binaries within 25 parsecs of the sun. By far the majority of these stars show small space motions typical of young disk objects. The polygon (as in Fig. 4.1) delimits the region of kinematically young disk stars (age $\lesssim 5 \times 10^8$ years) and encloses a large fraction (~ 70) of the EUV sources. The box centred near $V = -26 \text{ km s}^{-1}$ defines the area inhabited by members of the Local Association (Eggen 1983). Fig. 4.11 shows very clearly that the CNS3–EUV source population is strongly dominated by young stars. This supports the results of Jeffries & Jewell (1993) who find that the S2NIPS coronal sources show a galactic velocity dispersion which is substantially less than that of a random sample of late-type stars. Observations of open clusters (e.g. Micela et al. 1988 [Hyades], Micela et al. 1990 [Pleiades]) have shown how X-ray emission decreases with age. Stars are born with a large quantity of angular momentum, and young stars tend to be the most rapidly rotating (Stauffer et al. 1991 and references therein). As stars age they lose angular momentum through magnetic braking and mass loss. Thus single stars spin down with age, and become less active. Binary systems are

able to maintain high rotation rates by decreasing their separation to compensate the angular momentum loss. So my finding here, that the EUV brightest sources in the solar neighbourhood are also amongst the youngest, is entirely in keeping with the age-rotation-activity paradigm (see e.g. Simon 1992).

4.6 Survival analysis

A luminosity function represents the distribution of the sample in luminosity parameter space. It can be seen as the space density of objects within a specified range of luminosities. One may use the function to obtain mean and median values for the luminosity and may make comparisons between the sample and other samples or subsamples selected on different criteria. For example I may wish to test the hypothesis that two different luminosity functions were drawn from the same underlying parent distribution.

The simplest way to construct a luminosity function is from the luminosities of only those stars which have been detected. But these will be biased if I do not take account of the detection threshold of the survey (e.g. the upper limits for undetected stars in a volume-limited sample as here, or the d_{\max} for a flux limited sample as in Warwick et al. 1993). How then does one incorporate the upper limits into the luminosity function? Astronomers have responded to the problem in a number of ways. Some have chosen to ignore the upper limits altogether, while others have handled them separately and inefficiently. Avni et al. (1980) and Pfeiderer & Krommidas (1982) independently discovered a way to deal with each detection and upper limit in an efficient and well defined way based on maximum likelihood theory. There are however, already in existence a large number of statistical methods specifically designed for the analysis of censored data. This branch of statistics has been referred to by Feigelson and Nelson (1985, hereafter FN85) as 'survival analysis' of 'lifetime data', terms adopted here.

The maximum-likelihood estimate of the true distribution found by Avni and Pfeiderer, for example, was first derived by Kaplan and Meier (1958) in a study of cancer treatments and is a cornerstone of nonparametric survival analysis. This use of nonparametric techniques is important. It may be quite wrong to make any assumptions about the underlying 'true' distribution.

Schmitt (1985) and FN85 provide good introductions to the field of survival analysis in as-

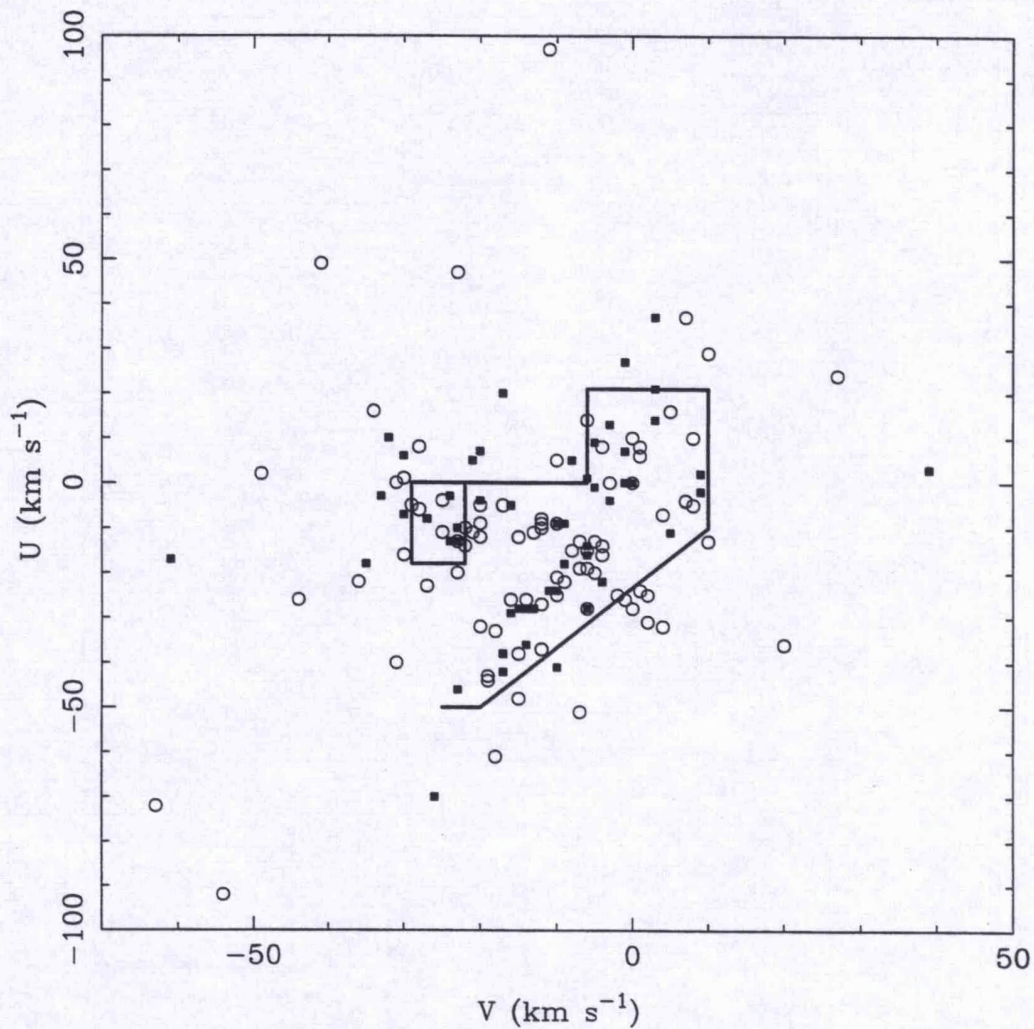


Figure 4.11: The (U, V) distribution of the EUV detections. The polygon delimits the region of kinematically young disk stars. The smaller box defines the area inhabited by members of the Local Association. Single stars are shown with an open circle while spectroscopic binaries are represented by a solid square.

tronomy and document procedures for computing the Kaplan Meier Product Limit Estimator (KMPL) which represents the true, unique maximum likelihood function for the distribution function.

The KMPL is defined fully in FN85 and Schmitt (1985). Briefly it is calculated as a normalised integral step function. In an uncensored data set, it converges to the obvious solution where the function drops by a step $1/N$ at each of the N data values (detections). In a censored data set, it drops at each of the detected values by an amount weighted according to the number of nondetections. The size of the step and the growing uncertainty in the estimator as more censored points are included, are given by the formulae developed by Kaplan & Meier (1958).

To calculate the KMPL for my datasets I have used the ASURV package (Rev. 1.2) developed by Isobe, La Valley & Feigelson (see Starlink User Note 13, Allan 1992).

4.7 The EUV luminosity functions

Fig. 4.12 shows the cumulative EUV luminosity functions (ELFs, but labelled as CDFs in the figures) for the full sample of F, G, K and M stars in filters S1a and S2a out to the limiting distance. In Fig. 4.13 I plot all four S2a functions on the same diagram to enable direct comparisons to be made. Table 4.6 summarises the results of applying the KMPL.

To provide a simple parameterisation, the ELFs have been fitted with a power law function of the form

$$N(> L) = N_0 L^\alpha \quad (4.12)$$

using no weighting. Even though the KMPL provides errors, these are not independent, and cannot be used to aid the fitting in a straightforward manner. The resulting values of the power-law index (or slope) α are also shown in Table 4.6.

It is immediately obvious that there is very little difference between the ELFs in the two filters. Although it is possible to test this statistically with the two-sample tests included in the ASURV

Table 4.6: CNS3 EUV luminosity functions

Sample (Sp. Type)	log(Mean L_{EUV})		log(Median L_{EUV})		α			
	S1	error	S2	error	S1	S2		
<i>Total (Single + Binary):</i>								
F	27.80	0.05	27.92	0.06	27.68	27.86	-1.53	-1.66
G	26.94	0.10	27.09	0.12	26.66	26.81	-0.82	-0.79
K	27.21	0.11	27.47	0.06	27.13	27.42	-1.06	-1.11
M	26.81	0.04	26.72	0.05	26.60	26.56	-1.09	-1.04
<i>Single:</i>								
F	27.72	0.06	28.03	0.04	27.54	27.89	-1.52	-1.86
G	26.92	0.15	27.00	0.13	26.66	26.81	-1.01	-0.97
K	27.19	0.11	27.40	0.06	27.13	27.25	-1.15	-1.26
M	26.80	0.05	26.72	0.06	26.60	26.56	-1.19	-1.09
<i>Binary:</i>								
F	27.93	0.06	28.00	0.09	27.80	27.91	-1.34	-1.37
G	27.66	0.10	27.82	0.12	27.29	27.38	-0.67	-0.65
K	27.80	0.09	27.89	0.08	27.72	27.63	-0.87	-0.88
M	27.21	0.12	27.22	0.12	26.75	26.86	-0.69	-0.69

package, the results of simulations indicate that these tests are not valid for such heavily censored data (see Section 4.7.1 and Appendix B). There are however some obvious differences between the ELF's for different spectral types. All the functions are rather 'flat', implying that the source counts ($\log N - \log S$) will be heavily influenced by the higher luminosity objects in each ELF. This is in keeping with the finding that the bulk of the detections are either kinematically young or are spectroscopic binaries. The F-star luminosity function is 'steeper' than that of the later-type stars. The G-star function is flattest of all with a high luminosity tail extending out to $L_{\text{EUV}} \sim 10^{30} \text{ergs}^{-1}$. The mean EUV luminosity ($\langle L_{\text{EUV}} \rangle$) for the F-stars is high; the ELF spans only 1.5 orders of magnitude in luminosity. By comparison, the G-star ELF spans nearly 3.5 orders of magnitude in luminosity, with a highly significant (in the sense that it has a large effect on the ELF) low luminosity detection (α Cen A, G2V, $L_{\text{EUV}, \text{S1}} = 4.6 \times 10^{26} \text{erg s}^{-1}$). The K-star function extends over 2 orders of magnitude, with a high $\langle L_{\text{EUV}} \rangle$ presumably as a result of no low luminosity detections or upper limits. In contrast, the M-star ELF extends to very faint luminosities (because of the detection of nearby, intrinsically faint sources) and spans 2.5 orders of magnitude in luminosity.

Theoretically, the high luminosity tails of the ELFS should be well reconstructed, but the small

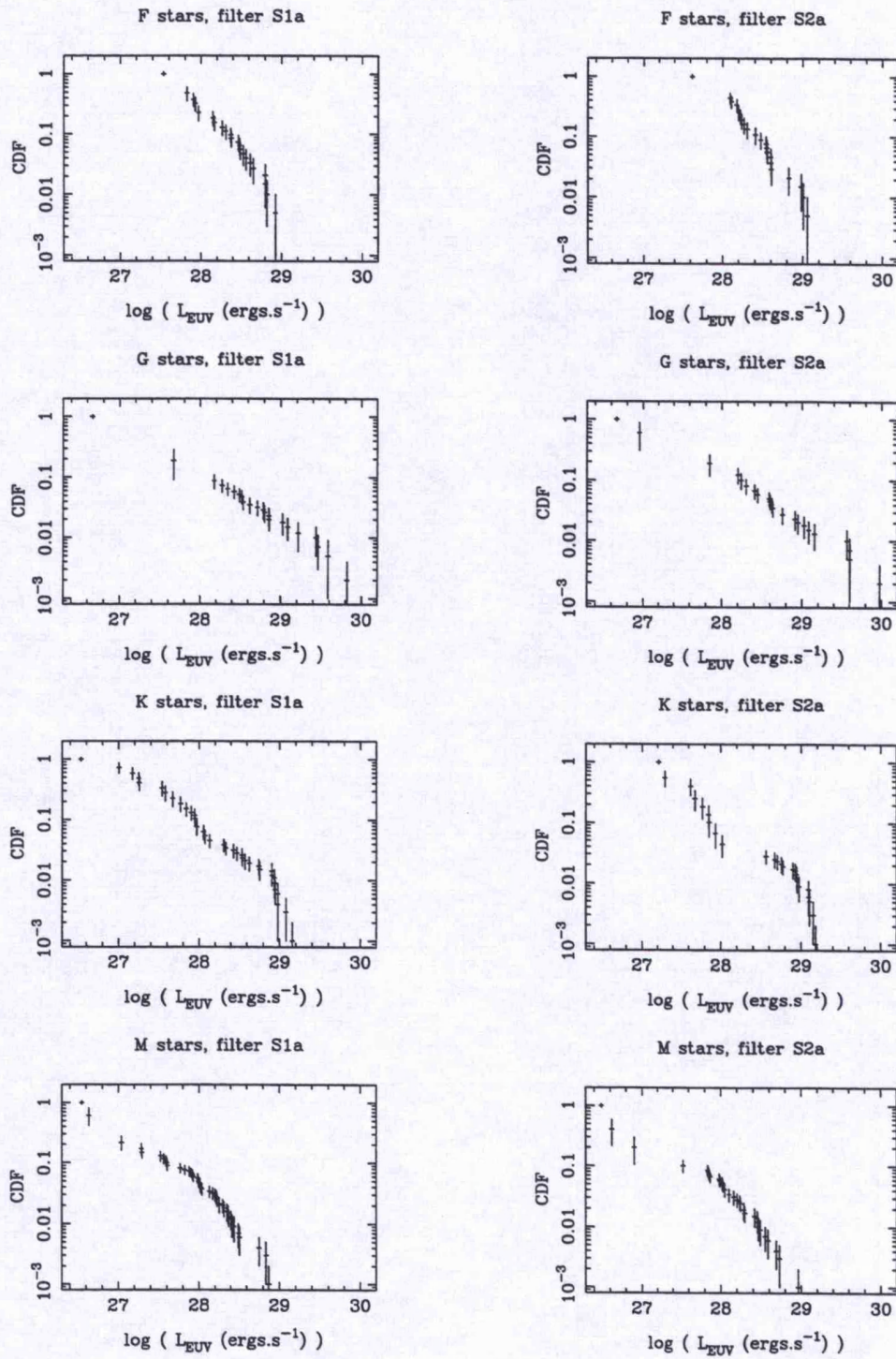


Figure 4.12: The Cumulative EUV Luminosity Functions for the total sample of F,G,K and M stars in filters S1a and S2a out to 25, 25, 25 and 16 parsecs respectively.

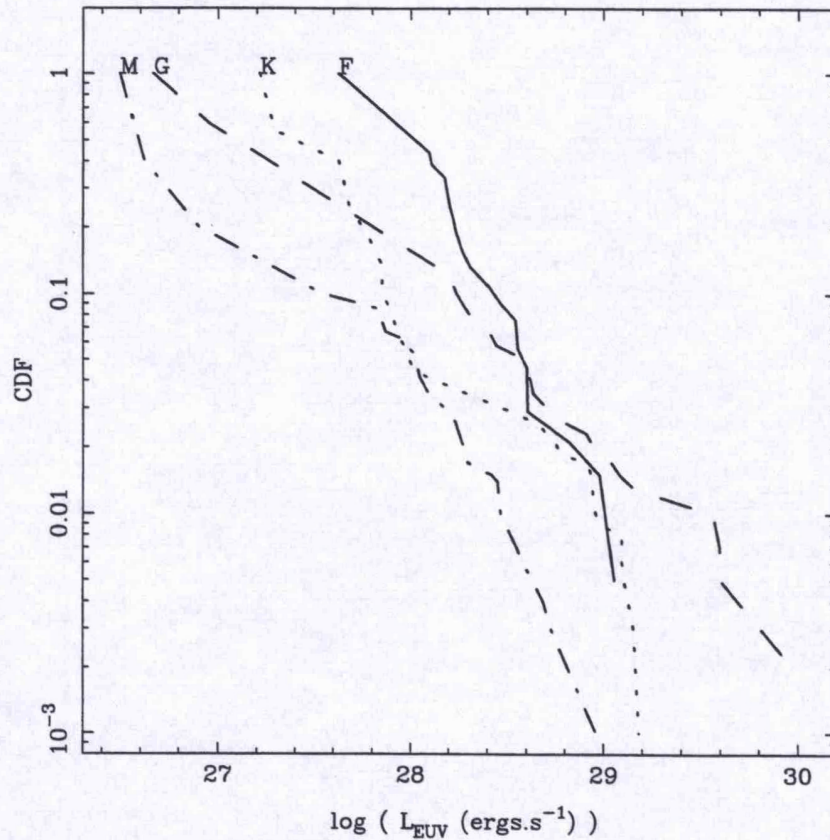


Figure 4.13: The S2a Cumulative EUV Luminosity Functions.

number of objects at high luminosities resulting from the volume-limited nature of the sample will give rise to large statistical uncertainties at the bright end. The shape and truncation at the low luminosity end is subject to the limiting sensitivity of the survey. At the flux limit of the WFC survey, an EUV faint M-dwarf with $L_{\text{EUV}} \sim 10^{27} \text{ergs}^{-1}$ will only be detected out to about 5 parsecs. The effect on the luminosity function is to 'steepen' it towards low L_{EUV} . In addition the KMPLE truncates the ELF at the lowest point - converting an upper limit to a detection if this is the lowest point. Hence the estimated mean values are likely to be artificially high.

4.7.1 Summary of simulations

These EUV luminosities are, in the language of survival statistics, 'highly censored'; that is there are many more upper limits than detections. Typically, the sample contains $\sim 10\%$ detections. Also since the EUV survey is approximately flux limited (strictly it is significance limited), there is a correlation between the censoring pattern and the statistic of interest, L_{EUV} (cf. FN85). Therefore it was considered prudent to perform simulations to test the validity of applying survival analysis methods to these data. Presented here are the main conclusions from the simulations; Appendix B discusses the work in more detail.

1. The simulations represent a good model for the WFC survey with which I can test the applicability of the survival analysis techniques employed in this study.
2. The KMPLE (with associated error estimates) is a good estimate of the 'true' distribution, which appears to converge with 'reality' as the level of censorship is decreased. At the censorship levels at which the ELF's have been constructed ($\sim 10\%$ detections), the KMPLE over-estimates the mean and median of the input function. The truncation at low L_{EUV} causes a steepening of the slope towards low luminosities. In spite of these effects, these simulations have shown that the KMPLE may be used on very heavily censored data to show differences between luminosity functions manifest in their slopes, mean and median values. The observed differences between the survey ELF's may be interpreted with a fair degree of confidence.
3. Both the effects of Poisson noise in the WFC data and uncertain spectral shape have been simulated. In general, over the simulations performed, the computed means, medians (in log units) are within $\Delta \log 0.2$ of the true values, while the power law slopes α are within 0.3 of their true values.
4. On the basis of insufficient data it is not possible to allocate a measured column density and temperature to each star, and an average value for the conversion factor must be used. If the conversion factor is randomised for the S2a filter, the resultant estimate of the input function gets worse (but still within the limits noted above). The mean and median increase, while the measured slope is flatter than the input slope. In the case of the S1a

filter no significant difference between the two techniques is observed. Thus the survey ELFS are not heavily affected by the assumption of a constant conversion factor.

5. An investigation of the two-sample tests has supported the warning of Feigelson (1990), that all the tests may give unreliable significance levels in very small or (as in this case) very heavily censored samples. Hence I have not used them in this analysis.

4.7.2 Effects of multiplicity

The EUV luminosity functions presented so far include contributions from both single stars and spectroscopic binaries. As far as possible visual binaries have been resolved into their counterparts. Spectroscopic binaries show enhanced emission above that which would be expected for the combined flux of two single stars of similar age and spectral type. It is likely that the enhanced emission arises as the result of high rotation rates maintained by synchronous orbits and/or the interaction of the magnetic fields of the two components. Therefore luminosity functions for the single stars and the spectroscopic binaries have been computed separately.

The single-star and SB ELFs are displayed in Figs 4.14 and 4.15 respectively, while Table 4.6 summarises their parameters. In Fig. 4.17 I show, for each spectral type, the mean and power-law indices for the total, single and SB samples. Again the ELFs may be adequately described by power laws. The SB ELFs have higher mean and median luminosities and flatter slopes than the single stars, though the contrast for F stars is much less than for later spectral types. The high luminosity tail apparent in the total G star ELF can be almost entirely attributed to spectroscopic binaries, the majority of which are RSCVn systems.

4.7.3 Comparison with *Einstein* X-ray luminosity functions

In order to compare the EUV luminosity functions with the *Einstein* IPC X-ray luminosity functions, it is necessary to allow for the different energy bandpasses of the instruments. Schmitt et al. (1990a) have shown that the median temperature for main-sequence late-type stars observed with the IPC is 3.2×10^6 K for those spectra for which a single temperature fit was adequate. The WFC however is more sensitive to lower temperature plasmas. The *Einstein* luminosity functions have been constructed from IPC count-rates assuming (in most cases) a flux to count-

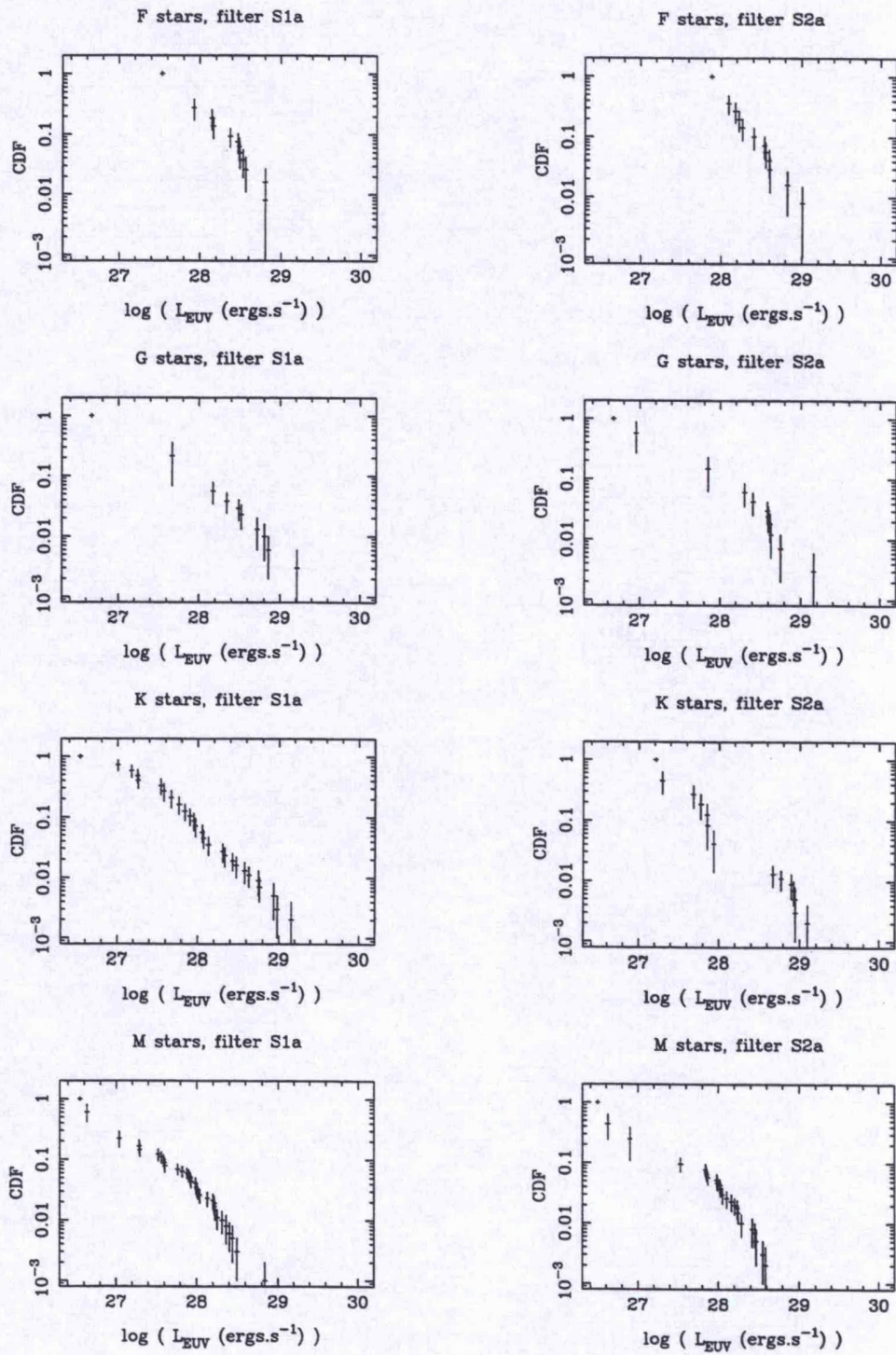


Figure 4.14: The Cumulative EUV Luminosity Functions for single stars.

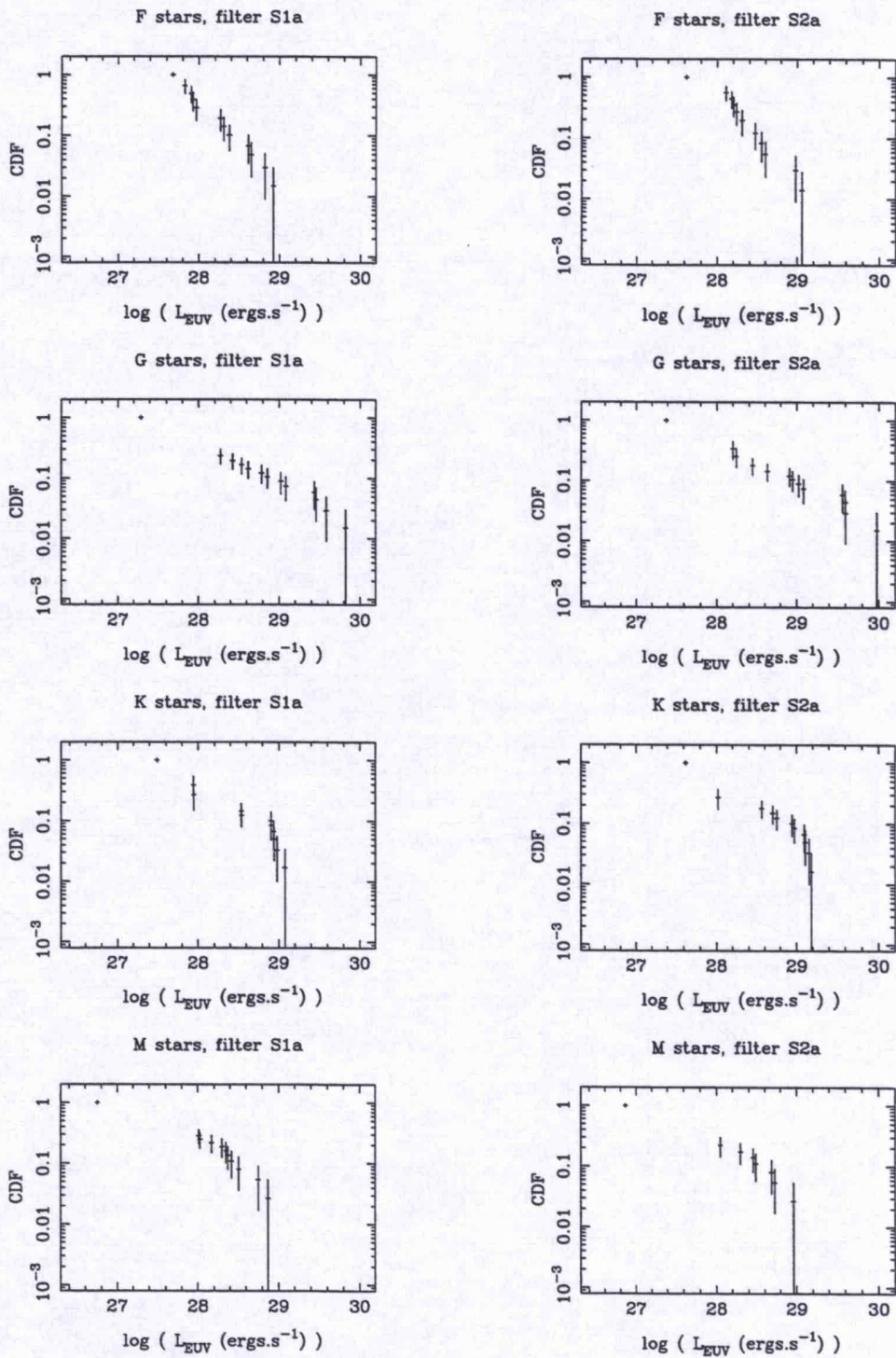


Figure 4.15: The Cumulative EUV Luminosity Functions for spectroscopic binaries.

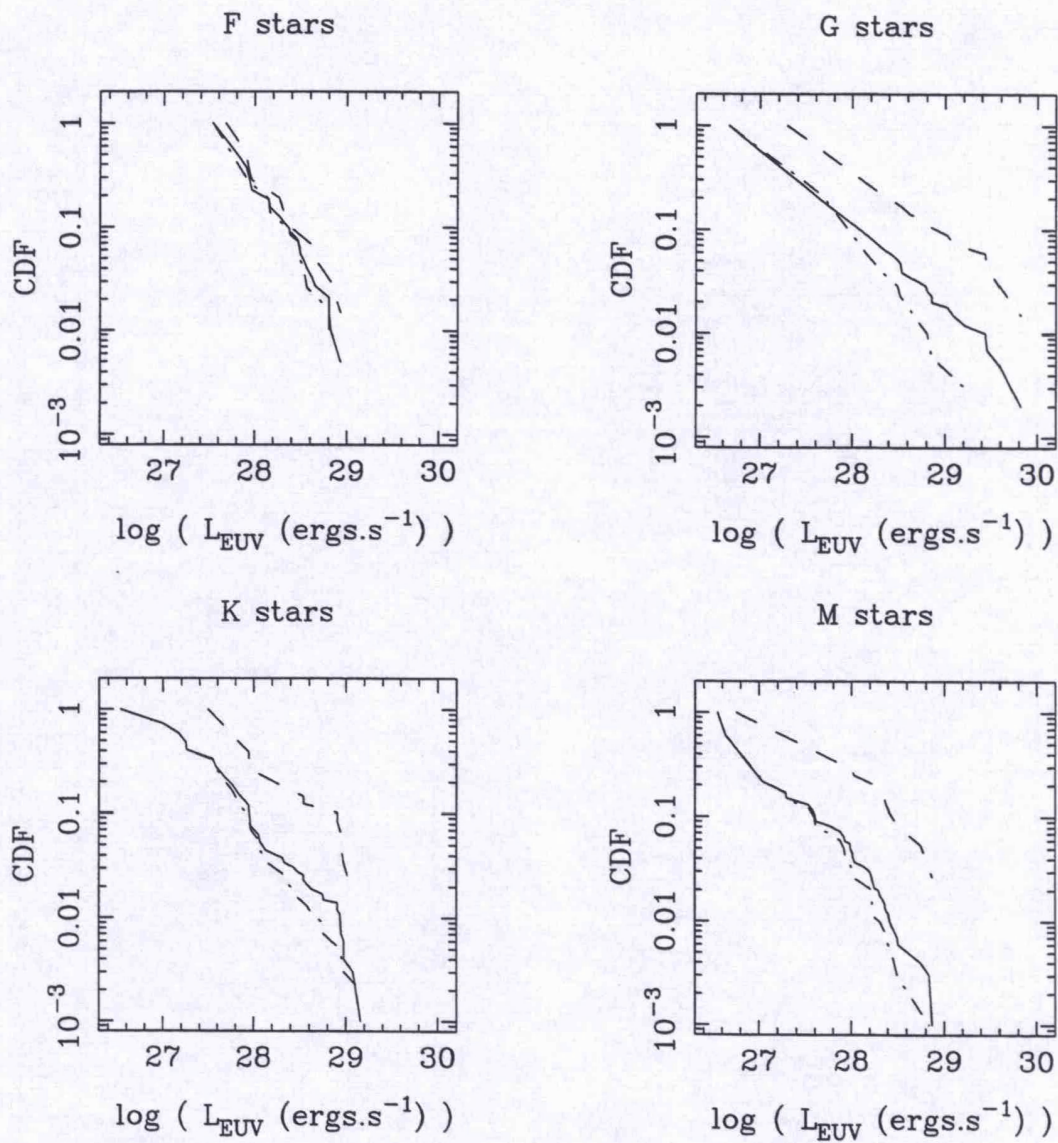


Figure 4.16: The Cumulative EUV Luminosity Functions for the single (dashed-dotted line), spectroscopic binary (dashed line) and total (solid line) samples in filter S1a for F, G, K and M stars.

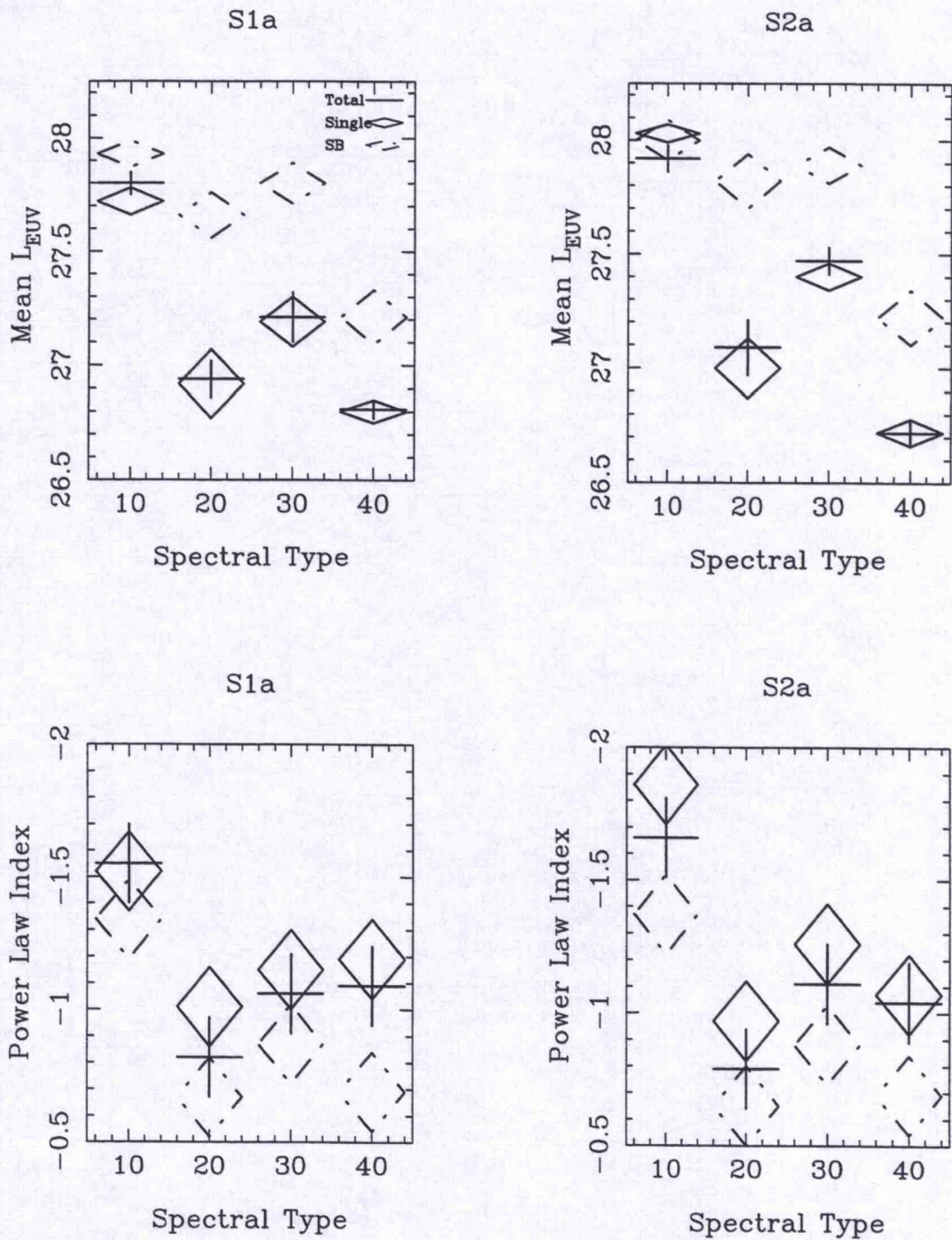


Figure 4.17: Comparison of the means and slopes of the F, G, K & M Cumulative EUV Luminosity Functions for the total, single and spectroscopic binary samples in each filter.

rate conversion factor (f_X) of $2 \times 10^{-11} \text{ erg cm}^{-2} \text{ count}^{-1}$ in the 0.15 to 4.0 keV band. By comparing the WFC-BSC late-type star count rates with the *Einstein* IPC count-rates for the same objects (Fig. 4.18) I find mean count rate ratios of 7.2 IPC counts per S2a count and 11.1 IPC counts per S1a count from least mean squares fit to the data. There is a lot of dispersion in this relation, presumably due to either or both of source variability and/or differences in the coronae of the stars. The ratio of the flux of a star (and therefore the luminosity) in the EUV band to the flux in the 0.15–4.0 keV band is given by:

$$\frac{F_{\text{EUV}}}{F_X} = \frac{f_{\text{EUV}} C_{\text{EUV}}}{f_X C_X}. \quad (4.13)$$

where f_{EUV} is the count-rate to flux conversion factor for the WFC and is in the range $4.2 \times 10^{-11} - 5 \times 10^{-11} \text{ erg cm}^{-2} \text{ count}^{-1}$ for the S1a (0.09–0.19 keV) filter assuming $\log(N_H) \leq 18.5$ and a plasma temperature of $1 - 3 \times 10^6 \text{ K}$. For the S2a (0.06–0.10 keV) filter f_{EUV} is in the range $1.8 - 4.4 \times 10^{-11} \text{ erg cm}^{-2} \text{ count}^{-1}$ for the same temperature and N_H range. Using the count-rate ratios determined above I find $L_X/L_{\text{EUV}} = 4.44 - 5.33$ for filter S1a and $L_X/L_{\text{EUV}} = 1.77 - 3.24$ for filter S2a.

The mean and median luminosities for the ELF's have been scaled to the *Einstein* bandpass and a comparison is shown in Fig. 4.19 (see also table 4.7). The S2a derived luminosities are systematically lower than those obtained from the S1a filter. This may result from the greater plasma temperature and hydrogen column dependence of the S2a filter. The ELF's seem to be in agreement with the *Einstein* G and K-star functions. The EUV F-star function lies somewhat (\sim factor 2) below the *Einstein* XLF, but taking account of the uncertainties, this may not be significant. There is a large discrepancy between the EUV M-star luminosity function and the majority of the *Einstein* results. It appears that these *Einstein* functions are dominated by a high luminosity tail. This difference has important implications for the stellar source count predictions that have been made for the WFC and ROSAT all-sky surveys, and is dealt with in the next section. Additionally I show the results of Barbera et al. (1993) in Fig. 4.19, where they have split their (incomplete) volume limited sample into young disk and old disk populations with the M stars split between early M ($8.5 < M_V \leq 13.4$) and late M ($M_V > 13.4$) samples. I show only the young disk results because the CNS3 luminosity functions are dominated by the luminous young disk stars. I find that these results are in good agreement with my own.

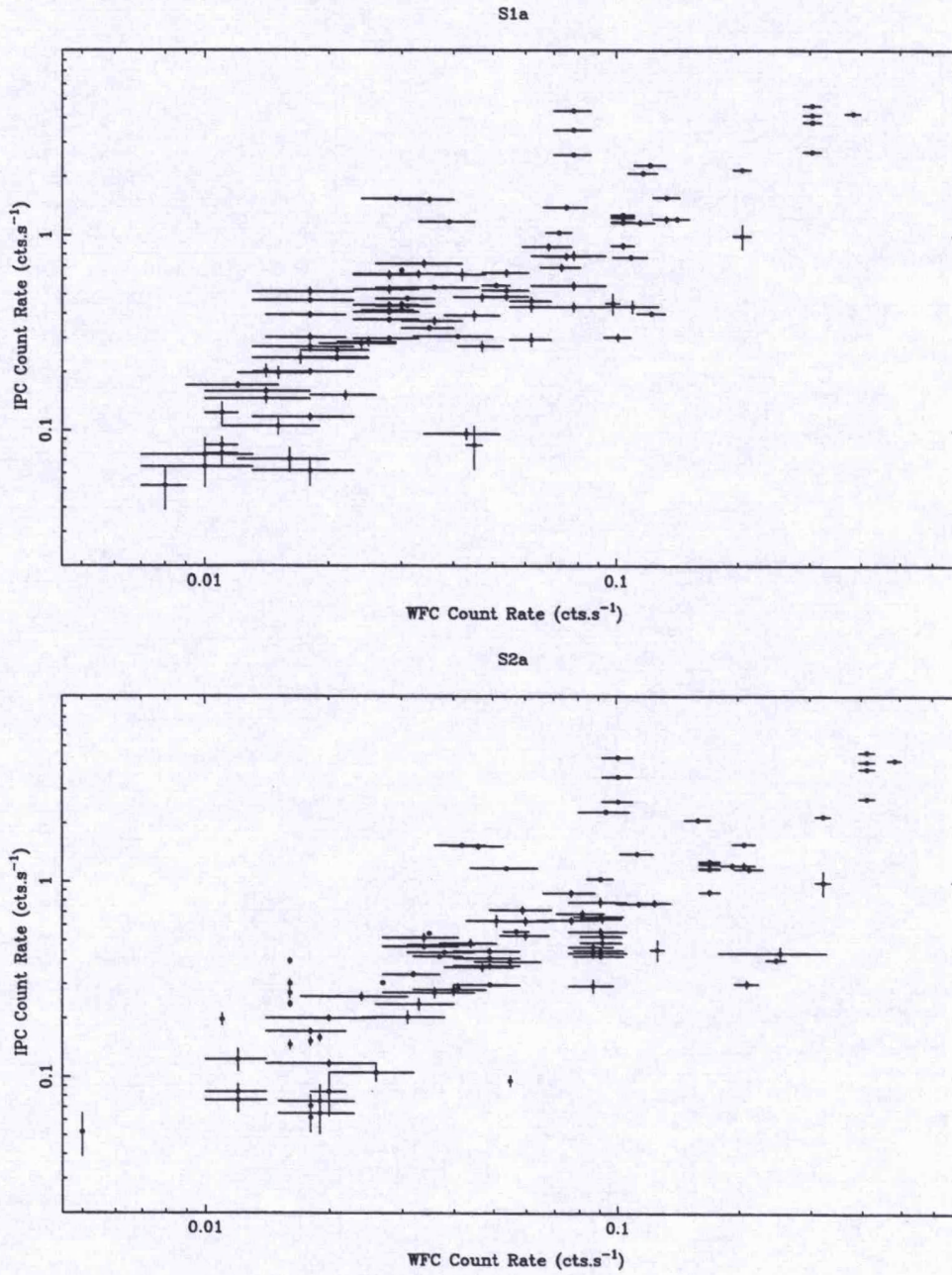


Figure 4.18: *Einstein* IPC count-rates against WFC-BSC count-rates for filters S1a and S2a.

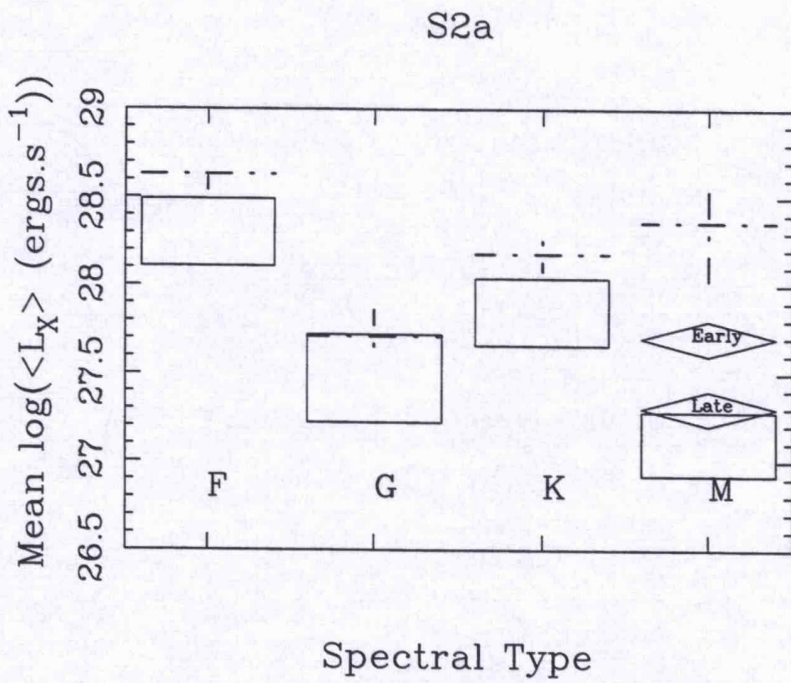
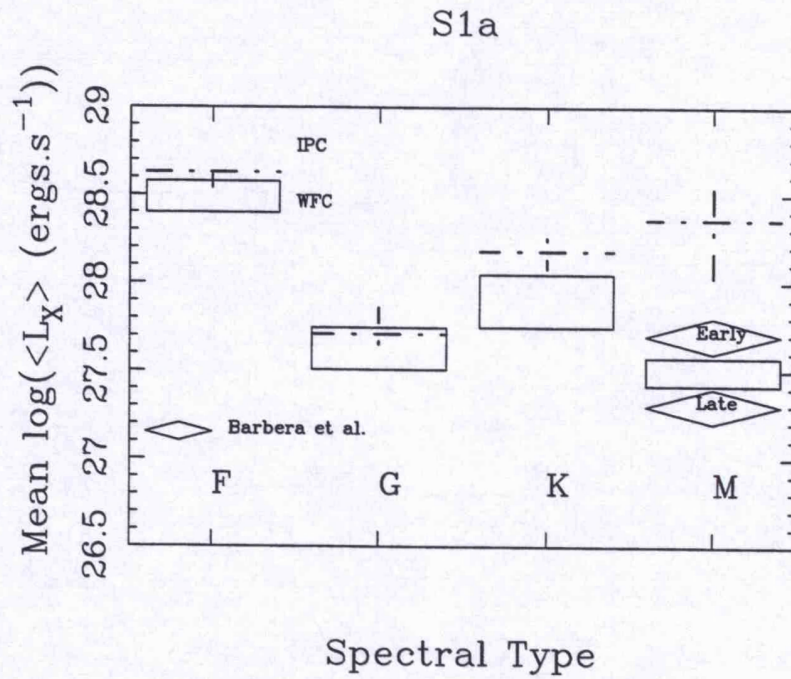


Figure 4.19: A comparison between the *Einstein* mean L_X values for late-type stars, and the WFC mean L_{EUV} normalised to the same energy band (0.15-4.0 keV).

Table 4.7: Comparison of the ELF's with the *Einstein* XLFs

Type	Multiplicity	$\log \langle L_{0.15-4.0} \rangle$						Ref
		WFC	LL	UL	Einstein	LL	UL	
F	S	28.63	28.29	28.84	28.29	28.16	28.43	1
F	B	28.50	28.14	28.73	28.76	28.65	28.88	1
G	S	27.79	27.23	28.22	27.4	27.2	27.6	2
G	S+B	27.75	27.25	28.12	27.71	27.62	27.86	3
K	S	27.99	27.63	28.23				
K	S+B	28.05	27.69	28.28	28.18	28.08	28.28	3
M	S	27.42	27.06	27.66				
M	S+B	27.42	27.06	27.66	28.36	27.95	28.55	5

Refs: 1. Schmitt et al. (1985); 2. Maggio et al. (1987); 3. Micela et al. (1988); 5. Caillault et al. (1986).

The WFC derived luminosities are converted from the S2a filter.

The (1σ) confidence regions for the WFC luminosities incorporate the uncertainty in the conversion to the 0.15-4.0 keV bandpass.

The (1σ) confidence regions for the Einstein $\langle \log(L_X) \rangle$ are obtained from the references.

4.7.4 logN-logS distribution

The EUV luminosity functions can be used to predict the stellar contribution to the total WFC source counts (logN-logS) distribution down to the flux limit of this survey. Pounds et al. (1993) and Warwick et al. (1993) have measured the intrinsic EUV source counts for the whole of the WFC-BSC and for the white dwarf and late-type star subsamples. A comparison of the ELF derived logN-logS distributions (obtained from a volume-limited sample) with those of the WFC-BSC (obtained from a flux-limited sample) will show how representative the local stellar population is of the brightest coronal EUV sources. Whilst there is a fair degree of overlap between the two samples, there are sufficient differences such that this exercise is not merely a check for consistency (see Fig. 1 in Warwick et al. 1993.) For a population of objects, uniformly distributed in space, with no line of sight absorption, the integral logN-logS distribution will have an 'Euclidean' slope, $\beta = -1.5$. The flatness of the white dwarf logN-logS distributions (-0.6 in S1a and -0.5 in S2a) indicate significant absorption. For the late-type stars the measured slopes are -1.4 and -1.3 in filters S1a and S2a respectively, showing little evidence for absorption (See Pounds et al. 1993 for details).

In this analysis, the differential source counts are used since the differential form gives inde-

pendent data points which are much more amenable to a proper statistical treatment. The coverage-corrected differential logN–logS has been derived from the WFC-BSC according to the method of Pounds et al. (1993) and Warwick et al. (1993) with a lower count rate cut-off of 0.0133 counts s⁻¹ in both filters. Fig. 4.20 shows the differential counts obtained for the F, G, K and M star samples together with the predicted logN–logS derived from the ELF's in the S1 band. The values plotted in each bin correspond to:

$$\frac{\Delta N}{\Delta C} = \frac{\sum_i f_i^{-1}}{\Delta C} \quad (4.14)$$

where the summation is over all the sources contributing to the bin and ΔC is the binwidth in counts s⁻¹. The errors on each point are given by:

$$\sigma = \frac{(\sum_i f_i^{-1})^{\frac{1}{2}}}{\Delta C} \quad (4.15)$$

The predictions assume an ISM volume number density $n_H = 0.05 \text{ cm}^{-3}$ (cf. Warwick et al. 1993). To estimate the errors on the predicted source counts, the above process was repeated with the KMPLE errors both added to and subtracted from the ELF. These are the error bars shown for the K stars in Fig. 4.20. It is important to note that this is not a rigorous handling of the errors, but should give an approximate idea of the uncertainties involved.

For both filters, the predicted source counts appear to lie below the measured source counts. To quantify the apparent differences the χ^2 statistic has been applied to test the hypothesis that the ELF derived source counts are representative of the measured source counts. Table 4.8 lists the reduced χ^2 statistic (for 3 degrees of freedom) for both filters.

Significant differences are apparent for the K-star (and to a lesser extent the M star) distributions in both filters. When the errors on the K-star ELF's are taken into consideration, the confidence that the distributions are different drops to 0.89 for S1 and 0.96 for S2. But this is the extreme case, thus these confidences should be considered a lower limit. The F and G star predicted and measured distributions are not statistically distinguishable. There is no obvious trend between the two filters. In their paper Warwick et al. (1993) fit the source counts for both late-type stars and white dwarfs with a power law relation ($dN/dC = KC^{-\gamma}$). For the cool stars they find slightly flat slopes of $\gamma = 2.36(\pm 0.11)$ in S1a and $\gamma = 2.27(\pm 0.13)$ in S2a compared with the canonical differential slope of $\gamma = 2.5$ expected for an unabsorbed uniform distribution of

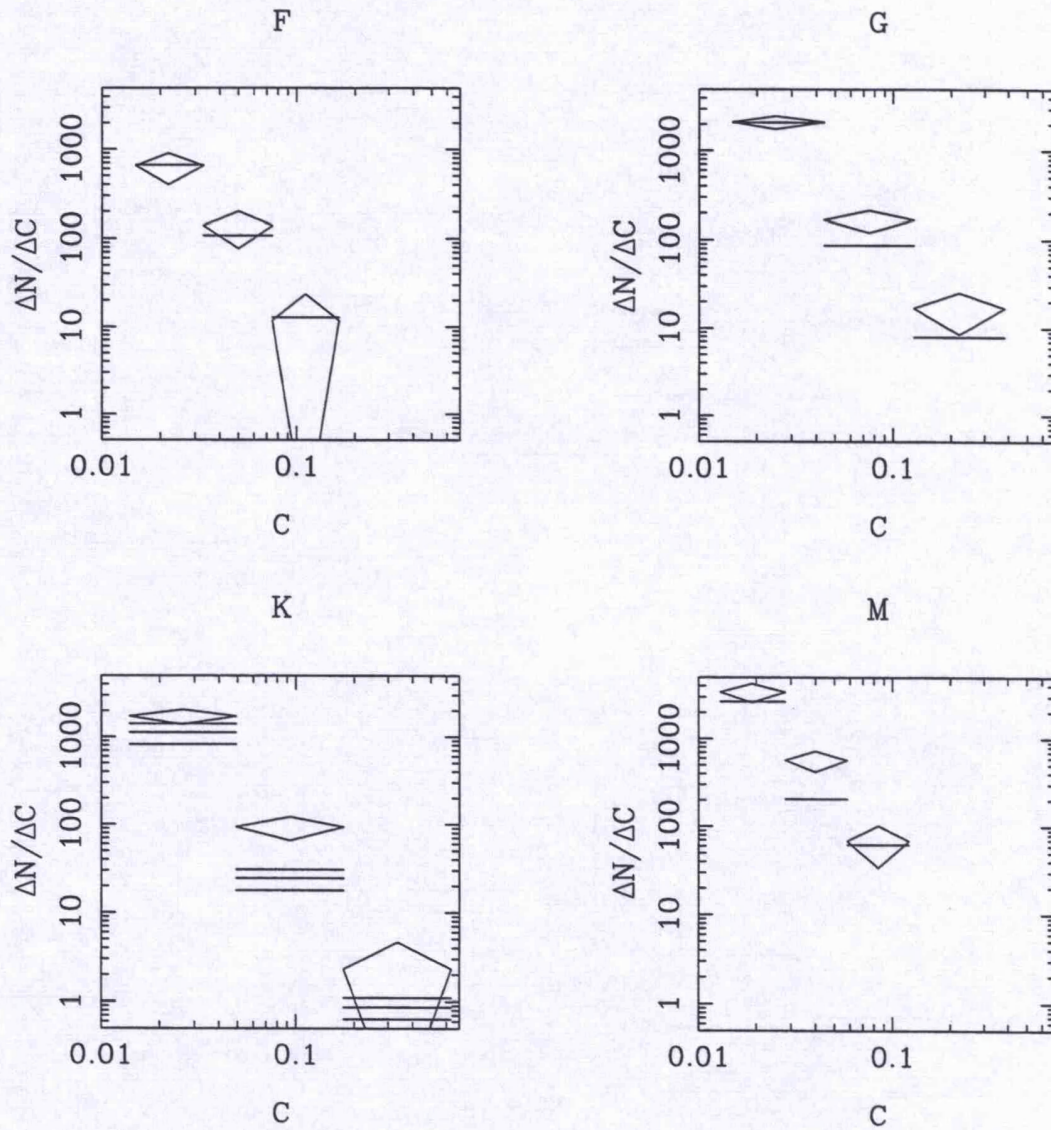


Figure 4.20: The differential source counts for F, G, K and M stars in the S1a filter derived from the WFC-BSC (shown as diamonds) compared with the differential source counts predicted from the nearby star ELFs (solid lines). For the K stars, the estimated errors on the predicted source counts are also shown (see text for derivation).

Table 4.8: Results of χ^2 test to source count comparison

Type	S1a		S2a	
	χ^2_{red}	Prob	χ^2_{red}	Prob
F	0.088	0.967	-	-
G	1.393	0.243	1.587	0.190
K	3.203	0.022	3.416	0.017
K ⁺	2.016	0.109	2.745	0.041
K ⁻	4.945	0.002	4.427	0.004
M	2.174	0.089	2.268	0.078

Prob is the confidence at which the two distributions are indistinguishable from each other.

For K⁺ the statistics are derived from the ELF with the KMPLE errors added, whilst for K⁻ the errors are subtracted from the ELF.

sources. I note in passing that the predicted differential source counts shown in Fig. 4.20 all have slopes which are consistent with $\gamma = 2.5$.

4.7.5 K-Star discrepancy

The measured and predicted K-star source counts are significantly different; the implication is that there is a population of K-stars, which are contributing significantly to the total WFC-BSC source counts, but are not represented in the nearby star luminosity function. From the integral functions this difference translates to 33 sources in S1a and 27 sources in S2a (down to a flux limit of 0.0133 counts s⁻¹). It does not seem likely that the underprediction is a result of incompleteness in the CNS3; I have shown in Section 4.2.1 that the K stars can be considered complete out to 25 parsecs. Therefore I have investigated individually the stars that make up the sample, to shed light on this problem. The similar effect observed for the M-stars is less significant, especially when the errors in the luminosity function are taken into consideration. Additionally incompleteness is a factor for dM stars, therefore the underprediction may be explainable in these terms alone.

There are 52 sources in the WFC-BSC identified with K stars; of these, 18 are in CNS3. Of the remaining 34, 13 are previously known to be spectroscopic binaries (RS CVn, BY Dra and W UMa systems) and 2 (AB Dor and V343 Nor) are previously known young single stars. 18 of the remaining 19 sources have been subsequently identified as active (and noted as such in the WFC-BSC) from optical follow-up studies of WFC sources (Mason et al. 1991, 1995). The

other star is the Hyades cluster member γ Tau (K0III + dF-dG?). In the CNS3 there are no detected K stars classified as RSCVn systems and 5 dK BY Dra detections (compared with 8 G star RSCVn and no BY Dra systems). One possible explanation for the underprediction is the low space density of RS CVn systems. In this case I would expect the discrepancy to be fully explained in terms of the spectroscopic binaries which are present in the WFC-BSC but lacking in the CNS3. To test this the K star source counts, both predicted and measured, have been recomputed for single stars and SBs separately. In Fig. 4.21 the source counts are shown for the total, single and SB samples. The results of a χ^2 test (see above) show that both the single and SB predicted distributions are distinguishable from the measured source counts at a confidence of ~ 0.90 in both filters. This confidence drops significantly when the errors on the ELF's are taken into account; the small sample sizes do not provide a significant result. However, the integral source counts show that the bulk of the discrepancy can be accounted to the single stars. The single star underprediction translates to 26 sources in S1a (21 in S2a) while for the SBs it is only 7 sources in S1a (6 in S2a). In other words the bulk of the discrepancy in terms of numbers (rather than significance) can be attributed to the underprediction of the measured single-star source counts by the single star ELF. This then refutes the earlier suggestion that the discrepancy can be solely attributed to the lack of K star RS CVn systems in the solar neighbourhood. It would appear that the so called "single" stars in the WFC-BSC are in fact contributing significantly more (by almost a factor two) to the source counts than I would expect given the ELF for single stars.

Further observations of new WFC-BSC coronal sources have been carried out at Mount Stromlo (Robin Jeffries priv. comm.). Of these 18 stars, 12 have been included in this detailed follow up program, which has concentrated on the measurement of rotational broadening of the Na D lines, radial velocity solutions for the spectroscopic binary systems, and measurement of the Li I 6707 line. At the time of writing, the data for 6 stars had been analysed. Two are found to be double-lined spectroscopic binaries (SB2), making them good candidates for RS CVn or BY Dra systems. The other 4 show strong lithium absorption coupled with very high rotation rates (e.g. Bromage et al. 1992, Jeffries & Bromage 1993, Jeffries 1995). These stars are likely to be very young with ages and kinematics that may place them in the Local Association (see e.g. Jeffries & Jewell, 1993, and references therein), co-eval with the Pleiades cluster.

A very similar result is discussed by Favata et al. (1993a, 1993c), with respect to the *Einstein*

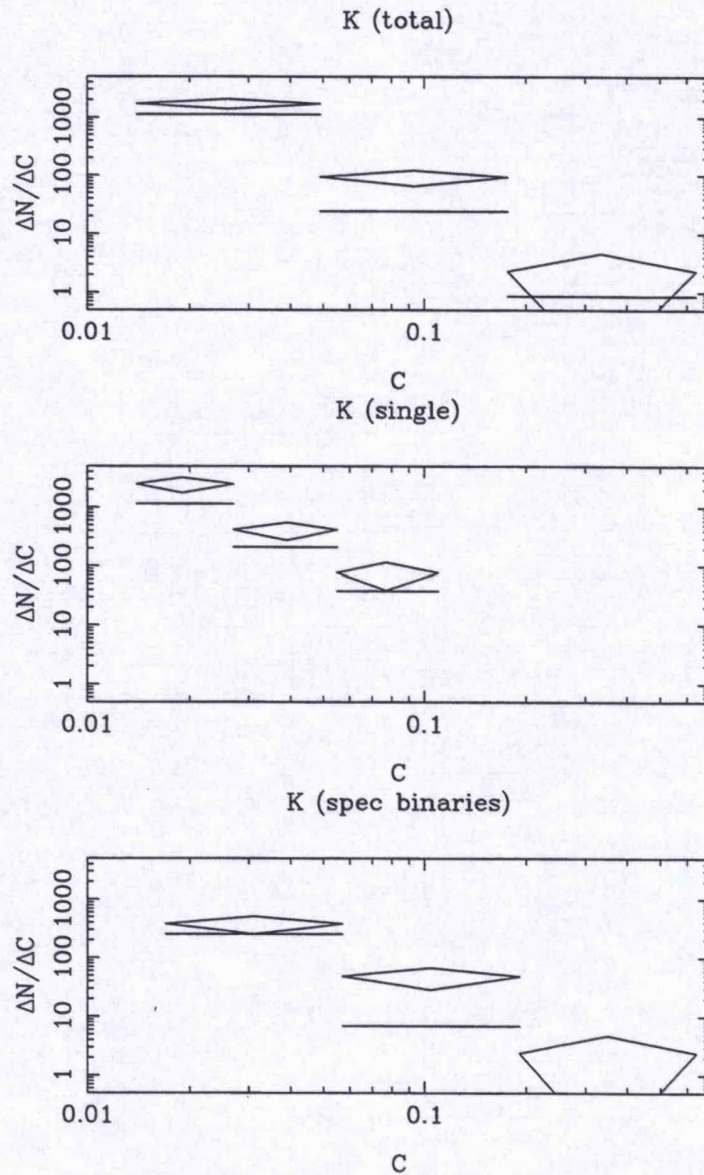


Figure 4.21: The differential source counts for K stars in the S1a filter derived from the WFC-BSC (shown as diamonds) compared with the differential source counts predicted from the nearby star ELF's (solid lines). The source counts are shown for the total, single star and SB samples.

Extended Medium Sensitivity Survey (EMSS). They find an excess of 'yellow' stars (spectral types G–K) in the EMSS, over the number predicted by *Einstein* volume limited luminosity functions. Follow up optical observations (Favata et al., 1993b) reveal high Lithium abundances for a statistically large fraction of these stars, supporting his argument that the excess is largely composed of very young, active stars, some of which may still be in their pre-main sequence stage. None of the stars in my sample overlap with the sample of Favata et al..

It seems likely that my results reflect a similar effect. I may partly explain the WFC-BSC K-star excess in terms of a number of previously unknown, high luminosity, spectroscopic binaries. Perhaps the most significant fraction of these newly identified coronal sources, however, will turn out to be very young, rapidly rotating, active stars.

4.7.6 dM stars

Pre-flight estimates predicted ~ 700 M-star detections (Pye and McHardy 1988, Vedder 1991) down to a flux limit of $1\mu\text{Jy}$ in the S1a filter (equivalent to a count-rate of ~ 0.015 counts s^{-1}) compared with the 50 or so detections predicted from the ELF (and the 50 detections in the WFC-BSC). Similar predictions for the F, G and K stars were within a factor two. For the M dwarfs this huge discrepancy can be explained in two possible ways. First, the source counts are very sensitive to assumed coronal temperature. The effect of varying the coronal temperature between 1×10^6 and 1×10^7 K is to change the predicted number of stars (at any given count-rate level) by a factor ~ 5 . Second, the published predictions have all been based on scaling from the *Einstein* X-ray stellar luminosity functions (e.g. Rosner, Golub & Vaiana 1985). As shown above the *Einstein* M-star luminosity functions are rather flat with a very high $\langle L_X \rangle$ resulting from the high luminosity tail. The surveys used to generate the M-star luminosity functions in Rosner et al. (1981) and Caillault et al. (1986) have been based on pointed and serendipitous surveys of catalogued sources in the former case, and a serendipitous survey in the latter. In both cases, the catalogues used suffer from incompleteness, being preferentially biased to the brightest, best-studied, and most 'interesting' M stars. Caillault et al. use an X-ray flux limited sample to accurately reconstruct the high luminosity tail of the M-star function. The EUV luminosity functions constructed here do not suffer from such significant incompleteness in the catalogue (although this is still a factor at distances greater than ~ 10 parsecs) and

are not EUV or X-ray biased, therefore they are more representative of the 'true' underlying luminosity distribution. The fact that the logN-logS distribution predicted from the ELF is in reasonable agreement with the WFC-BSC distribution adds weight to this claim. Some 70% of the M-dwarfs in the WFC-BSC are catalogued in the CNS3. This high degree of overlap leads me to expect good agreement between the two methods. Thus I have confidence in the consistency of the techniques. In addition the recently published M dwarf luminosity functions of Barbera et al. (1993) have reduced the high- L_X tail, and hence give better agreement with my M dwarf ELF (see Fig. 4.19).

4.7.7 Relative contributions

In Fig. 4.22 I show the relative contributions of the different spectral types to the total stellar coronal source counts as derived from the ELFs. It is clear that the M dwarfs do not dominate the source counts in the EUV survey, as was predicted pre-flight, but that each spectral type contributes approximately equally to the total stellar EUV source counts. Within the flux range of the WFC all-sky survey, the contributions to the logN-logS from F, G, K, M stars are in the (approximate) ratios 1:3.8:2.1:2.4 respectively, for the S1-band, and 1:2.6:1.7:1.6 for the S2-band.

4.8 Summary

Using the WFC survey database and a preliminary version of the Catalogue of Nearby Stars (CNS3), EUV luminosity functions have been constructed for volume-limited samples of F, G, K and M-type stars. The CNS3 contains a total of 3803 entries out to a nominal distance limit of 25 parsecs, and can be considered complete for F, G and K stars out to 25 parsecs. For the M stars, the measured number density begins to drop beyond 6 parsecs, with serious incompleteness starting outside our chosen distance limit of 16 parsecs.

For each object in the CNS3, the count rates and upper limits were measured directly from the $2^\circ \times 2^\circ$ images created during the standard "S2" processing of the WFC survey data. The detection threshold was set rather lower than in the standard processing; valid because there are only ~ 4000 test locations rather than $\sim 4 \times 10^7$ (the number of effectively independent survey

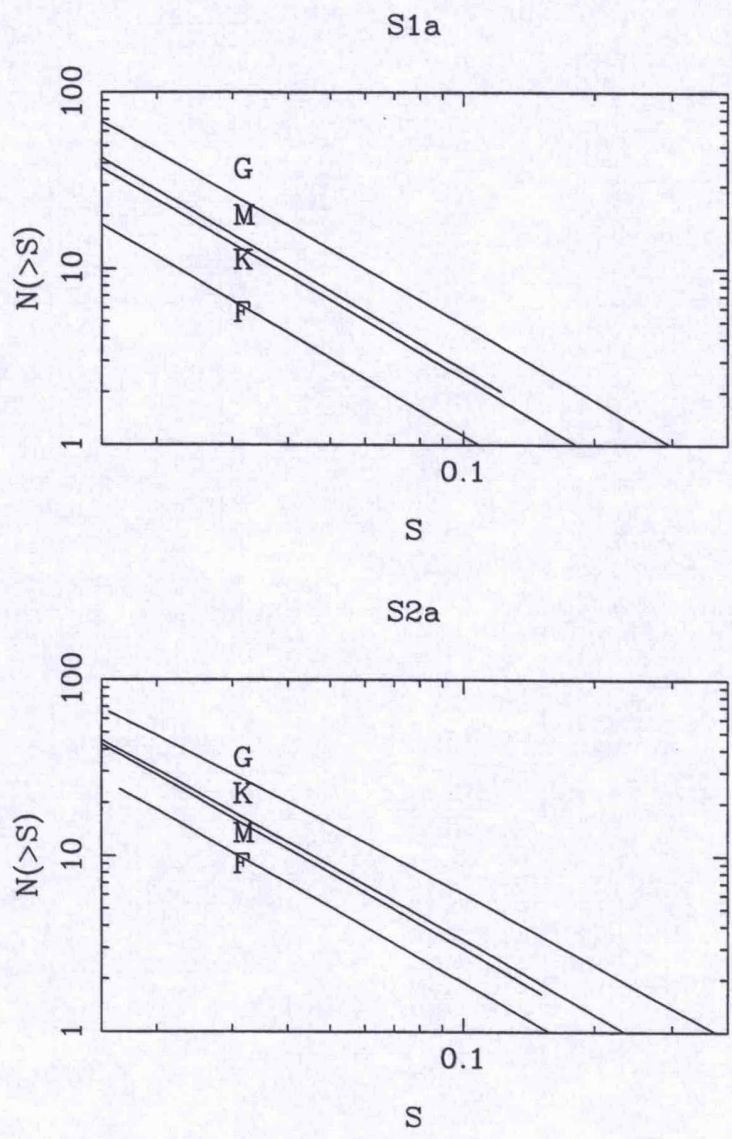


Figure 4.22: Relative contributions to the total stellar source counts of the F, G, K and M stars in both filters as predicted from the ELFs.

beam areas in the whole sky). Consequently more CNS3 stars were detected than have been found in either the WFC-BSC or the S2NIPS (~ 1500 detections) source lists. The flux of each CNS star has been constrained between upper and lower bounds using the Bayesian approach. For multiple systems the flux has been divided between the candidate objects according to information from previous observations in all wavebands where available; otherwise on a 'best efforts' basis.

I have detected 5 M dwarfs with spectral types dM5 or later which show no evidence for a lower level of activity than earlier dM stars. This tentatively supports the results of Fleming et al. (1993) that coronal heating efficiency is maintained for stars with very low mass, but stress that a more sensitive survey with a more complete sample of VLM stars is required to properly resolve the issue.

I have investigated the kinematics of the detected stars, and found (as have Jeffries & Jewell 1993) that the bulk of the objects ($\sim 70\%$) are members of the young disk population with ages $\lesssim 5 \times 10^8$ years.

Both the upper limits and detections have been used in the construction of volume-limited luminosity functions using survival analysis techniques - specifically the Kaplan-Meier Product Limit Estimator. Cumulative distribution functions have been computed for spectral types F, G, K and M in both WFC survey passbands, and both for single-stars and spectroscopic binaries. I find that the functions may be adequately described by power laws. All the functions are 'flatter' than would be expected if there were equal contributions to the stellar source counts from both high and low EUV luminosity sources (i.e. the measured LF slopes are greater than -2.5), hence the stellar source counts will be dominated by the higher luminosity objects. I find that the spectroscopic binaries have a significantly higher $\langle L_{\text{EUV}} \rangle$ than the single stars. The luminosity functions for the spectroscopic binaries are also flatter. The high luminosity tail apparent in the luminosity function of the G-stars can be almost entirely attributed to spectroscopic binaries. The single star luminosity functions are also dominated by high luminosity objects. This is consistent with the high fraction of kinematically young stars which make up the detections. By comparing the EUV derived luminosity functions with various *Einstein* X-ray luminosity functions we find broad agreement for the mean and median luminosities of the F-, G- and K-stars. However, the mean and median L_{EUV} for the M-stars are an order of magnitude below most

of the *Einstein* values. I attribute this discrepancy to the high luminosity tail in these *Einstein* M-star luminosity functions, resulting in the main from the flux-limited nature of the majority of M-star surveys. A much debated question concerns the M-star contribution to the M-band (0.5-1.2 keV) X-ray background, hence the focus on constraining the high-luminosity tail by using flux limited samples such as the EMSS. Previous volume limited surveys have been handicapped by very small samples. Rosner et al. (1981) had < 30 objects within a volume of 6 pc radius. More recently, Barbera et al. (1993) find *Einstein* M-star luminosity functions which are in agreement with the CNS3/WFC EUV luminosity functions (which are not EUV/X-ray biased). The completeness of the WFC all-sky survey ensures that the sample size is large, although heavily censored. My results are statistically representative of the 'true' EUV properties of the local late-type dwarf population.

Although there is some degree of overlap between the WFC-BSC stellar content and the CNS3 sample, the WFC-BSC contains many more (by a factor ~ 2) coronal sources which lie outside the distance limits imposed by the CNS3 sample. Hence the WFC-BSC is representative of a spatially more disparate sample of EUV brighter late-type stars. The EUV luminosity functions have been successfully used to demonstrate that the predicted stellar contribution to the WFC source counts agrees very closely to that measured from the WFC-BSC for the F, G and M stars. Thus at least for these spectral types I have demonstrated that the local stellar population is representative of a purely flux-limited sample. For the M-stars particularly, where the degree of overlap is high, this has proved to be a good test for the validity of our luminosity functions.

The discrepancy for the K-star measured and predicted $\log N$ - $\log S$ distributions (where the WFC-BSC source counts lie significantly above the levels predicted by the nearby-star LF) has helped to shed light on a previously known problem. Favata (1993c) has discussed the apparent excess of 'yellow' stars in the EMSS, and has attributed this excess to a population of young (possibly even pre-main sequence) stars, not adequately represented by the *Einstein* volume limited luminosity functions. Observations of the Li I 6707 Å line for a number of these stars have supported this theory. The underprediction of the WFC-BSC measured source counts by the K-star luminosity function, which cannot be fully explained by excluding all known RS CVn systems and spectroscopic binaries from the two samples, leads to the suggestion that the WFC has also detected a population of EUV bright coronal sources which are not significantly represented in the solar neighbourhood (due to low space density). Follow up observations have

revealed a number of these to be spectroscopic binaries, though the larger proportion appear to be young, rapid rotators.

Contrary to pre-launch predictions based on early *Einstein* luminosity functions, the EUV source counts are not dominated by M-stars; however agreement with the latest published *Einstein* luminosity functions is much better. The contributions from the different spectral types are well within a factor 2 of each other for the G,K and M-stars; the F stars contribute less because of their low space density coupled with their steep luminosity function.

Given the high degree of censoring in the WFC sample, extensive simulations have been performed to investigate the validity of the survival analysis techniques employed in the construction of the EUV luminosity function. These tests confirm that the KMPLE is a good estimate of the underlying 'true' luminosity function.

Chapter 5

ROSAT observations of the Hyades: 1. A statistical study

5.1 Introduction

In this chapter I will present an X-ray and EUV study of the Hyades open cluster based on observations with the ROSAT PSPC and the WFC. The data were all obtained by J.P. Pye, except for one field where the principal investigator was R.A. Stern. The Hyades catalogue used in both this chapter and the next was supplied to J.P. Pye and myself by R.A. Stern.

Apart from the very extended U Ma cluster, the Hyades is the nearest open cluster to the Sun, at a distance of about 45 parsecs. Its age is $\sim 7 \times 10^8$ years, it contains > 400 known members, and extends over $\sim 40^\circ$ diameter on the sky. The proximity of the Hyades to the Sun allows the detection of relatively low luminosity sources with little absorption of soft X-rays and EUV radiation. Because of its closeness and fairly rich membership, the Hyades cluster has been used in establishing many of the fundamental bases of astrophysics, including the mass-luminosity relationship and the location of the main sequence in the Hertzsprung-Russell diagram. The distance of the cluster has served as one of the foundations upon which the distance scale of the universe has been extrapolated. Consequently the relative abundance of optical data available for the cluster, especially for very low mass (VLM) stars ($M \lesssim 0.3 M_\odot$), makes the Hyades an ideal target for the study of the (age independent) X-ray properties of a well defined and coeval sample. Comparisons with the X-ray properties of such open clusters as the Pleiades, α Per and Praesepe, together with surveys of the disk and halo stars of the galaxy, will then enable the

effects of age on X-ray emission to be investigated. In recent years, the Hyades has been shown to have a population of rapidly rotating M dwarfs (Stauffer, Hartmann and Latham 1987), and a wide range of H α emission indicative of varying levels of chromospheric activity for lower main sequence stars (Stauffer et al. 1991). Through comparisons with stellar samples of other ages, these studies raise significant questions regarding the time-scale for the decay of stellar activity along the main sequence and its relationship to the 'spin-down' time for the magnetically braked outer convection zone of low-mass and VLM stars.

I will first summarise the major results from previous X-ray studies of the Hyades in Section 5.2. In Section 5.3 I will describe the optical catalogue which I have used for this survey and in Section 5.4 the observations and analysis will be presented. Section 5.5 details the construction of the dK-dM X-ray luminosity functions.

5.2 Previous X-ray observations

Einstein

Coronal X-ray emission was first detected from the Hyades by *Einstein* in 1980. *Einstein* detected 66 members (out of 121 in the IPC fields) in a survey which mainly concentrated on a region within a few degrees of the cluster centre (Stern et al. 1981, Micela et al. 1988). These observations allowed a good determination to be made of the F- and G-type stellar X-ray luminosity functions, and demonstrated that X-ray emission was a common property of the F-G cluster stars: a typical Hyades G dwarf exhibits $L_X \simeq 10^{29} \text{ ergs s}^{-1}$, ~ 50 times that of the active Sun. However, the somewhat low sensitivity of the *Einstein* IPC precluded a detailed investigation of the X-ray faint members, especially at spectral types K-M (with detection rates of 50% and 33% respectively). Comparison of the Hyades luminosity functions with those of the Pleiades, Young Disk and Old Disk showed a clear decrease in X-ray luminosity with age.

Longer follow-up observations of a number of the X-ray brightest F and G dwarfs with the *Einstein* IPC enabled Stern, Antiochos and Harnden (1986) to perform spectral modeling of the coronal X-ray emission. They were unable to achieve fits using isothermal thin plasma models. Addition of a second temperature component provided acceptable fits, as did their attempt to

describe the coronae using models consisting of an ensemble of loops with a single maximum temperature. Stern, Underwood and Antiochos (1983) reported the detection of a giant X-ray flare in the Hyades binary VB 22.

EXOSAT

Westergaard et al. (1985) use *EXOSAT*LE observations together with the *Einstein* survey results to perform 3 band filter spectroscopy. They find coronal temperatures of a few million degrees for the 9 stars in their sample and measure a column density of 1 or $2 \times 10^{19} \text{ cm}^{-2}$. They acknowledge, however, that their results are susceptible to temporal variations.

The ROSAT all-sky survey

With the launch of ROSAT in 1990, and the subsequent all-sky X-ray and EUV surveys, an opportunity arose to obtain a complete cluster survey. Preliminary results of this survey have been reported by Stern et al. (1992a), but are briefly summarised here with emphasis on the WFC results.

The ROSAT PSPC detected 108 Hyades cluster members with $L_X \gtrsim 3 \times 10^{28} \text{ ergs s}^{-1}$. With the WFC 7 Hyads were detected in the S1a (90-190 eV) filter with $L_{\text{EUV}} \gtrsim 3 \times 10^{29} \text{ ergs s}^{-1}$. Because of the higher background in the S2a filter, no cluster members were detected in this waveband. In Table 5.1 are listed the numbers of detections and catalogued members by spectral type and luminosity class, while Table 5.2 shows the brightest PSPC sources together with the WFC sources (Tables 1 and 2 from Stern et al. 1992a).

The X-ray/EUV brightest cluster member is V471 Tau (Barstow et al. 1992), a well known red dwarf/white dwarf eclipsing binary undergoing mass transfer. The second brightest cluster member (as with *Einstein*) is VB 141 = 71 Tau = HR 1394. The Hyads span a large range of X-ray luminosities down to the survey limit (see Fig. 2 in Stern et al. 1992a). Of the brightest 13 X-ray emitters, 6 are spectroscopic binaries with periods of less than 6 days, and of the 10 such systems known (from either Batten et al. 1989, or Griffin et al. 1988), only one has not yet been detected in the all-sky survey (the Am system 60 Tau, a marginal X-ray detection by *Einstein*, Stern et al. 1981, and implying a flux limit close to the ROSAT survey limit). Among the stars

Table 5.1: Survey detections by B-V colour using the PSPC

Approx Sp Type	A-F	G	K	M	M (V>14)	Total
B-V	(-0.1-0.49)	(0.5-0.79)	(0.8-1.44)	(1.45-2.0+)	(No B-V)	
Main Sequence	24	32	25	20	3	104
White Dwarfs	1	0	0	0	0	1
Giants	0	0	3	0	0	3
Total Detected	25	32	28	20	3	108
Cataloged	71	63	134	135	76	479
Fraction Detected	0.35	0.51	0.21	0.15	0.04	0.23

Table 5.2: Brightest PSPC sources and WFC detections

Name	Count Rate ($c s^{-1}$) ^a		Spectral Type	Orb. Per. (days)	Notes
	PSPC	WFC S1A			
V471 Tau	1.741±0.069	0.320±0.016 ^b	dK+WD	0.52	60% WD
VB 141	1.043±0.089	0.025±0.006	F0+(G4V?)	>53?	^c
VB 71	0.902±0.059	0.018±0.005	K0 III+(dG?)	3000?	θ^1 Tau ^c
BD +22°669	0.579±0.081	0.015±0.005	K1V+K5V	1.89	
BD +23°635	0.534±0.036	n.d.	K3V+K8V	2.39	L20
VB 28	0.381±0.034	0.021±0.005	K0 III	-	γ Tau
VA 677	0.230±0.025	n.d.	K	1.5?	L60, J288
VB 22	0.223±0.025	n.d.	G6V+K6V	5.61	HD 27130 ^d
VB 85	0.216±0.024	n.d.	F5V	-	BD +15°640 ^e
VA 771	0.213±0.023	n.d.	G0V+K1V	1.87	Hyades group only?
VB 50	0.199±0.053	n.d.	G1V	-	susp. bin. ^e
L74	0.197±0.021	n.d.	dM	-	vis. bin. ^e
VA 351	0.196±0.044	n.d.	dMe	-	susp. bin.
VB 34 ^f	0.171±0.028	0.015±0.004	F6V	3.06	HR 1358
EG37 ^g	0.045±0.016	<0.011±0.006	DA	-	VR16,VA490

^a n.d = not detected, 3σ upper limit $\approx 0.02-0.03 c s^{-1}$. ^b V471 Tau also detected in S2A at $1.100 \pm 0.028 c s^{-1}$. ^c Companion detected in lunar occultations: see Peterson et al. (1981) and references therein. ^d *Einstein* X-ray flare: see Stern, Underwood, and Antiochos (1983). ^e Photometric binary candidate: see Carney (1982). ^f Last two sources included because of WFC detections. ^g Detected in sum of S1A+S2A filters.

detected in both X-rays and the EUV is the Hyades white dwarfs EG 37, confirming an earlier serendipitous *EXOSAT* detection (Koester et al. 1990); it is one of the coolest DA white dwarfs so far detected at soft X-ray wavelengths ($T_{\text{eff}} \simeq 24000\text{K}$, Kidder et al. 1992).

All four of the Hyades giants (ϵ Tau, θ^1 Tau, γ Tau and δ Tau) were detected by the PSPC in the all-sky survey. This is the first X-ray detection of ϵ Tau. Both θ^1 and γ Tau were detected in the WFC. In X-rays, θ^1 Tau was observed to be a factor of ~ 50 times brighter than ϵ Tau. Both pointed and survey observations of the Hyades giants will be discussed in more detail in Section 6.4.2.

5.3 The optical catalogue

The catalogue of probable or possible Hyades members used here, is a currently still evolving collection of some 450 stars for $m_V \lesssim 16$ developed primarily from the published literature and discussed in Stern et al. (1992a).

For completeness a full list of references is given here:

1. van Bueren (1952)
2. van Altena (1969)
3. Pels, Oort & Pels-Kluyver (1975)
4. Hanson (1975)
5. Upgren, Weiss & Hanson (1985)
6. Weiss & Hanson (1988)
7. Griffin et al. (1988)
8. Schwan (1991)
9. Latham (priv. comm.)
10. Weiss (priv. comm.)

Table 5.3: ROSAT pointings

SEQ ID	α	δ	Start Date	T_{obs}	T_{clean}	PI
US200020	04 08 50	15 06 00	27-Feb-1991		32.1	Stern
UK200441	04 21 12	14 42 00	24-Feb-1991	15.1	8.0	Pye
UK200442	04 21 12	17 31 48	24-Feb-1991	20.2	16.7	Pye
UK200443	04 32 31	17 31 48	07-Mar-1991	20.3	15.4	Pye
UK200441	04 32 31	14 42 00	06-Mar-1991	14.7	11.8	Pye
UK200775	04 19 48	15 37 48	22-Feb-1993		3.4	Pye
UK200776	04 20 53	13 51 36	30-Aug-1991	23.2	22.7	Pye
UK200777	04 25 36	15 56 24	30-Aug-1991	16.5	15.8	Pye
UK201368	04 30 07	15 38 24	10-Sep-1992		13.7	Pye
UK201369	04 26 24	16 51 00	24-Feb-1993		13.2	Pye
UK201370	04 21 32	18 25 12	23-Feb-1993		11.7	Pye

This catalogue contains an estimated $\lesssim 10\%$ potential non members in its current form. More recently, this catalogue has been extended, to include possible members from other sources, by Stern, Schmitt & Kahabka (1995).

5.4 ROSAT pointed observations and source identifications

The Observations were performed with the PSPC and the co-aligned WFC (see Chapter 2 for details of the instruments). Eleven separate pointings have been acquired in the central region of the Hyades; some of these overlap in both the PSPC and WFC. A merged image of all 11 PSPC fields is shown in Fig. 5.1, with the Hyads shown as circles.

As discussed in Chapter 2 the WFC underwent a dramatic loss in efficiency at the end of the all-sky survey which had a serious effect on the Hyades pointings completed early in AO1 (S1 efficiency was 0.1 of initial value) and a significant effect on all later pointings (S1 efficiency was 0.15 of initial value). An examination of the WFC images reveals no obvious sources. Using PSS, I find only very marginal detections for a few Hyads, so for the purposes of this study at least, there is very little additional information to be gained by a thorough analysis of the WFC data and so I will concentrate almost solely on the PSPC data. The WFC survey count-rates will be incorporated into the spectral fitting where possible.

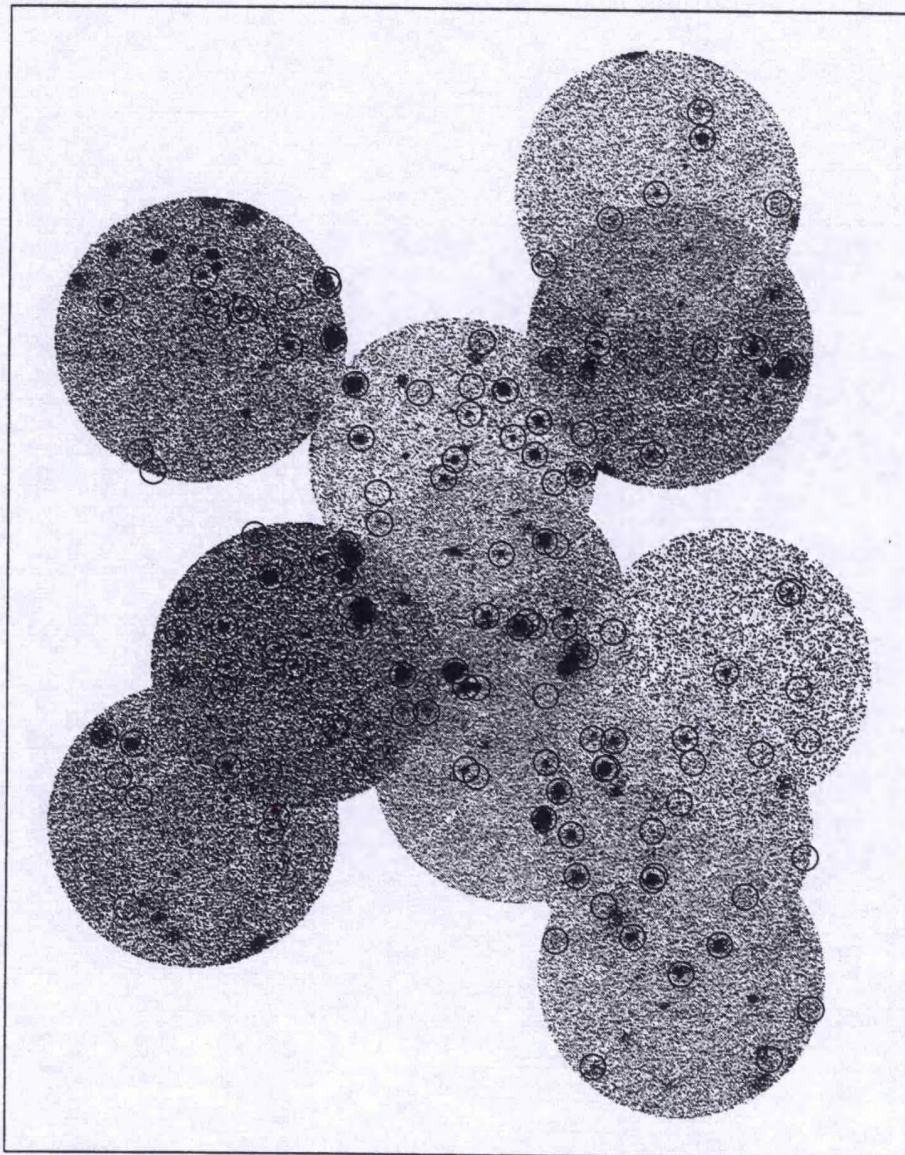


Figure 5.1: Merged image of all 11 PSPC fields included in the survey. The images have been exposure corrected to remove the effects of the ribs. Members of the input catalogue are shown with a circle.

For the PSPC, the actual useful exposure time was somewhat less than the full duration of the pointing because of the need to clean the data. Firstly data taken when the satellite pointing was drifting were rejected to avoid inclusion of aspect errors in the conversion of detector coordinates to sky coordinates. Secondly periods of high background (particle or X-ray) were rejected - see the discussion in Section 2.5).

5.4.1 Source detection and identification

In order to search for X-ray sources, the data for each field were binned into a (1° radius) sky image of 512×512 pixels centred on the nominal pointing direction, with each pixel being 15×15 arcsec². For each dataset the 'standard' TOTAL energy band was used, corresponding to a photon energy of about 0.1–2.4 keV (PI channels 7–240). The source detection program PSS (version 1.6-1, Allan, Ponman & Jeffries 1993) was used as part of the STARLINK ASTERIX X-ray data analysis package. The detection algorithm uses a maximum-likelihood ratio statistic (Cash 1979) to fit the spatially varying PSPC point-spread function to the data image and to produce a significance map. For each local maximum in the map, where the value exceeded a specified threshold, the best-fit values of detected counts and position, and associated error ranges, were evaluated. For the purposes of this analysis a low significance threshold was chosen, corresponding to '3.0 σ ', or a probability of $\lesssim 0.001$ that the detection is due to Poisson noise in the background. Comparisons with runs at higher significance threshold showed that extra, probably spurious, detections are produced at '3.0 σ ', however, because I wish to cross-correlate the detections with the positions of known stars, the chances of producing a spurious *Hyades* detection are greatly reduced. In total 957 sources were detected at 3σ within the full 60 arcmin radius field of view. The exposure correction was performed using the SASS standard exposure maps. For comparison, the sources were also exposure corrected by calculation using the vignetting function of the PSPC. However, this approach is unable to obtain exposure times for the sources which are partially obscured by the ribs in the PSPC window support structure. After checking that the two methods were consistent for those sources that were not behind ribs, the exposure map method was adopted. The resulting list of X-ray source positions was cross-correlated against the Hyades star catalogue, taking a generous separation of 2 arcmin to allow for inaccuracies in the catalogue, as well as aspect errors in the satellite, especially at large off-axis angles. PSS was also run to measure the upper limit to the count-rate for each star in

the catalogue. Upper limits were computed for 99% confidence. These lists were hand edited to remove:

- All Hyad-PSS sources with a separation $\gtrsim 1$ arcmin.
- Sources > 50 arcmin off-axis
- Extra PSS detections for the same Hyad in the same field.
- More than 1 Hyad correlating with the same PSS detection in the same field.
- Upper limits, where the same Hyad is detected in any field.
- Duplicates; where the same Hyad is detected in more than one field, the best detection (i.e. most significant, nearest center of detector, not obscured by rib [all the Hyads fully or partially obscured by the inner ring or support ribs were flagged]) is kept. Duplicate upper limits are dealt with in the same way.

This left a total of 121 Hyads after the above criteria had been enforced (within a total survey coverage of ~ 18 degrees²), of which 90 are positive detections. In Table 5.4 the detections are summarised by spectral type. Note the significantly higher detection rate than the all-sky survey (0.75 compared with 0.23). The White Dwarf EG 37 [$T_{\text{eff}} \sim 24000$ K (Kidder et al. 1992)] is detected, while EG 36 [$T_{\text{eff}} = 18960$ K (Bergeron, Saffer & Liebert 1992)] is not. Four out of eight (non-degenerate) A stars are detected including the δ Scuti variable VB 72 = θ^2 Tau (A7IVn,A7III). Three of the four detections are known spectroscopic binaries including the Am star 60 Tau (=VB 38) which was not detected in the all-sky survey and was a marginal detection with *Einstein*; of the non-detections, one is a known spectroscopic binary, while another has a variable radial velocity. For the F-M stars, the detected fraction decreases with increasing spectral type. All 3 of the Hyades giants that fall in the PSPC fields were detected (VB 28= γ Tau, VB 41= δ^1 Tau, VB 71= θ^1 Tau); a full discussion is deferred to Section 6.4.2 in the next chapter.

In order to convert count-rates to luminosity (in the energy range 0.1–2.4 keV, and assuming a common distance of 45 pc for all cluster members) a conversion factor of 1 PSPC count $\text{s}^{-1} = 6 \times 10^{-12}$ ergs cm^{-2} $\text{s}^{-1} = 1.45 \times 10^{30}$ ergs s^{-1} was employed (using the conversion factor in Stern et al. 1992a).

Table 5.4: PSPC detections

Class	Spectral Type					Total
	A	F	G	K	M	
Main Sequence	4	16	10	18	39	87
Catalogued	8	16	11	25	57	117
Giants	0	0	0	3	0	3
Catalogued	0	0	0	3	0	3
White Dwarfs	1	0	0	0	0	1
Catalogued	2	0	0	0	0	2
Total Detected	5 ^a	16	10	21	39	91
Total Catalogued	10 ^a	16	11	28	57	122
Fraction Detected	0.50	1.00	0.91	0.75	0.68	0.75

^a Includes white dwarfs

In Fig. 5.2 L_X is plotted against apparent magnitude, m_V , for the 122 Hyads (detections and upper limits). The approximate ROSAT all-sky survey limit (roughly equal to the *Einstein* survey limit) is shown as a horizontal line, indicating the improvement of sensitivity of the pointed observations, especially for the (intrinsically fainter) low mass stars. By subtracting the distance modulus of the Hyades ($=3.3$) from m_V , the abscissa is transformed to absolute magnitude M_V . The brightest stars in this sample are VB 141 (F0V+G4V, a suspected long-period [>53 d.] binary which is also a fairly rapid rotator $v \sin i = 195 \text{ km s}^{-1}$) and the giants VB 71 (K0III, a suspected binary [Collura et al. 1993, Peterson et al. 1993]) and VB28 (K0III). The minimum detected X-ray luminosity, L_X , is $\sim 5 \times 10^{27} \text{ ergs s}^{-1}$ (for VA 203, $m_V = 16.6$, and for VA 321, $m_V = 15.0$). There is a spread of ~ 2 orders of magnitude in L_X , with the upper range delineated by the spectroscopic binaries in the sample (for dM stars very little is known as regards their binary nature).

5.5 XLFs of the dK & dM stars

As mentioned above, the *Einstein* survey was sensitive enough to allow good determinations of the F and G star luminosity functions. However the low numbers of K and M star detections precluded a detailed study at these spectral types. With this more sensitive survey I am now

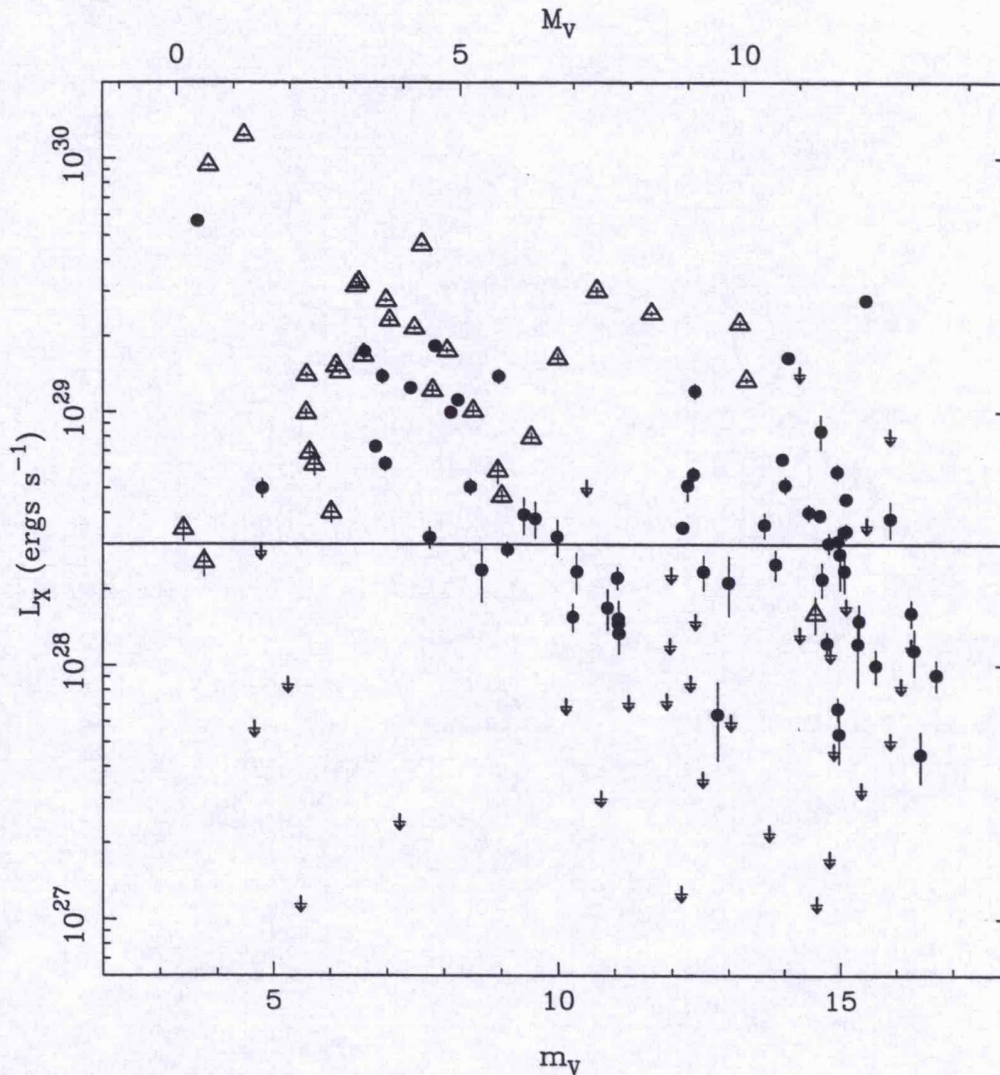


Figure 5.2: X-ray luminosity vs. m_V and M_V for all the Hyads in my sample. Detected single stars are denoted by filled circles, while detected binaries (known or suspected) are denoted by triangles. All 99% confidence upper limits are represented by arrows. A common distance of 45 pc has been assumed for all stars. The 1σ statistical errors for the detections range from about 20% for the weakest detections to 2% for the strongest. The *approximate* ROSAT all-sky survey limit (Stern et al. 1992a) is shown as a horizontal line.

able to investigate fully the properties of these fainter stars.

5.5.1 Definition of the sample

For the purposes of deriving the XLFs I have defined the samples from the input catalogue as follows:

(i) **dM-stars:** $m_V \geq 12.0$, plus VA 334 ($m_V = 11.65$, on the basis of $R-I = 0.75$), but excluding the WD star VA 292. The WD+dM5e binary VA 673 (=HZ 9) was *not* excluded since there is strong evidence that the dMe star dominates the X-ray emission (the WD is too cool at $T_{\text{eff}} \simeq 15600$ K, and the X-ray spectrum is consistent with that of a coronal system [see Section 2.1]).

(ii) **dK-stars:** $B-V \geq 0.8$ and $m_V < 12.0$, but excluding VA 334 (taken as a dM) and the Hyades K giants.

Stars were included only in the *final* samples if their Hyades membership probability according to Hanson (1975) was $\gtrsim 50\%$ or there was good evidence for membership from other sources e.g. Griffin et al. (1988), Reid (1993). The resulting dK and dM Hyad samples are listed in Tables 5.5 and 5.6 and contain 17 and 32 entries respectively. Six of the dK's and five of the dM's are known or suspected spectroscopic binary systems. However while there are estimates of (or at least bounds on) the periods for five of the dK stars, the only dM with a measured period (0.56 days, Lanning & Pesch 1981) is the spectroscopic binary VA 673. For completeness, in Table 5.7 I list those dK-dM stars in the input catalogue which were finally excluded from the analysis on the grounds of poor membership qualifications.

5.5.2 The XLFs

XLFs have been constructed for both the dK and the dM samples using survival analysis techniques, specifically the Kaplan-Meier Product Limit Estimator (KMPL), to incorporate the effects of censored data. The KMPL has been discussed by Feigelson & Nelson (1985) and is implemented in the ASURV package (rev 1.2). For a full discussion of survival analysis and the KMPL the reader is referred to Chapter 4 (Section 4.6). The resulting cumulative luminos-

Table 5.5: dK Hyads in the 11 ROSAT PSPC fields

Designation ^(a)		Photometry ^(b)			L _X ^(c)	σ(L _X) ^(d)	Notes
VA	H	m _V	B-V	R-I			
133	185	9.60	0.99	0.32	3.79	0.62	v=4.4 ^(e)
135	187	10.02	1.09	0.48	16.31	0.68	binary ^(f)
146	192	12.00	1.45	0.71	< 2.27	0.00	
276	290	10.52	1.21	0.49	< 4.99	0.00	v=3.2 ^(e)
279	292	9.12	0.86	0.28	2.86	0.19	
294	299	10.90	1.29	0.52	1.70	0.31	
310	312	9.99	1.06	0.38	3.21	0.53	v=4.1 ^(e)
342	342	10.27	1.04	0.38	1.56	0.19	v=5.0 ^(e)
475	422	11.08	1.36	0.58	1.34	0.23	
500	441	10.70	1.31	0.60	30.23	1.04	v=14.4 ^(e) ; binary, P > 5400 ^(f)
502	442	12.00	1.42	0.71	< 1.19	0.00	
587	491	9.01	0.84	0.32	4.65	0.25	binary, P=358.4 ^(f)
622	505	11.85	1.44	0.72	< 0.72	0.00	
627	509	9.55	0.97	0.37	7.93	0.32	binary, P=844.6 ^(f)
645	517	11.05	1.28	0.52	1.53	0.26	
684	544	8.92	0.88	0.33	5.85	0.63	v=6.7 ^(e) ; binary, P > 6000 ^(f)
727	578	8.50	0.84	0.30	10.09	0.53	binary, P ~ 5000 ^(f)

(a) VA: van Altena 1969; H: Hanson 1975. (b) See references in Stern et al. 1992a; also Stauffer 1982. R - I values are on the Kron system. (c) X-ray luminosity (10^{28} erg s⁻¹, in photon energy band 0.1-2.4 keV) computed from the ROSAT PSPC count rates, assuming a common distance of 45 pc for all the stars. (d) Error on L_X, computed from the standard deviation on the PSPC count rates due to counting statistics. (e) Radick et al. 1987. (f) Binary period P (days) (Griffin et al. 1988, Batten et al. 1989). Stars without a quoted period have been designated as photometric and/or radial-velocity binaries in the literature (Bettis 1975, Carney 1982, Stauffer 1982, Griffin et al. 1988).

ity distribution functions are shown in Fig. 5.3. For the dK Hyads, there is more information available on binarity (Griffin et al. 1988). All six known/suspected binaries are X-ray detected, and these 'dK-binaries' are all more X-ray luminous than any of the other dK stars (the latter will be designated as 'dK-singles', with 7 detections + 4 upper limits). In order to test that the dK-binary XLF cannot be explained in terms of the superposition of the X-ray flux from 2 single dk stars, I have convolved the dK-single XLF with itself. In Fig. 5.4 I show the XLFs for the dK-single and dK-binary samples as well as the convolved dK-single function. This convolution was performed by a 'Monte-Carlo' approach. For 100 test binary systems, two X-ray luminosities were extracted at random from the single star measured L_X's. These were added together to give the total binary star luminosity and the cumulative luminosity function for the 100 test systems was constructed.

In the sample of 32 dM-stars, there are only five or so suspected binaries (VA 288*, VA 334*, VA 351*, VA 638, VA 673*); all of them are X-ray detections, and four (asterisked) are amongst the most X-ray luminous in the dM sample. (c.f. Tables 5.5 and 5.6). VA 638 is a visual binary (with LP415-175), separation ~ 4 arcsec (van Altena 1969, Reid 1993), and does not exhibit

Table 5.6: dM Hyads in the 11 ROSAT PSPC fields

Designation ^(a)		Photometry ^(b)			L_X ^(c)	$\sigma(L_X)$ ^(d)	Notes
VA	H	m _v	B-V	R-I			
115	172	12.52	1.47	0.85	2.35	0.37	
118	173	15.11	1.57	1.25	< 1.71	0.00	
122	176	15.00	1.63	1.21	2.75	0.76	
127	181	16.15	1.63	1.31	< 7.97	0.00	
203	232	16.62	1.62	1.39	0.45	0.10	
213	242	15.44	1.55	1.33	3.09	0.37	
216	247	15.64	1.50	1.27	1.00	0.15	
242	266	13.00	1.52	0.95	2.13	0.56	
260	280	16.68	1.66	1.37	0.92	0.13	
262	284	15.82	1.77	1.31	< 3.54	0.00	
275	291	14.94	1.59	1.28	5.81	0.39	
282	294	14.76	1.59	1.16	< 1.10	0.00	
288	296	13.30	1.55	1.17	13.35	0.29	v sin i = 13.5 ^(f) , binary ^(h)
297	300	12.55	1.47	0.81	< 0.36	0.00	v sin i < 10 ^(f)
321	321	14.98	1.58	1.21	0.54	0.13	
334	336	11.68	1.43	0.75	24.63	0.50	binary ^(h)
351	346	13.21	1.53	1.20	22.42	0.61	v sin i ~ 10 ^(f) , binary? ^(e)
352	348	16.37	1.66	1.33	1.62	0.19	
362	360	15.32	1.49	1.39	1.21	0.39	
368	366	16.25	1.58	1.34	0.68	0.07	
382	376	15.11	1.52	1.40	3.38	0.23	
383	378	12.19	1.44	0.74	3.49	0.16	
420	401	13.05	1.48	0.90	< 0.60	0.00	v sin i < 10 ^(f)
512	449	14.26	1.53	1.15	< 14.08	0.00	
529	456	12.34	1.46	0.75	< 1.49	0.00	
575	484	14.45	1.55	1.21	4.02	0.29	
637	513	12.23	1.47	0.79	5.12	0.66	
638	514	12.17	1.46	0.78	1.60	0.26	binary ⁽ⁱ⁾
657	521	15.23	1.57	1.24	1.23	0.13	
673	528	13.88	0.31	0.99	6.52	0.27	binary, P = 0.56 ^(g)
674	530	15.45	1.55	1.23	3.04	0.27	
731	581	12.33	1.44	0.68	< 0.85	0.00	

(a) VA: van Altena 1969; H: Hanson 1975. (b) See references in Stern et al. 1992; also Stauffer 1982. R - I values are on the Kron system. (c) X-ray luminosity (10^{28} erg s^{-1} , in photon energy band 0.1-2.4 keV) computed from the ROSAT PSPC count rates, assuming a common distance of 45 pc for all the stars. (d) Error on L_X , computed from the standard deviation on the PSPC count rates due to counting statistics. (e) Suspected spectroscopic binary or triple system (Latham & Stauffer 1993). (f) Stauffer et al. 1987. (g) DA white dwarf + dwarf M, spectroscopic binary (VA 673 = HZ 9), period = 0.56 days (Lanning & Pesch 1981). (h) Binary period P (days) (Griffin et al. 1988, Batten et al. 1989). Stars without a quoted period have been designated as photometric and/or radial-velocity binaries in the literature (Bettis 1975, Carney 1982, Stauffer 1982, Griffin et al. 1988). (i) Visual binary with LP 415-175, separation ~ 4 arcsec (van Altena 1969, Reid 1993).

Table 5.7: dK–dM possible Hyads excluded from the analysis

Designation ^a		Photometry ^b		L_X ^c	$\sigma(L_X)$ ^d	Membership	Notes
VA	H	m _v	B–V			Probability ^e	
	196	16.27	1.74	< 1.18	0.00	0	
	495	16.32	1.97	1.15	0.24	0	
125	180	11.25	1.29	< 0.71	0.00	0	
LP 414-158		16.09	-9.00	< 0.82	0.00	–	
191	220	12.16	1.08	< 0.13	0.00	0	
LP 415-543		15.34	1.76	1.50	0.24	–	
200	229	13.85	1.58	2.51	0.33	0	
GH 7-178	264	14.64	0.84	3.91	0.21	0	
241	265	14.89	1.73	< 0.46	0.00	21	Reid (1992, 1993)
265	285	15.90	1.48	< 0.50	0.00	76	Weis & Upgren (1982), Reid (1993)
305	303	15.11	1.74	4.52	0.17	0	
306	304	14.58	1.64	< 0.11	0.00	2	
329	330	14.81	1.60	< 0.17	0.00	21	Reid (1993) prob.=1%
366	363	12.38	1.45	5.67	0.38	30	rejected by Griffin et al. (1988)
380	374	13.73	0.87	< 0.22	0.00	2	
478	423	15.38	1.09	< 0.32	0.00	7	
578	485	10.76	0.87	< 0.30	0.00	3	
	588	7.22	1.13	< 0.24	0.00	2	
750	601	12.41	1.45	12.10	0.84	0	

a) VA: van Altena 1969; H: Hanson 1975. b) See references in Stern et al. 1992; also Stauffer 1982. c) X-ray luminosity (10^{28} erg s⁻¹, in photon energy band 0.1–2.4 keV) computed from the ROSAT PSPC count rates, assuming a common distance of 45 pc for all the stars. d) Error on L_X , computed from the standard deviation on the PSPC count rates due to counting statistics. e) Hanson 1975.

an exceptional X-ray luminosity. There are insufficient objects to construct a separate, useful, dM-binary XLF. The lack of known dM binaries is likely to be an observational selection effect (see e.g. Reid 1993) and comparison with the dK sample supports the suggestion (Stauffer 1982) that binaries may be strongly influencing the derived XLF.

5.5.3 Test of results

As with the ELFs discussed in Chapter 4, the Hyades XLFs show apparent ‘features’ on various luminosity scales, including changes in slope. In order to investigate the reality or otherwise of these results (for a sample that is *not* heavily censored) I have generated a number of perturbed data-sets from the dM L_X values, and constructed the corresponding XLFs. The perturbations consisted of:

- (a) increasing all upper limits by a factor of 2,
- (b) decreasing all upper limits by a factor of 2,

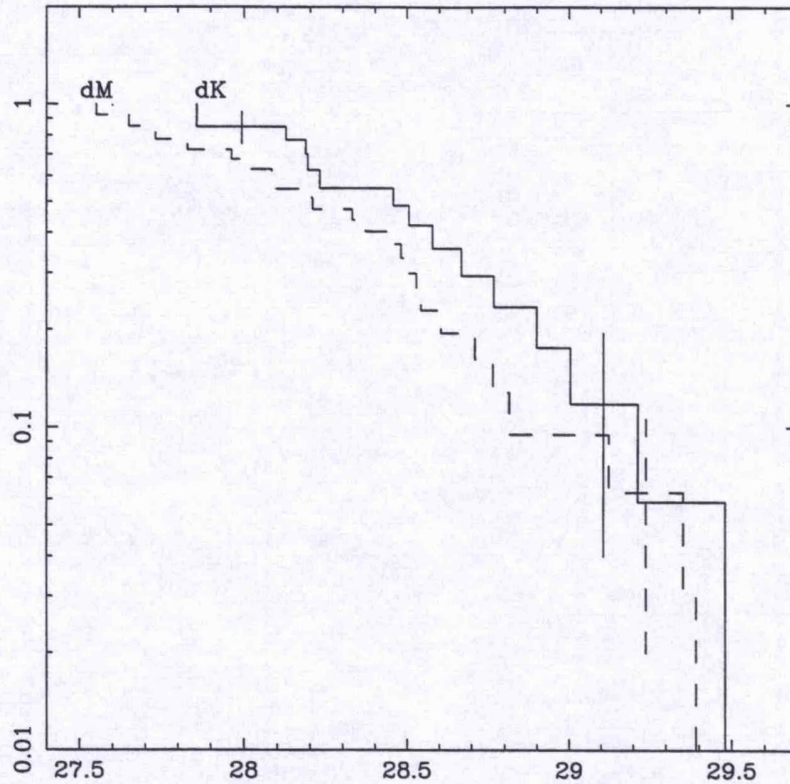


Figure 5.3: Cumulative X-ray luminosity function for the dK and dM Hyads. The vertical error bars are as computed by the ASURV KMPLE and are not independent.

(c) removing all upper limits,

(d) applying uniform random noise in the range ± 0.18 to $\log L_X$ for all detections and upper limits, and making ten different data-sets in this manner.

The resulting XLFs were compared with the original XLF both visually and by applying two-sample tests (specifically: Gehan's generalised Wilcoxon test - permutation variance, Gehan's generalised Wilcoxon test - hypergeometric variance, Logrank test, Peto & Peto generalised Wilcoxon test, Peto & Prentice generalised Wilcoxon test; Feigelson and Neslon 1985). It was found that:

(i) the XLF was insensitive to changes in the upper limits,

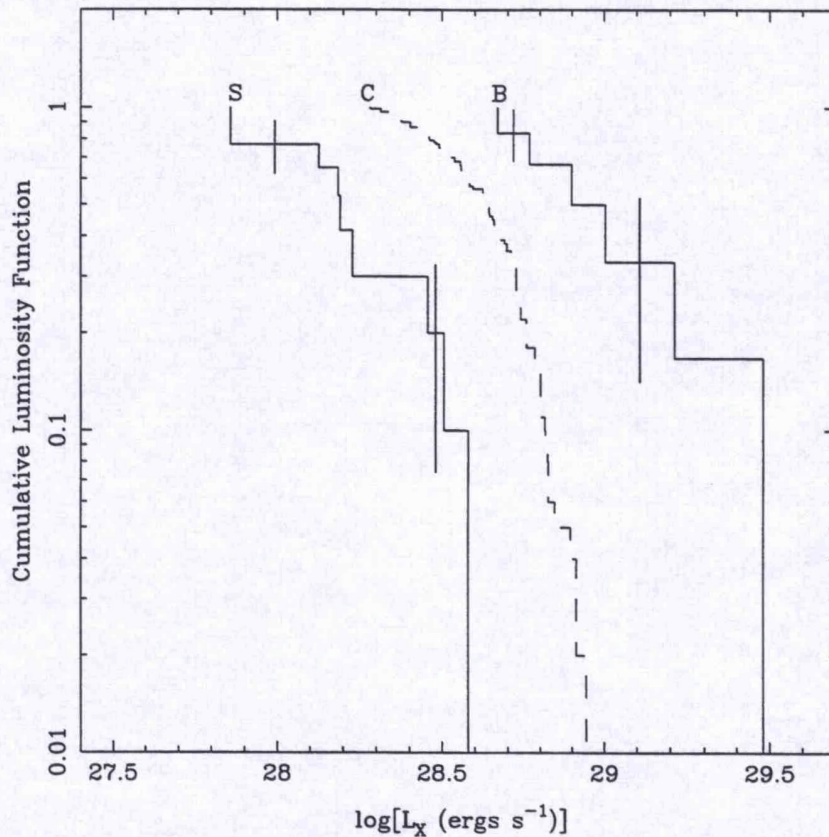


Figure 5.4: Cumulative X-ray luminosity function for the dK-single (S), dK-Binary (B) and the convolution of the dK single-star distribution with itself (C). The vertical error bars are as computed by the ASURV KMPLE and are not independent.

(ii) the flattening of the dM-star XLF slope for $L_X \lesssim 10^{28.3} \text{ ergs s}^{-1}$ was reproduced from all the modified data-sets,

(iii) the reality of small-scale features over $\Delta \log L_X \lesssim 0.5$ should not be relied upon.

In summary, the KMPLE XLFs derived here appear to be reliable within the calculated error estimates (as plotted in Fig. 5.3). Further, the range of uncertainty applied in test (d) gives confidence that the simplification of taking all Hyads at a constant distance of 45 pc has not significantly affected the XLFs.

5.5.4 The XLFs in summary

These ROSAT observations have allowed XLFs to be constructed for dK and dM stars down to $L_X \sim 10^{27.7}$ ergs s^{-1} , with approximately 75% of the sample stars being detected. This is a significant improvement over the *Einstein* survey where a limiting luminosity of $L_X \sim 10^{28.5}$ ergs s^{-1} was reached. Extending the measured range of X-ray luminosities is important not only for studies of stellar activity in the Hyades itself, but also in the wider context of comparisons with XLFs of other stellar samples such as nearby stars (e.g. Micela et al. 1988), galactic source count predictions (and hence stellar birthrate and evolution predictions, e.g. Micela et al. 1993), and estimates of the contribution of stellar coronae to the galactic X-ray background (e.g. Schmitt & Snowden 1990).

In Figs 5.5 and 5.6 I compare the *Einstein* and ROSAT dK and dM XLFs. Additionally the Young Disk dK and dM XLFs are shown (from Barbera et al. 1993). I see good agreement between the *Einstein* and ROSAT XLFs for dK and dM Hyads above $L_X \sim 10^{28.5}$ ergs s^{-1} which is born out by two-sample tests (as described above). Micela et al. (1988) have already mentioned the similarity between the Young Disk and Hyades dM star XLFs and possible similarity for the dK XLFs. I also note that the dM and dK XLFs are similar (c.f. Fig. 5.3) with a formal probability $> 15\%$ that the two samples are drawn from the same parent distribution.

In Fig. 5.7 I compare the Hyades dK-binaries XLF with that of the Pleiades dK stars (single+binary, *Einstein*, Micela et al. 1990). Two-sample tests are unable to distinguish between the two distributions with confidence $> 95\%$

Recalling Fig. 5.4, there is a low luminosity component to the dK XLF dominated by single stars. The probability that the binary and single star XLFs are drawn from the same parent population $< 0.4\%$. All the dK binaries in the sample have relatively long periods ($\gtrsim 1$ year) so it is not immediately obvious why they should show such high activity levels. It can not be attributed to the enhanced activity expected in short-period (\lesssim few days), BY Dra-type systems, nor can it be due simply to the summed luminosities of the multiple component stars. It is only possible to speculate as to the explanation. One possibility is the system started with a very high initial angular momentum. Alternatively, some interference with the normal processes which 'spin down' rapidly rotating stars may have occurred. Cameron & Campbell (1993) discuss

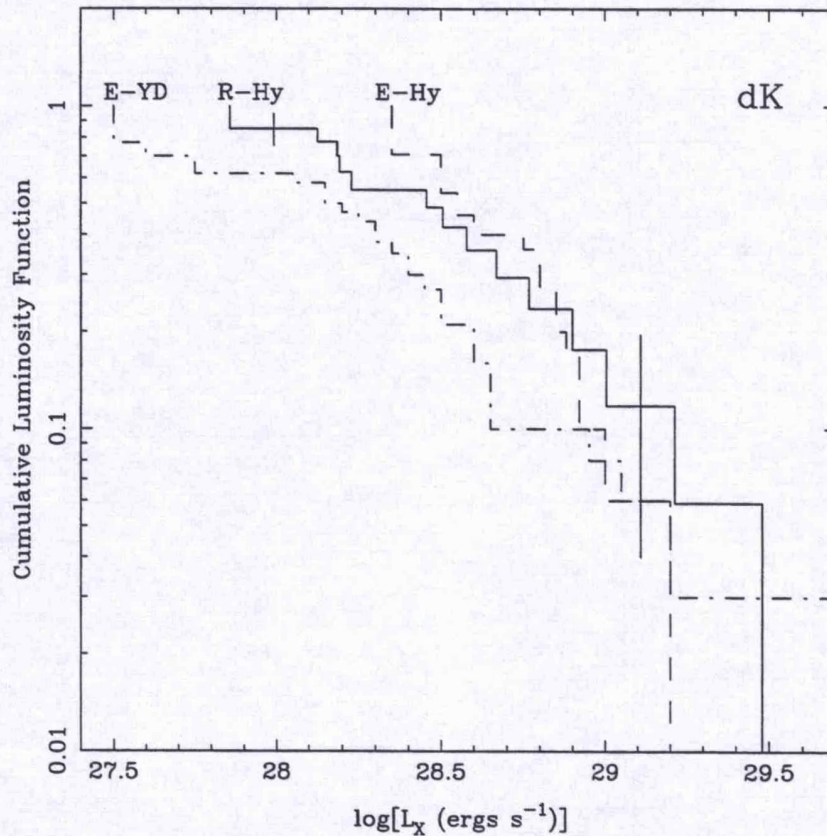


Figure 5.5: The ROSAT Hyades dK XLF (R-Hy) compared with XLFs derived from *Einstein* data (after Micela et al. 1988) for the Hyades (E-Hy) and Young Disk (E-YD) dK stars.

the exchange of angular momentum between protostar and accretion disc during Hayashi track evolution. They comment on the rapidly rotating solar-type stars seen in some open clusters and suggest that these stars may have become decoupled from their discs somewhat earlier than the majority of such stars. A binary companion, therefore, maybe disrupted the disc, leaving only the relatively inefficient braking mechanism of the magnetic stellar wind as a means of shedding angular momentum.

5.5.5 Coronal activity in the coolest stars

In Chapter 4 we have already seen evidence for coronal activity in stars with spectral types later than dM4. This has implications for models of the convection zone and magnetic dynamo for

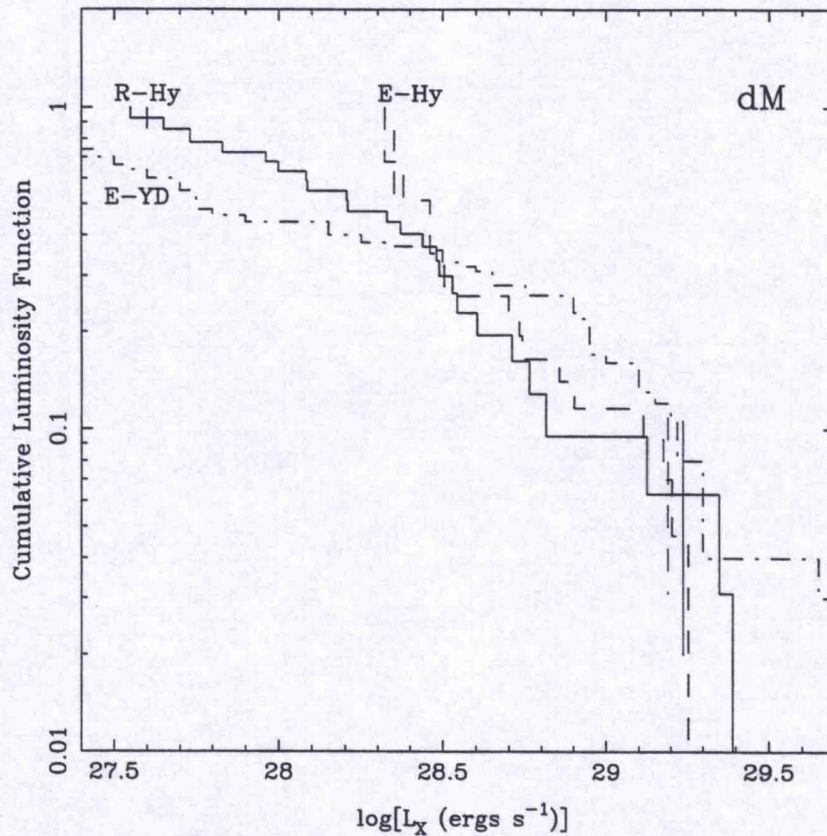


Figure 5.6: The ROSAT Hyades dM XLF (R-Hy) compared with XLFs derived from *Einstein* data (after Micela et al. 1988) for the Hyades (E-Hy) and Young Disk (E-YD) dM stars.

stars with very deep (or even fully) convective interiors (e.g. Liebert & Probst 1987; Cox et al. 1981; Dorman et al. 1989). From Table 5.6, the lowest-mass, X-ray detected Hyads so far are VA 203 and VA 260, both at $m_V \sim 16.6$. The number of low mass Hyads so far available in this survey is rather small, due to incompleteness in the optical catalogues and the intrinsic low X-ray luminosity of these stars.

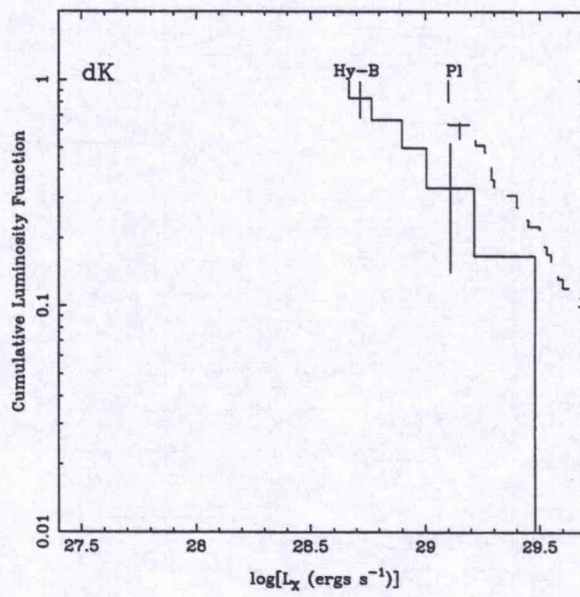


Figure 5.7: The ROSAT Hyades dK XLF for SB stars (Hy-B) compared with XLFs derived from *Einstein* data (after Micela et al. 1990) for the Pleiades (Pl) dK stars.

Chapter 6

ROSAT observations of the Hyades: 2. Spectra

6.1 Introduction

X-rays from stellar coronae originate by line and continuum thermal emission from optically thin (usually multi-temperature) plasmas (see Section 2.1 and e.g. Raymond 1988). In order to infer in detail the temperature structure in the emitting source, high-resolution spectral observations are required. Unfortunately, only a limited number of such observations were performed by the *Einstein* Observatory, using the solid state spectrometer (SSS) and the objective grating spectrometer (OGS). These observations (see e.g. Swank et al. 1981) gave the first clear evidence for multi-component plasmas in nonsolar coronae.

The *EXOSAT* transmission grating spectrometer (TGS) obtained high resolution spectra for two RS CVn systems (Capella and σ CrB) and for Procyon (Lemen et al. 1989, Schrijver, Lemen and Mewe 1989) confirming the multi-temperature nature of these coronae. Individual lines were not resolved, but the broad line complexes visible in these spectra were sufficient to constrain fairly well the range of temperatures present in the sources.

An important question is whether the two-temperature structure found from spectral analysis of stellar coronae (see Chapter 1 and references therein) represents emission from spatially distinct regions (e.g. from two families of loop structures in different temperature regimes) or rather results from a continuous emission measure distribution, such as that observed in

solar coronal loops. Schmitt et al.(1990a) and Majer et al.(1986) have argued that the two-temperature solutions may be at least partly dependent on the detector energy response. Schmitt et al.(1987) and Pasquini et al.(1989) have shown with the help of Monte Carlo simulations that two-temperature fits can also be obtained for a continuous emission measure distribution and, therefore, two-temperature fits should more properly be regarded as instrument-weighted effective temperatures, and not as physical temperatures of the observed plasma. On the other hand, White et al.(1990) have argued that the observations of eclipsing binary systems with *EXOSAT* provide direct evidence that the two-temperature solutions found from spectral fits refer to spatially separated structures in the coronae of (at least) close binaries.

The very few high resolution observations have not enabled the characterisation of the general spectral properties of X-ray emission throughout the HR diagram. Early studies with the *Einstein* IPC have shown a dependence of the photon spectrum on the activity of the star, and that there may be a correlation between X-ray luminosity (L_X) and temperature (Schmitt et al. 1985, Schmitt et al. 1987, Vaiana 1990). Schmitt et al. (1990) have examined the *Einstein* IPC spectra for some 130 late-type stars and have used a variety of coronal models to describe these stars. They find that two-temperature solutions are usually obtained for data of sufficiently high S/N ratio, and that giants appear to be systematically hotter than main-sequence stars of similar spectral type. They also find that the IPC data can be fitted equally well by a continuous emission measure distribution. An additional finding was that M dwarfs prefer two-temperature fits, with as few as 500 counts in the spectra. Their interpretation is that the M dwarfs have hotter coronae than earlier spectral types.

With the advent of ROSAT and the data obtained from the pointed survey of the Hyades discussed in Chapter 5, I am in a position to exploit the high sensitivity and modest spectral response ($\Delta E/E \sim 0.3$ at 1 keV) of the PSPC and examine the spectral characteristics of a coeval sample. In this chapter my aim is to describe the coronae of the sample stars with simple models, and examine any trends in the dataset.

6.2 Procedure

As shown in Chapter 5, 108 sources corresponding to 86 Hyads have been detected in the survey (out to 50 arcminutes off axis). 18 Hyads have been observed twice and 2 have been observed three times. For those stars with more than one spectrum, the observations are spread between AOs 1–3 giving time separations of \sim days, 6 months, and just over one year in the case of VB 71 (θ^1 Tau). The observations are listed in Table 5.3 in Chapter 5.

The PHA spectra for all 108 sources were extracted (removing time slots with high background, as detailed in Section 2.5) using circular regions with variable radii. The radius for extraction was taken to be the larger of 4 arcminutes and the 95% encircled energy radius to avoid the problems of ‘ghost images’ in the lowest PHA channels (see Section 2.5 for more detail). For each field, a number of source-free background regions were determined. These were averaged to give one background PHA spectrum per field. The background subtraction and exposure correction were carried out using the ASTERIX programs XRTSUB and XRTCORR. For each spectrum, the appropriate offaxis response matrix was created using XRTRISP. Our understanding of the response matrix for the PSPC is still evolving, primarily in an attempt to eliminate small (typically less than 5%) systematic errors seen in the highest signal to noise spectra; I use the ROSAT detector response matrix of January 1993. In addition, after a series of tests on a representative sample of Hyades spectra, it was decided to ignore data below PI channel 20 and above PI channel 248 in the spectral fitting (PI channels are defined in Section 2.5). Inclusion of data below PI channel 20 required the inclusion of an additional absorption component (equivalent to an intervening hydrogen column of $N_{\text{H}} \sim 5 \times 10^{19} \text{ cm}^{-2}$) in the spectral fits to account for a systematic over-prediction of the data by the model in the lowest channels. This apparent N_{H} is felt to represent a problem with the PSPC detector response matrix for a number of reasons. Firstly, previous observations of the Hyades with *Einstein* and *EXOSAT* have consistently found $N_{\text{H}} \lesssim 10^{19} \text{ cm}^{-2}$ (which is consistent with models of the local bubble, e.g. Warwick et al. 1993, Paresce 1984). Secondly, the fall off in the data is not well modelled by the inclusion of hydrogen absorption – it is rather too steep. Additionally, uncertainties in the PSPC window transmission function, in-orbit gain changes and ‘afterpulses’ (see Snowden 1994b) all combine to particularly affect the lowest PHA channels.

The spectra were fitted using XSPEC (Version 8.34) on a Sun Sparcstation. The models used

were based on a recent (1991) update of the Raymond & Smith (1977) optically thin plasma emissivities. (This update was supplied to the X-ray astronomy group at Leicester by John Raymond). Before fitting, to improve signal to noise, the data were binned in accordance with the procedure described in Section 2.5, which attempts to maintain a constant oversampling of the response matrix as a function of energy ('SASS binning'). This resulted in 34 SASS bins, of which bins 1-5 (equivalent to PI channels 7-19) were ignored, leaving 29 spectral bins ranging from 0.20 keV to 2.48 keV (PI channels 20-248).

Given the modest spectral resolution of the PSPC and the relatively low signal-to-noise ratio of some of the data, the models used must be simple representations of coronal spectra. I have employed two different coronal models to investigate the observed spectral distribution of the incident X-ray flux. As an alternative to modelling, a non-parametric approach using hardness ratios has also been considered. The characterisations are summarised below:

1. Hardness ratio, R , defined as $\frac{H-S}{H+S}$, where H is the number of counts in PI channels 11-41 and S is the total counts in PI channels 52-201
2. An isothermal plasma with two adjustable parameters - T , EM . I refer to this as a one-temperature (1T) model hereafter.
3. A plasma consisting of two isothermal components, with four adjustable parameters - T_1 , EM_1, T_2 , EM_2 . This is referred to as a two-temperature (2T) model.

For all the fits, elemental abundances were assumed to be solar and were fixed. It was quickly found that the very faintest spectra did not sufficiently constrain any of the models. Inspection of the confidence regions around the best fit parameters for the acceptable 1T fits showed that these parameters were very poorly constrained for spectra with less than about 300 counts. Thus for the model fitting, I rejected all datasets containing less than 300 counts in the PHA spectra, leaving 64 spectra of 49 stars. For the hardness ratios, only those PHA spectra containing less than 100 counts were rejected - giving hardness ratios for 69 stars.

6.3 Results

6.3.1 Hardness ratios

It is possible to examine the spectral characteristics of the Hyades X-ray sources non-parametrically using hardness ratios derived from their PHA spectra. I define hard (H) and soft (S) bands to be PI channels 11–41 and 52–201 respectively (i.e. above and below the Carbon edge) in accordance with the SASS definition. The hardness ratio $R = \frac{H-S}{H+S}$ was formed for all Hyads with greater than 100 counts in their PHA spectra (still rejecting sources outside the 50 arcminute offaxis angle limit), giving ratios for a total of 69 stars (as with the spectra, discussed below, hardness ratios obtained from the longest pointings were retained, while those derived from shorter duplicate observations were rejected). The 1σ error in R is defined as $\sigma_R = 2\sqrt{(\delta H/H)^2 + (\delta S/S)^2}/[1 + (H/S)]^2$. In Fig. 6.1 R is plotted against B–V. Most of the hardness ratios are clustered between $R = -0.5$ and $R = 0$, as found by Vaiana (1990) for the IPC-detected Bright Star Catalogue (BSC) stars and Woolley (Woolley et al. 1970) stars. In the bottom left-hand corner of the figure is the White Dwarf EG 37. The two giants VB 28 (γ Tau) and VB 71 (θ^1 Tau) have hardness ratios $R > 0$, lying above all the other Hyads with the exception of the non-member candidates and one other interesting object (VB 47). The other giant in the sample, VB 41 (δ Tau) has insufficient counts for inclusion in the sample. This excess of hard counts is in line with the finding of Schmitt et al. (1990a) that giants have hotter coronae than dwarfs. Controversy surrounds the question of the possible binary nature of the Hyades giants and the possible contribution to the total X-ray emission from these potential companions. This is discussed fully in Section 6.4.2. Schmitt et al. (1990a) also argue that M dwarfs have hotter coronae than earlier spectral types. One would expect to see this as an increase in R at B–V ~ 1.5 . There is no evidence for such an effect within the limitations of poorer statistics for the less X-ray luminous dM stars.

Two of the known non-members (GH7-178, VA 444 – see Table 5.7 in Chapter 5) share a hardness ratio in excess of 0.5. This is an indication that the deficit of soft counts may be due to extra absorption, i.e. that these stars are objects lying behind the cluster. The rest of the known/suspected non-members do not show unusual hardness ratios. I expect these objects therefore to be lying \lesssim distances comparable with the cluster's. In Section 6.3.2 I discuss the

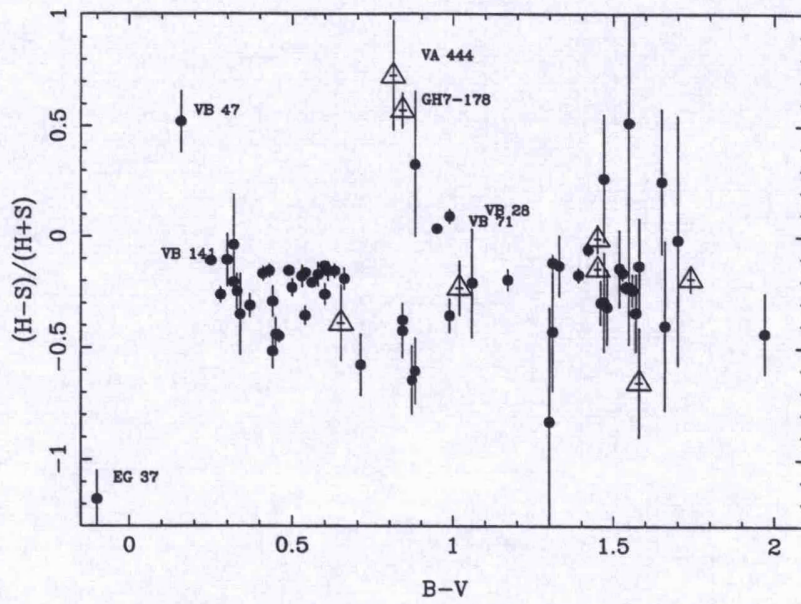


Figure 6.1: Hardness ratio $R = \frac{H-S}{H+S}$ against B-V for all Hyads with > 100 counts in their PHA spectra. Suspected and known non-members are shown with a triangle. The Hyades giants VB 28 and VB 71 are labelled.

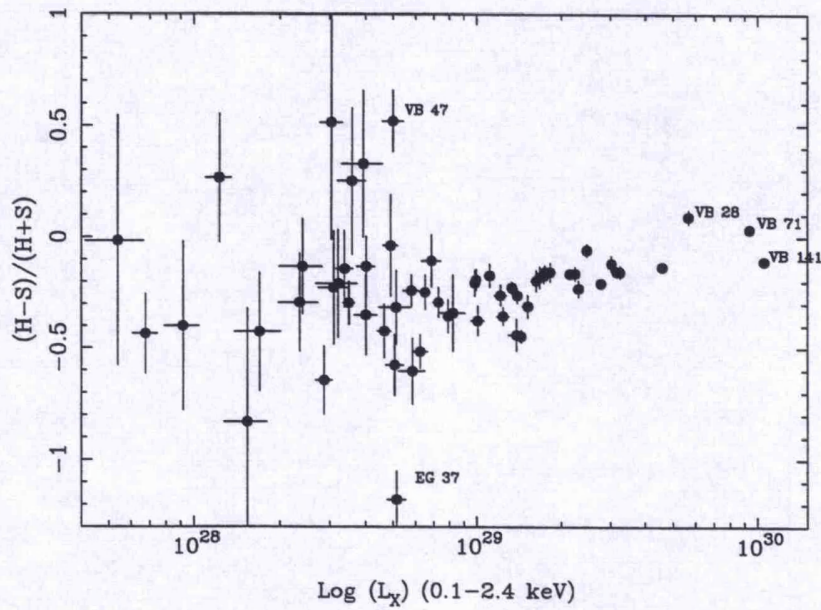


Figure 6.2: Hardness ratio $R = \frac{H-S}{H+S}$ against L_X for all Hyades members with > 100 counts in their PHA spectra. Non-members have been excluded from this plot.

case of GH7-178 in the light of more detailed spectral fitting, as well as the other object with $R = 0.5$, VB 47.

In Fig. 6.2 R is plotted against L_X , with known non-members removed, to investigate the effects of increasing luminosity on the spectra. A slight trend of increasing hardness with increasing luminosity is apparent, with significant scatter in R . One feature of the distribution is the lack of luminous soft sources. All but one of those stars with $R > 0.2$ do not have good statistics. The luminosity calculated for VB 47 may well be in error given its now suspect membership status which could place it at a different distance from the Hyades. The figure also shows that the giants VB 28 and VB 71 have significantly harder spectra for their luminosity than either VB 141 or VB 50 (non-flaring observation, see Section 6.3.4). Vaiana (1990) finds that the IPC-detected sample of BSC stars shows a clear trend of spectral hardening with increasing X-ray luminosity. He argues that the results of the *Einstein* survey of coronal temperatures (Schmitt et al. 1990a) support the view that this hardening is not caused by interstellar absorption. My results could suggest that the luminosity–hardness relationship is independent of absorption, as all cluster members should share approximately the same hydrogen column density.

6.3.2 One-temperature fits

One-temperature fits were attempted for all 64 spectra (48 stars) in the sample. In general, two local χ^2 minima were found in each case at approximately 10^6 K and 10^7 K, corresponding to the model attempting to fit one or other of the broad peaks in the PSPC response (see Fig. 2.9 in Section 2.5).

A one-temperature (1T) fit is deemed to be acceptable under the following circumstances:

- $\chi_{\text{red}}^2 \leq 1.5$ (i.e the data is described by the model with confidence exceeding 3%), and
- If $\chi_{\text{red}}^2 > 1$ (probability that the model could reproduce the data with $\sim 50\%$ confidence), an F test comparison with χ_{red}^2 for a two-temperature (2T) fit shows no significant improvement (at an arbitrary confidence level defined by the user – see below). The F test for additional terms is defined below

$$F = \frac{\chi^2(1T) - \chi^2(2T)}{N} \times \frac{1}{\chi_{red}^2(2T)} \quad (6.1)$$

The ratio is a measure of how much the additional terms have improved the value of the reduced chi-square. An improvement in the fit must be achieved to 99% confidence before a 2T fit is deemed to be required (where N is the number of additional terms).

In Fig. 6.3, χ_{red}^2 is shown for all the 1T fits against the number of counts in the spectrum. Those spectra which are fit significantly better by a 2T model are shown with a different symbol. All spectra with greater than 1000 counts require a 2T fit. Of the 64 PHA spectra, 18 are acceptably fit by a 1T model while 46 are not and show a significant reduction in χ^2 with a 2T model. The very tight correlation between χ_{red}^2 and counts is indicative that the 1T fits are a result of poor counting statistics, rather than a truly isothermal plasma. There are no notable deviations from the correlation.

Table 6.1 lists all the acceptable 1T fits. I now remove the multiple observations from the sample, retaining the longest observation in each case, leaving 14 fits to 14 stars, and briefly examine the model parameters in relation to other stellar parameters.

In Fig. 6.4 the acceptable 1T fits are shown as a scatter plot of EM against T. Most of the fits are tightly clustered in temperature, with a factor ~ 12 spread in EM. The three stars which show evidence for higher temperature coronae (VB 47, VA 444 and GH7-178) are those already found to have high hardness ratios ($R > 0.5$, Section 6.3.1). By including N_H in the fits to these three stars, I statistically improve the fits to VB 47 and GH7-178 (again using the F test with a 99% confidence threshold), while there is no significant reduction in χ^2 for VA 444. Although there is no apparent change in temperature, the counting statistics are so poor (especially in the soft channels), that it is not possible to put meaningful constraints on the plasma temperature or the N_H column for all but GH7-178, where a best fit column of $3.5 \times 10^{19} < N_H < 1.5 \times 10^{20} \text{ cm}^{-2}$ is found. The best fit temperature does not change appreciably. None of the other stars with $R > 0.2$ appear in the 1-T sample.

The PSPC spectrum of GH7-178 has already been discussed by Stern et al. (1994) who conclude that the star lies behind the Hyades cluster. It is easy to see that the optical colours and magnitude ($V=14.64$, $B-V=0.84$) place this star about 6 mags below the Hyades main-sequence,

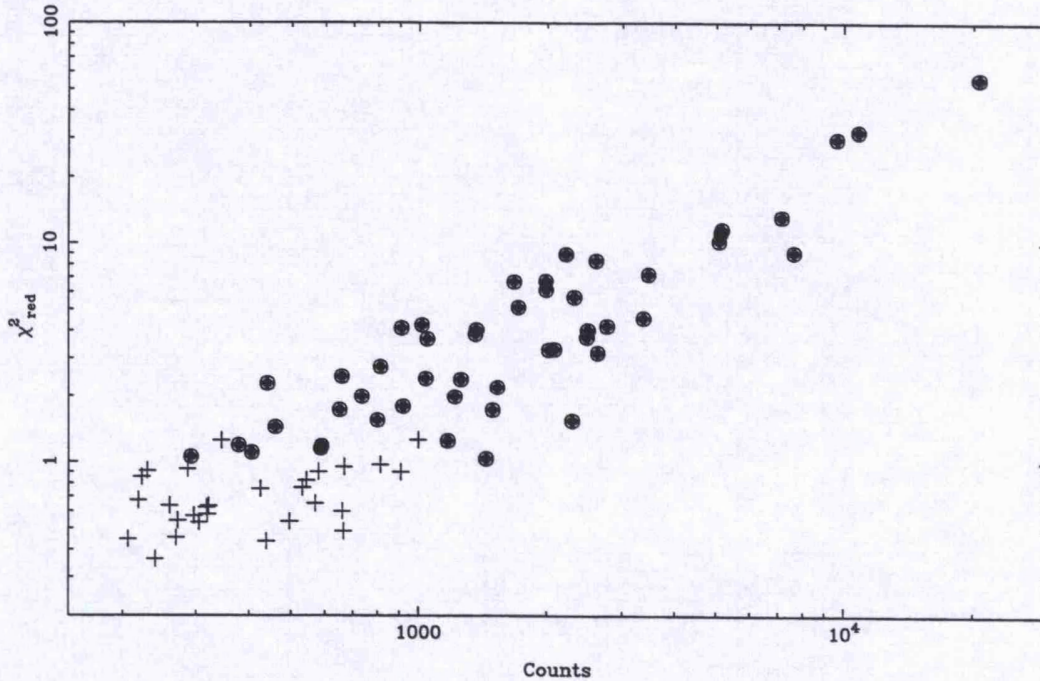


Figure 6.3: χ_{red}^2 for 1T fits vs. number of counts in the PSPC spectrum for all stars with >200 counts (remembering that fits are only attempted for spectra with >300 counts). Where a 1T fit is acceptable the star is marked with a cross (+). Those stars preferring 2T fits are marked with a filled circle (•).

with a corresponding distance of > 500 parsecs, if the star is on the main-sequence. This implies a factor 120 increase in L_X , i.e. $L_X \sim 6 \times 10^{30} \text{ erg s}^{-1}$, in the high-luminosity tail of the late-type star X-ray luminosity function (e.g. Rosner, Golub & Vaiana). The Paresce (1984) map of the local ISM would place an upper limit on the distance of around 150 parsecs if the N_H column derived from the fit to the PSPC spectrum is to be believed. Follow up work is required to rule out errors in the optical photometry. VB 47 (δ^2 Tau, A7.5 V, $V=4.80$, $B-V=0.16$) lies exactly on the Hyades main-sequence. It is in a wide binary system (separation ~ 2.5 arcmin with a faint companion ($V=13.3$) of unknown spectral type. The large offaxis-angle of the detection, and the corresponding uncertainty in the position of the source, does not rule out this faint companion as the X-ray source, nor indeed does it rule out a background object. VA 444 (K0V, $V=11.07$, $B-V=0.81$, already classified as a non-member) lies some 2 magnitudes below the main sequence, which would place it at a distance of some 110 parsecs from us.

Table 6.1: Best fit parameters to Hyades PHA spectra satisfied by one temperature models

Name	Counts	Seq	χ^2_ν	log T (K)			EM ⁺ (10^{50} cm^{-3})		
				ll	ul		ll	ul	
L61	496	201368	0.54	6.45	6.35	6.56	21.8	15.6	28.1
L63	666	200443	0.95	6.45	6.39	6.51	32.7	27.6	38.0
L70	664	200443	0.49	6.51	6.46	6.57	33.2	27.8	38.7
H366	425	200020	0.75	6.47	6.35	6.71	7.2	3.9	9.8
H500	304	201368	0.53	6.41	6.29	6.59	25.2	16.1	34.4
VB27	319	200442	0.58	6.38	6.28	6.46	19.3	14.4	24.2
VB34	542	200441	0.83	6.48	6.44	6.55	79.4	67.0	91.5
VB47	344	200442	1.25	7.18	7.07	7.51	54.7	54.7	54.7
VB65	813	201368	0.97	6.45	6.41	6.49	61.0	53.5	68.5
VB78	659	200443	0.60	6.43	6.38	6.48	54.7	46.2	62.9
VB79	569	200443	0.65	6.44	6.37	6.49	45.3	37.0	53.5
VB91	321	201368	0.63	6.32	6.13	6.46	21.2	12.4	29.5
VB96	579	200444	0.90	6.47	6.42	6.53	48.4	41.1	55.4
VA413	531	200020	0.77	6.49	6.41	6.58	12.0	8.9	14.9
VA444	318	200020	0.62	7.05	6.95	7.15	15.0	9.3	22.6
GH7-178	997	200020	1.26	6.99	6.95	7.03	31.7	26.4	38.0
GH7-187	907	200020	0.90	6.47	6.43	6.52	27.1	23.3	30.7
GH7-187	438	200776	0.44	6.99	6.82	7.11	20.5	12.2	35.3

+ Assuming Hyades distance.

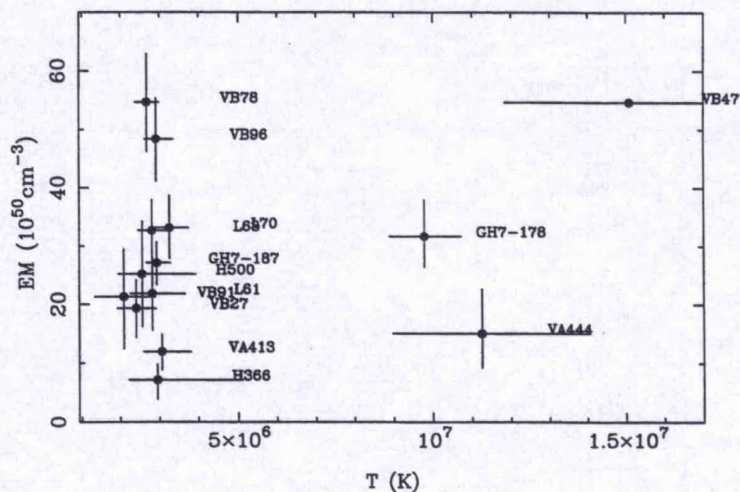


Figure 6.4: Emission measure against temperature for the 1T fits. The error bars are 90% for one parameter of interest ($\delta\chi^2 = 2.706$).

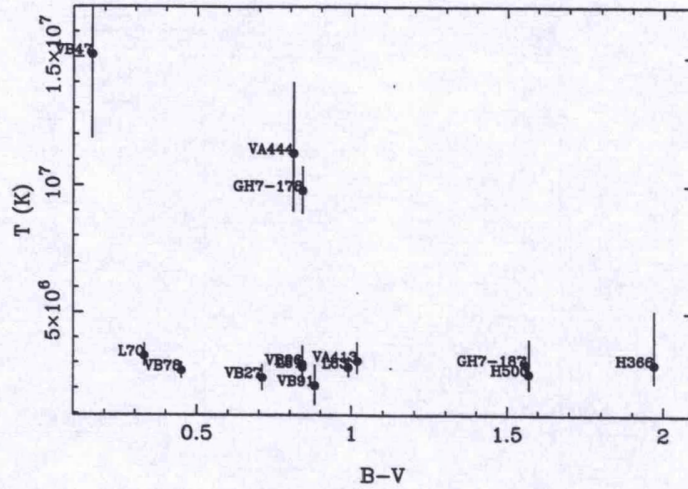


Figure 6.5: Temperature against B-V for the 1T fits. The error bars are 90% for one parameter of interest ($\delta\chi^2 = 2.706$).

There is no correlation between T and colour index (see Fig. 6.5); the poor counting statistics do not constrain the best-fit temperature well. A plot of EM against B-V shows evidence for a trend of decreasing EM with increase in redness (Fig. 6.6). As the photospheric temperature, mass and radius of a main-sequence star decreases, one may well expect the coronal volume to shrink proportionately. This effect mirrors the plot of L_X against m_V in Chapter 5 (Fig. 5.2).

A 1T fit can provide a useful description of data with poor counting statistics. The poor spectral resolution of the PSPC does not enable temperature differences between coronae to be measured with any confidence, the resultant 'best-fit' temperatures correspond to the peak sensitivity of the PSPC to a $\sim 10^6$ K plasma. There is no evidence that any of the stars in the whole sample with high signal-to-noise are satisfied by a 1T fit; all show evidence of multi-component coronae. The exception to this is GH7-178 which has some 1000 counts in the PHA spectrum. Intervening cool gas reduces the soft counts in the PHA spectrum, thus it is not surprising that a 1-T fit is adequate given that an additional component (N_H) is introduced to the model.

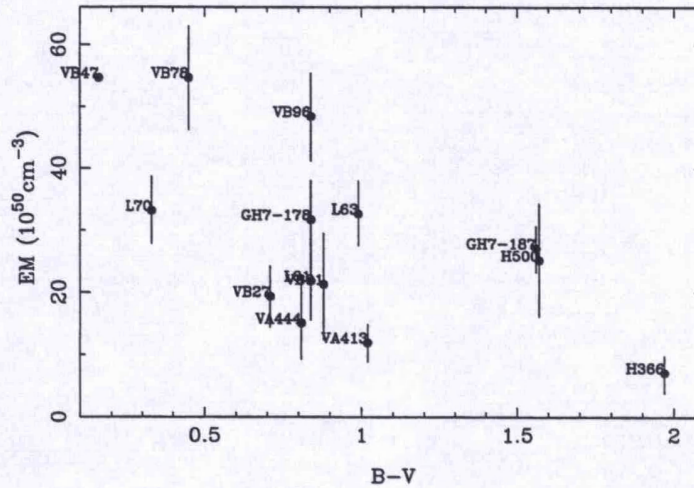


Figure 6.6: Best fit EM against B-V for the acceptable 1-T fits. The error bars are 90% for one parameter of interest ($\delta\chi^2 = 2.706$).

6.3.3 Two-temperature fits

46 spectra of 34 stars require (or prefer) a 2T fit. These stars are listed in Table 6.2, and the results of the fits are listed in Table 6.3. For 12 stars, there are two observations which require a 2T fit (VB 65 has been observed three times, one observation requires only a 1T fit). A comparison of the best-fit parameters (and their confidence regions) for the multiple observations shows that there is some evidence for variability in several of these stars. The best-fitting parameters (with 90% confidence error bars) are shown in Fig. 6.7. There is no clear case for temperature variations for any of these 12 stars. However, the normalisations (and therefore emission measures) for VA 334, VB 65, VB 40, and VB 50 do show very significant differences between the datasets. An examination of the lightcurves for these four systems shows strong flaring in one observation of VA 334 and one observation of VB 50. However, for VB 65 and VB 40, there is no suggestion of flaring activity. For VB 65, the two observations are separated by 6 months, while for VB 40 the observations are separated by only 2 days.

In order to investigate the *average* spectral characteristics of the Hyads, I have selected the longest observations of each star for inclusion in the sample, while the shorter observations have been discounted at this stage. The two flaring observations are excluded from the sample

Table 6.2: List of Hyades stars preferring two-temperature fits.

Index ¹	Name	Alt Name	V	B-V	Spectral Type	Counts	Seq
1	L30	VA135	10.00	1.10	K	1038	200442
2	L54	VA500	10.71	1.32	K8 V	1714	201368
3	H336	VA334	11.64	1.41	M0e	2767	200020
4	H336	VA334	11.64	1.41	M0e	2611	200777
5	H346	VA351	13.21	1.54	M2	1675	201369
6	H363*	VA366	12.30	1.45	M1	2483	200020
7	H363*	VA366	12.30	1.45	M1	1255	200777
8	H378	VA383	12.14	1.45	M2	800	200020
9	VB28	γ Tau	3.66	0.99	K0 III	1438	200775
10	VB30	VA182	5.59	0.28	F0 V	405	200441
11	VB30	VA182	5.59	0.28	F0 V	1994	200776
12	VB32	BD 18:624	†6.11	†0.37		813	201370
13	VB34	VA201	6.17	0.46	F6	2631	200776
14	VB36	HD27534	6.80	0.44	F6 V	658	201370
15	VB37	VA215	6.61	0.41	F4	586	200441
16	VB37	VA215	6.61	0.41	F4	2089	200776
17	VB40	VA249	6.99	0.56	F8 IV	5173	200020
18	VB40	VA249	6.99	0.56	F8 IV	1365	200441
19	VB46	VA279	9.12	0.86	K1 V	460	200020
20	VB49	H307	8.24	0.59	G0	919	200777
21	VB50	VA308	7.62	0.60	G1 V	10830	200020
22	VB50	VA308	7.62	0.60	G1 V	2224	200441
23	VB51	VA315	6.97	0.44	F6 V	440	201369
24	VB52	VA319	7.80	0.60	G1 V	912	201369
25	VB57	VA360	6.46	0.49	F7 V	3372	200777
26	VB59	VA384	7.49	0.54	F8 V	5092	200020
27	VB59	VA384	7.49	0.54	F8 V	2324	200777
28	VB63	VA389	8.06	0.63	G5 V	1992	201369
29	VB64	VA400	8.12	0.66	G6 V	1047	201369
30	VB65	VA446	7.42	0.54	F8 V	2298	200020
31	VB65	VA446	7.42	0.54	F8 V	377	200777
32	VB71	θ^1 Tau	3.85	0.96	K0 III	7145	200777
33	VB71	θ^1 Tau	3.85	0.96	K0 III	7640	201368
34	VB73	VA495	7.85	0.61	G1 V	1019	201369
35	VB75	VA511	6.59	0.53	F7 + G0	1216	201368
36	VB77	VA536	7.05	0.50	F7 V	1529	200443
37	VB80	VA569	5.58	0.32	F0 V	1170	201368
38	VB85	VA597	6.51	0.43	F5 V	2496	201368
39	VA211	H241	†14.08	†1.39		589	200441
40	VA211	H241	14.08	1.39		2023	200776
41	VA750*	H601	12.41	1.45		650	200444
42	VB141	71 Tau	4.48	0.25	F0 V	20650	200020
43	VB141	71 Tau	4.48	0.25	F0 V	9641	200777
44	GH7-190	VA288	13.34	1.55	M3e	3467	200020
45	GH7-190	VA288	13.34	1.55	M3e	734	200441
46	GH7-195 [†]	VA305	15.11	1.74		1490	200020

Notes: All photometry from Micela et al. (1988), except † from Stern, Schmitt & Kahabka (1995) and ‡ from SIMBAD. Spectral types from Micela et al. (1988). Suspected non-members are indicated with * and are classified from Chapter 5 (see Table 5.7). ¹ arbitrary running number.

Table 6.3: Best fit parameters to Hyades PHA spectra preferring two-temperature models

Index ¹	Name	χ^2_{ν}	log T _{cool} (K)			EM _{cool} (10 ⁵⁰ cm ⁻³)			log T _{hot} (K)			EM _{hot} (10 ⁵⁰ cm ⁻³)		
			ll	ul		ll	ul		ll	ul		ll	ul	
1	L30	0.66	6.25	6.06	6.39	31.2	21.0	46.7	6.98	6.88	7.11	44.5	33.2	66.3
2	L54	0.72	6.39	6.32	6.49	58.3	45.3	72.4	7.13	7.07	7.28	164.6	128.3	217.3
3	H336	0.81	6.39	6.29	6.47	38.5	27.8	47.7	7.01	6.96	7.07	54.5	46.2	66.3
4	H336	1.03	6.35	6.28	6.45	47.2	37.3	57.4	7.07	7.03	7.13	129.0	109.6	155.1
5	H346	0.63	6.34	6.27	6.41	55.9	44.5	69.7	6.97	6.90	7.04	62.9	50.6	75.7
6	H363	0.96	6.34	6.23	6.46	26.4	18.7	35.8	7.00	6.94	7.10	33.6	27.8	43.3
7	H363	0.56	6.26	6.10	6.37	25.4	16.9	34.8	6.94	6.88	7.00	44.0	36.8	54.7
8	H378	0.74	6.18	5.97	6.44	3.7	1.6	7.5	7.05	6.94	7.16	13.4	8.3	21.6
9	VB28	0.55	6.40	6.18	6.58	121.5	39.9	246.8	6.84	6.72	6.99	164.1	75.3	235.5
10	VB30	0.57	6.27	5.99	6.37	31.0	17.7	42.8	7.08	6.95	7.36	35.1	16.9	63.2
11	VB30	0.95	6.24	6.16	6.30	27.6	21.9	33.2	7.02	6.98	7.07	45.7	37.0	56.4
12	VB32	0.26	6.27	6.13	6.37	25.9	17.7	34.8	6.95	6.84	7.05	26.6	19.6	38.2
13	VB34	0.66	6.06	5.97	6.21	24.7	20.2	33.4	6.70	6.61	6.82	30.0	22.2	38.7
14	VB36	0.58	6.27	5.97	6.46	17.0	6.2	30.5	6.79	5.97	7.14	14.0	6.2	29.8
15	VB37	0.68	6.15	5.97	6.40	15.8	9.8	33.2	6.86	6.71	6.97	31.0	24.7	38.0
16	VB37	0.74	6.20	6.10	6.29	29.0	22.2	38.0	6.85	6.79	6.91	42.8	38.2	46.9
17	VB40	0.71	6.15	6.08	6.22	37.0	32.7	43.3	6.92	6.89	6.95	63.4	59.3	67.5
18	VB40	1.09	6.19	6.10	6.27	57.8	46.2	73.6	6.91	6.85	6.96	78.4	68.0	89.8
19	VB46	0.89	5.97	5.97	6.14	4.8	3.1	6.3	6.94	6.79	7.07	4.3	2.4	7.4
20	VB49	0.66	6.20	6.05	6.33	20.3	14.2	30.7	6.89	6.79	6.98	31.0	25.7	37.8
21	VB50	1.48	6.26	6.22	6.29	77.7	69.5	86.4	7.00	6.98	7.01	159.5	150.0	168.9
22	VB50	1.20	6.28	6.22	6.33	123.9	101.9	145.9	7.04	7.00	7.07	268.6	224.6	314.6
23	VB51	0.29	6.13	5.97	6.34	12.2	5.3	24.7	6.66	5.97	7.02	12.5	3.7	22.7
24	VB52	0.52	5.97	5.97	6.20	17.8	13.1	21.7	6.74	6.64	6.86	31.7	25.9	39.7
25	VB57	0.44	6.19	6.09	6.26	52.3	41.4	67.5	6.82	6.75	6.87	81.6	73.3	91.0
26	VB59	0.98	6.26	6.20	6.32	44.5	36.8	52.8	6.96	6.93	6.99	69.5	62.2	77.0
27	VB59	0.80	6.19	6.11	6.26	43.3	35.3	53.7	6.92	6.87	6.95	77.0	69.5	85.4
28	VB63	0.68	6.33	6.24	6.41	47.7	36.8	59.8	6.97	6.89	7.05	56.6	46.0	68.0
29	VB64	0.56	6.25	6.08	6.37	22.0	13.2	32.4	6.87	6.71	6.97	26.1	21.2	31.5
30	VB65	0.40	6.25	6.09	6.35	34.6	22.7	48.2	6.87	6.72	6.99	24.7	19.6	29.3
31	VB65	0.91	5.97	5.97	6.24	7.9	3.9	11.4	6.78	6.61	6.92	12.0	9.0	17.9
32	VB71	1.85	6.23	6.18	6.28	140.6	118.6	164.8	6.89	6.86	6.91	372.7	355.7	389.6
33	VB71	1.12	6.24	6.16	6.29	132.4	105.3	161.2	6.85	6.82	6.88	321.9	302.5	341.2
34	VB73	1.07	6.22	6.10	6.32	31.2	23.5	42.6	6.92	6.84	7.00	47.4	39.9	62.2
35	VB75	0.57	6.19	6.02	6.31	27.1	19.2	39.4	6.90	6.81	6.96	46.2	39.0	54.7
36	VB77	0.60	6.20	6.03	6.31	46.2	32.7	66.8	6.84	6.73	6.93	58.3	48.9	70.2
37	VB80	0.45	6.09	5.97	6.37	16.7	11.9	32.7	6.86	6.71	7.00	28.3	23.1	34.4
38	VB85	0.52	6.26	6.16	6.35	64.1	48.4	83.0	6.92	6.87	6.98	90.8	81.1	106.7
39	VA211	0.69	6.18	5.97	6.38	17.1	10.2	32.2	6.86	6.71	6.96	29.5	23.3	36.3
40	VA211	0.75	6.19	6.05	6.28	27.3	20.9	36.3	6.84	6.76	6.90	43.1	38.2	47.4
41	VA750	0.83	6.39	6.21	6.56	28.3	15.1	42.3	7.01	6.93	7.12	51.1	37.3	70.7
42	VB141	2.26	6.31	6.31	6.31	204.7	204.7	204.7	7.00	7.00	7.00	379.9	379.9	379.9
43	VB141	0.85	6.34	6.31	6.37	218.8	201.3	237.9	7.02	7.00	7.04	421.1	389.6	455.0
44	GH7-190	0.98	6.22	6.13	6.30	24.2	19.5	31.0	6.99	6.95	7.03	41.6	35.8	48.9
45	GH7-190	0.55	6.20	6.00	6.32	34.4	24.4	50.6	6.93	6.84	7.00	51.1	41.6	66.1
46	GH7-195	0.67	6.40	6.21	6.52	14.9	9.3	19.7	7.11	6.96	7.77	19.4	11.9	36.8

¹ from Table 6.2.

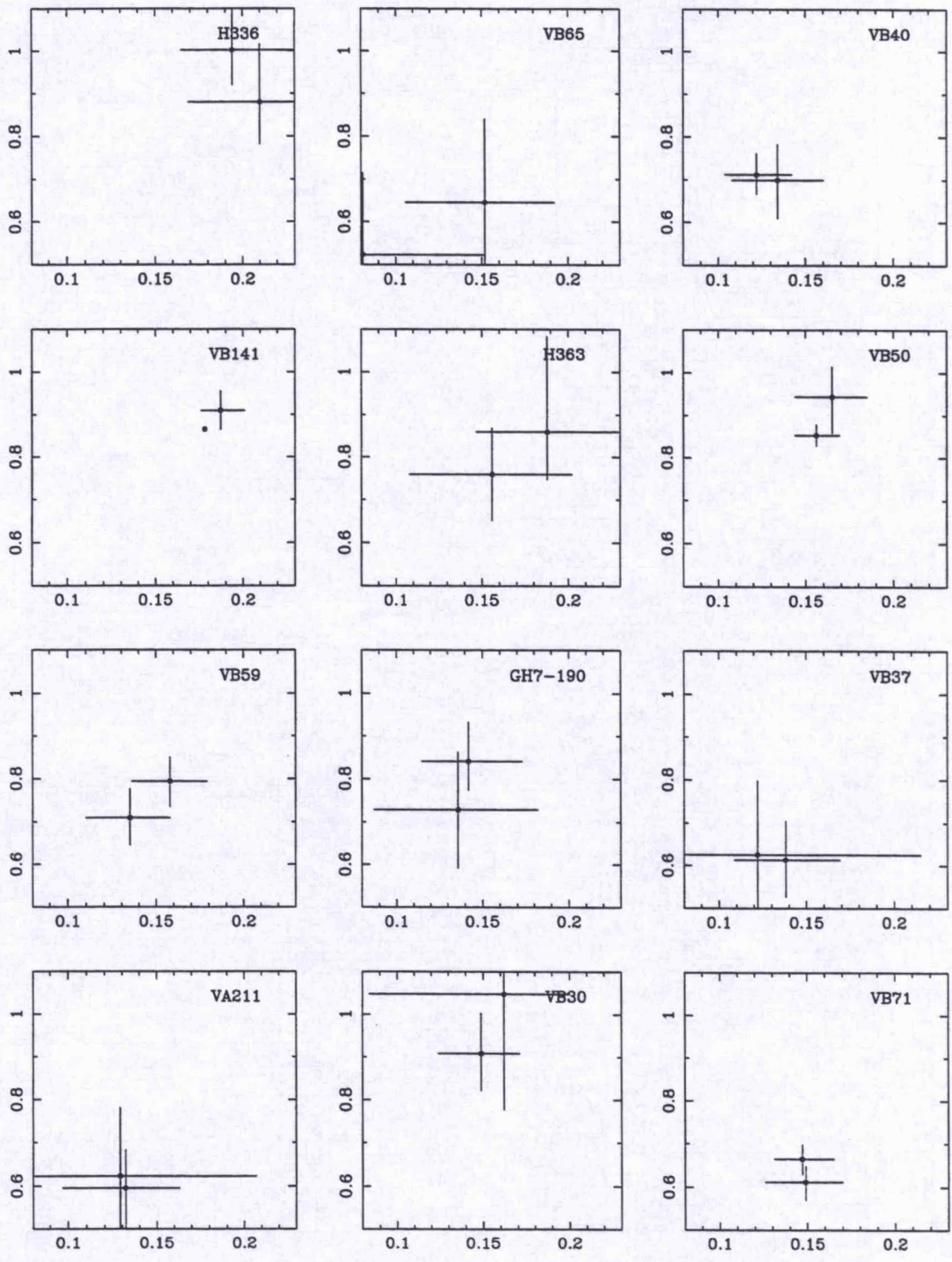


Figure 6.7: T_{hot} (keV) against T_{cool} (keV) for Hyads with two observations.

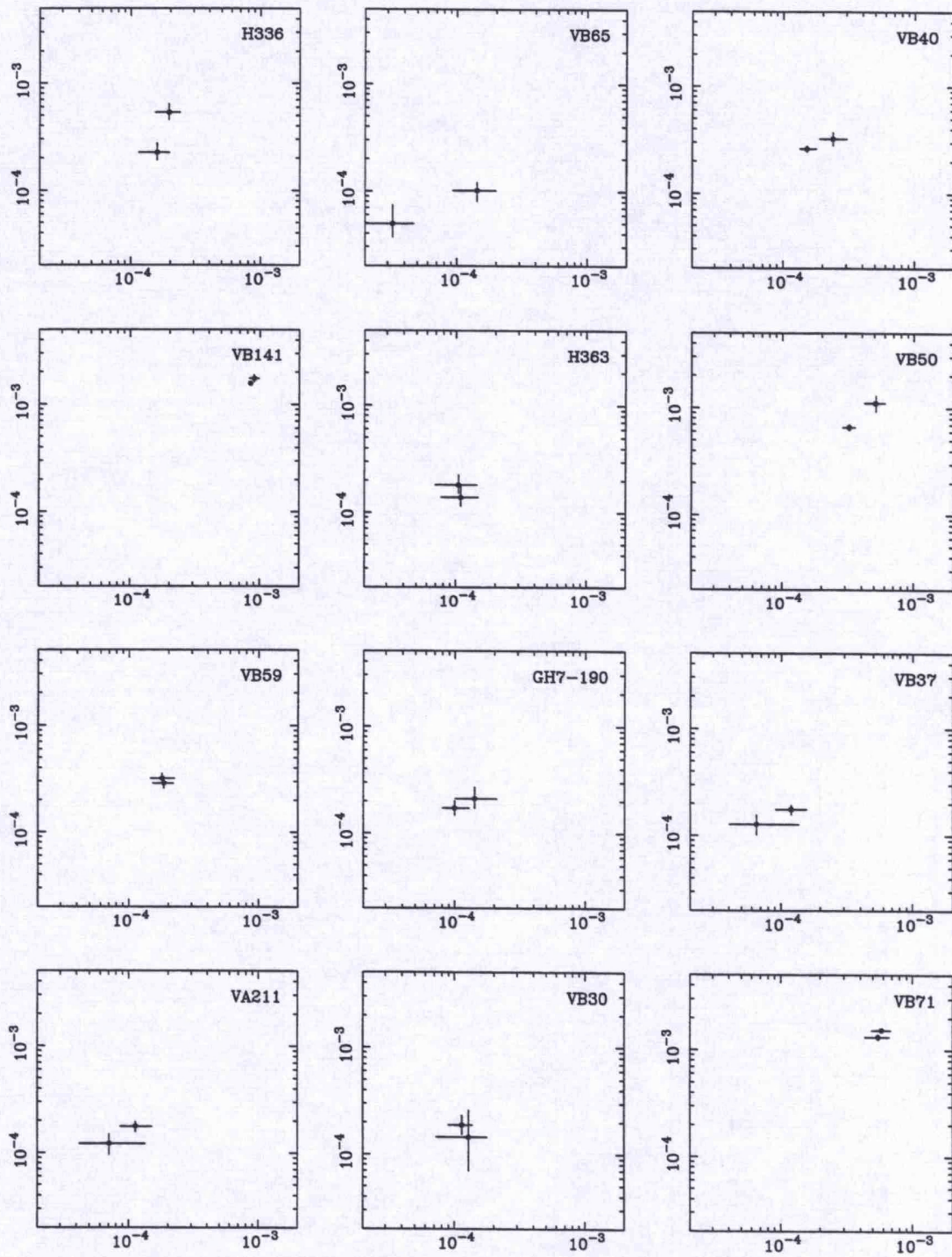


Figure 6.8: EM_{hot} against EM_{cool} for Hyads with two observations.

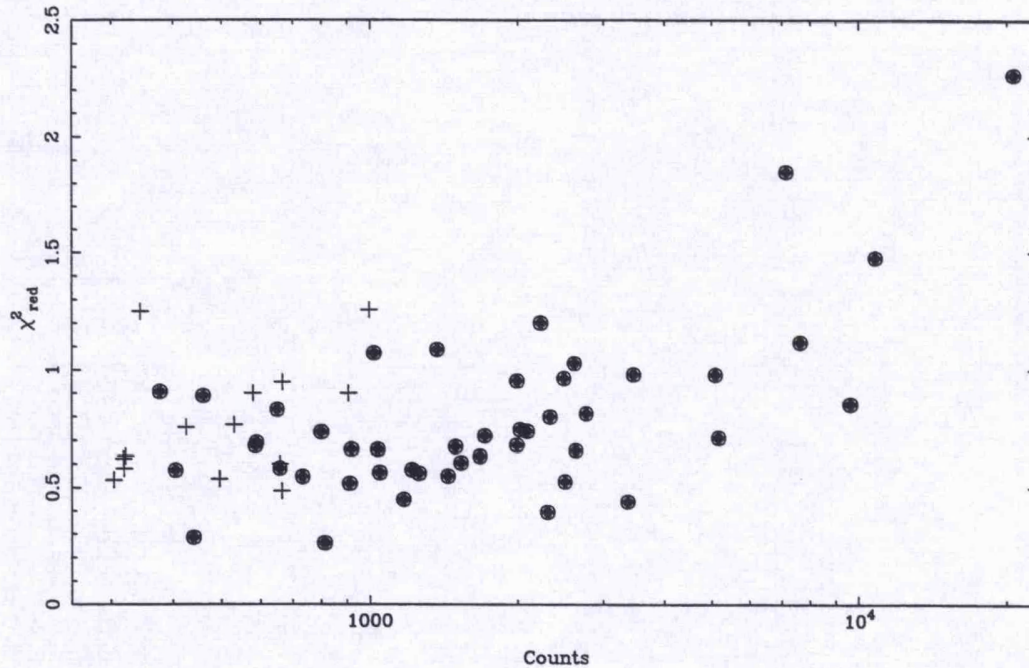


Figure 6.9: χ^2_{red} for 1T and 2T fits vs. number of counts in the PSPC spectrum for all stars with ≥ 300 counts. 1T fits are marked with a cross (+). 2T fits are marked with a filled circle (•).

and are deferred for a more detailed analysis in Section 6.3.4. Thus the sample now contains 34 observations of 34 stars, believed to represent the average coronal properties of the X-ray-brightest Hyades members within this survey. Of course, great caution must be exercised when I attempt to describe the average properties of a star. If the sun is a typical example, we must expect to observe some coronal variation on a wide range of timescales. Nevertheless, it is felt that the relatively large sample defined here will be representative.

In Fig. 6.9 χ^2_{red} is plotted against counts for all acceptable 1T fits and for the remaining 34 2T fits. This figure shows that a 2T model is a good description of the data for stars with ~ 1000 – 7000 counts in their PHA spectra. Above this, the increase in χ^2_{red} could suggest that the 2T model then becomes inadequate. However, while there is still significant uncertainty in the calibration of the PSPC detector response matrix, it is not possible to rule out small systematic errors as the cause of the increase in χ^2 ; the systematic errors showing up as the counting statistics improve.

These results show that a 2T model is a better description of the ROSAT data, but to what extent is it a physical model? Schmitt et al. (1990a) find a similar effect — that stars with > 1000 counts in their *Einstein* data (generally) require a 2T model. Both Schmitt et al. (1987) and Pasquini et al. (1989) have shown that two-temperature fits do not necessarily imply a bimodal emission measure distribution and may be obtained for a continuous emission measure distribution. The PSPC detector energy response (see Fig. 2.9 in Section 2.5) is strongly bimodal, with peak sensitivities at ~ 0.1 keV and ~ 0.5 keV. This, together with the modest energy resolution, tends to favour a 2T description of the data. It may be more appropriate to view the best fit temperatures as upper and lower ‘bounds’ of the temperature range to which the PSPC is sensitive, or *effective temperatures*. Thus the emission measures (EM) at these temperatures will tell us more about conditions in the stellar coronae than the temperatures themselves, where $EM = \int n_e^2 dV \simeq n_e^2 V$. Unfortunately, the modest spectral resolution of the PSPC mean that these emission measures (and temperatures) are badly constrained.

With this in mind, I now proceed to examine the parameter space inhabited by the best-fit models. Strictly, one should use confidence contours of constant χ^2 when attempting to compare pairs of model parameters. However, to first approximation, the 90% confidence error ranges for one parameter of interest ($\delta\chi^2 = 2.706$) are a good representation of the uncertainty in the best-fit parameters. With a large sample such as this, I am mainly interested in significant trends.

In Fig. 6.10, T vs. EM is plotted for both hot and cool components to see both the ranges of these parameters and the differences between the components. As with the 1T fits, I find that there is little evidence for systematic temperature differences between the stars. The two temperatures are separated into distinct bands at $\sim 2 \times 10^6$ K and 9×10^6 K. These temperatures are consistent with the results of modelling of the *Einstein* data (Schmitt et al. 1990a). They are also similar to, but lie slightly below, ROSAT results for RS CVn systems (Dempsey et al. 1993b), W UMa systems (McGale, Pye & Hodgkin 1995) and Pleiades cluster members (Gagné, Caillault & Stauffer 1995). Schmitt et al. (1990a) reported a correlation between the high and low temperature components, in the sense that as T_{cool} increased, so did T_{hot} . In Fig. 6.11 I see some evidence for a similar effect; again with the problem of poor parameter constraint. Whether this trend is an artefact of the fitting procedure or a real increase in the coronal temperature is not clear.

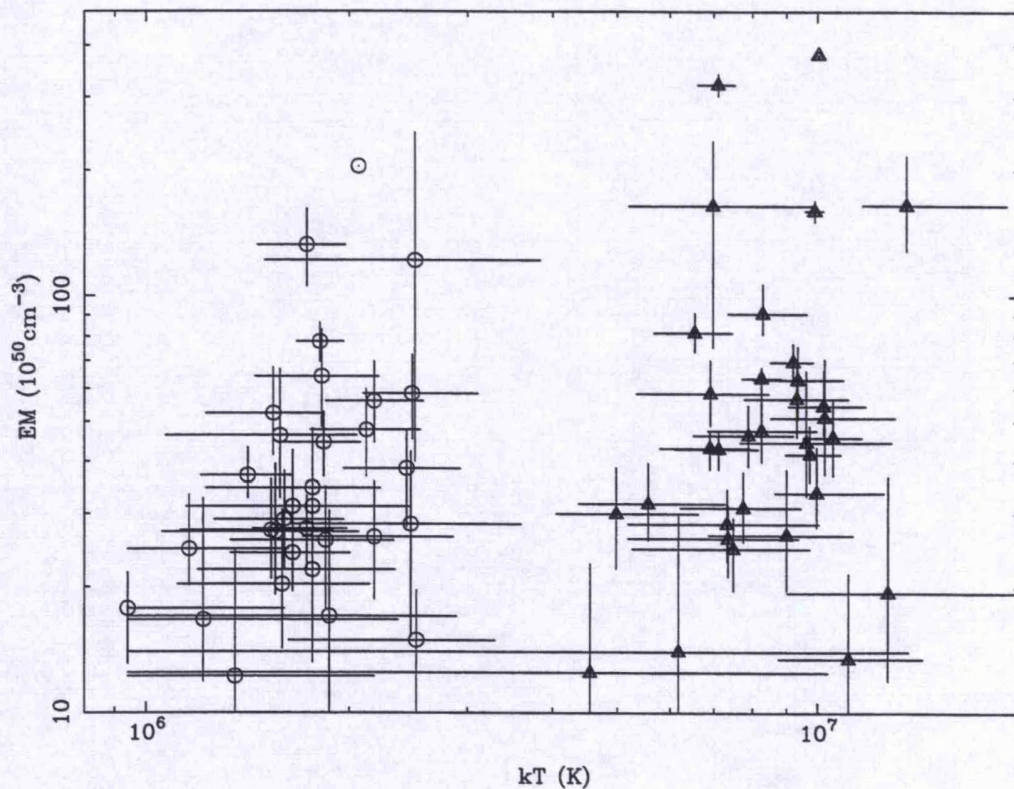


Figure 6.10: Temperature (K) against emission measure (cm^{-3}) for low-T (circles) and high-T RS components (triangles). The error bars are the 90% confidence errors for 1 parameter of interest ($\delta\chi^2 = 2.706$), equivalent to $\sim 75\%$ confidence errors for 2 parameters of interest.

The emission measures span some $10^{51} - 4 \times 10^{52} \text{cm}^{-3}$ for both hot and cool components. In Fig. 6.12 EM_{hot} is plotted against EM_{cool} for the sample. I see a very strong correlation, indicating a constant emission measure ratio for all the Hyads with few exceptions. A line of $EM_{\text{hot}} = EM_{\text{cool}}$ is shown together with the best fit line. The slope of this line is 1.96, i.e. $EM_{\text{hot}} \approx 2EM_{\text{cool}}$. Gagné, Caillault & Stauffer (1995) find similar values for their Pleiades composite spectra, with $EM_{\text{hot}}/EM_{\text{cool}} \sim 1.95$ for dK and dM stars. They further subdivide their samples into fast and slow rotators, showing that the fast rotators have consistently higher emission measure ratios. For RS CVn systems, the results of Dempsey et al. (1993b) indicate that almost all RS CVn systems have emission measure ratios greater than 2. Examining their table of spectral fits indicates an average $EM_{\text{hot}}/EM_{\text{cool}} \sim 4$, although values larger than 10 are recorded. McGale, Pye & Hodgkin (1995) find $EM_{\text{hot}}/EM_{\text{cool}} < 2$ for all W UMa systems in their sample (except during a period of enhanced activity in VW Cep when the ratio reaches

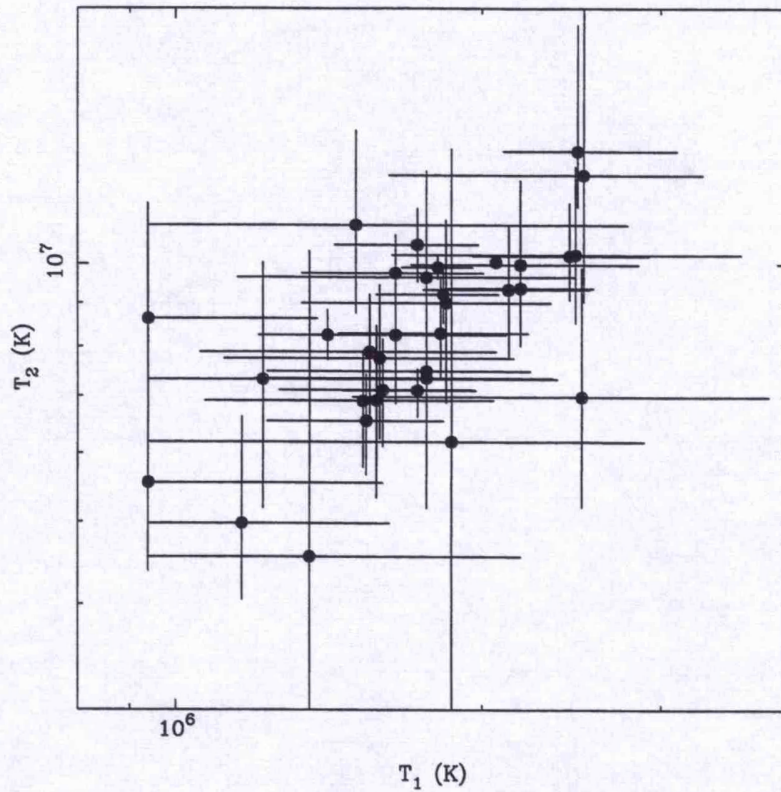


Figure 6.11: T_{hot} (K) against T_{cool} (K). The error bars are the 90% confidence errors for 1 parameter of interest ($\delta\chi^2 = 2.706$), equivalent to $\sim 75\%$ confidence errors for 2 parameters of interest.

2.2).

6.3.4 Spectral variability

For the two flares observed in VB 50 and VA 334 the PHA spectra of the stars have been time-resolved into 'flare' and 'post-flare' sections. The lightcurves for these stars showing the time-divisions are plotted in Figs 6.13 and 6.14. Unfortunately the stars are not bright enough in X-rays to enable anything other than a very coarse time resolution. The duration of the flare in VA 334 is some 40,000 seconds (~ 12 hours), while the flare in VB 50 lasts only $\sim 10,000$ seconds (~ 3 hours). For both flares it is difficult to accurately quantify the shape and duration of the impulsive and decay phases as the sampling is poor and the count rates relatively low. Similarly it is difficult to judge the exact maximum of the flare, especially for VA 334 which

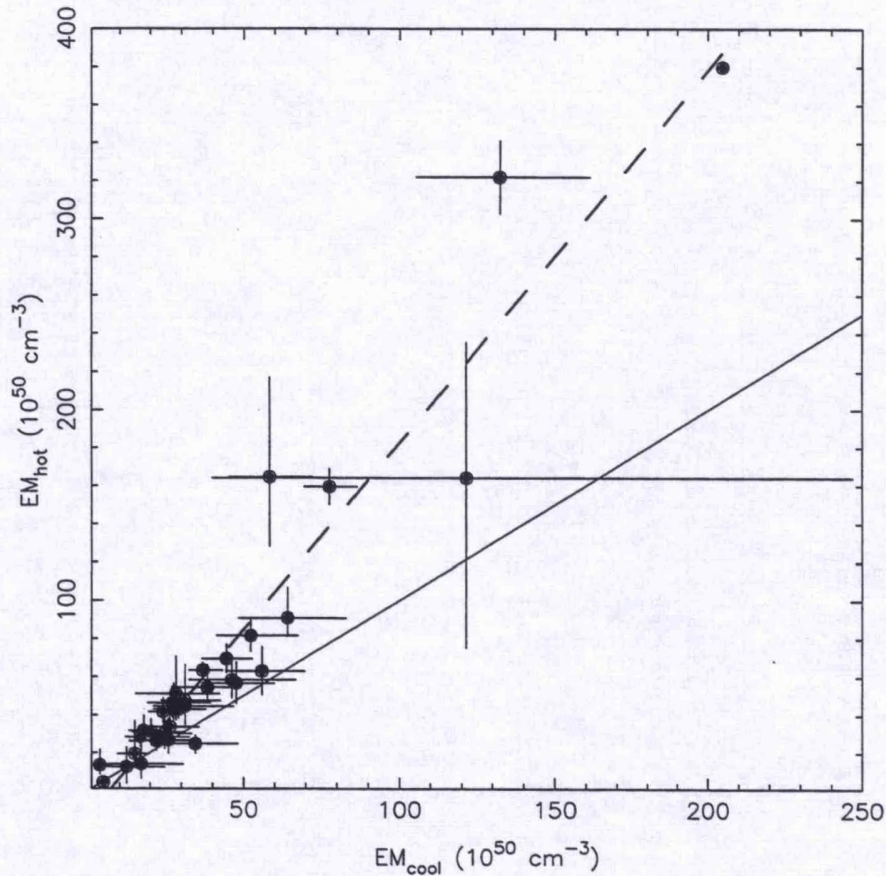


Figure 6.12: $EM_{\text{hot}}(\text{cm}^{-3})$ against $EM_{\text{cool}}(\text{cm}^{-3})$. The error bars are the 90% errors for 1 parameter of interest ($\delta\chi^2 = 2.706$), equivalent to $\sim 75\%$ errors for 2 parameters of interest. The solid line represents $EM_{\text{hot}} = EM_{\text{cool}}$. The dashed line is the best-fit regression to the data (ignoring the errors) and has a slope of 1.96.

shows significant fluctuations in the lightcurve. It is necessary to use such large time bins to overcome the variations introduced by the space-craft wobble (see Section 2.5). From the lightcurves, I estimate a factor > 2 increase in count-rate (and therefore luminosity) for VA 334, while the count-rate for VB 50 increases by roughly a factor three.

2T models were fitted for both stars. Figs 6.15 and 6.16 show the 68% and 90% confidence χ^2 contours in (kT_1, kT_2) space for VB 50 and VA 334 in 'quiescence' and 'flaring'. For VA 334 there is not only a significant increase in the emission measures of both cool (factor 1.5) and hot (factor 2.4) components, but also a significant increase in the temperature of the hot component. The temperature drops from 1.1 keV (1.3×10^7 K) during the flare to 0.9 keV (1.0×10^7 K) after

VB 50

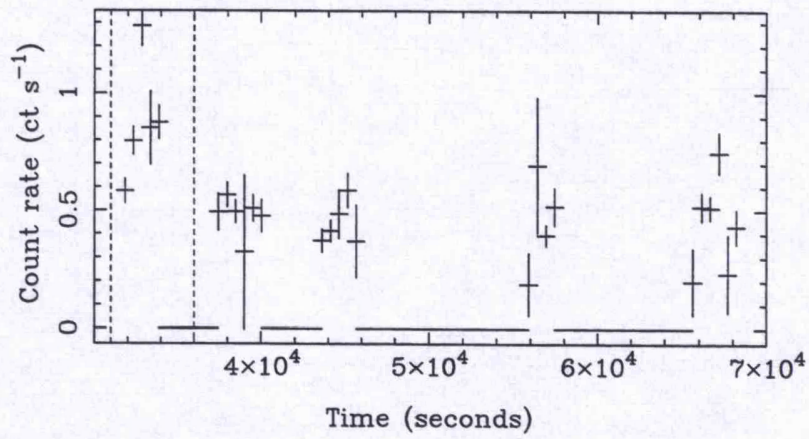


Figure 6.13: Lightcurve for VB 50. The region enclosed by dashed lines is designated 'flare' for the purposes of spectral fitting, while the remainder is 'quiescent'.

VA 334

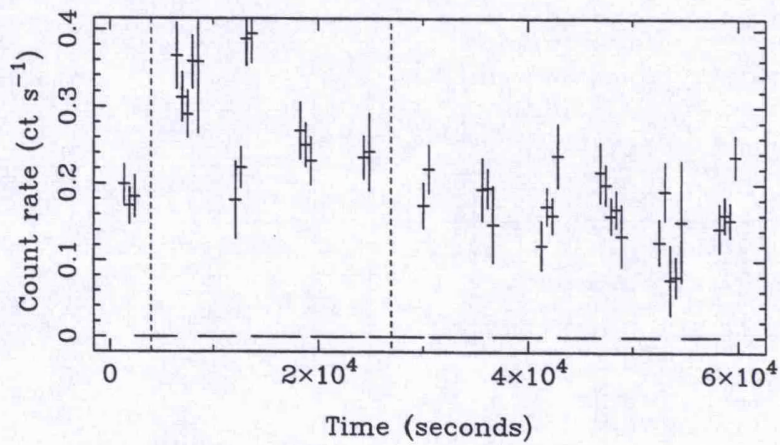


Figure 6.14: Lightcurve for VA 334. The region enclosed by dashed lines is designated 'flare' for the purposes of spectral fitting, while the remainder is 'quiescent'.

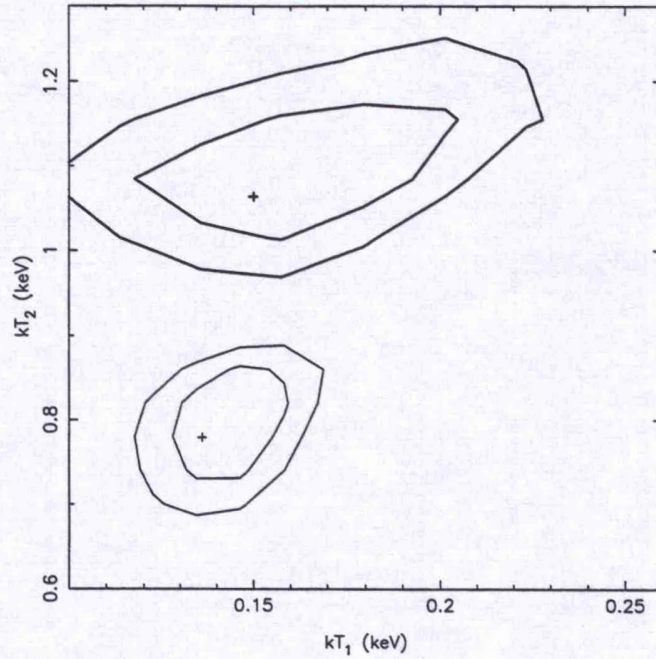


Figure 6.15: Confidence contours for the 2T fit to VB 50 during both flaring and quiescent phases. Contour lines correspond to confidence levels of 70% and 90% for two parameters of interest ($\delta\chi^2 = 2.3, 4.6$). The upper (and bolder) contours represent the flare.

the flare, while the best fit temperature of the cool component shows no change. The emission measure ratio decreases from $EM_{\text{hot}}/EM_{\text{cool}} = 3.4$ to 2.1.

For VB 50 also there is a very striking increase in the temperature of the hot component during the flare with a best fit temperature of 1.1 keV (1.3×10^7 K) decreasing to 0.8 keV (9.3×10^6 K). The EM of the hot component is some 6 times greater during the flare than afterwards, decreasing from $6.3 \times 10^{52} \text{ cm}^{-3}$ to $1.2 \times 10^{52} \text{ cm}^{-3}$. There is no noticeable change in the EM of the cool component, nor is there any discernable change in its temperature. The emission measure ratio is 1.5 in quiescence and 6.8 during the flare.

6.4 Discussion

It has been shown that an isothermal description of the coronae of the Hyades cluster members is not satisfactory so long as there are sufficient (i.e. greater than ~ 1000) counts in their spectra.

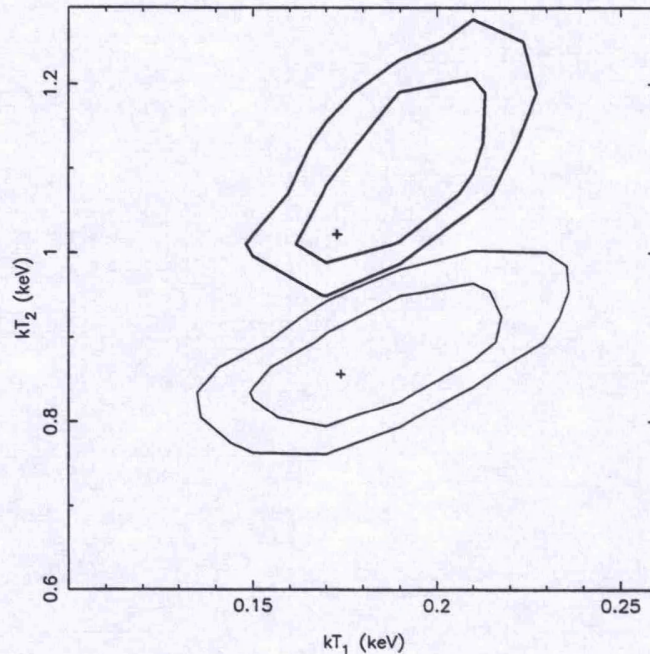


Figure 6.16: Confidence contours for the 2T fit to VA 334 during both flaring and quiescent phases. Contour lines correspond to confidence levels of 70% and 90% for two parameters of interest ($\delta\chi^2 = 2.3, 4.6$). The upper (and bolder) contours represent the flare.

I have shown that a two-temperature fit is adequate for every star in this survey. Whether the coronae are better described by a continuous emission measure distribution is open for testing. The results of the *Einstein* coronal temperatures survey (Schmitt et al. 1990a) suggest that such a model would give equally good fits as the 2T model used here. However, I cannot expect the PSPC to supply an answer to this problem where higher resolution instruments, such as the *Einstein* SSS and OGS, have not succeeded. However Dempsey et al. (1993b) claim that 2T fits reproduce the observations better than single or continuous temperature models in RS CVn systems.

I have found no evidence to support the results of Schmitt et al. (1990a) and Stern et al. (1994), that M dwarfs tend towards hotter coronae than earlier spectral types. In the Pleiades, Gagné, Caillault & Stauffer (1995), find a trend for increasing coronal temperature with increasing rotation rate and for stars of later spectral type. The lack of rotational period information for most of the late dK and dM stars (due to $v \sin i < 10 \text{ km s}^{-1}$ in many cases) prohibits such a study in the Hyades at present. This however must be a key step if we are to understand coronal

temperatures.

6.4.1 Cluster membership

These data have shown that the PSPC is a useful tool when considering cluster membership in the Hyades. GH7-178 has been confirmed as a non-member because of the deficit of soft counts in the X-ray spectrum, consistent with the star lying behind the cluster (although intrinsic absorption cannot be ruled out). VA 444 also shows very similar features in the PSPC spectrum, supporting the case for non-membership based on optical photometry. VB 47 is harder to explain; the spectrum indicates evidence of possible absorption. It may simply be that the large off-axis angle of the observation is the cause of a misidentification – i.e. VB 47 is not the source of the X-rays. An on-axis pointing with the HRI could resolve this.

6.4.2 The giants

The four Hyades giants, VB 71 (θ^1 Tau), VB 28 (γ Tau), VB 41 (δ Tau) and VB 70 (ϵ Tau), constitute a homogeneous (if small) sample of evolved stars. They share similar spectral types (K0III), effective temperatures, gravities, masses, metallicities and rotational velocities (Collura et al. 1993 and references therein). IUE observations of the four giants (Baliunas, Hartmann & Dupree 1983) showed a spread in chromospheric and transition region line fluxes. *Einstein* X-ray observations of the cluster (Stern et al. 1981, Micela et al. 1988) detected θ^1 Tau, γ Tau and δ Tau, while ϵ Tau was not observed. Although the first three stars are known to be spectroscopic binaries, Baliunas et al. (1983) and Micela et al. (1988) argued that the observed UV and X-ray emission originates from the K0III primaries, and not from a companion. More recently, Stern et al. (1995), reported the detection of all Hyades giants in the ROSAT all-sky survey and suggested that long term variability may be partly responsible for the observed spread in X-ray luminosity.

The hardness ratios derived here clearly show that VB 28 and VB 71 have ‘harder’ spectra than almost all of the dwarfs in the cluster, supporting the view that the X-ray emission does not originate from an unseen main-sequence companion. The two-temperature spectral fits do not distinguish the giants from the dwarfs so well.

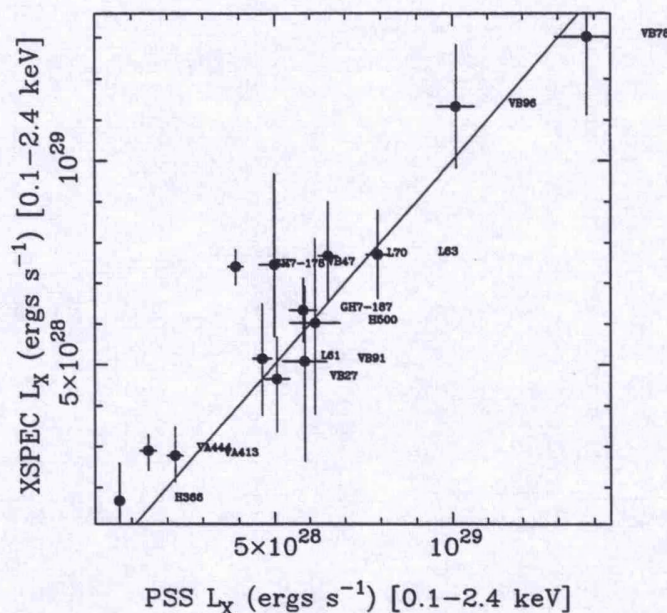


Figure 6.17: X-ray luminosity derived from 1T fit against X-ray luminosity derived from PSS, assuming an isothermal 3×10^6 K plasma. Note that the scale is linear in both axes.

6.4.3 Effect of a multi-temperature model on the derived X-ray luminosity

An important question arises from the rejection of an isothermal model for the Hyades coronae. How is the calculated luminosity affected? In Chapters 4 and 5 X-ray luminosities were derived from detector count-rates using conversion factors assuming a one-temperature spectral model. In Figs 6.17 and 6.18 I plot the X-ray luminosities derived from the best fit 1-T and 2-T models against the luminosity obtained in Chapter 5. Where there are discrepancies for the 1-T models, I may assume that these have come from deviations in the best-fit temperature from the single temperature (3×10^6 K) assumed for all stars in Chapter 5. For the 2-T models one can see that the naive assumption above systematically underestimates the total luminosity in the energy band 0.1–2.4 keV. This is however a small effect, being of the order of 10% on average. The most significant deviation is for H363, a star already classified as a non-member, which has a factor 3 higher L_x derived from the 2T model than that derived with the simple 1T assumption. Inspection of the PSPC image shows that an additional nearby source has been included in the spectral extraction region. A more careful extraction by hand does not significantly affect the best-fit temperatures. I may be confident, then, that the luminosities obtained in Chapter 5 are

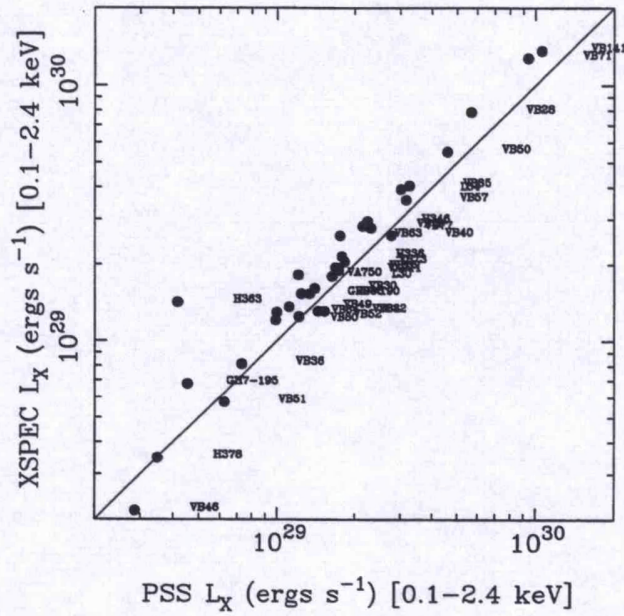


Figure 6.18: X-ray luminosity derived from 2T fit against X-ray luminosity derived from PSS count rates, assuming an isothermal 3×10^6 K plasma. Note that the scale is logarithmic in both axes.

not significantly affected by my assumption of an isothermal corona at the same temperature for all stars.

Chapter 7

Concluding remarks and future prospects

This thesis comprises a number of related projects which have all arisen from the ROSAT mission. The general theme revolves around the X-ray and EUV characteristics of late-type stars, although this did not prevent my involvement with the discovery of the white dwarf responsible for the strong WFC source originally identified with KW Aur. In Chapter 3 I summarised the steps taken to identify the true source of the EUV radiation with the hot ($T \sim 46,000$ K) DA white dwarf companion to HD 33959C (2RE J0515+32). Barstow et al. (1994) discuss this and eight other binary systems containing DA white dwarfs discovered in the WFC all-sky survey (to date) and show that these pairs of objects are far more likely to be physically linked than they are to be line-of-sight coincidences. These systems are important for evolutionary theories. Barstow et al. (1994) point out that the companion late-type stars show unusually high coronal activity given their relative old age. The implication is that these are stars whose rotational velocities have been reinforced by tidal interactions with what were once more massive late-type companions. An obvious suggestion is that they may once have been RS CVn-type or similar systems whose primaries have now evolved into white dwarfs. Even without such speculation, such binaries are important for the determination of more accurate measurements of mass, radius and distance than is possible with isolated objects. Thus the discovery of HD 33959C and objects like it has triggered a number of major astronomical programmes.

In Chapter 4 I discussed the WFC all-sky survey results for all known late-type stars within 25 parsecs of the Sun. The solar neighbourhood is rich in the diversity of objects therein; their

masses, ages, kinematics, metallicities and binarity are representative of the galaxy as a whole (with the caveat that 'rare' objects, such as RS CVn systems, W UMa systems etc. are poorly sampled). I have derived the first ever EUV luminosity functions for such a sample. They are also the first truly unbiased coronal luminosity functions, less prone to selection effects and therefore more useful than, for example, the *Einstein* X-ray luminosity functions presented by Rosner, Golub & Vaiana (1985). This is evident when the number of dM star WFC detections is compared with pre-launch predictions based on the *Einstein* luminosity functions. I have further shown that unresolved (i.e. spectroscopic) binaries have significantly higher EUV luminosities than single stars. By implication, such objects maintain higher rotation velocities through tidal interaction in a similar way to close binaries such as RS CVn systems. The real breakthrough must come from the PSPC all-sky survey, however, where far more accurate and deeper luminosity functions can be constructed for the solar neighbourhood. Fleming et al. (1995) have used PSPC observations of all known K-M stars within 7 parsecs of the Sun to show that there is no decrease in coronal heating efficiency (as measured by L_X/L_{bol}) among the lowest mass, presumably fully-convective late-M dwarfs (but see also Hodgkin, Jameson & Steele 1995 for a discussion of the Pleiades). Schmitt et al. (1995) construct the luminosity function for this same sample down to $\log L_X = 25.66$. Additionally there is the prospect of examining the temporal behaviour of these stars to an unprecedented level. Not only on timescales of hours-days (throughout the survey itself), but also by comparisons to the decade older *Einstein* stellar surveys. Of course the ROSAT surveys also stand as a baseline for comparison for all future surveys. Many of the closest and brightest objects are also in reach of the spectrometers on EUVE. It is only with such high spectral resolution that we will be able to resolve individual lines and really start to tie down the temperature structure and energy balance of stellar coronae.

In Chapters 5 and 6 I presented a deep PSPC survey of the Hyades, comprising 11 overlapping pointings. In Chapter 5 the emphasis was on the properties of the dK and dM stars, as earlier spectral types have been well sampled by *Einstein* (Micela et al. 1988) and the ROSAT PSPC all-sky survey (Stern et al. 1992; Stern, Schmitt & Kahabka 1995). Luminosity functions were constructed down to $L_X \sim 5 \times 10^{27} \text{ erg s}^{-1}$ (0.1–2.4 keV). The Hyades dK binaries were found to have significantly higher L_X than the dK single stars. However, all these binaries have relatively long periods ($\gtrsim 1 \text{ yr}$), and hence the high L_X levels cannot be attributed to the enhanced activity expected in short-period ($\lesssim \text{few days}$) systems.

In Chapter 6 I investigated the spectra of the more luminous Hyads, through their hardness ratios and 1-temperature (1T) and 2-temperature (2T) fits to the data. Hardness ratios were useful for the identification of objects with very unusual spectral signatures. Three stars in particular showed evidence for excess absorption in their spectra, supported by 1T fits, indicating that they are located at some distance behind the Hyades cluster. The two giants with sufficient counts (VB 71= θ^1 Tau, VB 28= γ Tau) also stood out with higher hardness ratios than the main-sequence stars. The white dwarf EG 37 is also easily identified with a hardness ratio close to -1 . Whether a 1T or 2T fit is preferred seems to be a sole function of the number of counts in the spectrum. 2T fits to the PSPC data do not permit detection of subtle temperature differences between stars due to the dominant bimodal energy response of the detector. However changes in temperatures and emission measures were found during two flaring episodes in VB 50 and VA 334. The potential to extract more information from these spectra still remains. Following Gagné, Caillault & Stauffer (1995) we may co-add spectra according to spectral type and rotation velocity to reduce confidence contours around the best fit parameters. This of course requires follow-up optical observations to determine $v \sin i$ measurements for many Hyads, in particular at the low-mass end of the main-sequence (several collaborators are doing just this). Also, one could consider using a differential emission measure model (either discrete or continuous) to parameterise the spectra. A few trials suggest that the same problems of parameter constraint as seen in the 2T fits appear. Again co-adding of spectra is probably required for all but the brightest sources. Collaborators in Palermo are currently fitting loop models to this dataset in an attempt to obtain a more physical description of stellar coronae. Variability analysis is underway at present (Pye et al. 1995a). Additionally more could be made of recent advances in the identification of faint cluster members. Reid et al. (1992, 1993) have presented a proper motion survey from Schmidt plates down to $V=19$ in the Hyades. These objects should be added to the optical catalogues used in this thesis.

By combining the X-ray and optical datasets now available for the field, open clusters (α Per, the Pleiades, Praesepe, U Ma and the Hyades) and star-forming regions (Orion, ρ Ophiuchi, Chamaeleon etc), we should now be in a better position to isolate those parameters which govern the levels of coronal and chromospheric emission in late-type stars. A first step will be to complete period measurements for all cluster members. Thus may the relationships between mass, gravity, metallicity, rotation, binarity, chromospheric activity and X-ray emission be un-

derstood. Observations of other open clusters which are scheduled or already completed include pointings in NGC6633, NGC6940, NGC2682 (M67), NGC2422, IC4651, NGC752, NGC2516, IC2602 (Randich et al.1995), NGC6475 (Jeffries et al.1994), NGC2264 (Patten et al.1994), NGC2451, IC2391 (Patten & Simon 1993), Coma, IC4665. Many of these require considerable effort and telescope time for the identification and classification of members.

Future Missions

To fully pin down the temperature structure and energy balance in stellar coronae we must await the next generation of X-ray missions. *ASCA* has already shown evidence for non-solar abundances in Algol (Antunes, Nagase & White 1994), especially in the Fe K (6.7 keV) line, found to be one-third the intensity predicted by both the Raymond & Smith (1978) and Mewe-Kaastra (Mewe, Gronenschild & van den Oord 1985; Kaastra 1992) models. Another interpretation is that the models are deficient (e.g. they assume ionization equilibrium). Spectra of β Ceti and π^1 U Ma (Drake et al.1994) and Castor AB and YY Gem (Gotthelf et al.1994) show similar effects.

With EUVE we see a glimpse of what may be to come. Analysis of the EUVE spectrum of Capella indicates a DEM which is very different from the solar case (Dupree et al.1993). It is only by identification of line-blends and individual lines that we may derive independent temperature and density measurements for stellar coronae. These lines also provide powerful diagnostics of ionization equilibrium, mass motions and element abundances. This will prove a very testing time for plasma models. To close, I briefly summarise some of the more important up and coming X-ray missions below.

- *JET-X* - 1996. The JET-X instrument on board *SPECTRUM-X-GAMMA* will have similar sensitivity and angular resolution to the ROSAT PSPC, but with superior energy resolution and energy range provided by the CCD detectors ($E/\Delta E = 10-70$ in the range 0.2-10 keV). Thus, we may start to address the spectral characteristics of large numbers of stars in much more detail than has been achievable with the PSPC.
- *AXAF* - 1999. With an energy range of 0.1-9.0 keV, angular resolution of 0.5 arcsecs and a sensitivity of 10^{-16} erg cm^{-2} s^{-1} , *AXAF* will add significantly to our knowledge of

faint sources and crowded fields. Thus more distant open clusters may be studied, and deeper surveys in those already tackled by ROSAT can be performed. For example, in the Pleiades, no stars are detected in the PSPC with masses below $0.1 M_{\odot}$ (Hodgkin, Jameson & Steele 1995). The authors argue that coronal volume shrinks with decreasing mass and, therefore, L_X decreases below the sensitivity limit of the survey. *AXAF* will be able to search for coronae down to the hydrogen burning limit and below, and at the same time examine the effects of the onset of full convection on coronal heating efficiency in a co-eval sample.

- *XMM-1999*. This satellite is one of the four 'Cornerstone' projects in the ESA Long-Term Programme for Space Science. It will comprise 3 mirror modules with a CCD array at the prime focus of each, while 2 reflection-grating spectrometers are fitted to two of the telescopes. In addition the payload includes an optical monitor. The CCD's provide high sensitivity (limiting sensitivity of 2×10^{-15} erg cm⁻² s⁻¹) over a wide bandwidth (0.1–10 keV) with broadband spectroscopy ($E/\Delta E = 5-60$) and medium spatial resolution (< 30 arcmin HEW). The spectrometers allow medium resolution spectroscopy between 0.1–3 keV ($E/\Delta E > 250$ at 0.5 keV). Simulations show that in a 50,000 second exposure of Capella, the reflection gratings will clearly resolve individual lines, where the *EXOSAT* TGS could see only line blends. For the first time, the CCDs will allow time-resolved modest-resolution spectroscopy; a 1000 second exposure of Algol would contain some 55,000 counts.

Appendix A

ROSAT EUV-detected nearby stars

Table A1 lists all the CNS3 stars (irrespective of distance or spectral-type) that have met our detection criteria in the WFC all-sky survey data. The table also indicates our division of the EUV fluxes where there are two or more CNS3 stars close ($\lesssim 8$ arcmin) together (see Section 4.3.4).

Table A.1 ROSAT EUV-detected nearby stars.

Name	Cmpnt	Dist	Spectral Type	m _v	B-V	α_{J2000}	δ_{J2000}	SB	S1 (ct/s)	S1 (11)	ul (12)	(ct/s)	S2 (14)	ul (15)	S1	S2	Det	Note	
(1)	(2)	(3)	(4)	(5)	(6)	(7)	(8)	(9)	(10)	(11)	(12)	(13)	(14)	(15)	(16)	(17)	(18)	(19)	(20)
GJ 1255	AB	24.75	K0 V	8.00	0.86	20 37 21	75 35 59	3	0.024	0.015	0.035	0.039	0.027	0.053	28.94	29.11	0	0	A
GJ 1255	C	24.75	K0 V	10.40	0.00	20 37 21	75 35 59	0	0.024	0.015	0.035	0.039	0.027	0.053	28.94	29.11	-1	-1	a
GJ 909	A	10.36	K3 V	6.40	0.98	23 52 37	75 32 37	3	0.014	0.006	0.023	0.018	0.008	0.031	27.94	28.02	0	0	A
GJ 909	B	10.36	M2	11.70	0.00	23 52 24	75 32 37	0	0.014	0.006	0.023	0.018	0.008	0.031	27.94	28.02	-1	-1	a
GJ 420	A	12.26	dK5	7.68	1.06	11 15 13	73 28 31	0	0.028	0.000	0.028	0.095	0.005	0.035	28.40	27.85	-1	0	B
GJ 420	B	12.26	M2	11.40	0.00	11 15 13	73 28 31	0	0.028	0.000	0.028	0.095	0.005	0.035	28.40	27.85	-1	0	B
GJ 713	AB	7.54	F7 V	3.57	0.49	18 21 02	72 44 02	3	0.014	0.000	0.014	0.014	0.005	0.023	27.68	27.63	-1	0	B
GJ 355.1		24.75	G4 III	4.86	0.77	09 34 29	69 49 48	0	0.045	0.030	0.063	0.044	0.027	0.064	29.22	29.16	0	0	
BD+68 949		19.61	F5 V	4.80	0.43	17 36 57	68 45 27	3	0.010	0.007	0.014	0.010	0.006	0.014	28.38	28.31	0	0	
GI 648		16.95	F6 V	4.89	0.48	16 56 01	65 08 08	3	0.005	0.001	0.010	0.010	0.006	0.017	27.97	28.24	0	0	
GI 311		13.85	G1 V	5.64	0.62	08 39 12	65 01 12	0	0.019	0.008	0.033	0.020	0.007	0.036	28.34	28.31	0	0	
BD+64 488		25.00	G0	7.74	0.00	04 33 54	64 38 01	0	0.014	0.004	0.027	0.026	0.000	0.026	28.71	28.93	0	-1	
GI 708.1		19.88	F5 V	5.03	0.38	18 13 53	64 23 49	0	0.006	0.003	0.009	0.006	0.002	0.010	28.15	28.10	0	0	
Steph 1676		25.00	M0	10.60	1.42	19 03 17	63 59 32	0	0.004	0.001	0.008	0.009	0.000	0.009	28.22	28.45	0	-1	
Wo 9809		22.73	dM0	10.82	1.42	23 06 03	63 55 11	0	0.011	0.000	0.011	0.015	0.005	0.027	28.52	28.60	-1	0	
GI 75		10.29	K0 V	5.63	0.81	01 47 44	63 51 11	0	0.013	0.005	0.022	0.025	0.000	0.025	27.90	28.14	0	-1	
GI 807		13.14	K0 IVe	3.43	0.92	20 45 17	61 50 09	0	0.008	0.000	0.008	0.009	0.002	0.018	27.90	27.93	-1	0	C
AC+61:27026		24.39	dK8	10.28	1.23	17 38 39	61 14 16	0	0.014	0.000	0.014	0.019	0.009	0.029	28.69	28.77	-1	0	
GSC 036B-821		24.39	dK8	14.70	0.00	17 38 41	61 14 02	0	0.015	0.000	0.015	0.020	0.009	0.030	28.74	28.79	-1	-1	c
G227-028		12.80	DC:9	15.65	0.97	18 21 19	61 00 59	0	0.008	0.000	0.008	0.008	0.002	0.014	27.91	27.83	-1	0	
GI 609.1		20.53	F8 IV-V	4.01	0.52	16 01 54	58 33 52	3	0.016	0.009	0.024	0.016	0.006	0.026	28.61	28.55	0	0	
GI 616.2		21.05	dM1.5e	9.96	1.48	16 17 07	55 16 13	0	0.012	0.006	0.020	0.019	0.010	0.030	28.51	28.66	0	0	
Wo 9584	C	23.26	M3 :	13.50	0.00	17 05 19	54 28 10	0	0.009	0.002	0.018	0.012	0.003	0.023	28.48	28.54	-1	-1	d
Wo 9584	A	23.26	F7 V	5.63	0.47	17 05 19	54 28 10	0	0.009	0.002	0.018	0.012	0.003	0.023	28.48	28.54	0	0	D
Wo 9584	B	23.25	F7 V	5.73	0.00	17 05 19	54 28 10	3	0.009	0.002	0.018	0.012	0.003	0.023	28.48	28.54	-1	-1	d
GI 212		11.61	M1	9.75	1.48	05 41 31	53 29 28	0	0.014	0.004	0.027	0.028	0.000	0.028	28.04	28.31	-1	-1	a
GI 211		12.09	K1 Ve	6.23	0.84	05 41 21	53 28 58	0	0.015	0.005	0.029	0.032	0.000	0.032	28.13	28.39	0	-1	A
BD+54 1499		22.73	K2	8.03	0.88	12 11 28	53 25 20	0	0.007	0.003	0.027	0.011	0.000	0.011	28.31	28.49	0	-1	B
LTT 13390		22.73	K3	8.23	0.00	12 11 27	53 25 08	0	0.007	0.004	0.028	0.014	0.000	0.014	28.33	28.58	0	-1	B
GI 549	A	12.35	F7 V	4.06	0.50	14 25 12	51 51 08	0	0.034	0.022	0.048	0.032	0.021	0.044	28.49	28.41	0	0	A
GI 549	B	12.35	M3	11.50	1.50	14 25 11	51 49 56	0	0.034	0.023	0.048	0.034	0.023	0.047	28.49	28.44	-1	-1	a
GI 719		17.24	K6 Ve	8.10	1.22	18 33 56	51 43 12	3	0.050	0.041	0.060	0.056	0.046	0.067	28.95	28.95	0	0	
GI 765	A	18.52	F4 V	4.48	0.38	19 36 27	50 13 15	0	0.012	0.004	0.021	0.021	0.000	0.021	28.37	28.58	0	-1	C
GI 765	B	18.52	F4 V	13.00	0.00	19 36 27	50 13 15	0	0.012	0.004	0.021	0.021	0.000	0.021	28.37	28.58	-1	-1	c
Steph 598		19.23	M0	11.09	1.50	06 31 01	50 02 53	0	0.017	0.007	0.030	0.025	0.000	0.025	28.58	28.70	0	-1	

Table A1

Name	Chmpnt	Dist	Spectral Type	mv	B-V	α_{J2000}	δ_{J2000}	SB	(ct/s)	SI	ul	(ct/s)	S2	ul	LgUV	Det	Note		
(1)	(2)	(3)	(4)	(5)	(6)	(7)	(8)	(9)	(10)	(11)	(12)	(13)	(14)	(15)	(16)	(17)	(18)	(19)	(20)
Gl 380		4.69	K2 Ve	6.59	1.36	10 11 23	49 27 21	0	0.011	0.002	0.023	0.024	0.000	0.024	27.17	27.44	0	-1	
Gl 275.2	A	11.56	dM5	13.56	1.71	07 30 44	48 12 14	0	0.011	0.002	0.022	0.015	0.000	0.015	27.93	28.02	0	-1	
Gl 575	A	11.75	F9 V n	5.19	0.65	15 03 48	47 39 16	0	0.077	0.063	0.092	0.091	0.073	0.112	28.80	28.82	0	0	A
Gl 575	B	11.75	dG2	5.96	0.00	15 03 48	47 39 16	3	0.077	0.063	0.092	0.091	0.073	0.112	28.80	28.82	-1	-1	a
W0 9832		20.79	G8 III	3.82	1.01	23 37 33	46 27 32	3	0.106	0.082	0.134	0.160	0.129	0.194	28.44	29.56	0	0	
Gl 368		13.28	G0.5 V	5.09	0.62	09 48 35	46 01 16	0	0.016	0.000	0.016	0.027	0.005	0.053	28.21	28.41	-1	0	
Gl 194	B	12.66	G0 III	0.96	0.00	05 16 41	45 59 59	0	0.400	0.358	0.445	0.470	0.424	0.519	29.58	29.60	-1	-1	a
Gl 194	A	12.66	G5 III	0.71	0.80	05 16 41	45 59 59	3	0.400	0.358	0.445	0.470	0.424	0.519	29.58	29.60	0	0	A
Gl 873		5.08	dM4.5e	10.26	1.61	22 46 50	44 20 07	3	0.097	0.076	0.120	0.146	0.122	0.171	28.17	28.30	0	0	
G190-028		14.88	M2	11.87	1.52	23 29 23	41 28 25	0	0.006	0.003	0.026	0.035	0.000	0.035	27.92	28.62	0	-1	E
G190-027		14.81	M3 :	12.44	1.61	23 29 22	41 28 13	0	0.006	0.003	0.026	0.038	0.000	0.038	27.92	28.65	0	-1	E
GJ 1124		18.48	K2 V	7.63	0.99	09 22 26	40 12 07	3	0.040	0.022	0.060	0.084	0.052	0.120	28.91	29.18	0	0	
Gl 815	A	15.13	dM3 e	10.34	1.52	21 00 05	40 04 17	3	0.015	0.007	0.024	0.025	0.010	0.043	28.30	28.49	0	0	A
Gl 815	B	15.13	dM3 e	11.90	0.00	21 00 05	40 04 17	0	0.015	0.007	0.024	0.025	0.010	0.043	28.30	28.49	-1	-1	a
Gl 820	B	3.46	K7 Ve	6.03	1.37	21 06 51	38 44 14	0	0.005	0.003	0.019	0.026	0.000	0.026	26.53	27.21	0	-1	B
Gl 820	A	3.46	K5 Ve	5.21	1.18	21 06 51	38 44 14	0	0.005	0.003	0.019	0.026	0.000	0.026	26.53	27.21	0	-1	B
Gl 161.1		23.26	F7 V	5.52	0.46	04 08 36	38 02 22	0	0.020	0.007	0.036	0.039	0.000	0.039	28.80	29.05	0	-1	
Gl 277	B	12.05	dM4.5e	11.78	1.52	07 31 57	36 13 48	0	0.013	0.014	0.039	0.095	0.009	0.052	28.04	28.05	0	0	B
Gl 277	A	12.05	dM3.5e	10.58	1.47	07 31 58	36 13 12	3	0.012	0.013	0.038	0.095	0.009	0.052	28.01	28.05	0	0	B
BD+36 2975		20.00	G5	7.84	0.00	17 55 25	36 11 18	3	0.026	0.015	0.038	0.038	0.021	0.057	28.79	28.91	0	0	
Gl 29.1		21.19	dM0 e	10.52	1.50	00 42 48	35 32 53	3	0.022	0.010	0.038	0.034	0.000	0.034	28.77	28.91	0	-1	
Gl 490	A	21.10	M0 Ve	10.68	1.44	12 57 40	35 13 32	2	0.007	0.006	0.026	0.029	0.000	0.029	28.29	28.84	0	-1	B
Gl 490	B	21.10	dM4 e	13.20	1.64	12 57 39	35 13 20	0	0.007	0.006	0.025	0.029	0.000	0.029	28.27	28.84	0	-1	B
BD+33 4828		20.41	G2 V	6.11	0.62	00 04 53	34 39 34	1	0.014	0.002	0.029	0.032	0.000	0.032	28.54	28.85	0	-1	
Gl 615.2	A	22.52	F8 V	5.64	0.51	16 14 41	33 51 29	3	0.218	0.191	0.247	0.353	0.316	0.393	29.82	29.98	0	0	A
Gl 615.2	B	22.52	G1 V	6.72	0.00	16 14 41	33 51 29	0	0.218	0.191	0.247	0.353	0.316	0.393	29.82	29.98	-1	-1	a
GJ119-062		12.20	dM4	12.38	0.00	11 11 52	33 32 09	0	0.018	0.006	0.035	0.022	0.000	0.022	28.20	28.23	0	-1	
GJ 1108	A	17.24	dM0.5e	10.05	1.35	08 08 56	32 49 15	0	0.008	0.007	0.029	0.095	0.012	0.051	28.16	28.37	0	0	A
GJ 1108	B	17.24	dM3 e	12.12	1.53	08 08 55	32 49 06	0	0.008	0.007	0.029	0.095	0.010	0.049	28.16	28.34	0	0	A
BD+32 1398		21.23	K3 V	8.77	0.96	06 46 05	32 33 20	0	0.004	0.002	0.019	0.018	0.000	0.018	28.07	28.63	0	-1	B
G087-004		21.23	M0.5	12.17	1.53	06 46 07	32 33 15	0	0.004	0.002	0.019	0.017	0.000	0.017	28.07	28.62	0	-1	B
Gl 856	B	10.99		11.60	0.00	22 23 29	32 27 33	0	0.019	0.009	0.031	0.023	0.010	0.037	28.13	28.16	-1	-1	a
Gl 856	A	10.99	dM0 e	11.41	1.57	22 23 29	32 27 33	0	0.019	0.009	0.031	0.023	0.010	0.037	28.13	28.16	0	0	A
Gl 278	A	14.64	A1 V	1.94	0.04	07 34 36	31 53 20	3	0.056	0.041	0.074	0.081	0.057	0.109	28.86	28.97	-1	-1	a
Gl 278	B	14.64	A m	2.85	0.00	07 34 36	31 53 20	3	0.056	0.041	0.074	0.081	0.057	0.109	28.86	28.97	-1	-1	a

Table A1

Name	Cmpnt	Dist	Spectral Type	mv	B-V	α_{J2000}	δ_{J2000}	SB		SI		ul	(ct/s)	S2		ul	I _{GUUV}		Det	Note
								(9)	(10)	(11)	(12)			(13)	(14)		(15)	(16)		
GI 501	A	19.34	F5 V	4.98	0.45	13 09 59	17 31 45	3	0.028	0.000	0.028	0.020	0.005	0.039	28.79	28.60	-1	0	I	
GI 202		15.34	F8 Ve	4.99	0.53	05 24 25	17 22 59	0	0.026	0.014	0.041	0.029	0.011	0.050	28.56	28.55	0	0		
GI 505	B	11.91	M1 V	9.60	0.00	13 16 51	17 01 02	0	0.011	0.003	0.022	0.016	0.000	0.016	27.97	28.08	-1	-1	j	
GI 505	A	11.91	K1 V	6.59	0.94	13 16 51	17 01 02	0	0.011	0.003	0.022	0.016	0.000	0.016	27.97	28.08	0	-1	J	
GI 494		11.12	dM1.5e	9.75	1.47	13 00 47	12 22 33	0	0.028	0.008	0.056	0.029	0.011	0.052	28.31	28.29	0	0		
W0 9207		23.04	F5 IV-V	5.04	0.42	06 16 26	12 16 20	0	0.009	0.002	0.018	0.040	0.000	0.040	28.47	29.05	0	-1		
GI 208		11.62	dM0	8.80	1.40	05 36 31	11 19 40	0	0.013	0.005	0.023	0.022	0.006	0.042	28.00	28.20	0	0		
J.P 476-207		7.04	dM3	11.47	1.52	05 01 59	09 59 00	0	0.022	0.012	0.036	0.037	0.014	0.063	27.82	27.99	0	0		
GI 206		14.11	dM4 e	11.52	1.63	05 32 15	09 49 18	3	0.022	0.013	0.034	0.031	0.000	0.031	28.42	28.52	0	-1		
GI 504		13.48	G0 V	5.20	0.58	13 16 47	09 25 26	0	0.027	0.000	0.027	0.040	0.021	0.064	28.47	28.59	-1	0		
G041-014		4.46	k	10.89	1.67	08 58 56	08 28 30	0	0.029	0.016	0.046	0.045	0.024	0.070	27.54	27.68	0	0		
GI 735		11.29	dM3 e	10.11	1.53	18 55 28	08 24 10	3	0.014	0.005	0.026	0.032	0.060	0.032	28.03	28.34	0	-1		
BD+ 6 211		15.15	G5	7.33	0.00	01 22 57	07 25 07	3	0.077	0.058	0.100	0.087	0.060	0.118	29.02	29.02	0	0		
GI 408		2.39	M6	13.45	2.00	10 56 32	07 01 21	0	0.017	0.000	0.017	0.026	0.009	0.048	26.77	26.90	-1	0		
GI 178		7.51	F6 V	3.19	0.45	04 49 50	06 57 38	0	0.044	0.029	0.061	0.062	0.030	0.098	28.17	28.27	0	0		
GI 35		4.33	D27	12.38	0.55	00 49 09	05 23 44	0	0.010	0.002	0.022	0.020	0.000	0.020	27.05	27.31	0	-1		
GI 280	B	3.50	DA	10.70	0.00	07 39 18	05 13 41	0	0.111	0.089	0.137	0.199	0.165	0.236	27.91	28.11	-1	-1	a	
GI 280	A	3.50	F5 IV-V	0.38	0.42	07 39 18	05 13 41	3	0.111	0.089	0.137	0.199	0.165	0.236	27.91	28.11	0	0	A	
W01F1494		16.39	m	14.34	0.00	13 48 49	04 06 05	0	0.009	0.001	0.020	0.011	0.000	0.011	28.14	28.18	0	-1		
GI 285		6.21	dM4.5e	11.20	1.60	07 44 40	03 33 13	0	0.033	0.020	0.049	0.051	0.029	0.077	27.88	28.02	0	0		
GI 106.1	C	23.81	K5	10.16	1.36	02 42 30	03 22 32	0	0.042	0.009	0.081	0.036	0.000	0.036	29.16	29.04	0	-1		
GI 137		9.57	G5 Ve	4.82	0.68	03 19 21	03 22 13	2	0.034	0.016	0.061	0.058	0.014	0.119	28.27	28.45	0	0		
GI 748		10.06	dM4	11.10	1.51	19 12 13	02 53 22	0	0.015	0.000	0.015	0.024	0.004	0.046	27.94	28.10	-1	0		
G099-049		5.37	M4	11.33	1.68	06 00 04	02 42 21	0	0.011	0.004	0.022	0.022	0.006	0.041	27.29	27.53	0	0		
GI 702	A	5.02	K0 Ve	4.21	0.86	18 05 28	02 30 10	3	0.070	0.000	0.070	0.095	0.013	0.118	28.02	27.63	-1	0	B	
GI 702	B	5.02	K5 Ve	6.00	1.15	18 05 28	02 30 10	3	0.070	0.000	0.070	0.095	0.013	0.118	28.02	27.63	-1	0	B	
GI 207.1		15.08	dM2.5e	11.53	1.57	05 33 44	01 56 41	0	0.012	0.004	0.023	0.015	0.000	0.015	28.22	28.25	0	-1		
GI 182		16.39	dM0.5	10.09	1.39	04 59 35	01 46 56	0	0.013	0.005	0.025	0.051	0.000	0.051	28.32	28.86	0	-1		
GI 449		10.12	F9 V	3.61	0.55	11 50 41	01 45 56	2	0.011	0.003	0.023	0.028	0.000	0.028	27.83	28.18	0	-1		
G045-011		16.67	m	13.85	0.00	10 52 04	00 32 40	0	0.012	0.000	0.012	0.025	0.006	0.048	28.30	28.56	-1	0		
GI 402.1		21.37	dK8	10.20	0.90	10 52 03	00 09 37	0	0.010	0.002	0.021	0.015	0.000	0.015	28.43	28.56	0	-1		
GI 159		18.12	F6 V	5.37	0.50	04 02 37	00 16 06	1	0.043	0.028	0.063	0.055	0.035	0.078	28.93	28.98	0	0		
GI 157	A	14.71	K4 V	8.04	1.11	03 57 29	-01 09 31	0	0.017	0.007	0.031	0.032	0.000	0.032	28.35	28.57	-1	-1	k	
GI 157	B	14.71	dM3 e	11.61	1.47	03 57 29	-01 09 31	3	0.017	0.007	0.031	0.032	0.000	0.032	28.35	28.57	0	-1	K	
GI 482	A	10.13	F0 V	3.46	0.36	12 41 40	-01 26 56	1	0.014	0.011	0.050	0.095	0.020	0.101	27.93	28.18	0	0	L	

Table A1

Name	Cmpnt	Dist	Spectral Type	mv	B-V	α_{J2000}	δ_{J2000}	SB	$\frac{ct/s}{(10)}$	S1	ul	(ct/s)	S2	ul	I _{JUV}	Det	Note	
(1)	(2)	(3)	(4)	(5)	(6)	(7)	(8)	(9)	(10)	II	(12)	(13)	II	(15)	S1	(18)	(20)	
Gl 482	B	10.13	F0 V	3.52	0.00	12 41 40	-01 26 56	0	0.014	0.011	0.050	0.095	0.020	0.101	27.93	28.18	0	L
Steph 497		14.71	M1	10.59	1.45	04 37 37	-02 29 32	0	0.020	0.008	0.036	0.066	0.000	0.066	28.40	28.88	0	-1
Gl 234	A	4.13	M4.5	11.13	1.71	06 29 23	-02 48 43	0	0.019	0.011	0.030	0.041	0.000	0.041	27.29	27.57	0	-1
Gl 234	B	4.13	M4.5	11.13	1.71	06 29 23	-02 48 43	0	0.019	0.011	0.030	0.041	0.000	0.041	27.29	27.57	-1	a
Gl 23	B	16.29	G1 V	6.40	0.00	00 35 14	-03 35 36	3	0.033	0.000	0.033	0.095	0.004	0.044	28.72	28.20	-1	0
Gl 23	A	16.29	F6 V	5.65	0.57	00 35 14	-03 35 36	3	0.033	0.000	0.033	0.095	0.004	0.044	28.72	28.20	-1	0
W0 9721		22.42	dM2	9.44	1.13	21 08 45	-04 25 36	0	0.011	0.003	0.022	0.025	0.000	0.025	28.52	28.83	0	-1
W0 9721	B	22.42	dM2	9.44	1.13	21 08 45	-04 25 36	0	0.011	0.003	0.022	0.025	0.000	0.025	28.52	28.83	-1	a
Gl 159-003		10.00	m	14.60	0.00	01 51 04	-06 07 08	0	0.017	0.005	0.034	0.017	0.000	0.017	28.01	27.95	0	-1
Gl 166	A	4.83	K1 Ve	4.43	0.82	04 15 18	-07 38 38	0	0.028	0.014	0.046	0.027	0.009	0.040	27.59	27.52	-1	a
Gl 166	B	4.83	DnA	9.52	0.03	04 15 24	-07 38 57	0	0.024	0.011	0.042	0.040	0.000	0.040	27.52	27.69	-1	a
Gl 166	C	4.83	dM4.5e	11.17	1.67	04 15 24	-07 38 57	0	0.024	0.011	0.042	0.040	0.000	0.040	27.52	27.69	0	-1
BD-8 801		23.81	G2 IV-V	7.04	0.00	04 09 41	-07 53 37	3	0.085	0.063	0.110	0.132	0.102	0.165	29.46	29.60	0	0
Gl 643		5.82	sdM4	11.80	1.69	16 55 26	-08 19 13	3	0.074	0.054	0.098	0.130	0.099	0.163	28.18	28.37	-1	-1
Gl 644	B	6.50	M3	9.90	0.00	16 55 29	-08 20 01	0	0.065	0.045	0.088	0.118	0.089	0.150	28.22	28.42	-1	-1
Gl 644	A	6.50	M3	9.69	1.57	16 55 29	-08 20 01	0	0.065	0.045	0.088	0.118	0.089	0.150	28.22	28.42	0	0
Gl 517		19.23	K5	9.31	1.21	13 34 44	-08 20 30	0	0.019	0.009	0.033	0.032	0.000	0.032	28.63	28.80	0	-1
Gl 644	C	6.50	M7	16.78	1.99	16 55 36	-08 23 31	0	0.028	0.000	0.028	0.041	0.018	0.068	27.85	27.97	-1	-1
Gl 144		3.27	K2 V	3.73	0.88	03 32 56	-09 27 31	0	0.092	0.057	0.137	0.105	0.042	0.191	27.77	27.78	0	0
Gl 355		19.23	K0	7.82	0.92	09 32 26	-11 11 06	0	0.039	0.026	0.056	0.043	0.025	0.065	28.93	28.93	0	0
Gl 105.4	B	14.58	F5 V	5.60	0.00	02 39 34	-11 52 17	0	0.030	0.000	0.030	0.026	0.006	0.052	28.57	28.47	-1	-1
Gl 105.4	A	14.58	F5 V	5.50	0.44	02 39 34	-11 52 17	3	0.030	0.000	0.030	0.026	0.006	0.052	28.57	28.47	-1	0
Gl 256		21.28	K4 V	9.15	1.16	06 58 26	-12 59 29	2	0.012	0.000	0.012	0.024	0.006	0.045	28.52	28.75	-1	0
Gl 838.5		21.88	F1 III	5.08	0.37	21 53 17	-13 33 08	0	0.035	0.000	0.035	0.040	0.014	0.071	29.00	29.01	-1	0
Gl 225		13.62	F1 III	3.72	0.33	05 56 25	-14 10 04	0	0.015	0.000	0.015	0.017	0.005	0.032	28.22	28.22	-1	0
BD-14 3902		25.00	K4 V	10.40	1.28	14 14 22	-15 21 24	0	0.021	0.000	0.021	0.014	0.002	0.030	28.89	28.67	-1	0
Gl 837		14.68	A6 m	2.87	0.29	21 47 02	-16 07 35	3	0.044	0.025	0.067	0.047	0.023	0.074	28.75	28.73	0	0
Gl 244	B	2.63	DA2	8.44	-0.03	06 45 10	-16 42 48	0	3.163	3.055	3.275	8.415	8.231	8.605	29.11	29.49	0	0
Gl 244	A	2.63	A1 V	-1.43	0.00	06 45 10	-16 42 48	1	3.163	3.055	3.275	8.415	8.231	8.605	29.11	29.49	-1	a
Gl 859	A	16.45	G3 V	6.21	0.62	22 26 35	-16 44 30	0	0.021	0.008	0.080	0.028	0.000	0.028	28.52	28.61	0	-1
Gl 859	B	16.45	G3 V	6.40	0.00	22 26 34	-16 44 31	0	0.021	0.008	0.080	0.029	0.000	0.029	28.52	28.62	0	-1
Gl 897	A	12.90	M3.5	10.95	1.51	23 32 46	-16 45 05	0	0.023	0.009	0.042	0.032	0.010	0.060	28.36	28.45	0	0
Gl 897	B	12.90	M3.5	10.95	1.51	23 32 46	-16 45 05	0	0.023	0.009	0.042	0.032	0.010	0.060	28.36	28.45	-1	o
Gl 898		12.90	K5/M0	8.60	1.28	23 32 49	-16 50 41	0	0.023	0.004	0.023	0.032	0.000	0.032	28.22	28.45	-1	o
Gl 54.1		3.74	dM5 e	12.05	1.84	01 12 30	-17 00 05	0	0.013	0.003	0.026	0.028	0.000	0.028	27.04	27.32	0	-1

Table A1

Name	Compnt	Dist	Spectral Type	mv	B-V	α_{J2000}	δ_{J2000}	SB	SI	ul	(ct/s)	S2	ul	S1	ul	(ct/s)	S2	ul	LgUV	S1	S2	Det	Note
(1)	(2)	(3)	(4)	(5)	(6)	(7)	(8)	(9)	(10)	(11)	(12)	(13)	(14)	(15)	(16)	(17)	(18)	(19)	(20)	(21)	(22)	(23)	(24)
GI 84		8.47	M3	10.19	1.51	02 05 03	-17 36 53	0	0.013	0.000	0.013	0.004	0.037	27.75	27.84	-1	0	0					
GI 65	B	2.63	dM5.5e	12.70	0.00	01 38 59	-17 57 07	0	0.010	0.011	0.034	0.095	0.004	0.034	26.64	26.50	0	0	P				P
GI 65	A	2.63	dM5.5e	12.57	1.85	01 38 59	-17 57 07	0	0.010	0.011	0.034	0.095	0.004	0.034	26.63	26.49	0	0	P				P
GI 31		18.35	K1 III	2.04	1.01	00 43 35	-17 59 09	0	0.055	0.000	0.055	0.070	0.040	0.104	29.04	29.10	-1	0	0				0
GI 867	A	8.67	dM2 e	9.10	1.51	22 38 45	-20 37 12	3	0.053	0.035	0.112	0.095	0.060	0.138	28.38	28.46	0	0	Q				Q
GI 867	B	8.67	dM4 e	11.45	1.60	22 38 45	-20 37 12	0	0.018	0.035	0.112	0.095	0.060	0.138	27.90	27.98	0	0	Q				Q
Steph 545		12.05	M3:	11.66	1.51	05 06 49	-21 35 05	0	0.036	0.023	0.052	0.044	0.021	0.071	28.50	28.53	-1	-1	a				a
BD-21 1074		12.05	M2	10.29	1.52	05 06 50	-21 35 05	0	0.036	0.023	0.052	0.044	0.021	0.071	28.50	28.53	0	0	A				A
GI 1257		20.24	K5 V	9.70	1.11	20 41 42	-22 19 01	0	0.012	0.004	0.024	0.033	0.000	0.033	28.47	28.85	0	-1	R				R
GI 216	B	8.01	K2 V	6.13	0.94	05 44 26	-22 25 14	0	0.010	0.003	0.020	0.023	0.000	0.023	27.58	27.89	0	-1	R				R
GI 216	A	8.01	F6 V	3.58	0.47	05 44 28	-22 26 50	0	0.010	0.003	0.020	0.018	0.006	0.034	27.58	27.79	-1	-1	r				r
GI 416.1		19.12	A2 III	4.48	0.03	11 11 40	-22 49 29	0	0.135	0.107	0.167	0.422	0.369	0.478	29.47	29.91	0	0	0				0
GI 97		12.05	G1 V	5.20	0.60	02 22 32	-23 49 01	0	0.017	0.003	0.035	0.024	0.000	0.024	28.17	28.26	0	-1	0				0
CD-23 3577		16.39	G5 V	6.38	0.72	06 13 45	-23 51 45	0	0.019	0.012	0.028	0.030	0.010	0.053	28.49	28.63	0	0	0				0
GI 455.3		14.14	F2 III	4.02	0.32	12 08 25	-24 43 43	3	0.015	0.005	0.031	0.047	0.000	0.047	28.27	28.69	0	-1	0				0
GI 663	A	5.33	K1 Ve	5.07	0.85	17 15 21	-26 36 54	0	0.011	0.005	0.042	0.050	0.000	0.050	27.26	27.87	0	-1	S				S
GI 663	B	5.33	K1 Ve	5.11	0.86	17 15 21	-26 36 00	0	0.011	0.004	0.042	0.050	0.000	0.050	27.25	27.88	0	-1	S				S
CD-27 6141		21.74	G5 V	6.87	0.69	08 59 43	-27 48 59	3	0.026	0.015	0.039	0.035	0.016	0.058	28.86	28.95	0	0	0				0
GI 127	B	13.76	G7 V	6.70	0.00	03 12 04	-28 59 20	0	0.041	0.000	0.041	0.040	0.013	0.072	28.66	28.60	-1	-1	l				l
GI 127	A	13.75	F7 IV	3.95	0.51	03 12 04	-28 59 20	0	0.041	0.000	0.041	0.040	0.013	0.072	28.66	28.60	-1	-1	l				l
GI 60	C	17.24	M2 V	10.40	0.00	01 35 01	-29 54 36	0	0.032	0.019	0.048	0.056	0.038	0.076	28.76	28.94	-1	-1	a				a
GI 60	A	17.24	K3 V	7.78	0.92	01 35 01	-29 54 36	0	0.032	0.019	0.048	0.056	0.038	0.076	28.76	28.94	0	0	A				A
GI 60	B	17.24	K4 V	8.00	0.00	01 35 01	-29 54 36	0	0.032	0.019	0.048	0.056	0.038	0.076	28.76	28.94	-1	-1	a				a
NN		11.36	M4	13.00	0.00	02 16 34	-30 58 10	0	0.005	0.002	0.019	0.021	0.000	0.021	27.56	28.16	0	-1	B				B
CD-31 909		11.36	M4	12.00	0.00	02 16 40	-30 59 22	0	0.005	0.002	0.020	0.019	0.000	0.019	27.59	28.11	0	-1	B				B
GI 803		9.35	M0 Ve	8.81	1.42	20 45 09	-31 20 24	0	0.132	0.103	0.166	0.082	0.051	0.118	28.84	28.58	0	0	0				0
GI 799	A	8.14	dM4.5e	10.99	1.57	20 41 51	-32 26 04	0	0.024	0.028	0.075	0.095	0.062	0.144	27.98	28.25	0	0	U				U
GI 799	B	8.14	dM4.5e	11.00	0.00	20 41 51	-32 26 04	0	0.024	0.028	0.075	0.095	0.062	0.144	27.98	28.25	0	0	U				U
GI 525.1		21.28	F3 IV	4.23	0.38	13 45 41	-33 02 36	3	0.017	0.006	0.032	0.026	0.000	0.026	28.65	28.80	0	-1	0				0
GI 773.4		19.38	F8 V	5.66	0.49	20 00 20	-33 42 13	1	0.030	0.011	0.052	0.052	0.000	0.052	28.82	29.02	0	-1	0				0
GI 886.2		19.92	F0 IV	5.11	0.29	23 03 30	-34 44 58	3	0.032	0.000	0.032	0.054	0.015	0.102	28.88	29.06	-1	0	0				0
GI 755		20.83	G5 V	6.48	0.62	19 21 30	-34 58 57	0	0.025	0.009	0.044	0.030	0.000	0.030	28.81	28.84	0	-1	0				0
GI 320		10.43	K1 V	6.56	0.93	08 43 18	-38 53 03	0	0.011	0.002	0.021	0.018	0.000	0.018	27.84	28.01	0	-1	0				0
GI 620.1	A	12.82	G3/5 V	5.39	0.63	16 24 02	-39 11 36	0	0.038	0.019	0.060	0.133	0.104	0.167	28.57	29.06	-1	-1	a				a
GI 620.1	B	12.82	DA2	11.00	-0.14	16 23 34	-39 13 44	0	0.219	0.182	0.261	0.653	0.589	0.721	29.33	29.76	0	0	A				A

Table A1

Name	Cmpnt	Dist	Spectral Type	mv	B-V	α_{J2000}	δ_{J2000}	- continued -										Det	Note	
								(1)	(2)	(3)	(4)	(5)	(6)	(7)	(8)	(9)	(10)			(11)
GI 370		9.69	K5 V	7.64	1.18	09 51 07	-43 30 06	0	0.016	0.005	0.029	0.016	0.000	0.016	0.000	0.016	27.95	27.91	0	-1
GI 103		11.47	K7 Ve	8.85	1.39	02 34 22	-43 47 42	3	0.044	0.031	0.060	0.052	0.033	0.076	0.076	28.54	28.56	0	0	
GI 375		14.47	M3.5	11.27	1.55	09 58 34	-46 25 24	0	0.022	0.010	0.037	0.026	0.012	0.045	0.045	28.44	28.47	0	0	
GI 52.1		21.28	K1 V	8.85	0.94	01 06 47	-50 59 28	0	0.035	0.007	0.069	0.038	0.000	0.038	0.038	28.98	28.97	0	-1	
GI 841	A	14.62	M0	10.40	1.50	21 57 41	-50 59 45	3	0.025	0.013	0.041	0.043	0.026	0.064	0.064	28.51	28.69	0	0	
GI 81	B	18.25	G5 IV	3.70	0.85	01 55 57	-51 36 33	0	0.044	0.000	0.044	0.032	0.007	0.062	0.062	28.94	28.75	-1	0	
GI 81	B	18.25	G5 IV	3.70	0.85	01 55 57	-51 36 33	0	0.044	0.000	0.044	0.032	0.007	0.062	0.062	28.94	28.75	-1	0	
GJ 2036	B	10.53		12.15	1.60	04 53 30	-55 51 08	0	0.026	0.028	0.079	0.047	0.000	0.047	0.000	28.23	28.44	0	-1	
GJ 2036	A	10.53	M2 Ve	11.13	1.57	04 53 30	-55 51 08	0	0.026	0.028	0.079	0.047	0.000	0.047	0.000	28.23	28.44	0	-1	
GI 189		13.70	F7 V	4.71	0.52	05 05 31	-57 28 21	0	0.030	0.014	0.049	0.040	0.020	0.064	0.064	28.53	28.60	0	0	
GJ 1075		12.35	K7 V	9.02	1.40	05 05 47	-57 33 17	0	0.014	0.000	0.014	0.025	0.007	0.046	0.046	28.09	28.31	-1	-1	
NN		20.41	m	13.40	0.00	18 52 02	-60 45 47	0	0.077	0.013	0.151	0.059	0.000	0.059	0.059	29.28	29.12	0	-1	
GI 559	A	1.33	G2 V	0.01	0.64	14 39 41	-60 50 14	0	0.043	0.113	0.167	0.095	0.264	0.346	0.346	26.66	26.95	0	0	
GI 559	B	1.33	K0 V	1.34	0.84	14 39 41	-60 50 14	0	0.095	0.113	0.167	0.095	0.264	0.346	0.346	27.00	27.29	0	0	
CP-61 688		21.74	G0 V	6.34	0.62	06 38 00	-61 31 60	0	0.025	0.018	0.033	0.016	0.007	0.026	0.026	28.55	28.60	0	0	
NN		21.74		8.30	0.00	06 38 00	-61 31 60	0	0.025	0.018	0.033	0.016	0.007	0.026	0.026	28.55	28.60	-1	-1	
GI 551		1.29	dM5 e	11.05	1.83	14 29 49	-62 40 56	0	0.035	0.022	0.052	0.047	0.028	0.070	0.070	26.55	26.62	0	0	
GI 865		11.12	k-m	11.48	1.61	22 38 28	-65 22 42	0	0.013	0.004	0.025	0.026	0.011	0.045	0.045	27.99	28.23	0	0	
W0 9791		22.94		14.00	0.00	22 38 25	-65 22 53	0	0.013	0.004	0.026	0.030	0.014	0.049	0.049	28.62	28.92	-1	-1	
GJ 1280		22.73	K4 V	8.78	1.02	23 10 21	-68 50 24	0	0.012	0.003	0.024	0.025	0.000	0.025	0.025	28.58	28.84	0	-1	

Key: (1) star name [GI = Gliese (1969) number, GJ = Gliese & Jahreiss (1979) number, W0 = Woolley et al. (1970) number, NN = star not yet assigned a number in CNS3, otherwise an additional identifier is used if known]; (2) component (for multiple systems); (3) distance (pc) obtained from resultant parallax; (4) spectral type; (5) apparent V magnitude; (6) B-V colour index (in some cases B-V = 0.0 indicates that the colour is not available); (7-8) equatorial coordinates (epoch J2000, epoch 1980.0); (9) spectroscopic-binary flag (3=SB, 2=SB¹, 1=variable radial velocity, 0=no information); (10-15) WFC S1 and S2 count rates with corresponding 99 per cent lower and upper limits; (16-17) EUV luminosity for the S1 and S2 bandpasses; (18-19) detection flags for S1 and S2 bands (0: detection, -1: upper limit); (20) The letter refers to the notes following, and indicates how the EUV flux has been divided between visual binaries. When in capitals, the counterpart has been taken to contribute to the EUV flux. When in lower-case, the counterpart has been assumed not to contribute.

Notes to Table A1

- A This star has been designated as the EUV source according to information given in the WFC BSC (Pounds et al. 1993).
- B No useful information has been found in the literature, therefore the EUV flux has been divided equally between the components in the case of a detection. Upper limits have not been changed.
- C Where one star has no spectral type, the EUV flux has been attributed (albeit arbitrarily) to the classified star.
- D We follow Schmitt et al. (1990a) and Walter (1982) in assuming that HD 154906 is the *Einstein* source and hence the WFC source.
- E Found to be active by the WFC optical identification programme (Mason et al. in preparation), and is therefore a probable contributor to the EUV flux. As yet no measurements of the H α or Ca II H & K equivalent widths are available, therefore the EUV flux has been divided equally between the components.
- F Wolff, Boesgaard & Simon (1986) imply that ρ Gem (=GI 274A) is active. We assume it is the EUV source.
- G GI 2069B = CV Cnc, spectral type = dM5e (SIMBAD). Both stars assumed to be equally active.
- H Soderblom & Mayor (1993): 'Both stars have consistently high chromospheric emission levels in all indices'. EUV flux divided equally.
- I Vilhu & Waller (1987) show that GI 501A is a single-lined binary with Mg II in emission. Therefore assumed to be the EUV source.
- J GI 505A is a young active star (Noyes et al. 1984; Soderblom 1990). Assumed to be the EUV source.
- K No information relating to activity levels found for the K star. Therefore GI 157B assumed to be the EUV source.
- L Blanco et al. (1982) proposes that Mg II is in emission in the spectra of both stars, hence EUV flux is divided equally.
- M Johnson (1987) resolves the system with the *EXOSAT* LE. GI 644AB is much the stronger source, so the flux has been allocated to GI 644A (as no information regarding spectral type/activity is available for GI 644B). The upper limit for GI 644B has been set to this flux. GI 644C = VB 8 shows no evidence for EUV emission in the WFC image, and the upper limit has been set to that allocated to GI 644B.
- N ϵ Cet (=GI 105-4A) shows evidence for youth with a Li 6707-Å absorption feature (Balachandran 1990), and is assumed to be the EUV source.
- O GI 898 is offset from the centroid of the source in the WFC image (separation ~ 4.5 arcmin), while GI 897AB is coincident (separation ~ 17 arcsec). The EUV flux has been allocated to GI 897A, while the upper limit for GI 898 has been set to that measured for GI 897B.
- P The two components could not be resolved by *EXOSAT* (Pallavicini, Tagliaferrri & Stella 1990), hence the EUV flux has been divided equally between them.
- Q Pollock, Tagliaferrri & Pallavicini (1991) use a maximum likelihood technique to determine an *EXOSAT* LE flux in the ratio 3:1 for components A:B. We use this ratio for the EUV flux division.

R Schmitt et al. (1990b) discuss an *Einstein* HRI observation which resolves the components. They find that GI 216A is ~ 8 times brighter than GI 216B. Therefore we assume that all the EUV flux arises from GI 216A, and have set a corresponding upper limit for GI 216B.

S Schrijver, Dobson & Radick (1992) assume both components to be equally active. The EUV flux has been divided equally between the components.

T GI 127A has a slightly filled-in H α feature (Pasquini & Pallavicini 1991). It is assumed to be the EUV source.

U AT Mic. Both stars are assumed to contribute equally to the EUV flux on the basis of their spectral types (both dM4.5e).

V GI 81A shows single-line emission in Ca II H & K (Pasquini, Pallavicini & Drawius 1989).

W An *Einstein* HRI observation (Vaiana et al. 1981) gives the count rate for α Cen A as 0.15 count s^{-1} and for α Cen B as 0.32 count s^{-1} . This flux ratio has been adopted here.

Appendix B

Simulations

B.1 Aims

There are a number of questions which arise as the result of using survival analysis techniques in the study of such heavily censored data. Feigelson (1990) urges caution when dealing with censorship levels greater than about 60–70%. Our levels of censorship are in the range 90–95%. Some problems to be addressed are:

1. Does the KMPLE successfully reconstruct the true and therefore unknown underlying luminosity functions? How does it behave with such heavily censored data? Specifically, how accurate are the mean median and ‘shape’ (which can be defined here in terms of the power law index and upper and lower bounds)?
2. What are the effects of noise on the measured count rates (and hence on the luminosities)?
3. How dependent are the ELF’s on the assumption of a fixed temperature and column density for all stars (as represented by the luminosity/count-rate conversion factor)?
4. How are changes in the adopted detection threshold and confidence levels propagated through to the luminosity functions?
5. How representative are the results of the two-sample tests? Do any of the tests discussed by FN85 seem to be particularly good/bad?

B.2 Procedure

A simulated parent population of objects with a power law luminosity function was numerically constructed, and randomly located in space (out to a distance limit of 25 parsecs) with a uniform space density, k (number per parsec³). The form of the function is $N(>L) = N_0 L^\alpha$ between the upper and lower bounds L_{\min} and L_{\max} , where $N(>L)$ is the number of objects with luminosity greater than L , and N_0 is the number of objects with $L > 1$. The number of objects in the sample is defined such that at $L = L_{\min}$, $N_{\text{tot}} = 4/3\pi kd^3$ where d is the distance occupied by the sample in parsecs. The slope, α , of the input function could be varied over the range of measured values for the survey ELF's.

The luminosities of the sample were converted to count rates at the earth using a fixed conversion factor (i.e the same values as discussed in section 1.8) or in some cases (discussed below) by taking a range of conversion factors. By assuming a mean exposure for each 'source' (2000 seconds is the mean exposure time for a source in the WFC all-sky survey in one filter), the raw counts could be obtained. Likewise a typical mean background count-rate (1 count/2000sec/arcmin⁻² in the S2a filter) was allocated. Random Poisson fluctuations were incorporated in the raw counts to represent the uncertainties inherent in measurements with small numbers of counts, resulting in detect and background cell counts for each simulated source. Using the same analysis techniques employed for the survey, the ELF's were constructed.

As a result of including Poisson noise, faint objects could now be moved downwards in luminosity, out of the luminosity function, with as yet no corresponding mechanism to move low luminosity objects (below the lower bound of the input function) upwards. To avoid the resultant flattening of the output function at low luminosities the contribution from objects in the bins below the lower bound (down to a factor 2 fainter) were incorporated.

By varying the input parameters (observation time and background count rate) it was possible to alter the sensitivity of the simulated survey to faint sources - i.e the ratio of detections to upper limits could be changed. In addition the sensitivity of the KMPLE to the slope and bounds of the power law could also be examined.

Table B.1 lists the input parameters for the simulations, the results of which are discussed below.

Table B.1: Simulations: Input Parameters

Simulation	Trials	N _{obj}	α	$\log(L_{\min})$	$\log(L_{\max})$	Bgd	CF	T _{obs} (s)
1	100	222	-1.60	27.6	29.2	1.0	S2a N	2000
2	100	399	-0.82	26.6	30.0	1.0	S2a N	2000
3	100	686	-1.11	27.2	29.3	1.0	S2a N	2000
4	100	734	-1.01	26.4	29.0	1.0	S2a N	2000
5	100	222	-1.60	27.6	29.2	1.0	S2a Y	2000
6	100	399	-0.82	26.6	30.0	1.0	S2a Y	2000
7	100	686	-1.11	27.2	29.3	1.0	S2a Y	2000
8	100	734	-1.01	26.4	29.0	1.0	S2a Y	2000
9	100	222	-1.60	27.6	29.2	1.0	S1a N	2000
10	100	399	-0.82	26.6	30.0	1.0	S1a N	2000
11	100	222	-1.60	27.6	29.2	1.0	S1a Y	2000
12	100	399	-0.82	26.6	30.0	1.0	S1a Y	2000
13	100	222	-1.60	27.6	29.2	0.1	S2a N	20000
14	100	399	-0.82	26.6	30.0	0.1	S2a N	20000

Simulation is the label given to the particular series of runs.

Trials is the number of individual passes produced for each simulation.

α is the slope of the input integral power law.

$\log(L_{\min})$ and $\log(L_{\max})$ are the upper and lower bounds of the input luminosity function.

Bgd is the mean background rate in units of counts.arcmin⁻²/2000secs.

CF shows which filter the conversion factor is derived for in the left hand column. The right hand column is a flag, such that Y means the conversion factor is varied and N means that it is held constant.

T_{obs} is the input observation time for each 'source' in seconds.

The simulations have been deliberately constructed to represent the WFC luminosity functions. To this end the slopes, upper and lower bounds, and the normalisations of the F–M star ELFs have been used to parameterise the input functions. For each simulation, 100 trials have been run in order to provide a statistical spread in the results.

B.3 Results

Simulations 1–4 have as their input the fits to the ELFs derived for the survey in the S2a filter.

In Fig. B.1 is shown an example output luminosity functions for each spectral type. Fig. B.2 is a plot of all the G-star runs on one set of axes to give some idea of the spread of the results.

Simulations 5–8 are parameterised in the same way as 1–4 except that the conversion factor

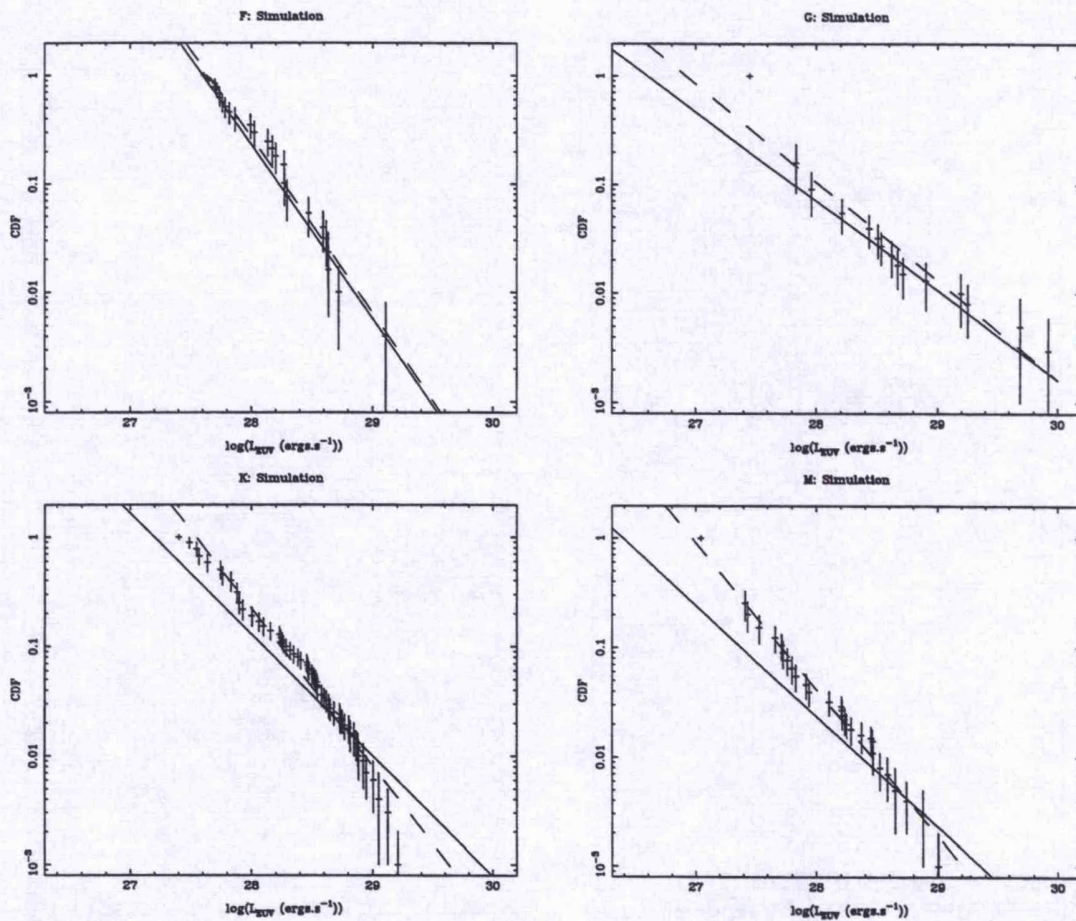


Figure B.1: An example output simulated luminosity function for each spectral type. The solid line represents the input (parent) function. The dashed line is the best-fit line to the data (ignoring error bars).

has been uniformly randomly chosen from a grid of seven points representing a range of N_H from $1 \times 10^{18} \text{ cm}^{-2}$ to $1 \times 10^{19} \text{ cm}^{-2}$ and plasma temperature between 10^6 K and 10^7 K . As can be seen in Fig. 2.6 (Section 2.4) our seven points at 0.05, 0.225, 0.350, 0.525, 0.700, 0.875 and 1.05 will bias the sample to higher temperatures and higher resulting count rates.

Simulations 9–12 have been set up to examine the effect of varying the conversion factor over the same range of column densities and plasma temperatures as simulations 5–8, but with a conversion factor appropriate to the S1 filter which (as can be seen in Fig. 2.6, Section 2.4) is much less temperature sensitive.

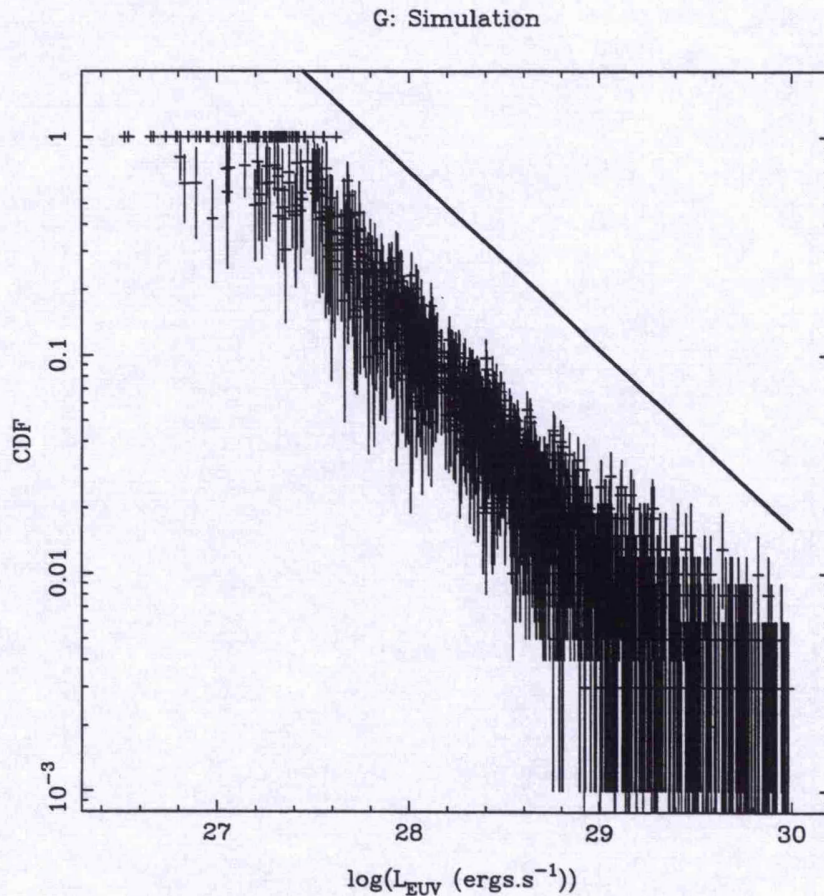


Figure B.2: 100 trials for the G star simulation to show the spread in the results. The input function is also shown, shifted in the Y-axis by an order of magnitude.

Simulations 13-14 represent the effects of altering the sensitivity of the 'survey' by increasing the observing time (and hence the ratio of detections to upper limits) for the F and G functions. These two functions represent the extremes in slope and upper and lower bounds.

The results of the simulations are listed in table B.2. Note that the median value produced by the KMPLE in this version of ASURV (1.2) is not reliable, and sometimes has an unreasonably low value, hence in each case the median has been estimated from the KMPLE itself. In the same way we have measured the upper and lower bounds of the output functions. The lower bound is defined by the point at which the function reaches 1.0, while the upper bound corresponds to the value of L at which there is one object per 'sky'.

Table B.2: Simulations

Sim (1)	True values of LF			KMPLE results										Detections	
	Slope (2)	Mean (3)	Median (4)	Mean (5)	Err (6)	Median (7)	Err (8)	LB (9)	Err (10)	UB (11)	Err (12)	α (13)	Err (14)	N (15)	%age (16)
1	-1.60	27.87	27.79	27.97	0.03	27.92	0.08	27.63	0.07	28.85	0.15	-1.71	0.16	25.2	11.4
2	-0.82	27.12	26.97	27.40	0.19	27.26	0.07	27.16	0.24	29.39	0.23	-1.03	0.15	17.6	4.4
3	-1.11	27.58	27.47	27.73	0.05	27.67	0.08	27.28	0.09	29.11	0.10	-1.44	0.11	47.9	7.0
4	-1.01	26.82	26.69	27.01	0.14	26.90	0.11	26.72	0.21	28.72	0.12	-1.34	0.16	23.5	3.2
5	-1.60	27.87	27.79	28.19	0.03	28.16	0.04	27.60	0.15	29.25	0.20	-1.39	0.11	76.5	34.5
6	-0.82	27.13	26.97	27.55	0.13	27.38	0.15	27.13	0.24	29.66	0.27	-0.95	0.11	30.1	7.5
7	-1.11	27.59	27.47	27.94	0.04	27.91	0.06	27.33	0.18	29.53	0.17	-1.20	0.07	106.8	15.6
8	-1.01	26.84	26.71	27.24	0.08	27.14	0.11	26.69	0.18	29.12	0.13	-1.15	0.11	54.1	7.4
9	-1.60	27.87	27.79	28.01	0.05	27.96	0.08	27.65	0.06	29.06	0.26	-1.52	0.20	31.7	14.3
10	-0.82	27.13	26.97	27.46	0.19	27.34	0.10	27.20	0.28	29.40	0.22	-1.05	0.14	17.0	4.3
11	-1.60	27.87	27.79	27.98	0.04	27.94	0.08	27.61	0.06	28.90	0.16	-1.63	0.14	31.5	14.2
12	-0.82	27.13	26.97	27.42	0.19	27.27	0.09	27.17	0.25	29.39	0.24	-1.04	0.17	16.7	4.2
13	-1.60	27.87	27.79	27.81	0.02	27.75	0.02	27.36	0.04	28.83	0.16	-1.55	0.11	203.5	91.7
14	-0.82	27.13	26.97	27.19	0.03	27.08	0.04	26.60	0.05	29.27	0.28	-0.89	0.06	105.6	26.5

Columns 2–4 contain the logarithms of the mean and median values of the randomly generated luminosities and their errors (see text for details).

Columns 5–8 contain the mean and median values for the KMPLE derived ELFs.

Columns 9–12 contain the upper and lower bounds for the functions measured from the graphs.

Columns 13–14 contain the best fit slope results to the functions.

Columns 15–16 list the number and %age of detections averaged over the trials.

The errors listed for the simulated functions and the ASURV results are the statistical standard deviations (1σ) on the mean of 100 runs in each case. For the median, upper bound and lower bound, for each run a lower and upper limit was measured. The resulting value is the average of the upper and lower limits, while the error is half the average difference of the upper and lower limits.

The slopes were fitted using an unweighted least squares procedure.

B.4 Discussion

Simulations 1–4

The correct ratio of detections to upper limits has been achieved with absolutely no ‘fiddling’ of the initial chosen values of the input parameters. This strongly supports the case that the simulations are a reasonable model for the WFC survey, and that the censoring pattern is similar to that of the survey. Apart from some discrepancy between the input and output K star functions (which is discussed below, the output functions strongly resemble the ELFs.

Power law index The slopes of the output functions are all steeper than the input slopes as expected (see Section 1.7.2). The slope of the F star ELF is within the 1σ statistical error on the slope of the 100 trials. With confidence we can distinguish the slopes of the F and G simulations from each other and from the K and M simulations. The K and M slopes however are indistinguishable from each other.

Mean and median Because there are so few detections below the median of the input function, the artificial truncation of the output luminosity function will push up the measured median value. The mean value of the KMPLE will be strongly dominated by the truncation of the lower luminosity function at the lower bound, and by the existence of a high luminosity tail, both raising the mean value. The simulations show that the KMPLE means and medians are indeed too high but in a systematic way. The output F, G, K and M means are as different from each other as are the means of the input luminosities. The same is true for the median values which also maintain their distinctness. There is a large spread in the output G and M mean and median values.

KMPLE errors The KMPLE produces error bars (allegedly 1σ) for each point at which the function steps - i.e. where there is a detection. To test these errors, a comparison was made between the value of the input function and the KMPLE at these points for simulations 1-4. The results of these tests are shown in table B.3, and the effects can be seen in Fig. B.1. The KMPLE is overestimating the 'true' input function at low luminosities, whilst in most cases the high luminosity end is fairly well defined. The net result is that the KMPLE does not define the luminosity function well at low luminosities. This is reflected by the total fraction of data points overlapping the 'true' function being somewhat lower than the nominal 68% that would be expected for 1σ error bars.

Truncation Both the lower and upper bounds show considerable spread. The lower bound is consistent with the effects of truncation. The large uncertainty in the upper bound is caused by the small number of objects sampled in this range. This indicates that we should not be surprised to see either a significant 'fall-off' or a high luminosity 'tail' in the simulations, and hence the ELFs.

Table B.3: Test of KMPLE errors

Simulation	KMPLE is...	Whole (percent)	26-27 (percent)	27-28 (percent)	28-29 (percent)	29-30 (percent)
1	an over estimate	61.8	-	77.8	55.8	3.0
	within error	35.3	-	17.2	42.2	97.0
	an under estimate	2.9	-	5.0	2.0	0.0
2	an over estimate	36.3	78.6	78.8	30.8	13.7
	within error	57.9	14.3	21.2	61.9	79.8
	an under estimate	5.8	7.1	0.0	7.3	6.5
3	an over estimate	49.8	-	91.6	39.9	0.0
	within error	34.9	-	7.5	45.6	33.3
	an under estimate	15.3	-	0.9	14.5	66.7
4	an over estimate	36.9	82.2	64.6	11.6	0.0
	within error	51.7	17.8	35.2	68.2	0.0
	an under estimate	11.4	0.0	0.2	20.3	100.0

Column 3 shows the percentage of all points that were in the given regions.

Columns 4-7 show the same, but divided into four quadrants, i.e. column 4 is for those data points between $\log(L_{EUV}) = 26$ and $\log(L_{EUV}) = 27$.

K and M stars With the K stars we consistently achieve a significantly higher detection rate in the simulations than was seen in the survey. The survey luminosity function shows a significant fall-off at high luminosities for both the K and M stars.

Two sample tests

The ASURV package contains a number of two-sample tests, which enable comparisons to be made between two or more samples. These are the Gehan test, the logrank test, the Peto & Peto test and the Peto & Prentice test. They are generalisations of the Wilcoxon and Savage nonparametric two-sample tests. The statistics are based on the number of data points in Sample 1 greater or less than each point in Sample 2. The tests differ in how they weight the censored points, and consequently have different sensitivities and efficiencies with different parent distributions and censoring patterns. The tests are discussed in more detail in Feigelson and Nelson (1985) and Feigelson (1990).

The tests have been applied to the simulated output functions. The results of these two-sample

tests support the caveats of Feigelson (1990), that they may be unreliable with very small or very heavily censored samples. By comparing trials from one simulation against other trials from the same simulation, it was hoped that the tests would provide confirmation that the two samples (in each case) were drawn from the same parent population. This was not the case; probabilities were seen to vary from 0.5% to 50% that the two trials were taken from the same parent distribution.

These two-sample tests have not been further pursued, as it is clear that the very high level of censorship in all these samples, and the survey ELFs, render the tests unpredictable and unreliable.

Simulations 5–12: conversion factor

In simulations 5–8, the flux to count rate conversion factor is allowed to vary over a range of values appropriate for the S2a filter (see above). The number of detections increase, and the mean and median values of the output luminosity functions also increase. While there is little change in the lower bound of the KMPLE, the upper bound is extended to higher luminosities. The slope is also seen to flatten significantly. All these effects are compatible with an increase in the number of high luminosity objects in the observed sample, caused by the bias in the selection of the conversion factor towards higher count rates.

In simulations 9–12 we perform a similar test for the S1a filter. We see that the output functions produced by varying the conversion factor (9–10) are indistinguishable from those where the conversion factor is left constant (11–12). This result was entirely expected. The WFC S1a filter shows much less sensitivity to the temperature of the input spectrum and the amount of intervening absorption than the S2a filter (see Fig. 2.6 in Section 2.4).

Simulations 13–14: sensitivity

The effect of increasing the observing time and lowering the background is to significantly improve the chance of detection. In fact the background is found to be considerably less significant than the observation time. As the ratio of detections to upper limits has increased, we see that the measured output parameters more closely match the ‘true’ input parameters. The mean and

median as measured by the KMPLE are just outside the statistical 1σ errors, while the slopes agree extremely well. We note that the lower bounds are significantly lower - produced by the detection of fainter sources and the better constrained lower limits.

References

- Abt H.A., Cardona O., 1984, ApJ, 276, 266
- Abt H.A., 1988, ApJ, 331, 922
- Allan D.J., Ponman T.J., Jeffries R.D., 1995, in preparation
- Allan P.M., 1992, Starlink User Note 13.2
- Allen C.W., 1973, *Astrophysical Quantities*. Athlone Press, London
- Avni Y., Soltan A., Tananbaum H., Zamorani G., 1980, ApJ, 238, 800
- Ayres T.R., Linsky J.L., Vaiana G.S., Golub L., Rosner R., 1981, ApJ, 250, 293
- Balachandran S., 1990, ApJ, 354, 310
- Baliunas S.L., Hartmann L., Dupree A.K., 1983, ApJ, 271, 672
- Baliunas S.L., Jastrow R., 1990, *Nature*, 348, 520
- Barber C.R., 1994, PhD Thesis, University of Leicester X-ray Astronomy Group
- Barbera M., Micela G., Sciortino S., Harnden F.R. Jr., Rosner R., 1993, ApJ, 414, 846
- Barstow M.A., Pye J.P., Bromage G.E., Fleming T.A., Guinan E., Dorren D., 1992, in Jeffrey C.S., Griffin R.E.M., eds, CCP7 Workshop No. 7, *Stellar Chromospheres, Coronae and Winds*. CUP
- Barstow M.A., Denby M., Pye J.P., Pankiewicz G.S., Bromage G.E., Gonzalez-Riestra R., 1991, *Nature*, 353, 635
- Barstow M.A., Fleming T.A., Diamond C.J., Finley D.S., 1992, in Heber U., Jeffery C.S., eds, *Atmospheres of Early-Type Stars*. Springer-Verlag, p.329

- Barstow M.A., Fleming T.A., Finley D.S., Koester D., Diamond C.J., 1993a, MNRAS, 260, 631
- Barstow M.A., Fleming T.A., Diamond C.J., Finley D.S., Sansom A.E., Rosen S.R., Koester D., Marsh M.C., Holberg J.B., Kidder K., 1993b, MNRAS, 264, 16
- Barstow M.A., Holberg J.B., Fleming T.A., Marsh M.C., Koester D., Wonnacott D., 1994, MNRAS, 270, 499
- Barstow M.A., Schmitt J.H.M.M., Clemens J.C., Pye J.P., Denby M., Harris A.W., Pankiewicz G.S., 1992, MNRAS, 255, 369
- Batten A.H., Fletcher J.M., McCarthy D.G., 1989, Publ. Dom. Astrophys. Obs., 17, 1 (as supplied on NSSDC CD-ROM)
- Bergeron P., Saffer R.A., Liebert J., 1992, ApJ, 394, 228
- Bertsch D. et al., 1992, Nature, 357, 306
- Bettis C.L., 1975, PASP, 87, 707
- Bignami G.F., Caraveo P.A., Mereghetti S., 1993, Nature, 361, 704
- Blanco C., Bruca L., Catalano S., Marilli E., 1982, A&A, 115, 280
- Bradt H., Ohashi T., Pounds K.A., 1992, in Maran S.P., ed., *The Astronomy and Astrophysics Encyclopedia*. CUP
- Bromage G.E., Kellett B.J., Jeffries R.D., Innis J.L., Matthews L., Anders G.J., Coates D.W., 1992, in Giampapa M.S., Bookbinder J.A., eds, ASP Conf. Ser. Vol. 26, *Seventh Cambridge Workshop on Cool Stars, Stellar Systems, and the Sun*. Astron. Soc. Pac., San Francisco, p. 80
- Bruner M.E., McWhirter R.W.P., 1988, ApJ, 326, 1002
- Caillault J.-P., Helfand D.J., Nousek J.A., Takalo L.O., 1986, ApJ, 304, 318
- Cameron A.C., Campbell C.G., 1993, A&A, 274, 309

Carney B.W., 1982, ApJ, 87, 1527

Cash W., 1979, ApJ, 228, 939

Catura R.C., Acton L.W., Johnson H.M., 1975, ApJ, 196, L47

Cox A.N., Shaviv G., Hodson S.W., 1981, ApJ, 245, L37

Collura A., Maggio A., Micela G., Sciortino S., Harnden F.R. Jr., Rosner R., 1993, ApJ, 416, 204

Cruddace R.G., Paresce F., Bowyer S., Lampton M., 1974, ApJ, 187, 497

Cruddace R.G., Dupree A.K., 1984, ApJ, 227, 263

David L.P., Harnden F.R. Jr., Kearns K.E., Zombeck M.V., 1995, U.S. ROSAT Science Data Center/SAO technical note, The ROSAT High Resolution Imager (HRI)

Dempsey R.C., Linsky J.L., Fleming T.A., Schmitt J.H.M.M., 1993a, ApJS, 86, 599

Dempsey R.C., Linsky J.L., Schmitt J.H.M.M., Fleming T.A., 1993b, ApJ, 413, 333

Dorman B., Nelson L.A., Chau W.Y., 1989, ApJ, 342, 1003

Drake J.J., Brown A., Patterer R.J., Vedder P.W., Bowyer S., Guinan E.F., 1994, ApJ, 421, L43

Dupree A.K., Brickhouse N.S., Doschek G.A., Green J.S., Raymond J.C., 1993, ApJ, 418, L41

Edlén B., 1942, Zs. Ap., 22, 30

Edwards S., Strom S., Hartigan P., Strom K., Hillenbrand L., Herbst W., Attridge J., Merrill K.M., Probst R., Gatley I., 1993, ApJ, 106, 372

Eggen O.J., 1973a, PAPS, 85, 289

Eggen O.J., 1973b, PASP, 85, 379

- Eggen O.J., 1973c, PASP, 85, 542
- Eggen O.J., 1983, MNRAS, 204, 391
- Favata F., Micela G., Sciortino S., 1993a, in Linsky J., Serio S., eds, *Physics of Solar and Stellar Coronae: G.S. Vaiana Memorial Symposium*. Kluwer, Dordrecht, p. 287
- Favata F., Barbera M., Micela G., Sciortino S., 1993b, in Linsky J., Serio S., eds, *Physics of Solar and Stellar Coronae: G.S. Vaiana Memorial Symposium*. Kluwer, Dordrecht, p. 303
- Favata F., Barbera M., Micela G., Sciortino S., 1993c, A&A, 277, 428
- Feigelson E.D., 1990, in Jaschek C., Murtagh F., eds, *Errors, Bias & Uncertainties in Astronomy*. Cambridge University Press, Cambridge, p. 213
- Feigelson E.D., Nelson P.I., 1985, ApJ, 293, 192
- Fitch W.S., Wiśniewski W.Z., 1979, ApJ, 231, 808
- Fleming T.A., Giampapa M.S., Schmitt J.H.M.M., & Bookbinder J.A., 1993, ApJ, 410, 387
- Fleming T.A., Schmitt J.H.M.M., Barstow M.A., Mittaz J.P.D., 1991, A&A, 246, L47
- Fleming T.A., Schmitt J.H.M.M., Giampapa M.S., 1995, ApJ, in press
- Frisch P.C., York D.G., 1983, ApJ, 271, L59
- Gagné M., Caillault J.-P., Stauffer J.R., 1995, ApJ, in press
- Gehrels N., Chen W., 1993, Nature, 361, 706
- Ghez A., 1993, PhD Thesis, Caltech.
- Gliese W., 1969, Veröff. Astron. Rechen-Inst., Heidelberg, No.22
- Gliese W., Jahreiss H., 1979, A&AS, 38, 423
- Gliese W., Jahreiss H., 1989, in Davis Philip A.G., Uppgren A.R., eds, *Star Catalogues: A*

- Centennial Tribute to A.N. Vyssotsky*. L. Davis Press, Schenectady, NY, p. 3
- Gliese W., Jahreiss H., 1991, *Third Catalogue of Nearby Stars*, Veröff. Astron. Rechen-Inst., Heidelberg, in preparation (as supplied on NSSDC CD-ROM)
- Georgantopolous I., Saxton R.D., Pye J.P., 1992, *The ROSAT PSPC PSF*. University of Leicester X-ray Astronomy Group.
- Golub L., Rosner R., Vaiana G.S., Weiss N.O., 1981, *ApJ*, 243, 309
- Gorenstein P., Harnden F.R. Jr., Fabricant D.G., 1981, *I.E.E.E. Nucl. Sc.*, NS-28, 869
- Griffin R.F., Gunn J.E., Zimmerman B.A., Griffin R.E.M., 1988, *ApJ*, 96, 172
- Grotian W., 1939, *Naturwissenschaften*, 27, 214
- Guinan E.F., Giménez A., 1993, in Sahade J., McCluskey G.E., Jr, Kondo Y., eds, *The Realm of Interacting Binary Stars*. Kluwer, Dordrecht, p. 51
- Haisch B.M., Simon T., 1982, *ApJ*, 263, 252
- Haisch B.M., 1983, in Byrne P.B., Rodono M., eds, *ASSL 102, Activity in Red Dwarf Stars*. Reidel, Dordrecht, P. 255
- Hall D.S., 1976, in Fitch W.S., ed., *Multiple Periodic Variable Stars*. Reidel, Dordrecht, p. 287
- Hall D.S., 1981, in Bonnet R., Dupree A.K., eds, *Solar Phenomena in Stars and Stellar Systems*. Reidel, Dordrecht, p. 431
- Halpern J., Holt S., 1992, *Nature*, 357, 222
- Hanson R.B., 1975, *ApJ*, 80, 379
- Harnden F.R. Jr., Branduardi G., Elvis M., Gorenstein P., Grindlay J.E. et al., 1979, *ApJ*, 234, L51
- Hodgkin S.T., Jameson R.F., Steele I.A., 1995, *MNRAS*, 274, 869

- Holt S.S., White N.E., Becker R.E., Boldt E.A., Mushotzky R.F et al., 1979, ApJ, 234, L65
- Innes D., Hartquist T., 1984, MNRAS, 209, 7
- Jahreiss H., Gliese W., 1989, in Davis Philip A.G., Upgren A.R., eds, *Star Catalogues: A Centennial Tribute to A.N. Vyssotsky*. L. Davis Press, Schenectady, NY, p. 11
- Jeffries R.D., 1995, MNRAS, 273, 559
- Jeffries R.D., Bromage G.E., 1993, MNRAS, 260, 132
- Jeffries R.D., James D.J., Prosser C.F., Stauffer J.R., Balachandran S., Bromage G.E., Caillault J.-P., Pye J.P., Stern R.A., 1994, in Caillault J.-P., ed., ASP Conf. Ser. Vol. 64, *Eighth Cambridge Workshop on Cool Stars, Stellar Systems, and the Sun*. Astron. Soc. Pac., San Francisco, p. 101
- Jeffries R.D., Jewell S.J., 1993, MNRAS, 264, 106
- Johnson H.M., 1987, ApJ, 316, 458
- Jordan C., 1976, Philos. Trans. R. Soc. London Ser. A, 281, 391
- Jordan C., Montesinos B., 1991, MNRAS, 252, 21
- Kaplan E.L., Meier P., 1958, J. Am. Statist. Assoc., 53, 457
- Kidder K.M., 1991, PhD Thesis, University of Arizona
- Koester D., Beuermann K., Thomas H.C., Graser U., Giommi P., Tagliaferri G., 1990, A&A, 239, 260
- Königl A., 1991, ApJ, 370, L39
- Kraft R.P., Burrows D.N., Nousek J.A., 1991, ApJ, 374, 344
- Kroupa P., Tout C.A., Gilmore G., 1993, MNRAS, 262, 545

Lampton M., Margon B., Paresce F., Stern R., Bowyer S., 1976, ApJ, 203, L71

Landini M., Monsignori-Fossi B.C., 1970, A&A, 6, 468

Landini M., Monsignori-Fossi B.C., 1985, ApJ, 289, 709

Landini M., Monsignori-Fossi B.C., 1990, A&AS, 82, 229

Lanning H., Pesch P., 1981, ApJ, 244, 280

Latham D.W., Stauffer J.R., 1993, private communication

Lemen J.R., Mewe R., Schrijver C.J., Fludra A., 1989, ApJ, 341, 474

Liebert J., Bergeron P., Saffer R.A., 1990, PASP, 102, 1126

Liebert J., Probst R.G., 1987, ARA&A, 25, 473

Linsky J.L., 1990, in Elvis M., ed., *Imaging X-ray Astronomy*. CUP, p. 39

Linsky J.L., Haisch B.M., 1979, ApJ, 229, L27

Maggio A., Sciortino S., Vaiana G.S., Majer P., Bookbinder J., 1987, ApJ, 315, 687

Majer P., Schmitt J.H.M.M., Golub L., Harnden F.R. Jr., Rosner R., 1986, ApJ, 300, 360

Mason K.O. et al., 1991, *Vistas Astron.*, 34, 343

Mason K.O., et al., 1995, MNRAS, 274, 1194

Mathioudakis M., Drake J.J., Vedder P.W., Schmitt J.H.M.M., Bowyer S., 1994, A&A, 291, 517

Maxson C.W., Vaiana G.S., 1977, ApJ, 215, 919

McCammon D., Burrows D., Sanders W., Kraushaar W., 1983, ApJ, 269, 107

McGale P.A., Pye J.P., Hodgkin S.T., 1995, MNRAS, submitted

McKee C., Ostriker J., 1977, ApJ, 218, 148

Mewe R., 1991, A&AR, 3, 127

Mewe R., Gronenschild E.H.B.M., van den Oord G.H.J., 1985, A&AS, 65, 511

Micela G., Sciortino S., Vaiana G.S., Schmitt J.H.M.M., Stern R.A., Harnden F.R. Jr., Rosner R., 1988, ApJ, 325, 798

Micela G., Sciortino S., Vaiana G.S., Harnden F.R. Jr., Rosner R., Schmitt J.H.M.M., 1990, ApJ, 348, 557

Micela G., Sciortino S., Favata F., 1993, ApJ, in press

Montmerle T., Koch-Miramond L., Falgarone E., Grindlay J.E., 1983, ApJ, 269, 182

Norton A.P., 1973, *Norton's Star Atlas*. 16th Edition, Gall & Inglis, Edinburgh

Noyes R.W., Hartmann L.W., Baliunas S.L., Duncan D.K., Vaughan A.H., 1984, ApJ, 279, 763

Nugent J., Garmire G., 1978, ApJ, 226, L38

Ottmann R., Schmitt J.H.M.M., Kuerster M., 1993, ApJ, 413, 710

Pallavicini R., Tagliaferri G., Stella L., 1990, A&A, 228, 403

Pan H.C., Jordan C., 1995, MNRAS, 272, 11

Paresce F., 1984, AJ, 89, 1022

Parker E.N., 1975, ApJ, 198, 205

Pasquini L., Pallavicini R., 1991, A&A, 251, 199

Pasquini L., Pallavicini R., Dravins D., 1989, A&A, 213, 261

Patten, B.M., Simon T., 1993, ApJ, 415, L123

- Patten B.M., Simon T., Strom S.E., Strom K.M., 1994, in Caillault J.-P., ed., ASP Conf. Ser. Vol. 64, *Eighth Cambridge Workshop on Cool Stars, Stellar Systems, and the Sun*. Astron. Soc. Pac., San Francisco, p. 125
- Pels G., Oort J.H., Pels-Kluyver H.A., 1975, *A&A*, 43, 441
- Peterson D.M., Baron R.L., Dunham E., Mink D., 1981, *AJ*, 86, 1090
- Petterson B.R., 1983, in Byrne P.B., Rodonò M., eds, ASSL 102, *Activity in Red-Dwarf Stars*. Reidel, Dordrecht, p. 17
- Pfeffermann E. et al., 1986, *Proc. SPIE*, 733, 519
- Pfleiderer J., Krommidas P., 1982, *MNRAS*, 198, 281
- Plucinsky P.P., Snowden S.L., Briel U., Hasinger G., Pfeffermann E., 1993, *ApJ*, 418, 519
- Pollock A.M.T., Tagliaferri G., Pallavicini R., 1991, *A&A*, 241, 451
- Pounds K.A. et al., 1993, *MNRAS*, 260, 77
- Pye J.P., Hodgkin S.T., Morley J., 1995a, in preparation
- Pye J.P., McGale P.A., Allan D.J., Barber C.R., Bertram D., Denby M., Page C.G., Rickets M.J., Stewart B.C., West R.G., 1995b, *MNRAS*, 274, 1165
- Pye J.P., McHardy I.M., 1988, in Havnes O., Pettersen B.R., Schmitt J.H.M.M., Solheim J.E., eds, *Astrophys. Space Sci. Library No.143, Activity in Cool Star Envelopes*. Kluwer, Dordrecht, p. 231
- Radick R.R., Thompson D.T., Lockwood G.W., Duncan D.K., & Baggett W.E., 1987, *ApJ*, 321, 459
- Randich S., Schmitt J.H.M.M., Prosser C.F., Stauffer J.R., 1995, *A&A*, in press
- Raymond J.C., Smith B.W., 1977, *ApJS*, 35, 419

- Raymond J.C., 1988, in Pallavicini R., ed., *Hot Thin Plasmas in Astrophysics*. Kluwer, Dordrecht, p. 3
- Reeves E.M., 1976, *Solar Phys.*, 46, 53
- Reid N., 1992, *MNRAS*, 257, 257
- Reid N., 1993, *MNRAS*, 265, 785
- Reid N., Hawley S.L., Mateo M., 1995, *MNRAS*, 272, 828
- Rosner R., 1980, in Dupree A.K., ed., *Cool Stars Stellar Systems and the Sun*. Smithsonian. Astron. Obs. Spec. Rep., No. 389, p. 79
- Rosner R., Avni Y., Bookbinder J., Giacconi R., Golub L., Harnden F.R., Jr., Maxson C.W. Topka K., Vaiana G.S., 1981, *ApJ*, 249, L5
- Rosner R., Golub L., Vaiana G.S., 1985, *ARA&A*, 23, 413
- Rosner R., Tucker W.H., Vaiana G.S., 1978, *ApJ*, 220, 643
- Rucinski R.M., 1993, in Sahade J., McCluskey G.E., Jr, Kondo Y., eds, *The Realm of Interacting Binary Stars*. Kluwer, Dordrecht, p. 51
- Sanduleak N., Pesch P., 1990, *PASP*, 102, 440
- Schmidt M., 1975, *ApJ*, 202, 22
- Schmitt J.H.M.M., 1985, *ApJ*, 293, 178
- Schmitt J.H.M.M., 1991, IAU General Assembly Proceedings (August), Buenos Aires
- Schmitt J.H.M.M., 1988, in Havnes O., Petterson B.R., Schmitt J.H.M.M., Solheim J.E., eds, *Astrophys. Space Sci. Library No.143, Activity in Cool Star Envelopes*. Kluwer, Dordrecht, p. 219
- Schmitt J.H.M.M., Pallavicini R., Mosignori-Fossi B.C., Harnden F.R. Jr., 1987, *A&A*, 179, 193

- Schmitt J.H.M.M., Golub L., Harnden F.R. Jr., Maxson C.W., Rosner R., Vaiana G.S., 1985, ApJ, 290, 307
- Schmitt J.H.M.M., Collura A., Sciortino S., Vaiana G.S., Harnden F.R. Jr., Rosner R., 1990a, ApJ, 365, 704
- Schmitt J.H.M.M., Micela G., Sciortino S., Vaiana G.S., Harnden F.R. Jr., Rosner R., 1990b, ApJ, 351, 492
- Schmitt J.H.M.M., Snowden S.L., 1990, ApJ, 361, 207
- Schrijver C.J., 1987, in Linsky J.L., Stencel R.E., eds, Lecture Notes in Physics 291, *Cool Stars, Stellar Systems and the Sun*. Springer, Berlin, p. 135
- Schrijver C.J., 1992, A&A, 258, 507
- Schrijver C.J., Dobson A.K., Radick R.R., 1992, A&A, 258, 432
- Schrijver C.J., Lemen J.R., Mewe R., 1989, ApJ, 341, 484
- Schwan H., 1991, A&A, 243, 386
- Simon T., 1992, in Giampapa M.S., Bookbinder J.A., eds, ASP Conf. Ser. Vol. 26, *Seventh Cambridge Workshop on Cool Stars, Stellar Systems, and the Sun*. Astron. Soc. Pac., San Francisco, p. 3
- Sims M.R., et al., 1990, Opt. Eng., 29(6), 649
- Skumanich A., 1972, ApJ, 171, 565
- Snowden S.L., Cox D.P., McCammon D., Sanders W.T., 1990, ApJ, 354, 211
- Snowden S.L., Hasinger G., Jahoda K., Lockman F.J., McCammon D., Sanders W.T., 1994a, ApJ, 430, 601
- Snowden S.L., McCammon D., Burrows D.N., Mendenhall J.A., 1994, ApJ, 424b, 714

- Snowden S.L., Plucinsky P.P., Briel U., Hasinger G., Pfeffermann E., 1992, ApJ, 393, 819
- Soderblom D.R., 1990, AJ, 100, 204
- Soderblom D.R., Mayor M., 1993, AJ, 105, 226
- Soderblom D.R., Stauffer J.R., Hudon J.D., Jones B.F., 1993, ApJS, 85, 315
- Stauffer J.R., 1982, ApJ, 87, 899
- Stauffer J.R., 1994, in Caillault J.-P., ed., ASP Conf. Ser. Vol. 64, *Eighth Cambridge Workshop on Cool Stars, Stellar Systems, and the Sun*. Astron. Soc. Pac., San Francisco, p. 163
- Stauffer J.R., Caillault J.-P., Gagné M., Prosser C.F., Hartmann L.W., 1994, ApJS, 91, 625
- Stauffer J.R., Giampap M.S., Herbst W., Vincent J.M., Hartmann L.W., Stern R.A., 1991, ApJ, 374, 142
- Stauffer J.R., Hartmann L.W., 1987, ApJ, 318, 337
- Stauffer J.R., Hartmann L.W., Latham D.W., 1987, ApJ, 320, L51
- Stern R.A., 1992, in Tanaka Y., Koyama K., eds, *Frontiers of X-ray Astronomy*. Universal Academy Press, Tokyo, p. 259
- Stern R.A., Antiochos S.K., Harnden F.R. Jr., 1986, ApJ, 305, 417
- Stern R.A., Bowyer S., 1979, ApJ, 230, 755
- Stern R.A., Schmitt J.H.M.M., Kahabka P., 1995, submitted
- Stern R.A., Schmitt J.H.M.M., Pye J.P., Hodgkin S.T., Stauffer J.R., Simon T., 1994, ApJ, 427, 808
- Stern R.A., Schmitt J.H.M.M., Rosso C., Pye J.P., Hodgkin S.T., Stauffer J.R., 1992a, ApJ, 399, L159

- Stern R.A., Uchida Y., Tsuneta S., Nagase F., 1992b, ApJ, 400, 321
- Stern R.A., Underwood J.H., Antiochos S.K., 1983, ApJ, 264, L55
- Stern R.A., Zolcinski M.-C., Antiochos S.K., Underwood J.H., 1981, ApJ, 249, 647
- Stocke J.T., Morris S.L., Gioia I.M., Maccacaro T., Schild R.E., Wolter A., Fleming T.A., Henry J.P., 1991, ApJS, 76, 813
- Strassmeier K.G., Hall D.S., Zeilik M., Nelson E., Eker Z., Fekel F.K., 1988, A&AS, 72, 291
- Swank J.H., Holt S.S., White N.E., Becker R.H., 1981, ApJ, 246, 208
- Swank J.H., 1985, in *The Origin of Nonradiative Heating/Momentum in Hot Stars*. p. 86
- Trümper J., 1983, Adv. Space Res., 2, 241
- Trümper J. et al., 1991, Nature, 349, 579
- Tsuru T. et al., 1989, Publ. Astron. Soc. Japan, 41, 679
- Turner M.J.L. et al., 1989, Publ. Astron. Soc. Japan, 41, 345
- Turon C. et al., 1992, The Hipparcos Input Catalogue. ESA, ESTEC, Noordwijk
- Ulmschneider P., 1991 in Ulmschneider P., Priest E., Rosner R., eds, *Mechanisms of Chromospheric and Coronal Heating*. Springer, Berlin, p. 328
- Ugoren A.R., Armandroff T.E., 1981, AJ, 86, 1898
- Ugoren A.R., Weis E.W., Hanson R.B., 1985, AJ, 90, 2039
- Vaiana G.S., 1990, in Elvis M., ed., *Imaging X-ray Astronomy*. CUP, p. 61
- Vaiana G.S., Davis J.M., Giacconi R., Krieger A.S., Silk J.K., Timothy A.F., Zombeck M.V., 1973, ApJ, 185, L47
- Vaiana G.S., Fabbiano G., Giacconi R., Golub L., Gorenstein P., Harnden F.R. Jr., Cassinelli

- J.P., Haisch B.M., Johnson H.M., Linsky J.L., 1981, ApJ, 245, 163
- Vaiana G.S., Reidy W.P., Zehnpfennig T., Van Speybroeck L., Giacconi R., 1968, Science, 161, 564
- van Altena W.F., 1969, ApJ, 74, 2
- van Bueren H.G., 1952, Bull. Astr. Inst. Netherlands, 11, 385
- Van Speybroeck L.P., Krieger A.S., Vaiana G.S., 1970, Nature, 227, 818
- Vedder P.W., Vallerga J.V., Jelinsky P., Marshall H.L., Bowyer S., 1991, in Malina R.F., Bowyer S., eds, *Extreme Ultraviolet Astronomy*. Pergamon, New York, p. 120
- Vilhu O., 1984, A&A, 133, 117
- Vilhu O., Walter F.M., 1987, ApJ, 321, 958
- Voges W., 1992, in MacGillivray H.T., Thompson E.B., eds, *Digitised Optical Sky Surveys*, p.453
- Walter F.M., 1982, ApJ, 253, 745
- Walter F.M., 1993, in Linsky J., Serio S., eds, *Physics of Solar and Stellar Coronae: G.S. Vaiana Memorial Symposium*. Kluwer, Dordrecht, p. 249
- Walter F.M., Cash W., Charles P.A., Bowyer S., 1980, 236, 212
- Walter F.M., Schrijver C.J., 1987, in Linsky J.L., Stencel R.E., eds, *Lecture Notes in Physics 291, Cool Stars, Stellar Systems and the Sun*. Springer, Berlin, p. 262
- Warwick R.S., Barber C.R., Hodgkin S.T., Pye J.P., 1993, MNRAS, 262, 289
- Weis E.W., Hanson R.B., 1988, AJ, 96, 148
- Weis E.W., Upgren A.R., 1982, PASP, 94, 475
- Weiss N.O., 1993, in Linsky J.L., serio S., eds, *Physics of Solar and Stellar Coronae: G.S.*

Vaiana Memorial Symposium. Kluwer, Dordrecht, P. 541

West R.G., Sims M.R., Willingale R., 1994, *Plan. and Space Sci.*, 42, 71

Westergaard N.J., Nørgaard-Nielsen H.U., Hansen L., Jørgensen H.E., Rasmussen I.L., Schnopper H.W., 1985, in *Cosmic X-ray Spectroscopy Mission*. ESA SP-239

White N.E., Parmar A.N., Culhane J.L., Kellett B.J., Kahn S., 1986, *ApJ*, 301, 262

White N.E., Shafer R.A., Parmer A.N., Horne K., Culhane J.L., 1990, *ApJ*, 350, 776

Withbroe G.L., 1975, *Sol. Phys.*, 45, 301

Withbroe G.L., Noyes R. W., 1977, *ARA&A*, 15, 363

Wolff S.C., Boesgaard A.M., Simon T., 1986, *ApJ*, 310, 360

Wood B.E., Brown A., Linsky J.L., Kellett B.J., Bromage G.E., Hodgkin S.T., Pye J.P., 1994, *ApJS*, 93, 287

Woolley Sir R., Epps E.A., Penston M.J., Pocock, S.B., 1970, *R. Obs. Ann.*, No.5

Acknowledgements.

First of all I'd like to thank John Pye for his patient and thorough supervision. In no way is the work in this thesis a solo effort, and I must thank all those in the X-ray astronomy group to whom I have turned during my moments of need. Notably Dick Willingale for Q, Clive Page for programming advice, Mike Watson for giving me the opportunity to go observing and of course Ken Pounds and Bob Warwick for offering me a place at Leicester.

A big sigh of relief goes out to my partners in crime for the duration of my stay in the top corridor - Peejay and Andy; together with Paul we formed Leicester's own Annus Horribilis. Thanks also to Jackie B and Mark J for being so welcoming, Paul N (for being so damned funky) and Tweedles (for being Tweedles). Thanks to the juniors: Colin for being the one person in the department with worse haircuts than myself; Richard W for sharing his dreams; Hassan for being so sexy; Matty for being a good friend. Life wouldn't have been the same without the denizens of the underpass. A ghoulish grin goes out to Gram, Luigi, Hell, Iain and Nige. Big Geoff and Little Geoff deserve a round of applause for keeping the system going and a small cheer to Richard S and Jezza (the only consistent source of parties) for help with Asterix.

To friends pre-Leicester — Pippa, Lucy, Angie, Dave, Rich, Cath — and post-Leicester — Gareth, Car, Pam, Nick, Shaun, Reiza, Elaine, Miles, Sam — thanks for all your support and fun times. An especially large hug to Jo, Sarah and Jacqui for talking/dancing/drinking/eating/listening/to/with me. Biggest thanks go to Jenny.